A Broadband Resonant Cavity Antenna Using a Metamaterial Superstrate Consisting of Two Identical Patch Arrays

Komsan Kanjanasit

Submitted for the degree of Doctor of Philosophy

Heriot-Watt University
School of Engineering and Physical Sciences

July 2015

The copyright in this thesis is owned by the author. Any quotation from the thesis or use of any of the information contained in it must acknowledge this thesis as the source of the quotation or information.

ACADEMIC REGISTRY
Research Thesis Submission

Name*:*	Komsan Kanjanasit		
School/PGI:	Engineering and Physical Sciences		
Version: *(i.e. First, Resubmission, Final)*	Final	Degree Sought (Award **and** Subject area)	PhD (Electrical Engineering)

Declaration

In accordance with the appropriate regulations I hereby submit my thesis and I declare that:

1) the thesis embodies the results of my own work and has been composed by myself
2) where appropriate, I have made acknowledgement of the work of others and have made reference to work carried out in collaboration with other persons
3) the thesis is the correct version of the thesis for submission and is the same version as any electronic versions submitted*.
4) my thesis for the award referred to, deposited in the Heriot-Watt University Library, should be made available for loan or photocopying and be available via the Institutional Repository, subject to such conditions as the Librarian may require
5) I understand that as a student of the University I am required to abide by the Regulations of the University and to conform to its discipline.

* *Please note that it is the responsibility of the candidate to ensure that the correct version of the thesis is submitted.*

Signature of Candidate*:*		Date:	9 July 2015

Submission

Submitted By *(name in capitals):*	KOMSAN KANJANASIT
Signature of Individual Submitting:	
Date Submitted:	9 July 2015

For Completion in the Student Service Centre (SSC)

Received in the SSC by *(name in capitals):*			
Method of Submission *(Handed in to SSC; posted through internal/external mail):*			
*E-thesis Submitted (**mandatory for final theses)***			
Signature:		Date:	

ABSTRACT

This thesis presents the research work on the development of a broadband resonant cavity antenna (RCA) using a two-layer metamaterial based superstrate and a wideband patch antenna as a primary source. It is shown that the resonant effect in a metamaterial consisting of two identical patch arrays can be used to design an RCA device for broadband performance. The large radiation bandwidth of 40~47% with 1-dB-ripple flat band response and the maximum gain of ~13 dBi have been achieved over the frequency band of 8~12 GHz. The dimensions of the compact RCA device are 45x45x24 mm^3 (or 1.5λx1.5λx0.8λ at 10 GHz). The two-layer metamaterial superstrate is based on an assembled structure using the two liquid crystal polymer (LCP) film substrates each with a printed patch array and separated by an air spacer of 4 mm. This air-based superstrate contributes antenna efficiency; it is lighter and requires less dielectric material. For comparison, the two-layer metamaterial superstrate design is implemented using an FR4 board and it has also been demonstrated to provide similar broadband performance in an RCA device.

The Fano resonance effect in the two-layer metamaterial design has been studied. It has been discovered that a sharp resonance can be obtained in such metamaterials when a dielectric spacer is very thin (~100 μm). Analysis of current and electric field distributions shows that the observed electromagnetically induced transparency (EIT) associated with the enhanced transmission originates from the effect of trapped-mode resonance in the two-layer metamaterials. The experimental work was carried out using both FR4 and LCP based dielectric spacers. It is shown that the LCP based metamaterials can also be used as an effective absorber near a design frequency of 10 GHz.

A broadband source antenna is based on an optimised coplanar waveguide (CPW) fed and aperture coupled patch antenna design. By exploiting the coupling effects of a triple resonances associated with the CPW structure, the aperture, and the patch element, the broadband patch antenna was obtained and used successfully in the development of the broadband RCA device. Impedance and radiation bandwidths of the practical device are measured to be as large as 41% and 43%, respectively. The new fabrication and assembly methods based on laser micromachining of the PMMA polymer have been developed for a successful construction of metamaterial structures and antenna devices.

ACKNOWLEDGMENTS

I would like to express my deep appreciation to my supervisor, Dr Changhai Wang. During the course of this study, he helped me in every aspect, support, and guidance throughout the research work.

I would like to thank Professor Jia-Sheng Hong who has offered me an opportunity of research visit at the Department of Microelectronics and Radio Engineering, St. Petersburg Electrotechnical University (ETU), St. Petersburg, Russia under the "MultiWaveS" exchange project. I am grateful to Professor Irina Munina for her support during my study visit.

I would like to thank Dr Paul Record for allowing me to use his computer facility to carry out the simulation work.

I would also like to take this opportunity to thank my research collages and friends at Heriot-Watt University, especially Soni Chandrasekar and Xin Jiang for their help in the microfabrication and laser machining work; Dr Lie Wei for characterisation of the fabricated samples; Dr Wenxing Tang and Dr Sumanth Kumar Pavuluri for assistance and discussion in microwave measurement; and Mr Mark Leonard for his support in cleanroom facilities.

Finally, I would like to thank my family, especially my parent, my grand-parents and my brothers for giving me their great and ever-lasting love and support.

TABLE OF CONTENTS

LIST OF PUBLICATIONS

K. Kanjanasit and C.H. Wang “Fano resonance in a metamaterial consisting of two identical arrays of square metallic patch elements separated by a dielectric spacer”, Applied Physics Letters, vol. 102, no. 251108, 2013.

K. Kanjanasit and C.H. Wang “A high directivity broadband aperture coupled patch antenna using a metamaterial based superstrate,” Antennas and Propagation Conference (LAPC), 2012 Loughborough, 12-13 Nov. 2012.

K. Kanjanasit and C.H. Wang “A wideband resonant cavity antenna based on a CPW fed patch source and a two-layer metamaterial superstrate”, IEEE Trans. Antennas and Propagation, (submitted)

CHAPTER 1 INTRODUCTION

1.1 Introduction

The study of antennas and metamaterials has been an active area with increased interest in research communities. In telecommunication, the X-band is an important frequency band covering a frequency range of 8–12 GHz which has been used in several commercial and scientific applications, for instance, satellite TV, space communication, oceanographic applications, and radar polarimetry. In the recent space exploration, the X-band communication is used to communicate between the Mars Reconnaissance Orbiter (MRO) and earth stations via an enormously large diameter antenna in the NASA led missions [1, 2]. Due to a compromise of the X-band radio wavelength, the impact of rain and the employment of antenna size can effectively make it a good comparison with other frequency bands such as the S-band (2–4 GHz) and the K-band (18–27 GHz). This can lead to the development of antenna devices which requires a high gain and a wide radiation bandwidth.

High-gain antennas currently used in the X-band frequency are based on aperture types such as the horn and the reflector antennas. The commercial X-band (8.2–12.4 GHz) horn antennas are available in a various range of gain performance. For example, the 20-dB standard horn antenna comes with the aperture dimension of 109 mm x 79 mm and its length is 245 mm (Flann Microwave Inc.). However, the horn antenna is bulky and heavy. For the alternative features, reflector antennas are employed in the X-band communication. The gains depend on a physical dimension of an aperture area and the feeding system is also considered in the operation. The conventional reflector antennas can cover one or two frequency bands leading to the limited bandwidth that is an issue for the broadband operation.

High performance antennas should ideally possess the attributes of compactness, high directivity, narrow beam, high efficiency, and broadband operation [3, 4]. Radiation bandwidth and gain are often the key issues in the existing antenna design. In addition, the material properties in antenna devices can influence the radiation efficiency and the related gain performance. These issues motivate the author to study design and practical demonstrations of high performance antennas based on metamaterials and resonant cavity devices.

The resonant cavity antenna (RCA) can enable radiation characteristics with high gain and narrow beam patterns [5]. The RCA device is simply formed by two reflective structures and a primary antenna. The bottom reflector is commonly made of a blank metal surface or a patterned (defected) surface or an impedance surface. The top reflector (superstrate) can be a dielectric layer or a frequency selective surface (FSS) behaving as a partially reflective surface (PRS). However, the narrow radiation bandwidth is often a nature of conventional PRS structures. In the recent works on a wideband RCA design, the percentages of the 3-dBi radiation bandwidth and the peak gains have been reported as 15.7% (16.2 dBi) [6], 20.7 % (16.5 dBi) [7], 28% (13.8 dBi) [8], 21.7% (18.2 dBi) [9], and 15% (19.5 dBi) [10]. The modified PRS design based on layered configuration of asymmetric dielectric materials or dissimilar FSS structures have shown the potential for the enhancement of radiation performance. Also, the influence of finite sizes of a PRS design has been considered. Nevertheless, the impedance-bandwidth capability of the primary antenna (radiating source) is a limiting factor in the development of broadband RCA devices.

This thesis presents the research study that has been carried out on the investigation of broadband RCA devices based on the novel characteristics of the Fano-resonance metamaterials consisting of two identical patch arrays and a wideband patch antenna based primary source. Sharp Fano resonances in a two-layer metamaterial based on symmetric square patches have been studied. A wideband coplanar waveguide (CPW) fed aperture coupled patch antenna was developed as a primary field source for the RCA device. Microfabrication, laser micromachining and assembly methods have been developed to construct the metamaterial based resonators, patch antennas, and RCA devices.

1.2 Thesis layout

Chapter 2 describes the literature review of the previous research work related to the thesis. Overall, the reviewed work covers three areas, planar metamaterials, wideband patch antennas, and resonant cavity antennas. Firstly, the previous studies on metamaterials and their characteristics are considered in terms of the material structures, coupling mechanisms, electromagnetic properties, and modelling methods. Secondly, the development of wideband patch antennas is discussed in terms of feeding and coupling methods. Finally, the existing resonant cavity antennas are described in their

structures, capabilities and limitations, especially in terms of gain and radiation bandwidth.

Chapter 3 presents the studied results of the Fano resonance in a two-layer metamaterial consisting of two identical patch arrays separated by a dielectric spacer. It has been discovered that such metamaterials can exhibit sharp Fano resonances associated with extraordinary optical transmission and spectral absorption. The behaviours of the Fano resonance are investigated in terms of designed parameters. The modelling work was carried out based on a finite element based method using the Ansoft HFSS software tool. It is shown that a high Q resonance can be obtained for a sub-millimetre spacer thickness. The origin of the Fano resonance in such materials is studied by analysing electric field and current distributions in patch elements in the two arrays. In the experimental work, the two types of designs, one with an FR4 based dielectric spacer and one using an LCP (liquid crystal polymer) thin film based spacer, are studied. Microfabrication methods have been developed to produce the metamaterials. Transmission and reflection measurements are made to study the characteristics of the Fano resonance in such materials. A good agreement between the simulation and the measurement results is obtained. Another LCP based design in which a back patch array is replaced with an un-patterned copper layer acting as a perfect reflector, is also investigated for applications as a near perfect thin-film absorber. The result shows that the near perfect absorber performance can be achieved using the resonance effects in these thin-film resonator structures.

Chapter 4 focuses on the development of a broadband micromachined patch antenna for a primary source of the resonant cavity antenna described in Chapter 5. The patch antenna is based on CPW (coplanar waveguide) fed aperture coupled design with a suspended patch above coupling aperture. Impedance matching methods are studied in order to design wideband devices. The technique of double-tuned method based on conjugate impedance matching was applied to obtain bandwidth broadening of a driven element. The aperture impedance was manipulated by tuning the impedance with a feed-line structure. The effects of device parameters were studied for optimised wideband performance. A wideband device was constructed based on microfabrication and laser micromachining techniques. The performance of the antenna was evaluated by the reflection and the radiation measurements. Excellent broadband performance was obtained.

Chapter 5 describes an implementation of broadband resonant cavity antennas. RCA devices are designed and constructed based on the results in Chapter 3 and 4. The mission focuses on design and simulation of a similar two-layer metamaterial as that in Chapter 3 but with a quarter wavelength period for patch arrays. The metamaterial was used as a superstrate in RCA devices. It was found that such design provides a better wideband characteristic of radiative Fano resonance than the design in Chapter 3 where a period is of order half wavelength. It has been found that the broad resonance behaviour is necessary for broadband RCA devices. The behaviours of metamaterials with different spacer thicknesses for antenna applications are studied using the electromagnetic image method and the plane wave excitation. Synthesis of RCA design was carried out by 3D full wave simulation using the HFSS software tool. The effect of finite size superstrates on broadband directivity was studied. Two types of RCA devices were constructed, one incorporating the air spacer based superstrate and the other one based on FR4 based metamaterial superstrate. Fabrication and construction methods were developed to produce RCA devices. The measurement of antenna performance shows that both types of RCA devices exhibit broadband performance as predicted in the design and the simulation work.

In Chapter 6, conclusions and future works will be given based on the research work described in the preceding chapters of the thesis. The main results on the investigation of sharp Fano resonance in two-layer metamaterials, the design and the implementation of a wideband patch antenna, and the design and the demonstration of broadband RCA devices, are summarised. Improvements and future areas of work are proposed.

CHAPTER 2 LITERATURE REVIEW

This review looks at three main areas of interest consisting of electromagnetic properties of metamaterials, mechanism of wideband patch antennas, and resonant cavity antennas. The motivation is to explore the extraordinary properties of metamaterials to develop a broadband resonant cavity antenna.

2.1 Metamaterials

2.1.1 Layer based metamaterials and their properties

This section addresses the material characteristics of the layer based metamaterials in electromagnetic applications. It is known that the novel properties of metamaterials and their characteristics are useful in numerous applications which relate to wave propagation and light-matter interaction. Several reviews have addressed the history of the metamaterials or engineered materials which offer the exotic properties [11-17]. The idea of the negative index of refraction was proposed by Veselago [18]. In addition, Pendry [19] has introduced the perfect lens based on that effect which is unavailable in the conventional materials. This behaviour can be used to improve the focusing effect in the light spectrum.

In the classical design, the periodic arrangement of the metallic split-ring resonators (SRRs) and short posts in metamaterials has been demonstrated [20] as shown in Fig. 2.1. The metamaterial is similar to a layer based configuration in that it exhibits unusual electric permittivity and magnetic permeability. The configuration has subsequently been modified in other forms as a square shape based SRR [21]. The same physical structure has also been introduced in other frequency regions by scaling and modifying the basic cell configurations. Consequently, the electric and magnetic responses are represented and clarified by the relative permittivity and permeability in a complex function.

Figure 2.1: Configuration of the metamaterial based on an array of the SRRs and metal posts fabricated by UCSD [20].

In application to deal with the electromagnetic field, the SRR based metamaterials have been used to demonstrate the cloaking function. The physical configuration based on a layered structure was formed by the arrangement of SRRs and showed capability in controlling the incident wave for concealing objects in the microwave band [22] as shown in Fig. 2.2. The direction of the wave propagation can be changed when interacting with the cloaking structure. The capability of that effect can make the objects invisible by bending the wave along the interface of the cloaking structure.

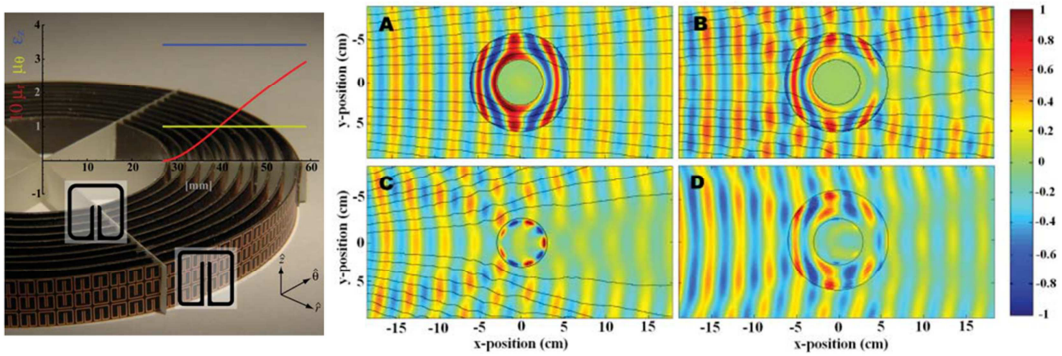

Figure 2.2: Configuration and effect of the cloaking application based on the layered SRR metamaterials in a microwave region [22].

The alternative electromagnetic loop resonator was formed by the electric ring based on an electric inductance-capacitance (ELC) resonator which was able to create the electric and magnetic response as illustrated in Fig. 2.3 [23]. The ELC array and gap inside the ELC cell play a role in the lateral coupling. Also, the modification of the capacitive elements in an ELC structure has potential for compactness in low frequency operation [24]. That element and relative shape become a new choice of designing a metamaterial.

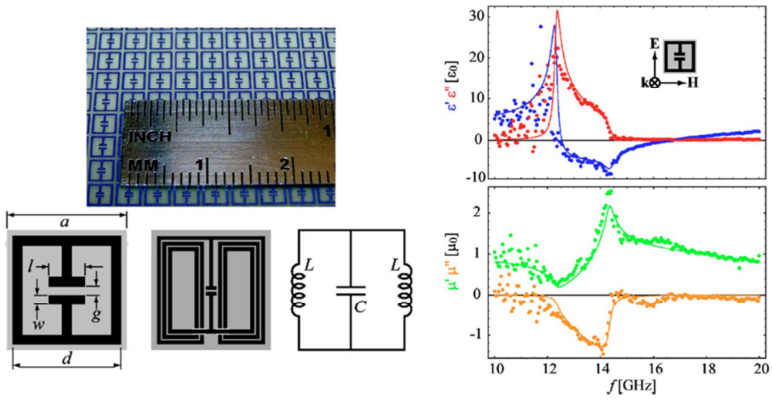

Figure 2.3: Configuration and characteristics of the metamaterial based on an array of ELC resonators and the relative permittivity and permeability responses [23].

In a two-layer structure based on symmetric elements, the metamaterial configuration was developed based on the original work of the SRR and wire inclusion. Fig. 2.4 shows a two-layer metamaterial based on a combination of wire-cuts and continuous wires providing the resonant magnetic permeability characterised by the scattering response [25]. The geometric configuration produces a crossover of the resonance between the electric permittivity and magnetic permeability [26]. In addition, a similar two layer configuration of a pair of H-shaped wires (modified wire-cut) seen in Fig. 2.5 has been studied to show the similar property [27]. Fig. 2.6 shows the structure of a pair of fishnet based elements that have been used to produce a metamaterial showing the property of negative index [28].

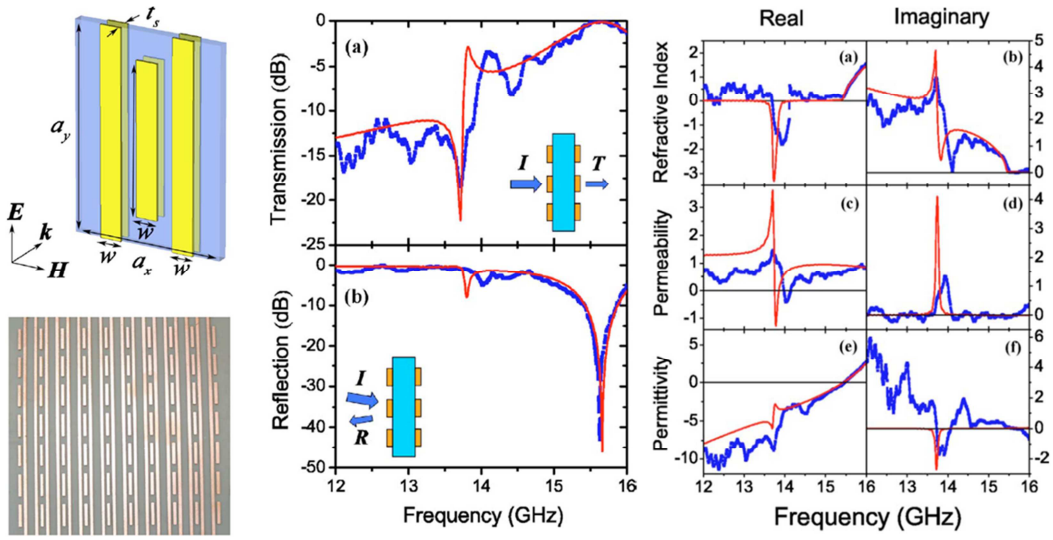

Figure 2.4: Configuration and characteristics of the two-layer metamaterial based on an array of the short wires pair and the refractive index, relative permittivity and permeability responses [25].

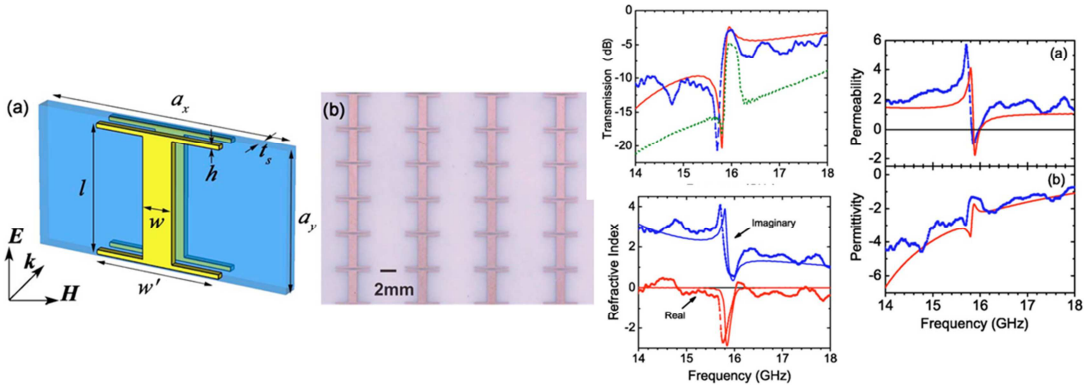

Figure 2.5: Configuration and characteristics of the two-layer metamaterial based on an array of H-shaped elements in transmission, refractive index, relative permittivity and permeability responses [27].

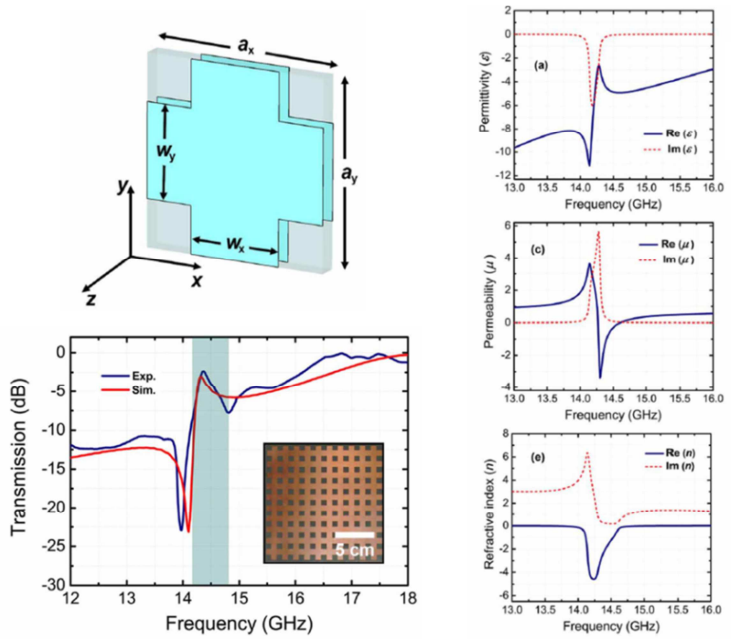

Figure 2.6: Configuration and characteristics of the two-layer metamaterial based on the fishnet pattern in terms of refractive index, relative permittivity and permeability responses [28].

To understand the metamaterial mechanism, the coupling effect on the metallic elements has been addressed in terms of dipole-dipole interaction [29]. With the assistance of the electromagnetic analogue in nanostructures, the coupling effect was associated with the plasmon response of a hybridisation mode which explains the energy level of the field-matter interaction [30]. In microwave region, the two-layer metamaterials formed by the wire cut elements [31, 32] and ELC resonators [33] have been reported based on the effect of the plasmon hybridisation resulting in the resonance behaviour in the scattering response as shown in Fig. 2.7.

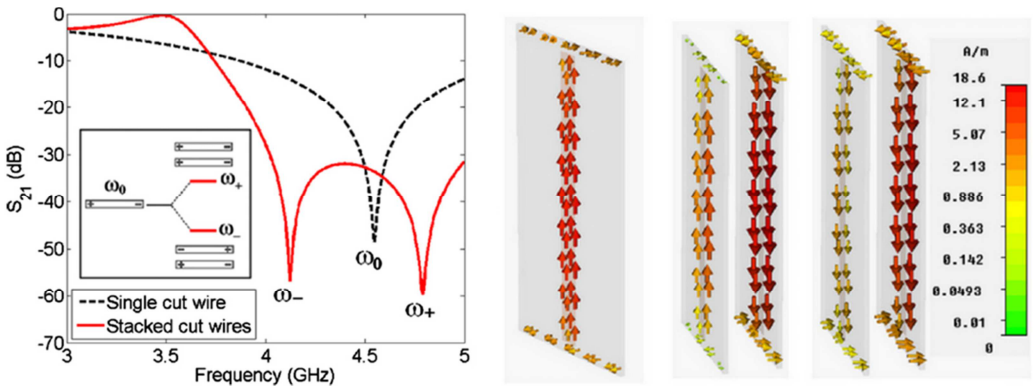

(a)

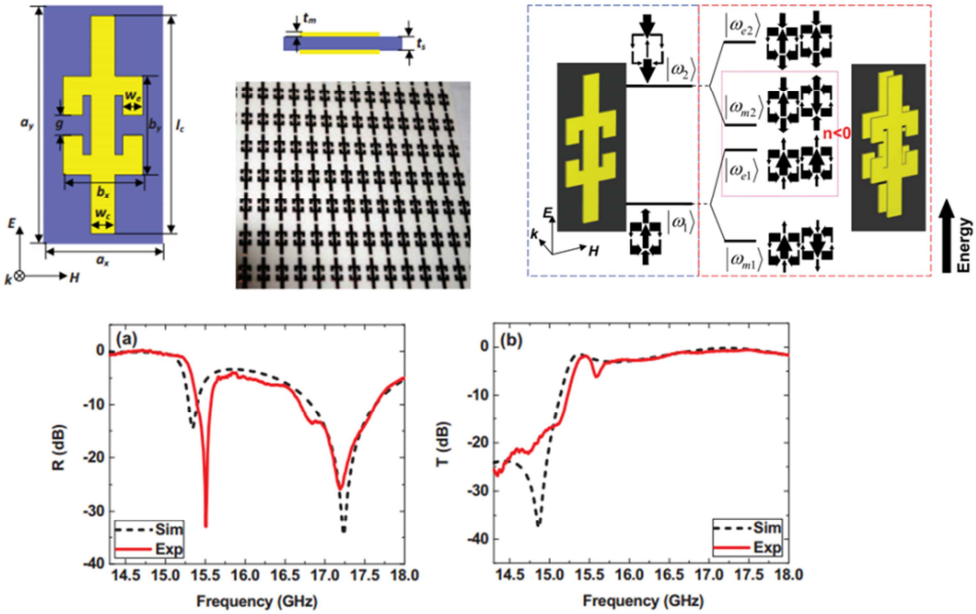

(b)

Figure 2.7: Configurations and characteristics of the metamaterials based on a hybridisation scheme, (a) pair of cut-wires [31] and (b) pair of ELC resonators [33].

2.1.2 Plasma frequency of metamaterials

The behaviour of the frequency response in complex media has been studied and in that the plasma frequency can be obtained by engineering the physical structure of artificial dielectrics [34]. The plasma effect is a phenomenon which can be used for the enhancement of the radiation characteristics. The artificial dielectric was showed to have an effective refractive index of less than unity in 1953 [35]. The configurations were firstly formed by an array arrangement of conducting rods (wires) and secondly the parallel structure of perforated plates. In 1996 Sievenpiper et al. [36] introduced the

3D wire-mesh configuration to provide the plasmon effect at the frequency of 6.5 GHz. Pendry [37, 38] has also documented the charge behaviour to obtain the plasma mode in a microwave region based on a periodic structure of the conducting wires. To deal with the material property, the dielectric function was defined to exhibit a zero electric permittivity that is associated with the plasma frequency. Consequently, this effect is a potential phenomenon to enhance the radiation capability.

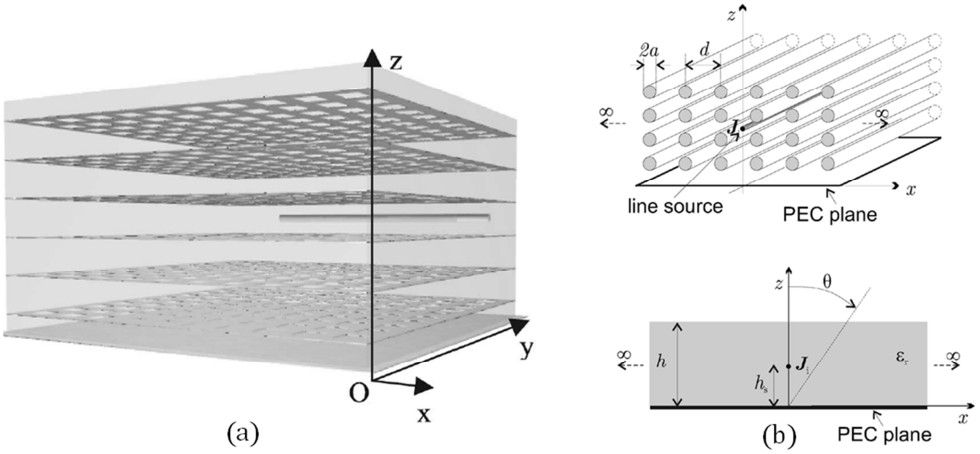

Figure 2.8: Configurations of the directive radiation metamaterials with an embedded source and the periodic elements, (a) the metallic grid structures [39], and (b) the conducting rods [40].

The radiation mechanism based on a zero or near-zero permittivity is shown in Fig. 2.8. The directive emission structure with a zero permittivity (epsilon) was addressed by Enoch et al. that the plasma frequency is involved in the periodic grid structure with an embedded source [39]. In addition, the periodic 2D rod structure behaving as an epsilon-near-zero (ENZ) medium was used to produce directive radiation [40]. Theoretical analysis based on a zero or ENZ has revealed the characteristics of the radiation behaviour of the engineered materials [41]. In association with magnetism [42], Pendry has also addressed the magnetic plasma frequency in the coupled structures which can influence the resonance effect of the permeability. It is shown that the characteristic of the resonant permeability based on the internal capacitance and inductance can be determined by the physical dimensions of a unit-cell in the periodic configurations.

2.1.3 Resonance effects in metamaterials

Light interaction with metamaterials has been observed to provide the effect on the surface plasmon resonance (SPR) [43]. The appearance of this resonance behaviour can imply a significant contribution to the capability of absorption in metamaterials. The existence of surface plasmon (SP) has also been observed in the microwave region [44]. The creation of the periodic metallic grating in the optical region has led to the resonant transmission as shown in Fig. 2.9 [45]. The key parameter was the thickness of the metal elements in the grating causing the anti-parallel coupled SP between the top and bottom surfaces associated with the waveguide resonance.

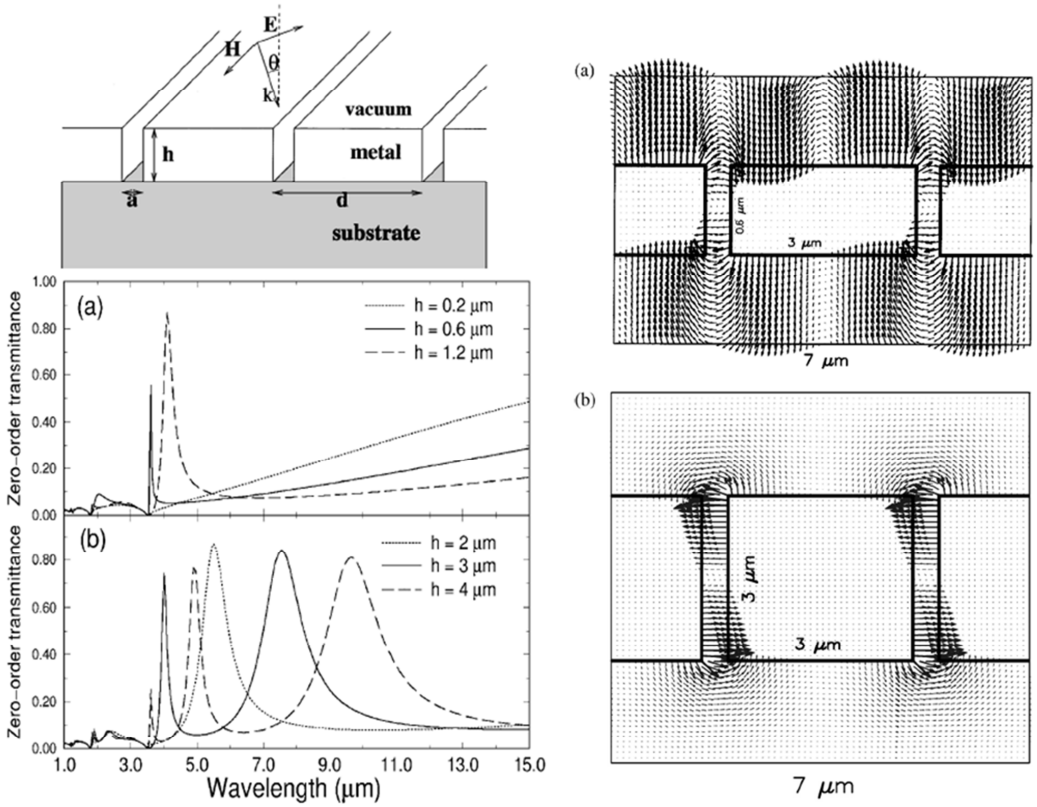

Figure 2.9: Configuration and characteristics of the transmission resonance in an optical region based on a periodic metallic grating structure [45].

Furthermore, the early experimental work using a perforated metal plate or an array of holes showed the behaviour of extraordinary optical transmission [46]. This effect can lead to the theory of the extraordinary transmission that deals with the zero-order transmittance based on geometric parameters of an array of holes [47].

In addition, the double metallic grating has been studied to show the same behaviour and this can result in a broad spectral region [48]. The extraordinary electromagnetic transmission was also shown in the microwave region around 60 GHz [49]. A model based on an electrical circuit associated with the extraordinary transmission has been developed [50, 51].

Apart from the perforated metal plate and the periodic grating configuration, a coupling mechanism based on an asymmetric inter-element cell has been observed under the resonance condition in several electromagnetic spectral bands in the microwave, THz, and optical frequency regions. The resonance behaviour originates from the ionisation showing the effect of a scattering phenomenon with an asymmetric line-shape response [52]. As reviewed in [53-56], there is strong evidence to show that the Fano resonance behaviour in the nanostructures and metamaterials originates from electromagnetic interaction of coupled oscillations. This effect is based on the constructive and destructive interference. The response can dominate at the adjacent locations in the spectral frequencies or exciting energy. The behaviour is described as enhancement and suppression. The resonant effect leads to the behaviour of super-radiance and sub-radiance modes, respectively. The Fano effect can also exhibit in the visible region known as bright and dark modes. The effect can results in radiation enhancement and the trapped absorption.

The asymmetric split ring (broken ring) resonator is an example configuration in which the field interaction results in a resonance effect. The resonance effect originates from the trapped-mode characteristics as shown in Fig. 2.10 [57]. A sharp resonance is shown resulting in the trapped-mode at the frequency region of an asymmetric line-shape. In addition, the surface current distribution in the resonant elements was shown as an anti-phase configuration which is a characteristic signature of the Fano resonance effect. Alternatively, a similar effect was found in an array of asymmetric dipole strips [58]. It is evident that the asymmetric line-shape resonance is obtained in a spectral region in which a resonant element is able to resonate by field interaction and another one can oscillate by near-field coupling. The term of the electromagnetically induced transparent (EIT) behaviour in optics is associated with the resonant transmission due to light matter interaction in a medium [59]. The electromagnetic activity of the broken square ring based design has been studied in the THz region, exhibiting the resonance characteristics associated with the EIT behaviour [60]. A strong resonance condition

depends on the geometric dimensions of the broken sectors as shown in Fig. 2.11. A similar effect in the THz metamaterial is also named as plasmon-induced transparency in the coupling mechanism [61]. The effect is described as a coincidence of interaction of two resonances in the same frequency window. The effect can modify the characteristic of susceptibility in their medium.

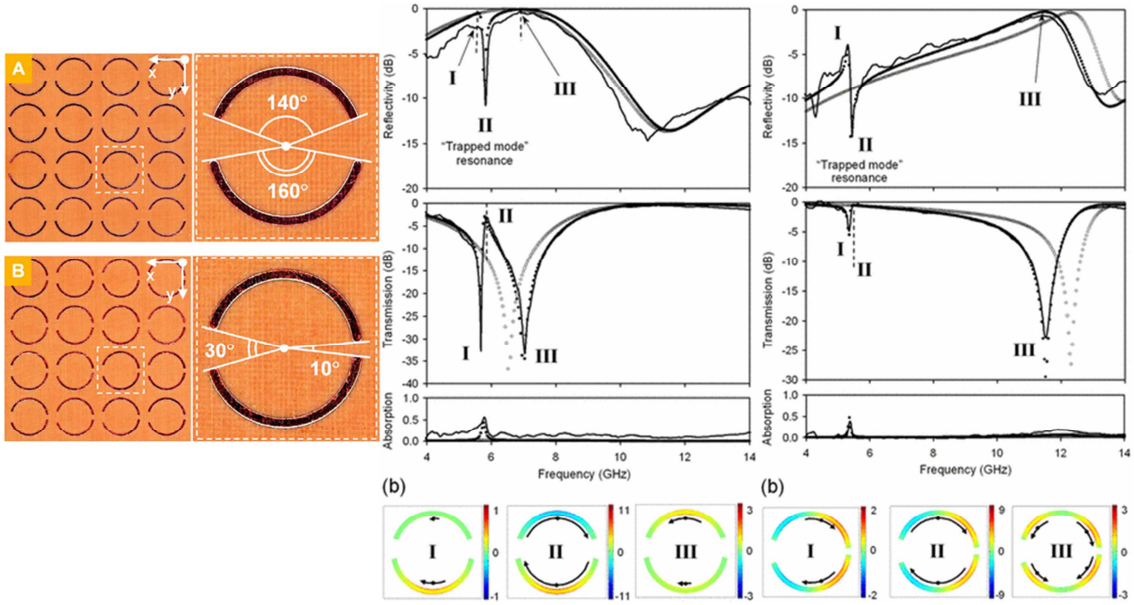

Figure 2.10: Configuration and characteristics of the microwave metamaterial based on the broken ring and the trapped-mode resonance [57].

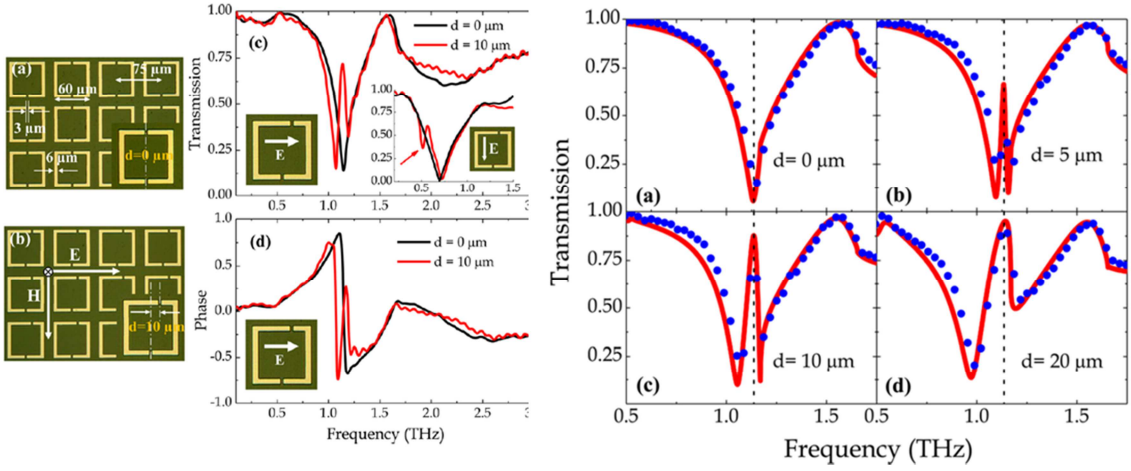

Figure 2.11: Configuration and characteristics of the THz metamaterial based on the asymmetric broken ring and the EIT effect [59].

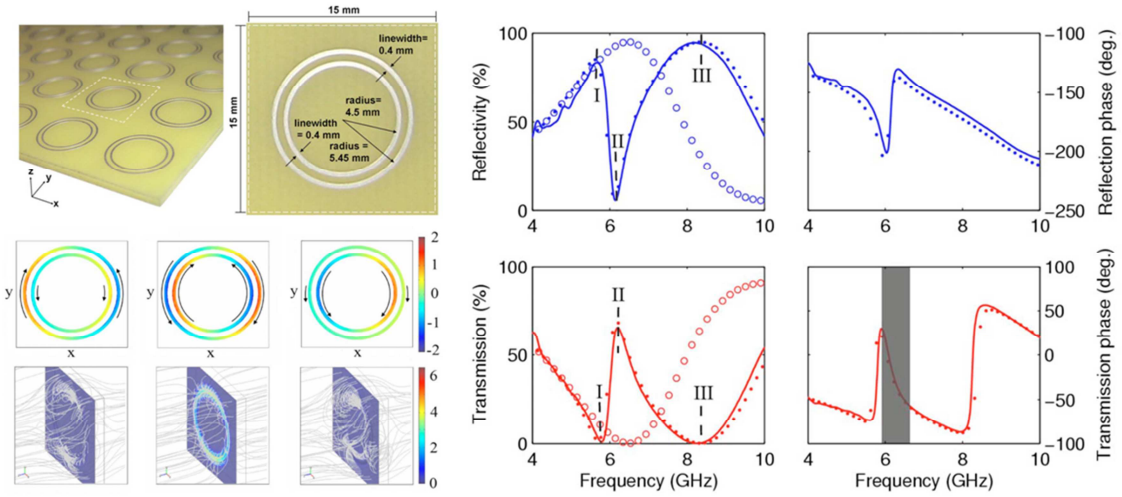

Figure 2.12: Configuration and characteristics of the microwave metamaterial based on coupled concentric ring resonators and the EIT effect [62].

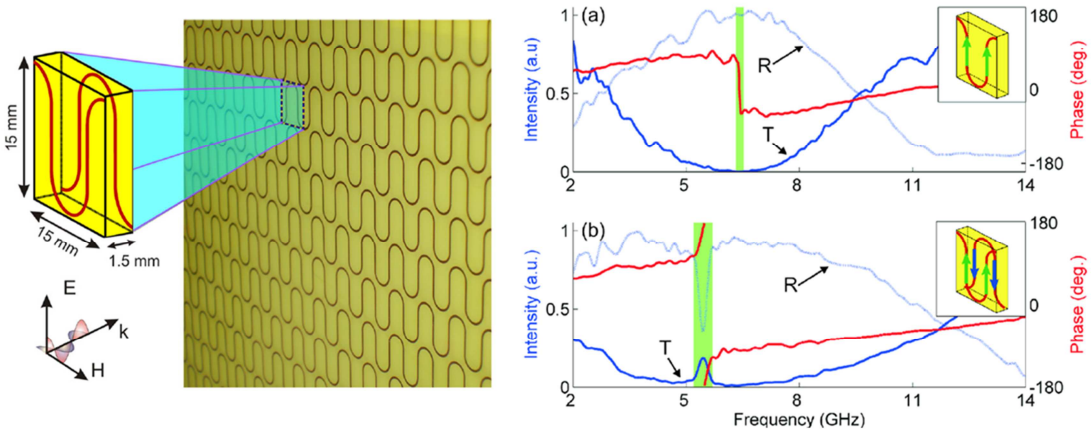

Figure 2.13: Configuration and characteristics of the metamaterial based on the bilayer fish-scale patterns and the EIT effect [63].

Apart from broken elements, an array containing a pair of concentric rings in a cell was shown to exhibit the EIT-like behaviour at the frequency of 6 GHz as shown in Fig. 2.12 [62]. The electromagnetic benefit is that the response is independent of polarisation. The asymmetric current distribution was also illustrated as the trapped-mode resonance.

Alternatively, a two-layer structure based on a fish-scale pattern was provided as the resonant transmission [63] as seen in Fig. 2.13. The patterns were created on both sides on a dielectric slab in a flipped alignment. It is evident that the characteristic of the anti-phase current configuration appears to cause a resonance condition in the electromagnetic behaviour.

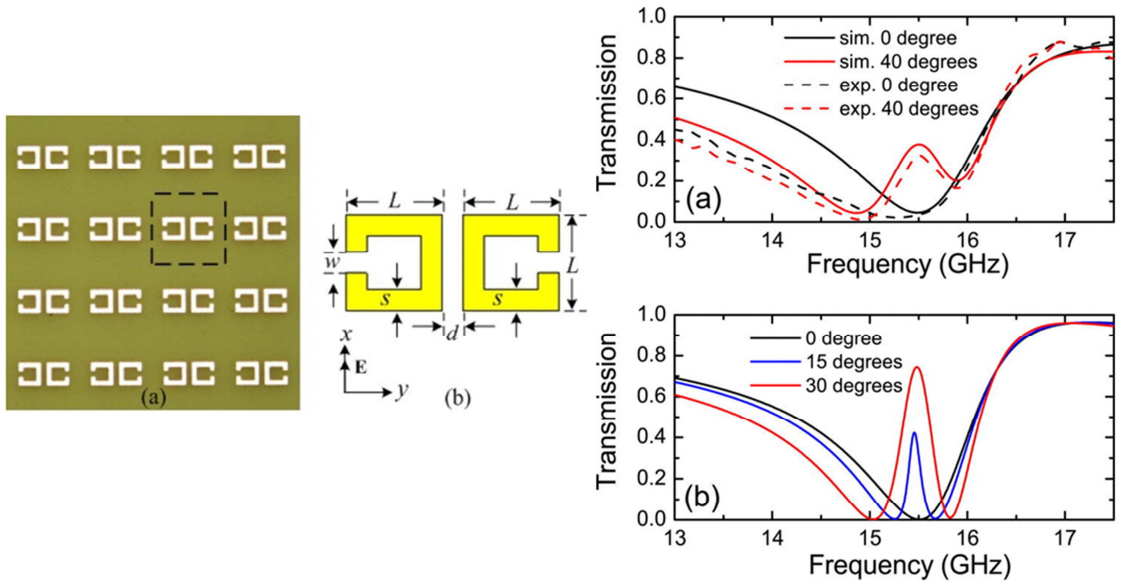

Figure 2.14: Configuration and characteristics of the microwave metamaterial based on the side coupling SRR and the EIT effect [64].

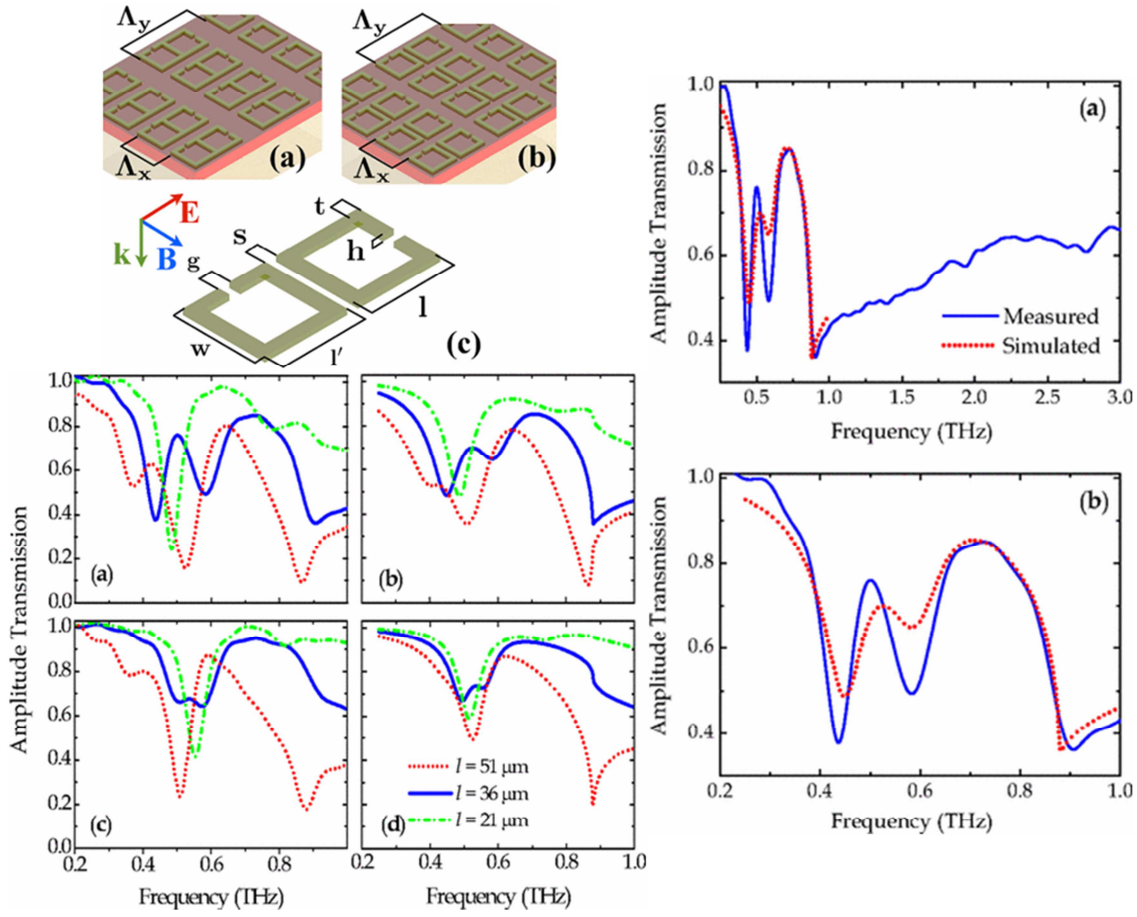

Figure 2.15: Configuration and characteristics of the THz metamaterial based on the side-coupling and touching SRRs, and the EIT effect [65].

In accordance to the side-coupling interaction, coupled SRRs can interact with the phase coupling dealing with the incident angle in a microwave region as shown in Fig. 2.14 [64]. The transmission characteristic showed the behaviour of the EIT-like resonance depending on an incident angle of the field excitation. The zero transmission occurred at the normal angle. A variation of the incident angle affected the magnitude of the resonant transmission. In THz operation, two types of the coupling element based on the proximate and merging topology of two SSRs showed the EIT behaviour as shown in Fig. 2.15 [65]. The optimised structure shows the resonance condition of coupling effect resulting in the strong EIT-like behaviour.

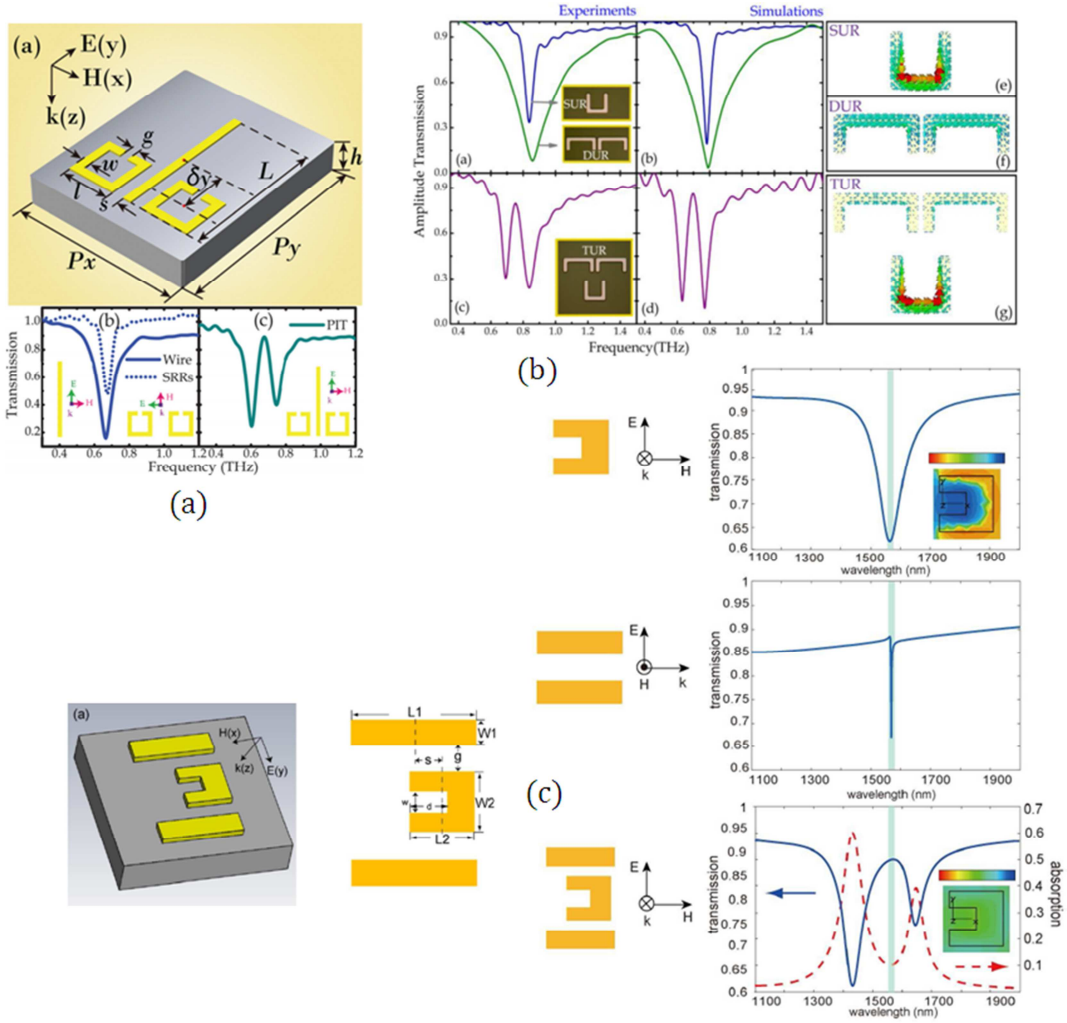

Figure 2.16: Configurations and characteristics of the metamaterials based on an inter-element coupling, (a) THz EIT metamaterial [66], (b) THz plasmon-induced transparent metamaterial [67], and (c) the near-infrared EIT metamaterial [68].

In addition, the THz metamaterial is obtained using an inter-element configuration in connection with the plasmon-induced transparency as shown in Fig. 2.16 [66-68]. The interference of two dark (dip) modes was from the interaction of the symmetric resonators interacted with the strip. It is shown that dark modes occurred at the same frequency as that found in EIT behaviour. The appearance of a peak transmission was induced by the coupling interference.

2.1.4 Resonant metamaterial absorbers

The metamaterials possess a complex function of the dielectric permittivity leading to applications as compact absorbers. The resonance condition causes a loss component that is able to deal with the matching condition of wave impedance. In behaviour, the characteristics of zero-transmission and zero-reflection are required in order to obtain a perfect absorption. In principle, the absorption characteristics can be associated with the complex refraction index in which the imaginary part represents absorption effect. The well-known absorber configuration is a Salisbury screen which is the classical structure based on a dielectric material with a quarter-wave thickness [69, 70].

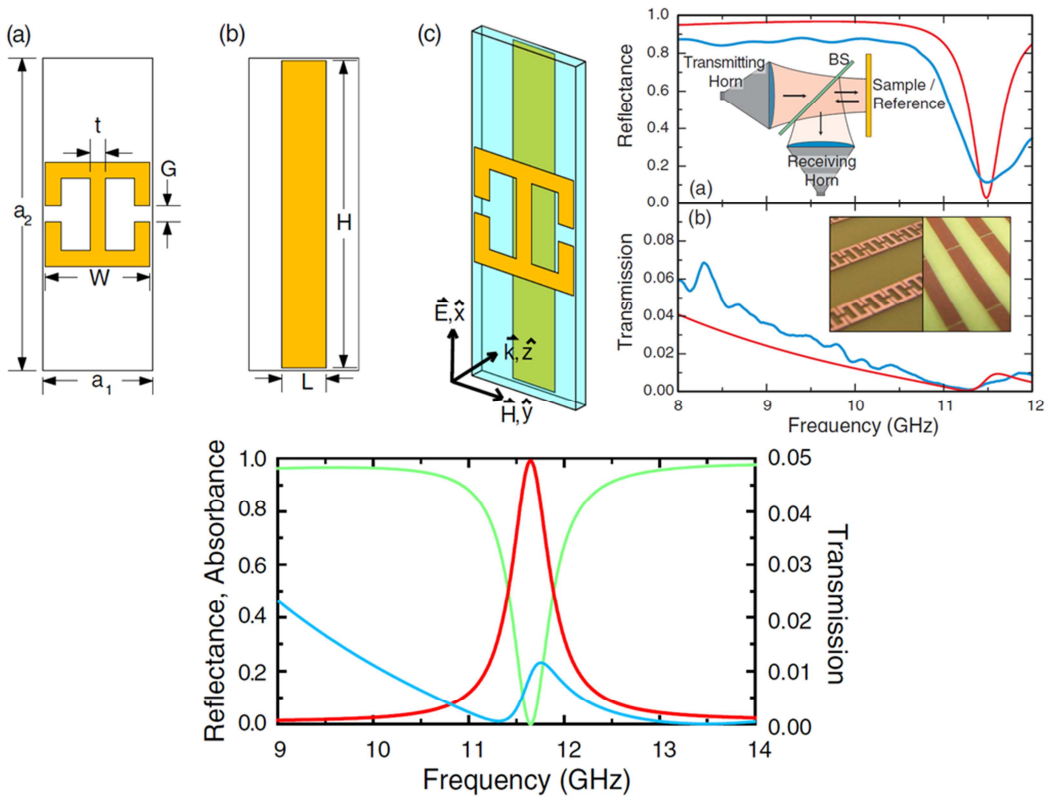

Figure 2.17: Configuration and characteristics of the perfect resonant metamaterial absorber based on a two-layer of the ELC and cut-wire structures [72].

The resonant metamaterial perfect absorber was reviewed in innovative configurations that are capable of trapping the electromagnetic field incidence in a variety of frequency ranges [71]. The interest in metamaterial-based absorbers is growing in a low profile and a wideband device. Landy et al. have introduced the design of a two-layer metamaterial formed by electric resonators and cut-wires on a dielectric FR4 based slab of thickness of 0.2 mm. The performance was able to operate at the microwave frequency of 11.5 GHz as shown in Fig. 2.17 [72]. The wave-impedance matched condition on an electromagnetic interaction was obtained resulting in the perfect absorption.

In addition, the multilayer FR4-slab configuration based on identical electric ring resonators (ERRs) was investigated and experimented in the trapped-mode characteristics as seen in Fig. 2.18 [73]. The observations of the current distribution were also depicted by the anti-phase configuration which was referred as the physical insight of a resonance condition.

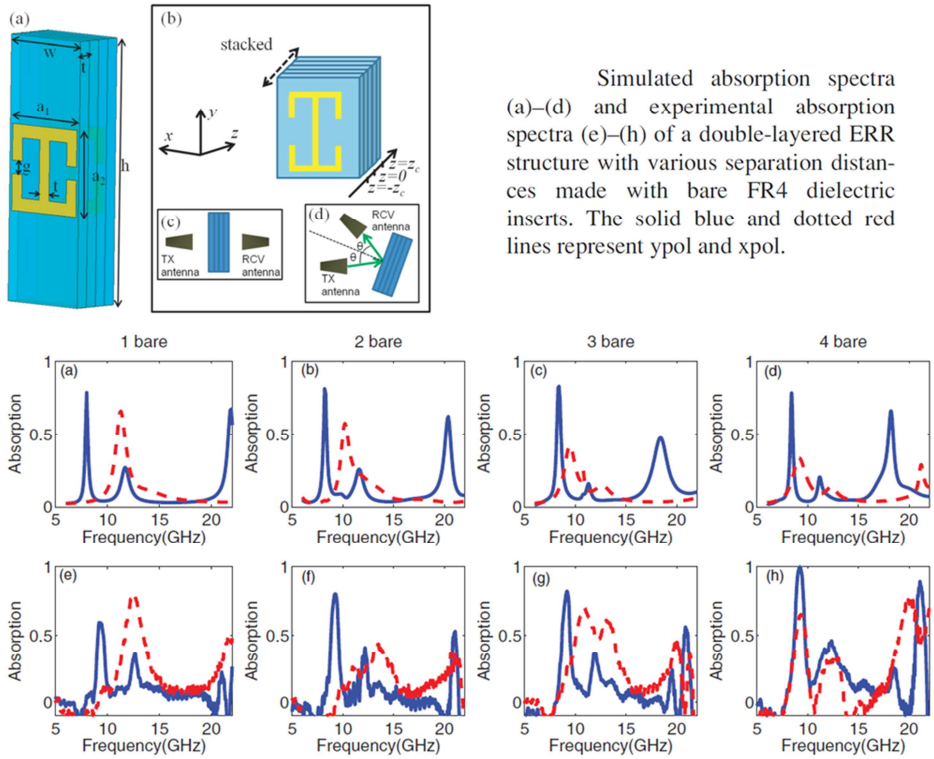

Simulated absorption spectra (a)–(d) and experimental absorption spectra (e)–(h) of a double-layered ERR structure with various separation distances made with bare FR4 dielectric inserts. The solid blue and dotted red lines represent ypol and xpol.

Figure 2.18: Configuration and characteristics of the metamaterial based on two layers of the symmetric electric ring resonators and the trapped-mode resonance [73].

The modification of the absorber configuration based on a high impedance surface (HIS) is made by a patch-type FSS structure with a low profile [74]. The electromagnetic activity is based on a phase response in a dielectric medium. Two layers of foam and dielectric were incorporated to optimise the electrical thickness in a matching condition with the perfect metal conductor. The performance was reported by the measured reflectivity bandwidth 18~32% with respect to the electrical thickness 0.7λ~0.14λ in the X band.

The perfect resonant absorber metamaterial is composed of a complex pattern as a flower-shaped resonator positioned on a FR4 slab with a blank metal surface as seen in Fig. 2.19 [75]. The performance of the perfect absorber was reported and the resonant frequency was dominated by the geometric dimensions of the flower-shaped cells. Also, the condition of the surface current configuration was considered as an anti-phase which is a key effect of the resonance condition.

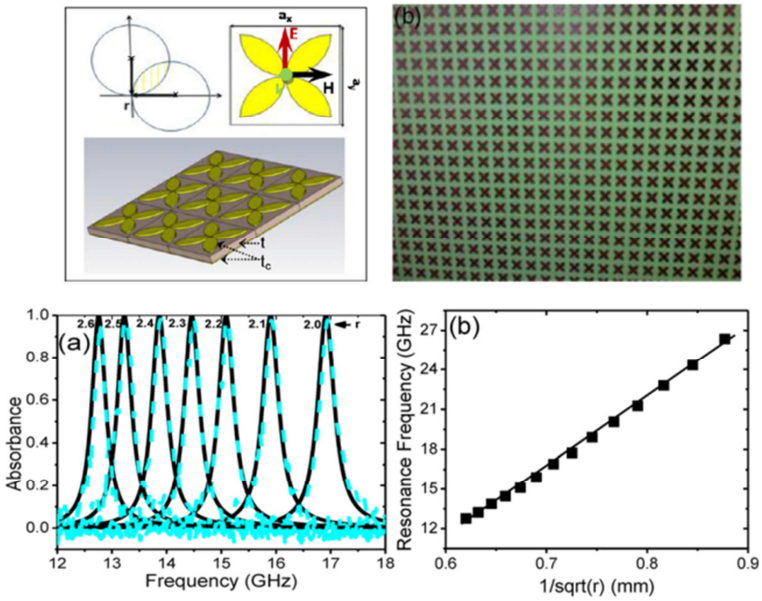

Figure 2.19: Configuration and characteristics of the resonant metamaterial absorber based on the flower-shaped array on the perfect metal conductor [75].

The classical SRR structure based on a magnetic response was modified to form the narrowband absorbers in minimising the reflection and transmission magnitude at the low frequency [76]. Fig. 2.20 shows a physical configuration that the unit cell is formed by the collection of SRRs positioned on a total reflective surface. In resonance, the coupling mechanism is equivalent to the oscillating circuit with LC elements. The geometric parameters of the design play a role in the resonant frequency.

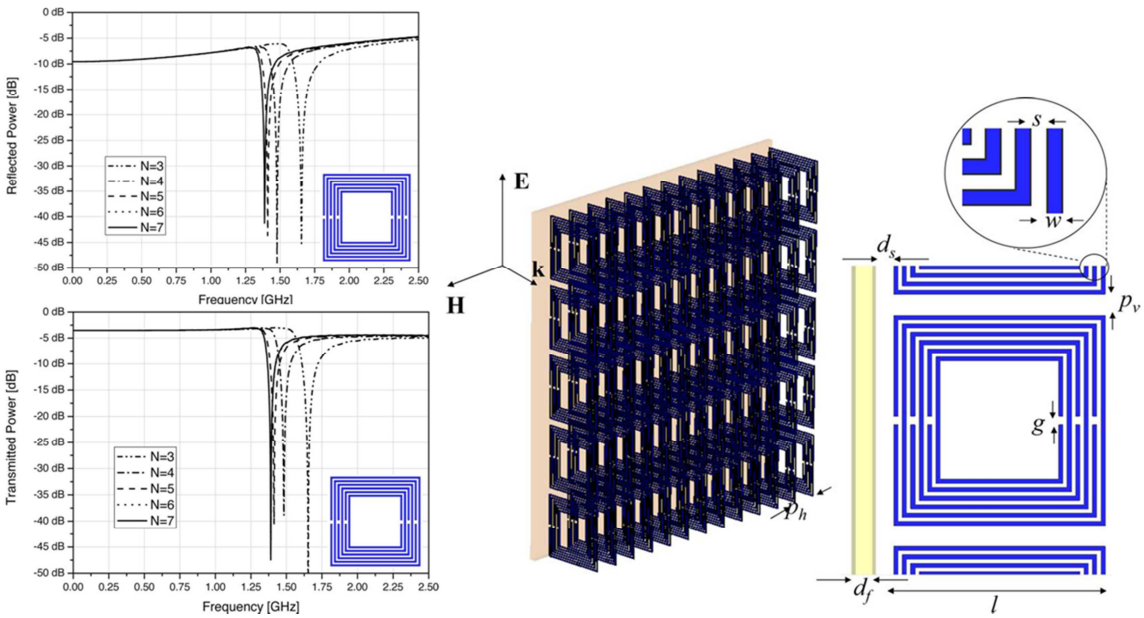

Figure 2.20: Configuration and characteristics of the resonant metamaterial absorber based on array of the miniaturised SRR resonators on the perfect metal conductor [76].

2.2 Wideband patch antennas

The challenging issue in development of wideband patch antennas is impedance matching over a wide range of frequencies. To overcome this problem, the multiple resonance based method has been introduced in design of wideband patch antenna devices. For example, the stacked patch structure is conventionally implemented that the resonant frequencies depend on a number of patch elements [77, 78]. The resonant elements are able to resonate in the adjacent frequencies in order to extend the impedance bandwidth. The patches can be usually considered as a driven component and a parasitic element in the case of two stacked patches. However, a disadvantage of the stacked patch antenna is the increase of the total thickness of the antenna due to the dielectric layers between layered patch elements.

The feeding techniques can be divided into two methods consisting of the connected and the coupled feeding schemes. In the first method, a conducting probe or a microstrip line is directly connected to a patch element. In the second method, the feeding element and the patch are separated by a dielectric or an air spacer. In this case, a small gap (distance) is able to create a coupling effect associated with the interference of the reactive near-field property that plays a role in the resonance behaviour of the antenna. This configuration can introduce another resonant condition leading to the enlargement of impedance bandwidth.

In a more complex technique for bandwidth enhancement in the directly connected approach, a structural modification of a patch element is constructed by slotting the resonant patch. This technique is useful for producing a compact antenna with enhanced bandwidth. The benefit is that a single resonant patch is able to produce a double resonance effect [79-82]. As shown in Fig. 2.21, the antenna structures based on a U-slotted and an E-shaped patch can have two closely coupled resonant frequencies which can improve impedance bandwidth. The coupling of guided modes is necessary to create adjacent resonances. The impedance bandwidth of the U-slotted and E-shaped patch fed by a probe are in a range of 20~40%.

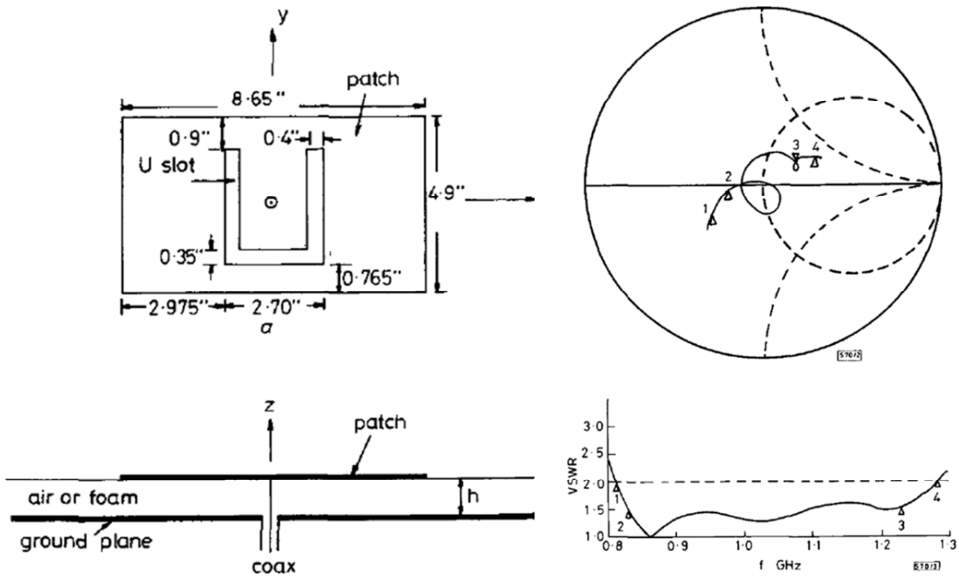

(a)

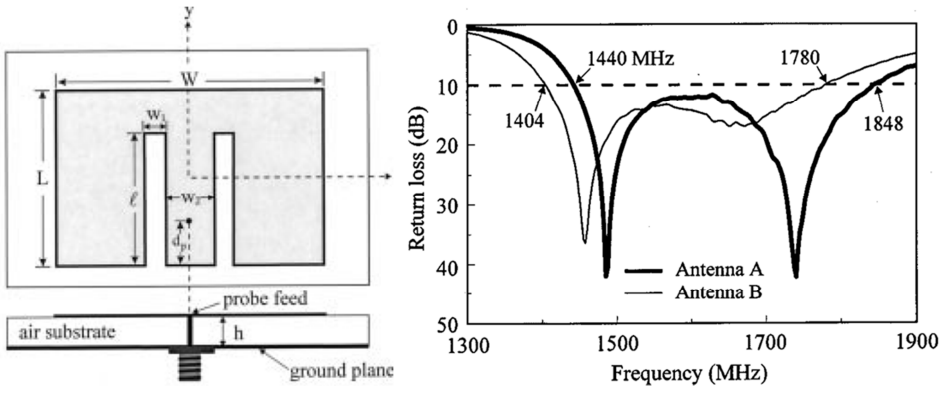

(b)

Figure 2.21: Configuration and characteristics of the wideband single patch antennas based on a slotted technique, (a) the U-slotted patch [79], and (b) the E-shaped patch [80].

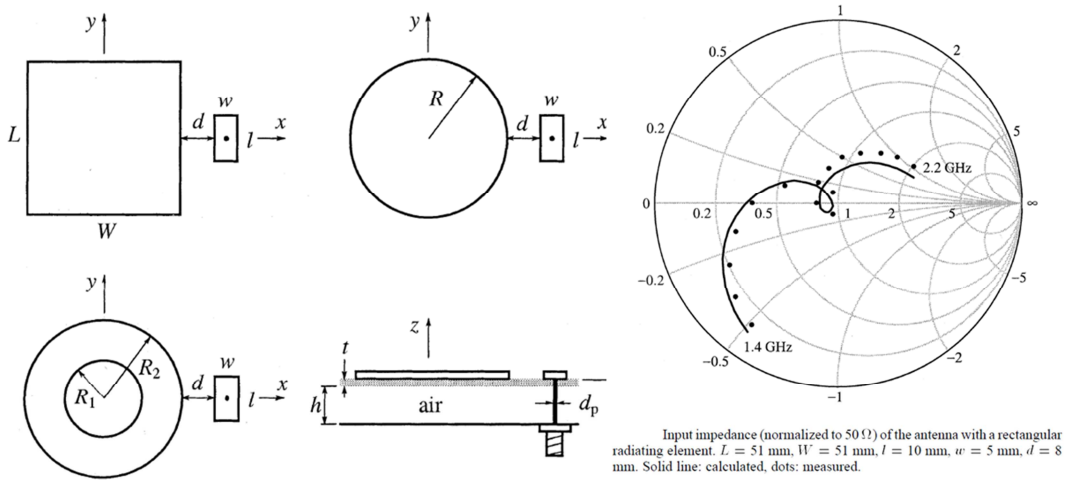

Input impedance (normalized to 50 Ω) of the antenna with a rectangular radiating element. $L = 51$ mm, $W = 51$ mm, $l = 10$ mm, $w = 5$ mm, $d = 8$ mm. Solid line: calculated, dots: measured.

(a)

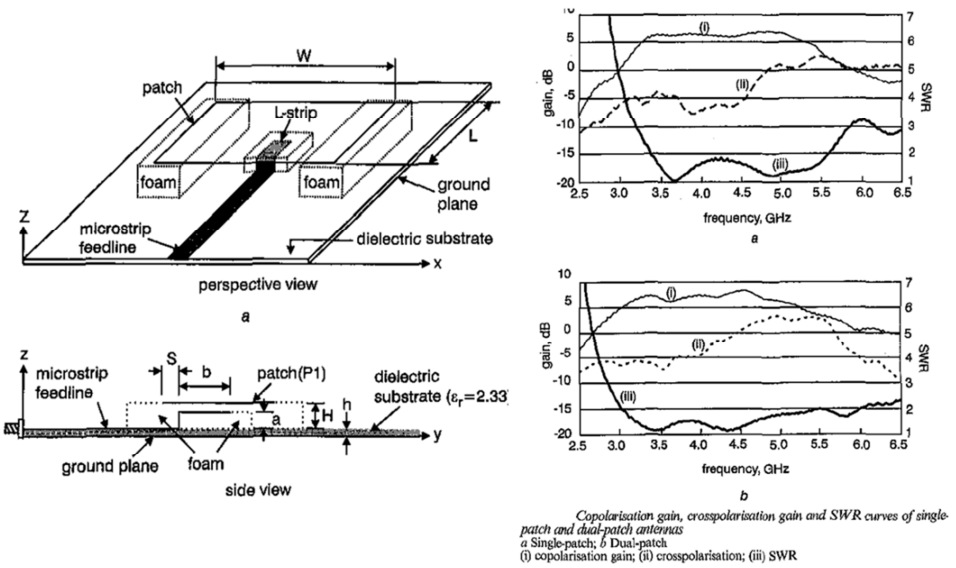

Copolarisation gain, crosspolarisation gain and SWR curves of single-patch and dual-patch antennas
a Single-patch; *b* Dual-patch
(i) copolarisation gain; (ii) crosspolarisation; (iii) SWR

(b)

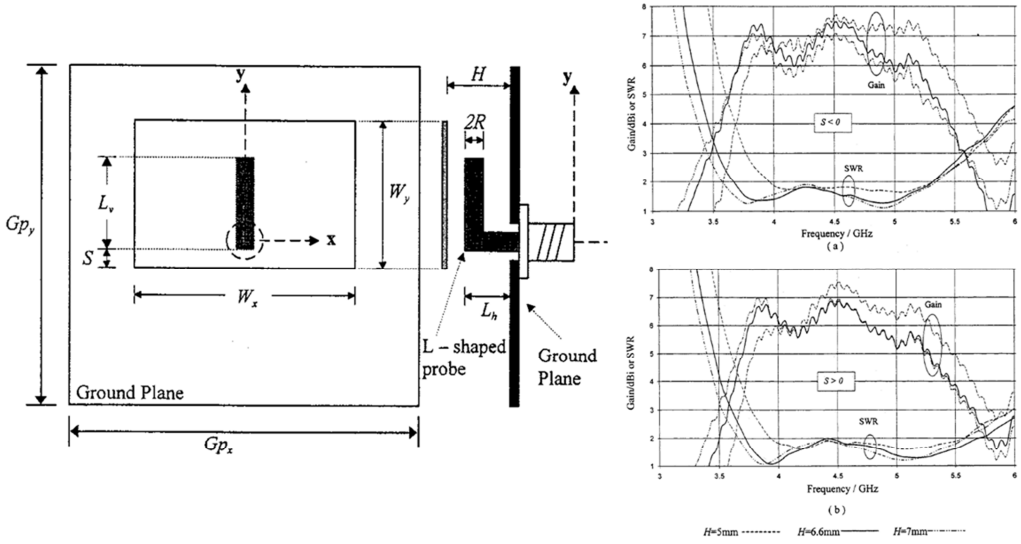

(c)

Figure 2.22: Configuration and characteristics of the wideband single patch antennas based on the coupled-feed technique, (a) capacitive feeding probe [83], (b) L-shaped feeding microstrip [85], and L-shaped feeding probe [86].

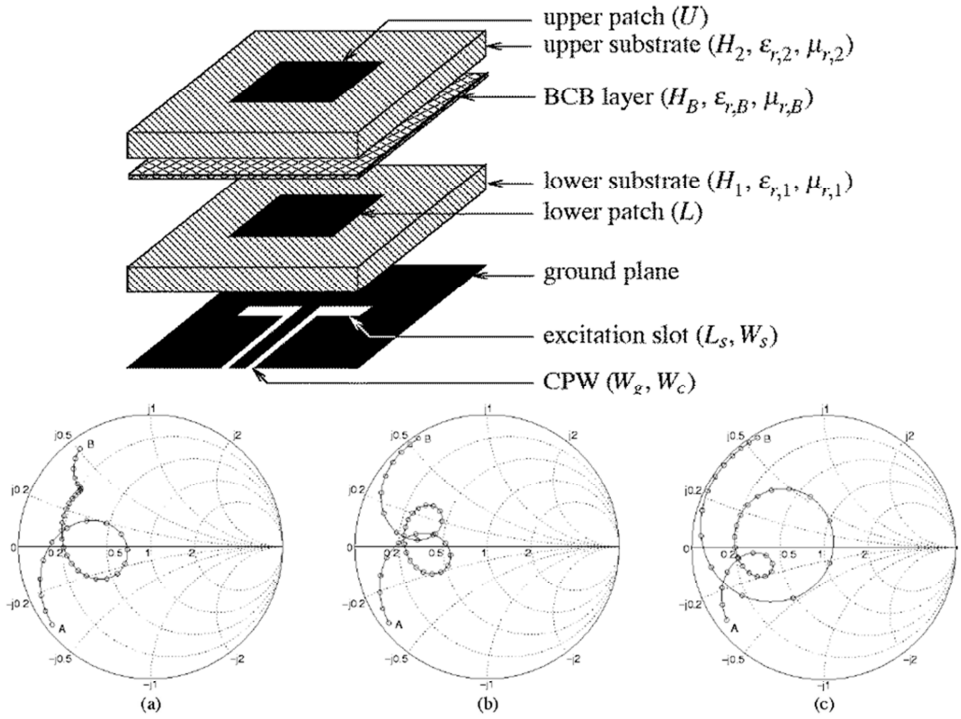

Impedance loci for (a) $U = 1.2$ mm, (b) $U = 1.35$ mm, and (c) $U = 1.5$ mm. Frequency range A–B: 21–38 GHz with 0.5-GHz increments. Other parameters: $H_1 = 0.3$ mm, $H_2 = 0.5$ mm, $L = 1.4$ mm, $L_s = 1.25$ mm, $W_s = 0.1$ mm, $L_{\text{stub}} = 0.8$ mm, $W_g = 25\ \mu$m, $W_c = 100\ \mu$m.

(a)

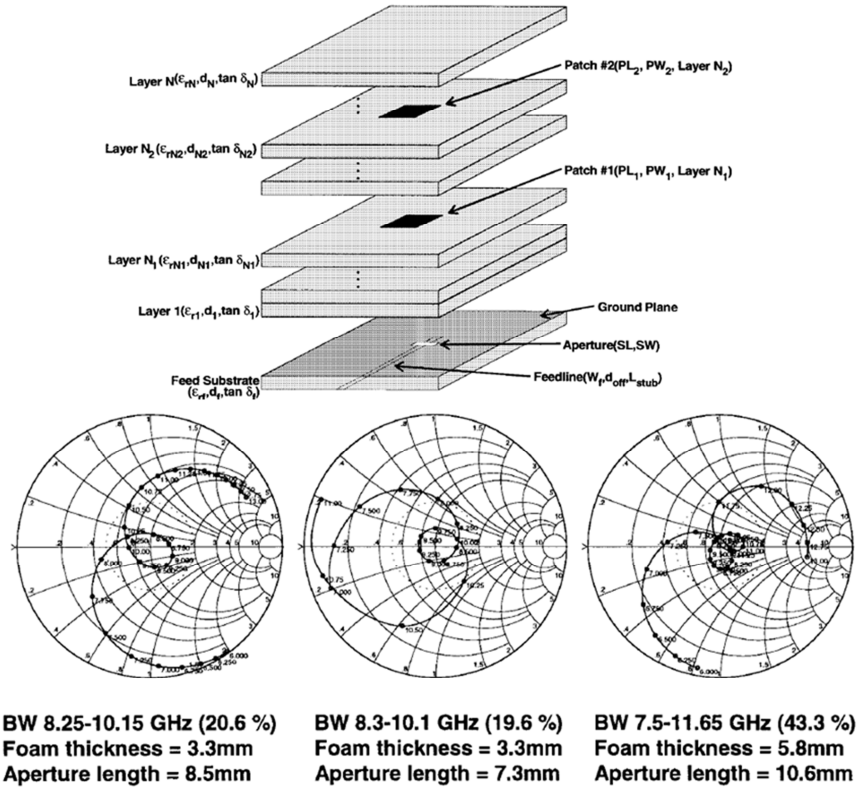

(b)

Figure 2.23: Configuration and characteristics of the patch stacked antennas with a coupling aperture, (a) short-end CPW feed-line [91] and (b) coupling microstrip [92].

In addition, the side-coupling on a single layer in a patch antenna with a small strip fed probe has resulted in the wideband responses of ~27% and ~50% as shown in Fig. 2.22(a) [83, 84]. Fig. 2.22(b) and (c) show patch antennas excited by coupling of that the impedance bandwidth were ~36% for an L-shaped probe [85], and 49% for an L-shaped strip [86]. The physical configurations were based on an unconnected structure between a feeding component and a resonant patch so that the coupling effect of the near-field interference transfers the excitation energy to the patch. A gap is the key parameter for broadening the frequency response.

An alternative coupling mechanism is via an aperture element that can lead to a simple physical structure and ease of a matching condition. The aperture structure is positioned on a ground plane and also interacts with the feeding element. There are typically two feeding structures to excite the aperture based on a microstrip and a coplanar waveguide (CPW) as shown in Fig. 2.23. Pozar introduced the circular aperture on a ground plane to separate the microstrip line and the resonant patch [87]; whereas the use of the CPW feed-line positioned on a ground plane was been reported by Menzel and Grabherr [88]. In both cases, the initial work was not aimed for a wideband response. However, a narrow aperture that behaves as a driven resonator is used to excite a patch. In that, the resonance conditions of both elements can be tuned to obtain the enhancement of impedance bandwidth [89]. In addition, antennas based on a combination of a coupled aperture and stacked patches have also been introduced and this type of antenna structure can lead to the enhancement of the impedance bandwidth to around 30~50% [90-92]. The drawback on that is a thick antenna profile.

In order to achieve a triple resonance, a mixed configuration can be used to improve impedance bandwidth as shown in Fig. 2.24. This can be realised in different designs based on the stacking, slotting, and coupling techniques. An impedance bandwidth of 50% has been obtained using a U- or V-shape slotted patch or stacked patches with a feeding probe in Fig. 2.24(a) [93, 94]. The aperture-coupled stacked patch design with two and three elements was also able to create a triple resonance to achieve impedance bandwidth of 44% in Fig. 2.24(b) [95]. Without a stacked patch, the use of additional slots is a technique to load with an existing U-shape slot on a single patch for a broad impedance bandwidth of more than 50% in Fig. 2.24(c) [96].

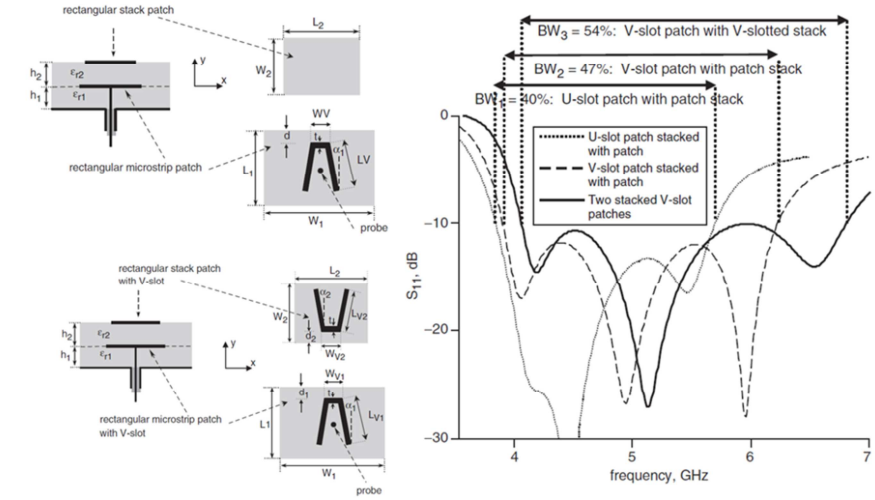

(a)

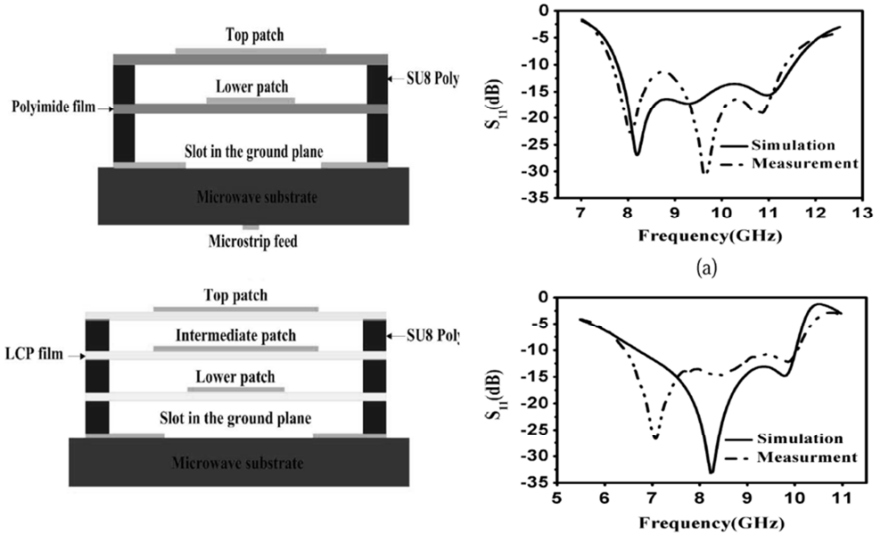

(b)

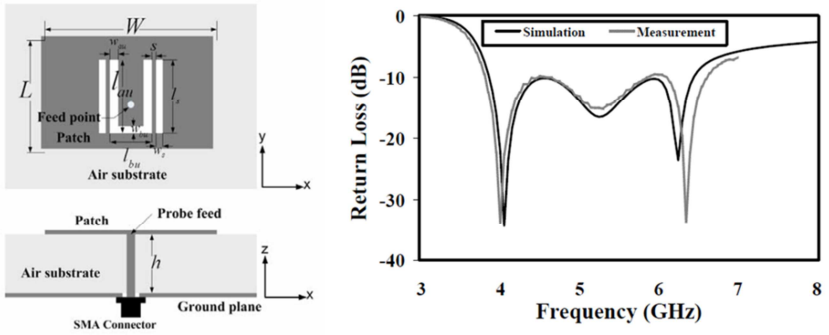

(c)

Figure 2.24: Configurations and characteristics of the wideband patch antennas with the triple resonances, (a) the V-slotted patch and typical stacked patch with a feeding probe [93], (b) the stacking configuration based on two and three typical patches coupled with an aperture element [95], and (c) the single slot-loaded and U-slotted patch with a feeding probe [96].

2.3 Antennas with a metamaterial based ground plane

In this section, antenna devices incorporating a metamaterial based ground plane are discussed. In the antenna applications, a metamaterial is incorporated as a part of the ground plane or reflector [97-105]. The planar structure formed by the two-layer of array elements and a perfect electric conductor (PEC) can produce a resonance. The inclusion of the metamaterial can improve directivity of antennas by eliminating, for example, a surface electromagnetic wave; or reducing a thickness of the antenna structure making it a more compact device. The metamaterial can be equivalent to an artificial magnetic conductor (AMC) behaving as a high impedance surface (HIS). This property contributes to compactness since a smaller distance is obtained between a radiating element and a grounded slab. As can be seen in Fig. 2.25, Sievenpiper et al. have introduced an HIS ground plane based on a periodic arrangement of mushroom like cells for supporting an interfacial propagation [97]. This configuration can improve the antenna gain by ~3 dBi [97-99]. The key characteristic of resonance of an HIS grounded material is a total reflection magnitude and a zero reflection phase.

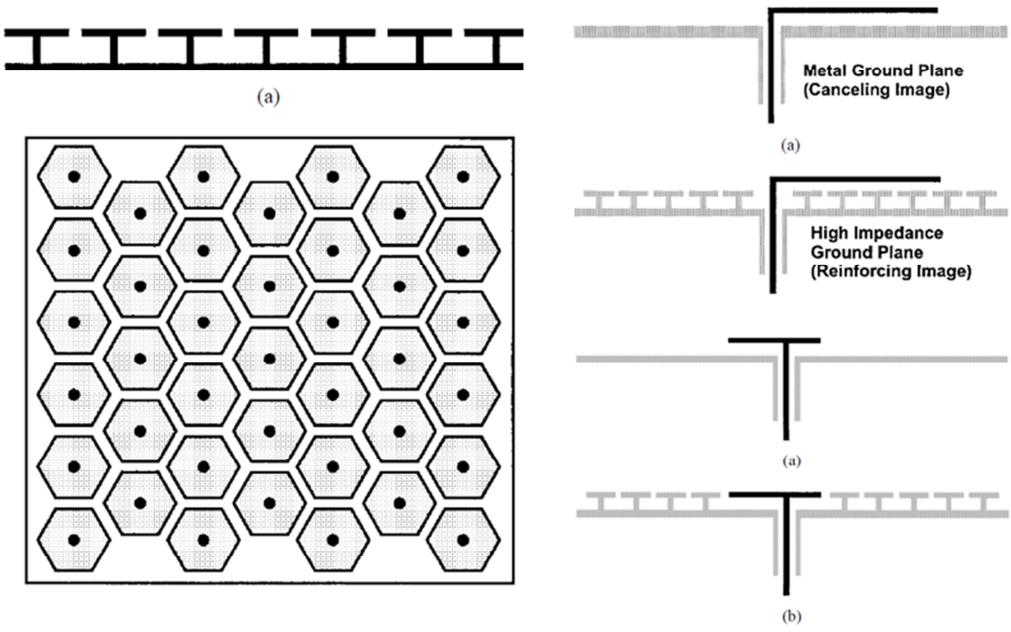

Figure 2.25: Configuration of the periodic mushroom-like structure for the HIS ground plane and antenna applications of a horizontal wire and patch antennas [97].

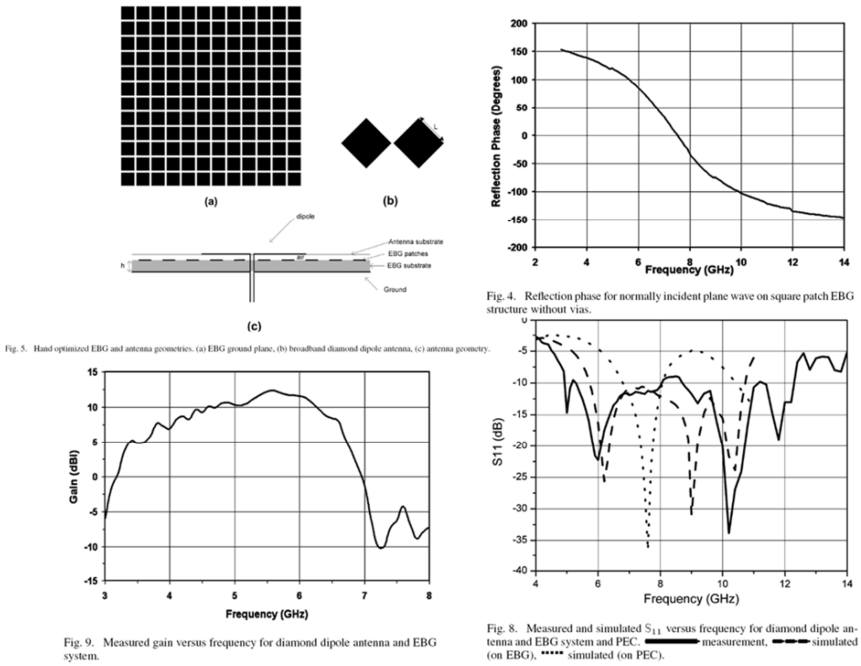

Fig. 5. Hand optimized EBG and antenna geometries. (a) EBG ground plane, (b) broadband diamond dipole antenna, (c) antenna geometry.

Fig. 4. Reflection phase for normally incident plane wave on square patch EBG structure without vias.

Fig. 9. Measured gain versus frequency for diamond dipole antenna and EBG system.

Fig. 8. Measured and simulated S_{11} versus frequency for diamond dipole antenna and EBG system and PEC. ——— measurement, - - - - simulated (on EBG), ***** simulated (on PEC).

Figure 2.26: Configuration of the diamond dipole antenna with the patch based EBG reflector for a wideband operation, and characteristics of the reflection phase of the EBG structure, gain and S_{11} parameter of the antenna structure [101].

The characteristic of a reflection phase in a mushroom array structure has been investigated in terms of an impedance surface for improving impedance matching [100]. It is seen that the effective reflection phase within a range of 90±45° is an important factor in interacting with the antenna element to obtain a perfectly matched condition with the input impedance. In addition, the application of a patch based dipole antenna with the mushroom structure was proposed for wideband radiation as shown in Fig. 2.26 [101]. The mushroom array structure was also used in an antenna to obtain broadband circular polarisation operation [102].

A version of a metamaterial based substrate was formed by the cylindrical EBG structure as shown in Fig. 2.27. The resultant patch antenna showed a gain enhancement of 2.9 dBi [103]. The unipolar photonic bandgap (UP-PBGP) as a grounded substrate exhibits the property for suppression of the surface wave [104]. The antenna radiator was a coplanar patch and the excitation was made using a coupled aperture as shown in Fig. 2.28. The antenna showed a gain improvement by 3 dBi. On the other hand, a metamaterial has been used to replace a blank metal conductor as a reflector to enhance antenna performance. Zhang et al. have studied a PMC structure in the investigation of an aperture coupled patch antenna with the back reflector [105]. The improvement of the side-lobe suppression is by 6 dBi in comparison with a PEC based reflector.

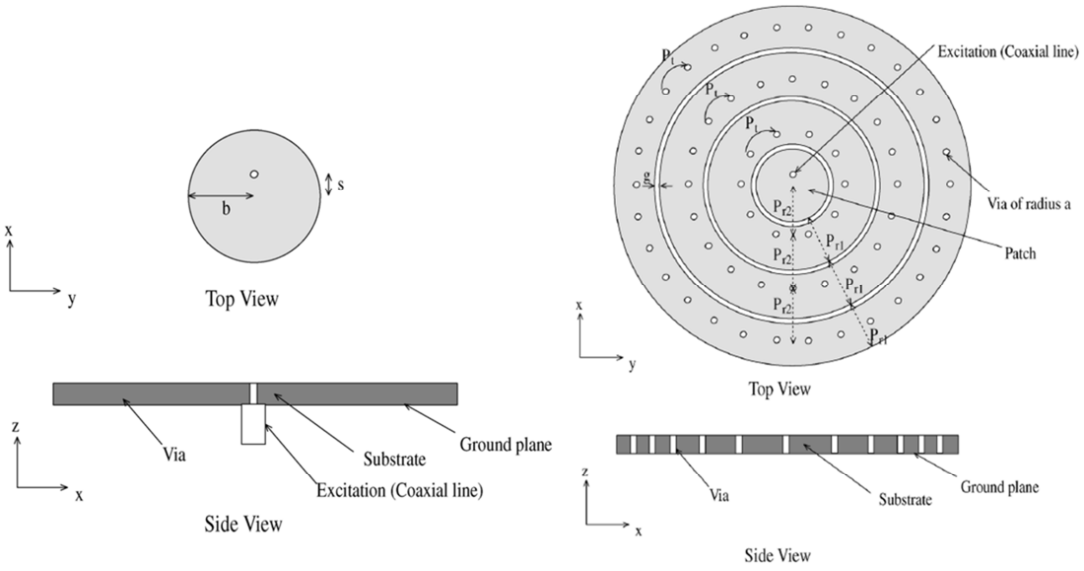

Figure 2.27: Configuration of the patch antenna with the cylindrical electromagnetic crystal substrate [103].

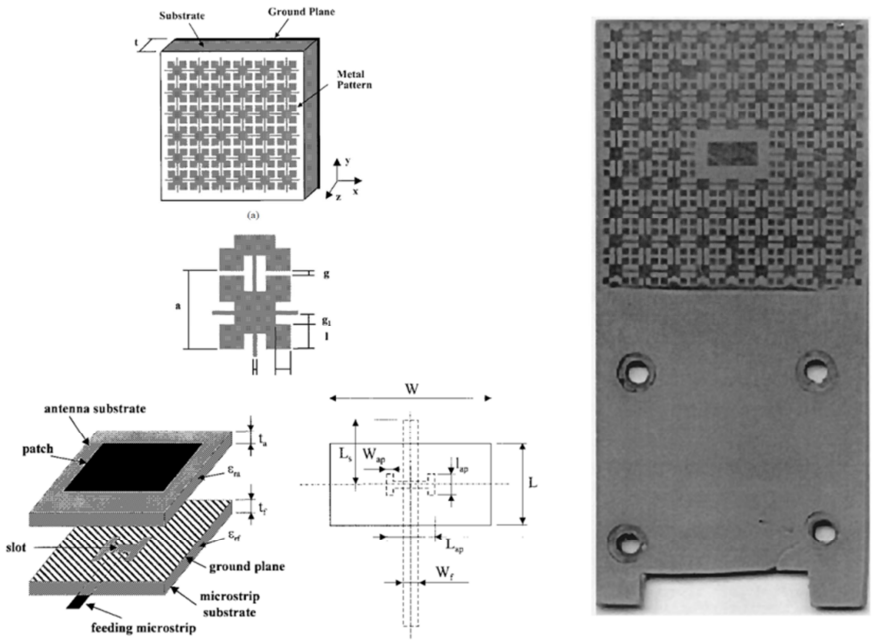

Figure 2.28: Configuration of the aperture coupled patch antenna with the uniplanar compact photonic bandgap (UC-PBG) structure [104].

2.4 Resonant cavity antennas

The resonant cavity antenna (RCA) for high gain applications has been studied for several decades [6-10,106-130]. In particular, the theoretical analysis has been based on electromagnetic and optic behaviours associated with the reflection characteristics. The fundamental configuration of a resonant cavity antenna consists of a pair of planar structures including a partially reflective surface (PRS) and a ground plane behaving as a total reflective surface. The PRS configuration can be formed by dielectric materials or a metallo-dielectric composition also known as a frequency selective surface (FSS).

A dielectric layer with a thickness of a quarter guided wavelength can function as a PRS resulting in the phase change of 180° (π) in reflection. However, the use of the dielectric based PRS structure relies on the intrinsic property of relative permittivity and requiring a particular thickness. On the other hand, the FSS based PRS has been studied as an effective superstrate in RCA devices. The periodic arrangement of metallic elements in a variety of patterns provides design flexibility in controlling the reflection coefficient. This superstrate configuration also gives a degree of freedom in choices of a dielectric material. The electromagnetic nature of a periodic structure is associated with the type of metallic element and dimensions in an array. This leads to the selection of a suitable type of periodic patterns.

In its operation, a primary source or a feeding antenna is positioned inside a cavity and is used to excite a RCA device. In general, the exciting antenna can be a dipole, aperture or slot, patch, open-end or slot-loaded waveguide based design. The high directivity (gain) with a narrow beam pattern is obtained based on a cavity effect. However, broadband radiation has been a challenging issue which is one of the main interests of this thesis work.

The feature of PRS structure has a key role in designing a RCA device. The RCA design can be analysed by several methods including the ray theory, the Fabry-Perot cavity, the transmission-line model, the leaky-wave propagation, and the electromagnetic band-gap (EBG) or photonic bandgap based approaches.

In 1956, Trentini [106] introduced an antenna configuration with the PRS structure based on periodic arrays of metal elements to form a resonant cavity antenna. In that work, the antenna had a pair of reflectors consisting of one total reflector and a partial reflector separated by a cavity distance or height. The theoretical analysis was based on the ray theory. The high antenna gain was achieved using an open-end waveguide based excitation source as shown in Fig. 2.29.

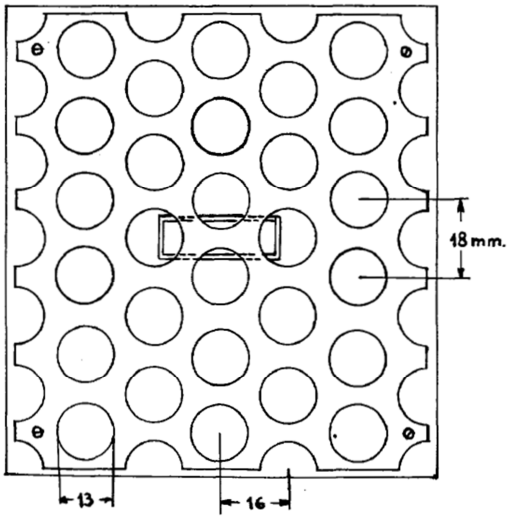

Fig. 4—Arrangement of the perforated grid in front of the waveguide aperture and screen.

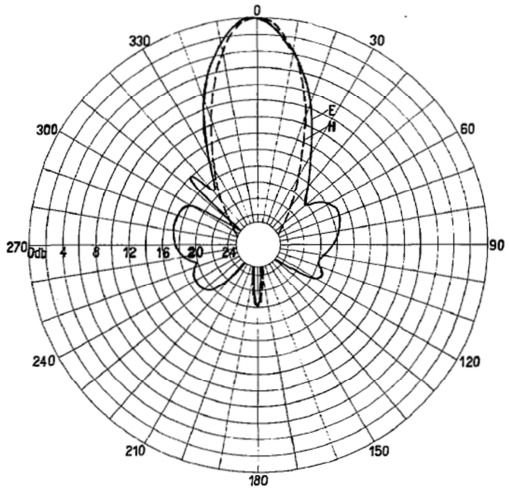

Fig. 5—Radiation pattern of the array of Fig. 4 in the H and E plane.

Figure 2.29: Configuration of the resonant cavity antenna based on a perforated-grid PRS [106].

In 1985, Jeckson and Alexopoulos [107] presented a high-gain antenna which dielectric layers were used for a PRS structure referred to as the “substrate-superstrate” structure to form a cavity with a ground-plane reflector as shown in Fig. 2.30(a). In wave propagation, the reflection phase of a quarter-wavelength dielectric PRS structure is determined at the resonant frequency at which the reflection magnitude is also dominated by the value of relative permittivity (ε_r). Based on the transmission-line model, the cavity structure was converted into sectional impedances by starting with the ground plane as a short load. The characteristic impedance of a transmission line can be determined of that the resonant condition requires a cavity height of a half-wavelength. Moreover, the superstrate based on multiple dielectric layers has been shown to provide narrow-beam radiation behaviour and the effect of leaky-wave propagation was analysed using attenuation constants as shown in Fig. 2.30(b) [108].

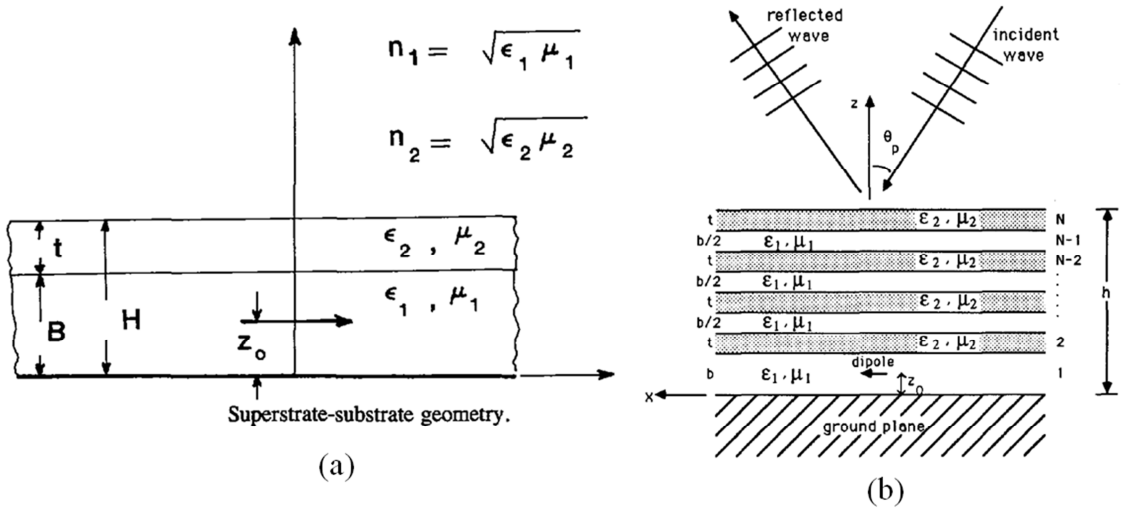

Figure 2.30: Configuration of the resonant cavity antenna based on a dielectric PRS, (a) the superstrate-substrate cavity structure [107] and (b) the narrow-beam structure based on a multi-layer dielectric superstrate [108].

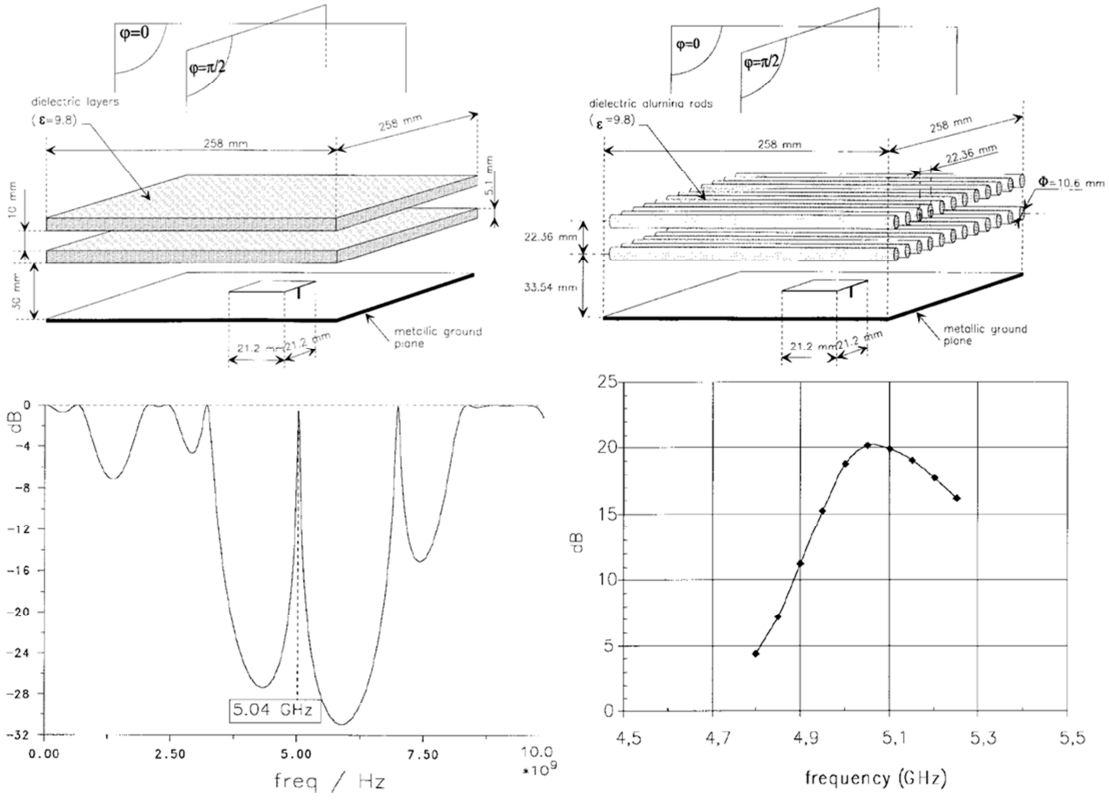

Figure 2.31: Configuration of a 1D and 2D dielectric PRS superstrate in a resonant cavity antenna, the characteristics of the resonant transmission of the EBG analysis and the antenna directivity [109].

In 1999, the analysis connected with the photonic bandgap (PGB) also known as the electromagnetic bandgap (EBG) approach has introduced to determine the resonance behaviour of the one-dimensional (1D) and two-dimensional (2D) dielectric structure as shown in Fig. 2.31. The directivity in the patch antenna was controlled by the absorption in the transmission response [109, 110].

The FSS based PRS as a 2D structure has been investigated extensively for resonant cavity antennas. In 2001, Feresidis and Vardaxoglou investigated a FSS structure based on dipole elements that was incorporated with the open-ended waveguide, producing a measured gain of ~22 dBi as shown in Fig. 2.32 [111]. The effect on a PRS size was also studied and optimised to obtain maximum antenna efficiency.

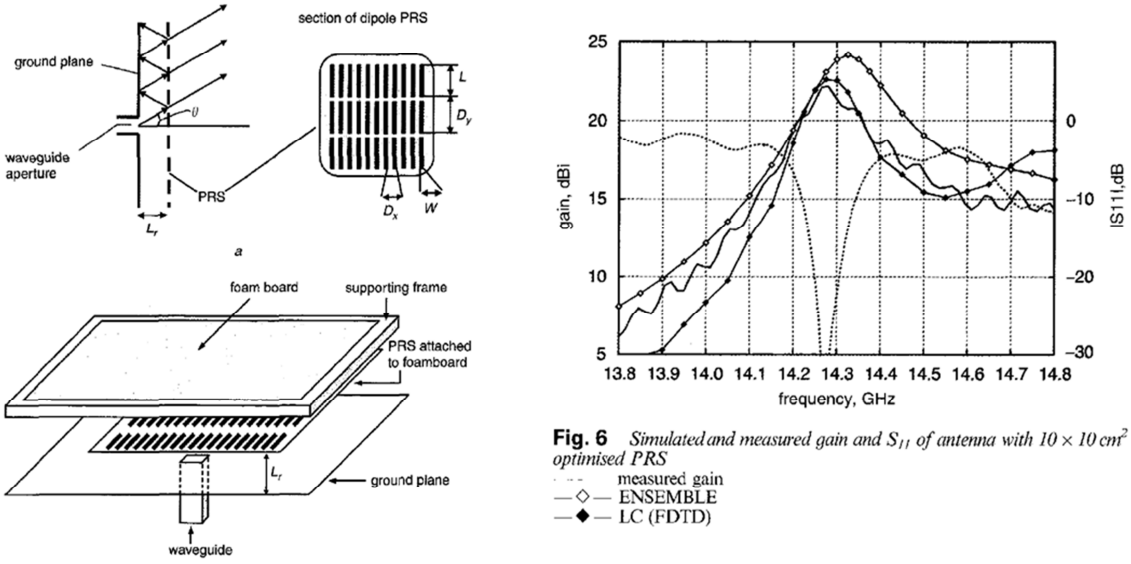

Fig. 6 *Simulated and measured gain and S_{11} of antenna with 10×10 cm^2 optimised PRS*

Figure 2.32: Configuration and characteristics of the resonant cavity antenna based on the strip dipole based PRS structure and the open-end waveguide source antenna [111].

In 2005, Weily et al. described a PRS structure consisting of a three-dimensional (3D) configuration based on a wood pile structure called as an EBG resonator as shown in Fig. 2.33 [112]. The unit cell has the dimensions of 11.2x11.2x12.8 mm^3 or 0.46x0.46x0.52λ^3 with a height of 3.2 mm (0.13λ) at the operation frequency of 12.31 GHz. The antenna directivity was investigated by varying a dimension of the EBG superstrate. The effective size of a square aperture around 6.3λ produced the highest radiation peak with a measured gain of 18.9 dBi using a patch based excitation source. The main benefit of a 3D dielectric PRS is a thinner superstrate as compared with a 1D dielectric based design for a same performance.

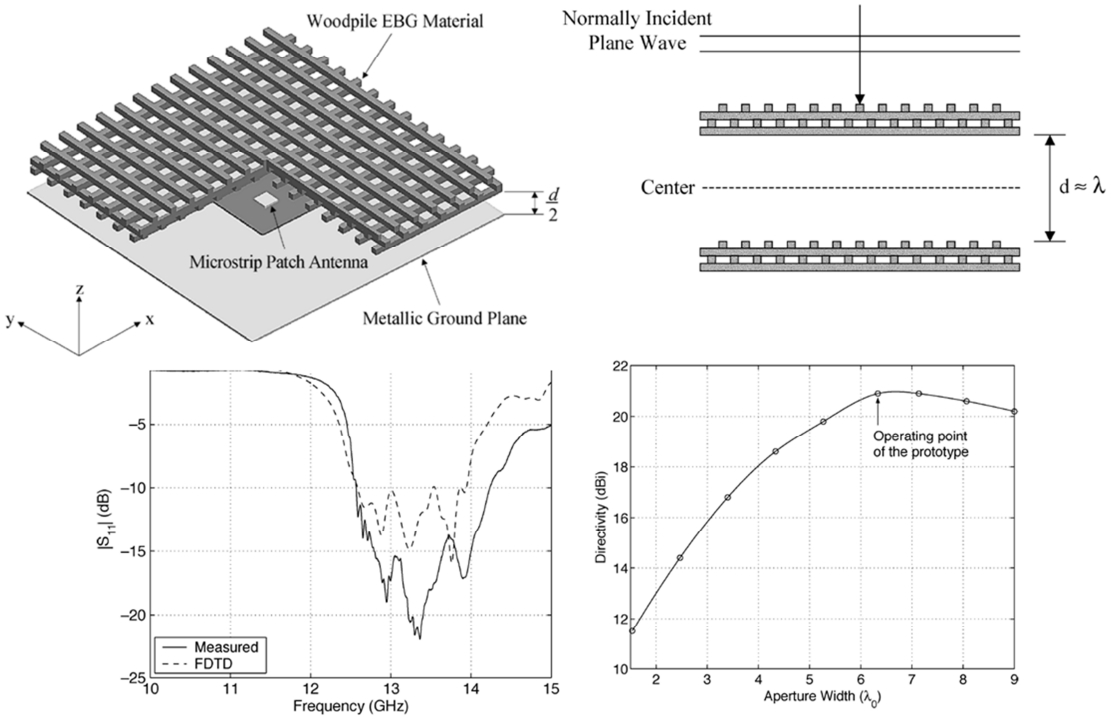

Figure 2.33: Configuration and characteristics of the resonant cavity antenna based on the woodpile EBG superstrate and the patch source antenna [112].

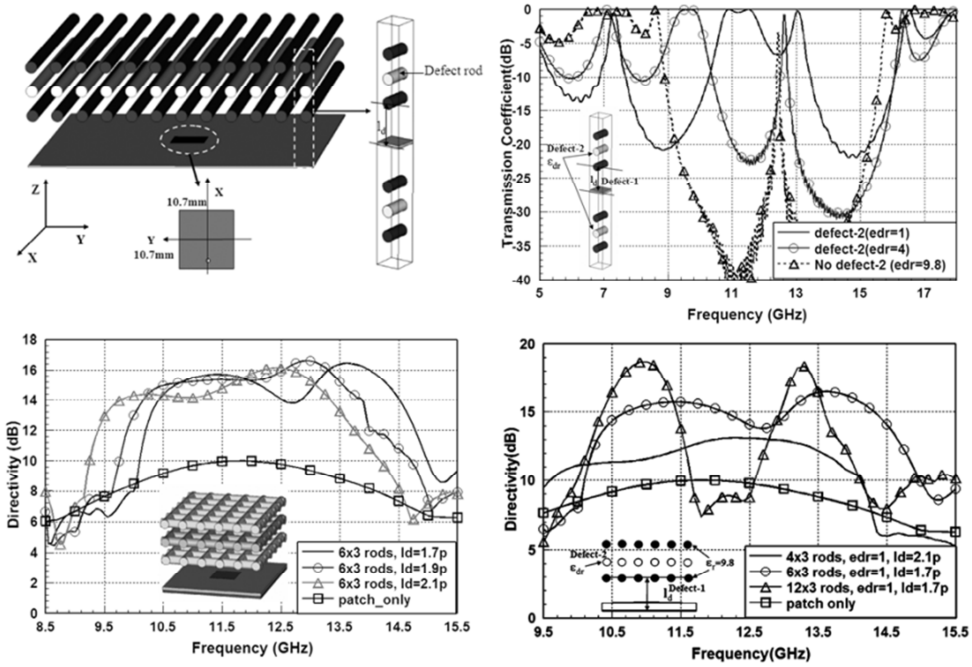

Figure 2.34: Configuration and characteristics of the wideband and double-band resonant cavity antenna based on the 2D dielectric rod superstrate and the patch source antenna [113].

In order to enhance a radiation bandwidth, more complex dielectric layers have been also formed to be a superstrate. A 2D dielectric rod based superstrate with a defect rod was studied to extend the radiation bandwidth for a double band and a wideband operation as shown in Fig. 2.34 [113]. The EBG characteristics of a rod based structure produce the wideband defect mode that was fed by a patch based source antenna. The size of a finite dielectric superstrate determines the behaviour for a double band or a wideband operation. However, this type of a wideband resonant cavity antenna suffers from a bulky configuration. The reflection coefficient was not reported in this study.

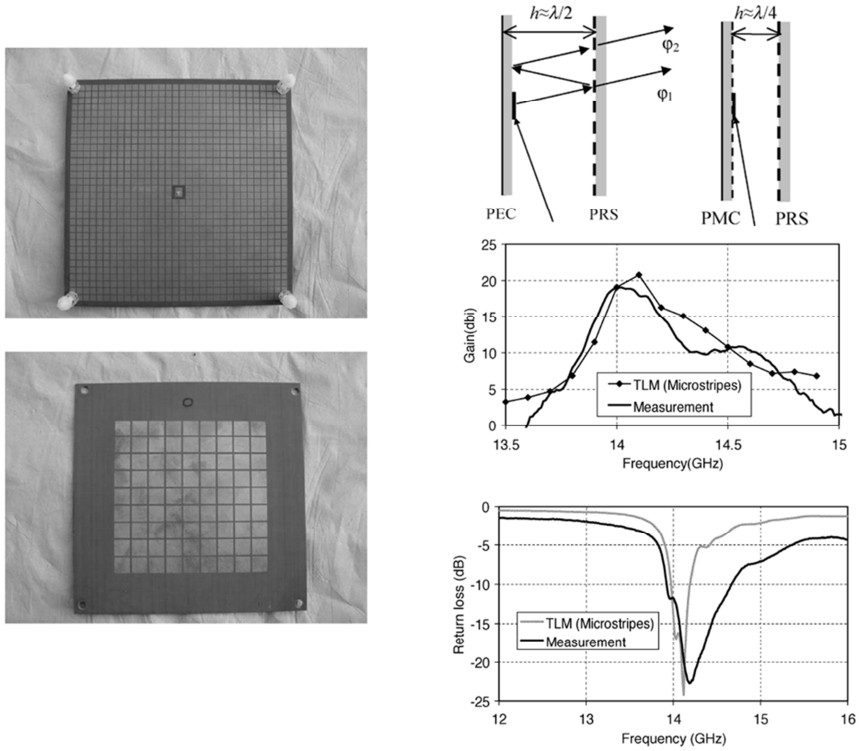

Figure 2.35: Configurations and characteristics of the sub-wavelength resonant cavity antennas based on the patch based HIS structure and patch based PRS superstrate [114].

Apart from the one-layer FSS based PRS superstrates, other cavity configurations using two FSS layers have also been investigated. In 2005, Feresidis et al. reported the study of a low-profile RCA structure including a ground-plane based on an artificial magnetic conductor (AMC) configuration as shown in Fig. 2.35 [114]. It was shown that the structure is feasible for a design in which the cavity height can be a quarter wavelength. In addition, the extended studies showed the possibility to reduce the cavity height to be less than the quarter wavelength [115-117]. The arbitrary reflection phases of a patch-type AMC and a mesh-type PRS were designed in accordance with the Fabrt-Perot approach leading to an extremely small cavity height as shown in Fig. 2.36 [117].

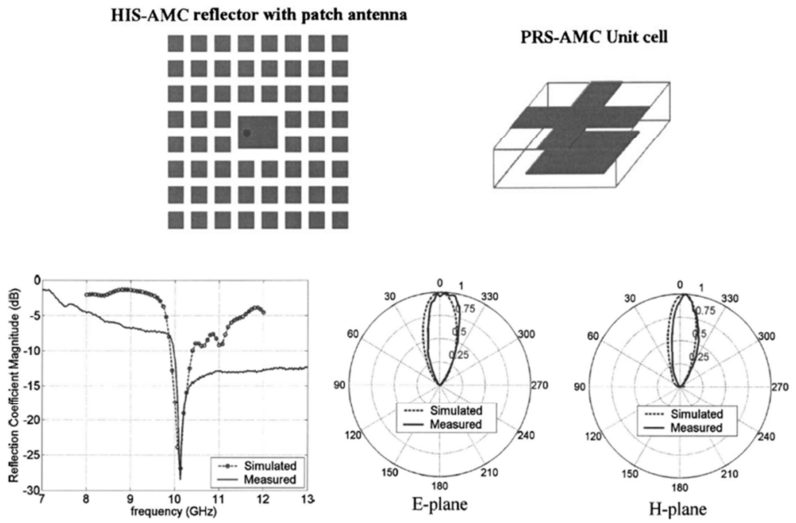

Figure 2.36: Configurations and characteristics of the sub-wavelength resonant cavity antennas based on the patch based HIS structure and mesh based PRS superstrate [117].

In 2006, Guerin et al. unveiled the investigation of aperture array based superstrates in a cavity antenna as shown in Fig. 2.37 [118]. The cavity antenna was excited by a patch antenna as a feeding source showing a high gain of more than 20 dBi. The radiation pattern provided a narrow directive beam as expected. It was shown that the large dimensions of a PRS structure of around ~11λx11λ were required to obtain the high gain performance.

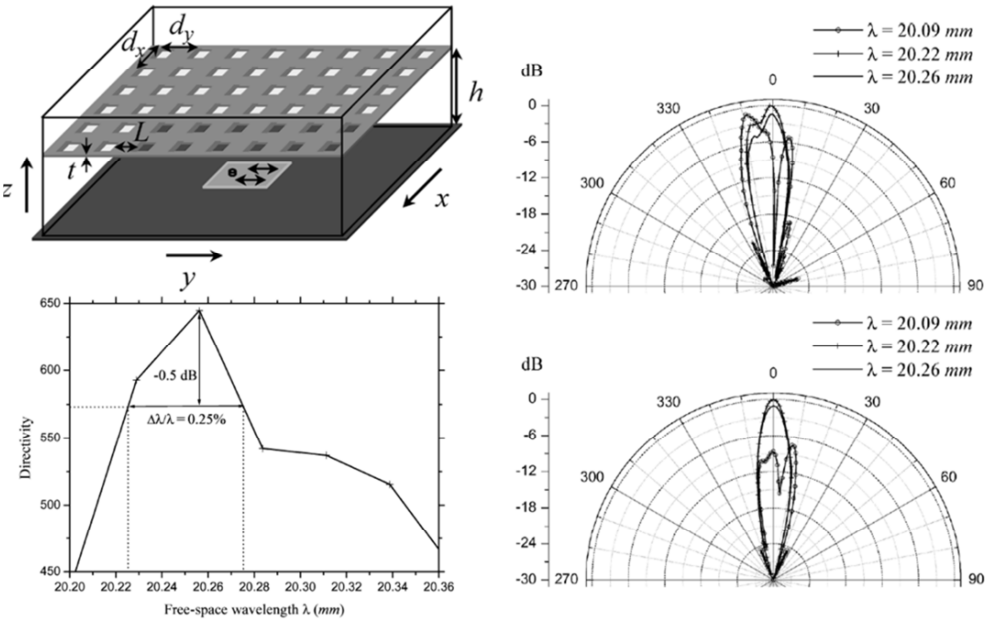

Figure 2.37: Configuration and characteristics of the resonant cavity antenna based on the array aperture PRS structure and the patch source antenna [118].

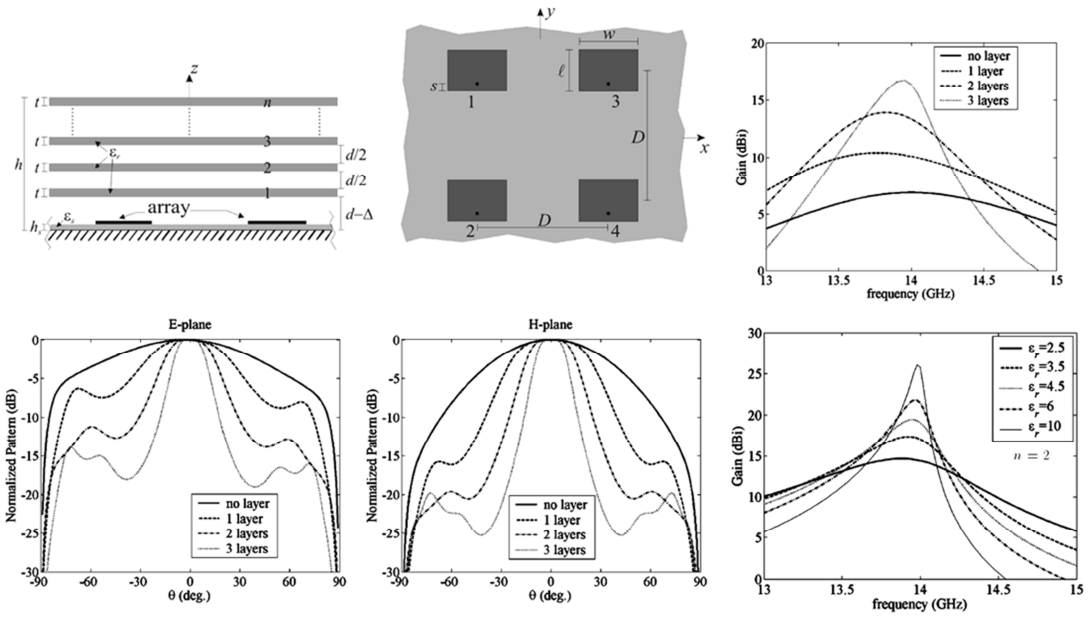

Figure 2.38: Configuration and characteristics of the resonant cavity antenna based on the multi-layer dielectric superstrate and the array patch source antenna [119].

Gardelli et al. reported the study of such layered dielectric superstrates in a cavity antenna as shown in Fig. 2.38 [119]. It was shown that the high gain performance depends on a reflection magnitude associated with the value of electric permittivity. Also, the number of dielectric layers plays a role in the performance of an antenna in terms of gain and beam pattern. This shows a trade-off between high gain and high radiation bandwidth.

To improve a radiation bandwidth in using a FSS structure, the two-layer PRS designs have been investigated in resonant antenna devices. In 2006, Feresidis and Vardaxoglou presented the work based on PRS designs with two dissimilar arrays for radiation enhancement as shown in Fig. 2.39 [120]. The superstrate configuration consists of two layers of a typical FSS with different patch dimensions. The separation between two arrays was 11 mm (~0.51λ) and it was 11.4 mm (~0.53λ) between a bottom array and a ground plane reflector. In this design, a positive gradient in the reflection phase as a function of frequency was used for wideband operation. The measured result of the 1-dB-ripple radiation bandwidth was around 9% with a peak gain of roughly 20 dBi at the centre frequency of 14 GHz. The finite size of a patch array was around 4λx4λ and the overall antenna size was 8λx8λ (including a dielectric edge space). However, the input impedance over the operation band is not ideal for the reflection characteristics due to the limitation of a primary radiator which was a slot-loaded waveguide.

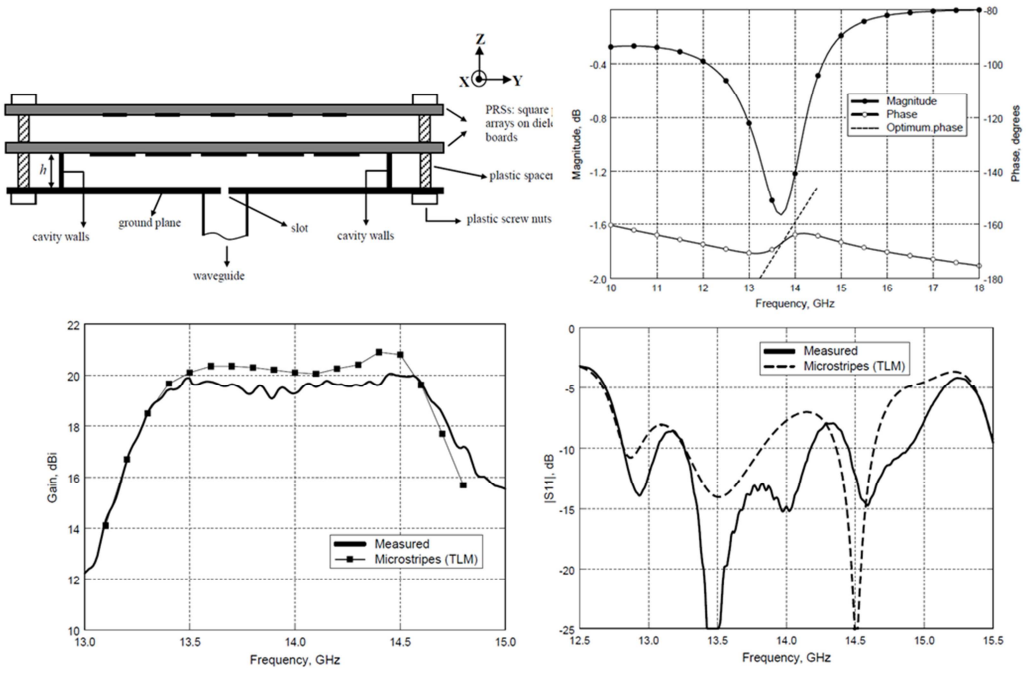

Figure 2.39: Configuration and characteristics of the broadband resonant cavity antenna based on the two-layer dissimilar patch PRS structure and the slot-loaded waveguide source antenna [120].

In 2007, Lee et al. presented the optimisation of two FSS layers of dissimilar array consisting of dipole elements on each side of a dielectric slab for double band operation as shown in Fig. 2.40 [121]. In this method, the physical dimensions of dipole elements were modified using an algorithm based process. The total size of a superstrate is 120x120 mm^2 or $4x4\lambda^2$ at the frequency of 8 GHz. The measured directivity was about 20 dBi both two peaks at the frequency of 8.2 GHz and 11.7 GHz using a separate source antenna for each band.

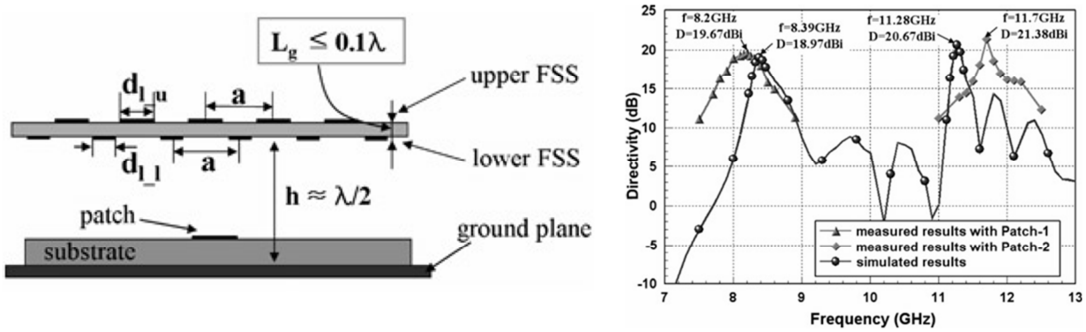

Figure 2.40: Configuration and characteristics of the double-band resonant cavity antenna based on the two-layer optimised strip dipole PRS structure and the different patch source antennas [121].

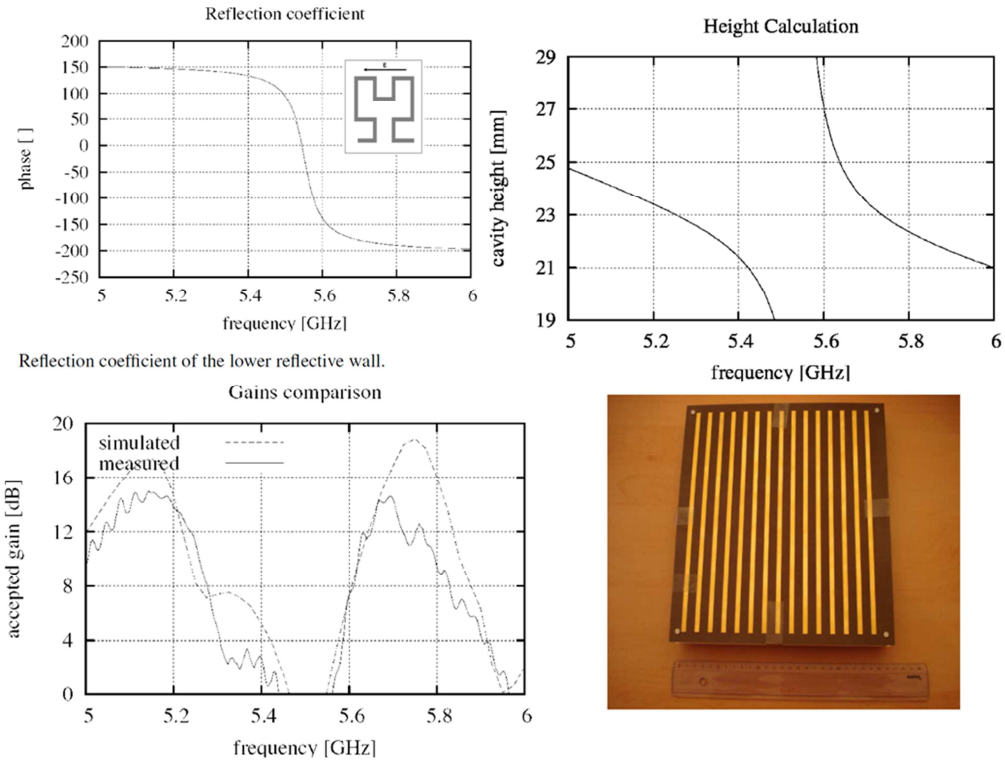

Figure 2.41: Configuration and characteristics of the double-band resonant cavity antenna based on two FSS layers consisting of the HIS layer and strip grating PRS structure and the dipole source antenna [122].

In addition, a dual band resonant cavity antenna was also demonstrated using an artificial ground plane. As considered in a phase compensation approach, the creation of a cavity structure was made with the high impedance surface (HIS) ground plane based on a Hilbert-curve array pattern and a strip grating based FSS superstrate as shown in Fig. 2.41 [122]. The two radiation bands occurred at the frequencies around the location of a zero reflection phase on a ground plane response. The cavity distance was 24 mm which is around 0.4λ at the frequency of 5 GHz. The relative size of an antenna configuration is 241.5x241.5x25.6 mm^3. A measured gain of about 14 dBi was obtained at the peak frequencies of 5.1 GHz and 5.7 GHz, respectively.

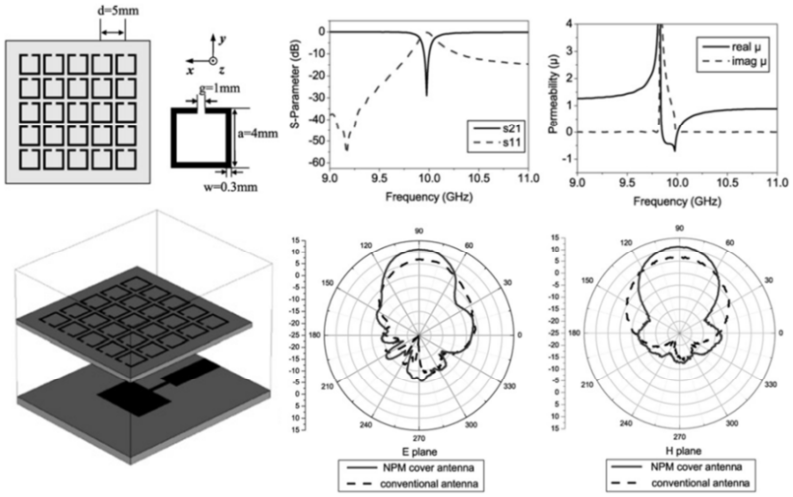

(a)

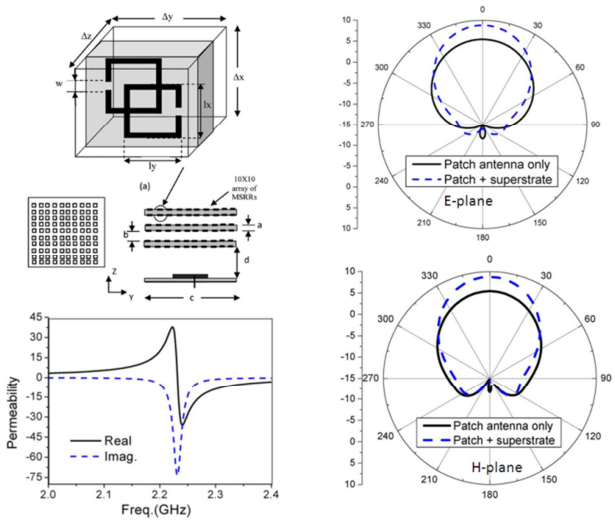

(b)

Figure 2.42: Configurations and characteristics of the patch antenna structure with the metamaterial-assisted superstrate, (a) the negative permeability medium superstrate [123] and (b) the high permittivity superstrate [124].

In 2008, Liu and Zhao proposed the use of a SRR based metamaterial positioned in front of a source antenna as a superstrate for gain enhancement as shown in Fig. 2.42(a) [123]. The periodic structure was based on SRRs in a metamaterial providing complex permeability. The conventional patch antenna was used to provide the field excitation and the antenna gain was enhanced by ~4 dBi. Also, Attia et al. reported the study of a multilayer superstrate come up with a 10x10 SRR array in each layer resulting in a gain enhancement by ~4 dBi as shown in Fig. 2.42(b) [124]. The disadvantages of that structure are a narrow band and a bulky superstrate structure in a case of the multilayer based design.

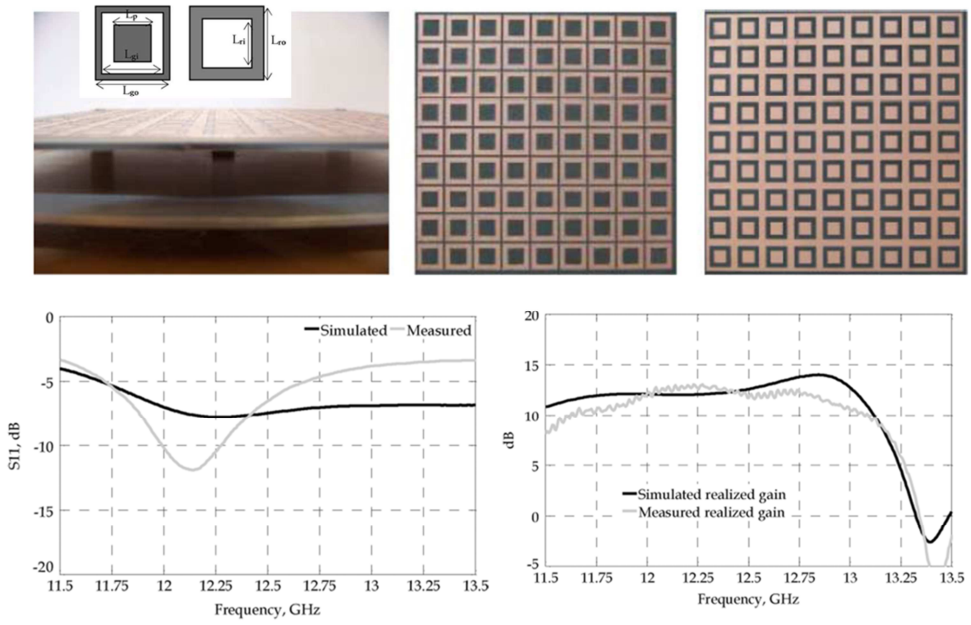

Figure 2.43: Configurations and characteristics wideband resonant cavity antennas based on the two-layer double-side of the loop and mesh with patch superstrate, and the patch source antenna [125].

In 2010, Moustafa and Jacko introduced the PRS configuration based on dissimilar patterns of double-layer complex FSS superstrate. It is consisting of an array of square rings on one side of a dielectric slab and a layer of mesh with concentric patches on the other side of a dielectric slab as shown in Fig. 2.43 [125]. A finite-size PRS of 5λx5λ was used and a primary source was a patch antenna. The experimental results showed poor reflection characteristics. The antenna gain was reported of around 13 dBi. However, the multi-feed technique has been proposed based on a simulation for enhancement of reflection coefficient and gain.

Another cavity antenna is based on a hybrid HIS ground plane and a single patch-type FSS based superstrate for wideband radiation. Two parts was consisting of a mushroom-like structure formed as an artificial ground plane, and a U-slotted patch used as a wideband primary source antenna as shown in Fig. 2.44 [126]. The special feature of a reflection phase on a ground plane was used to interact with the reflection phase of a patch-array superstrate. The optimisation of a mushroom-like geometry can extend a frequency response of phase compensation. The measured 1-dB radiation bandwidth was around 9.9% with a peak gain of 19.6 dBi. The physical dimensions of an antenna were 60x70x12 mm^3 and the cavity distance was 8.8 mm which is equivalent to 0.4λ (14 GHz).

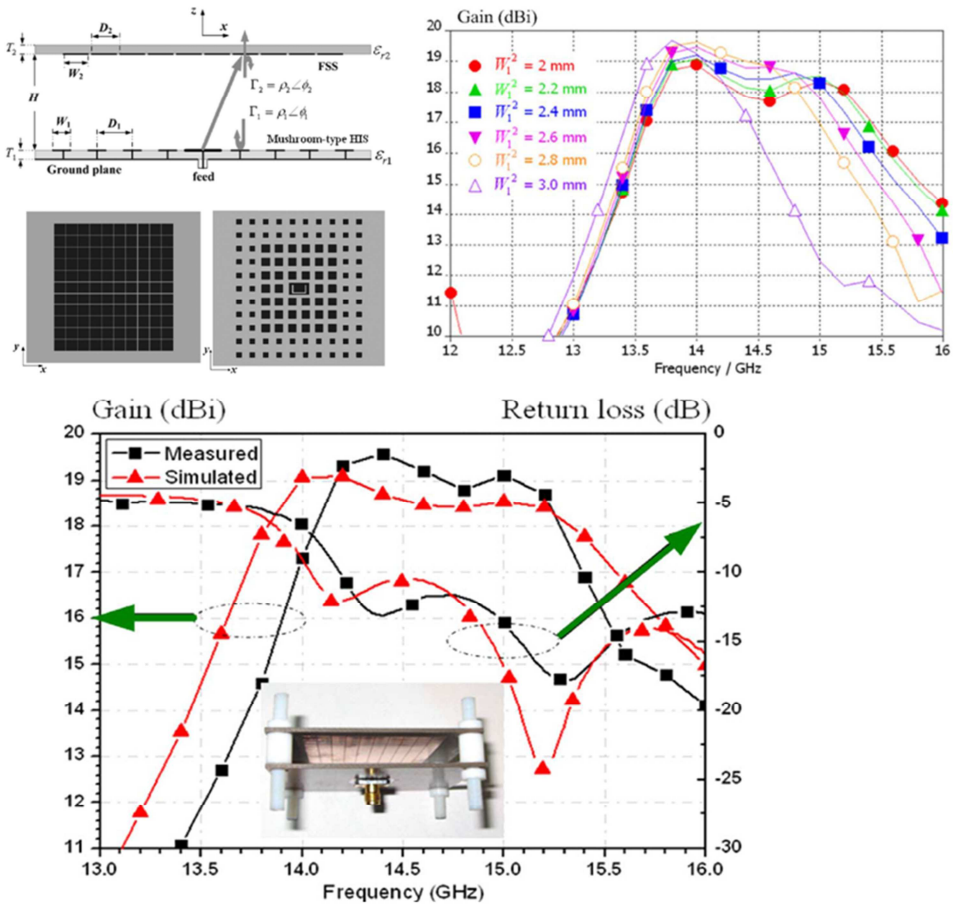

Figure 2.44: Configuration and characteristics of the wideband resonant cavity antenna based on the two FSS layers consisting of the hybrid mush room array HIS ground plane and the patch-type PRS structure and the U-slotted patch source antenna [126].

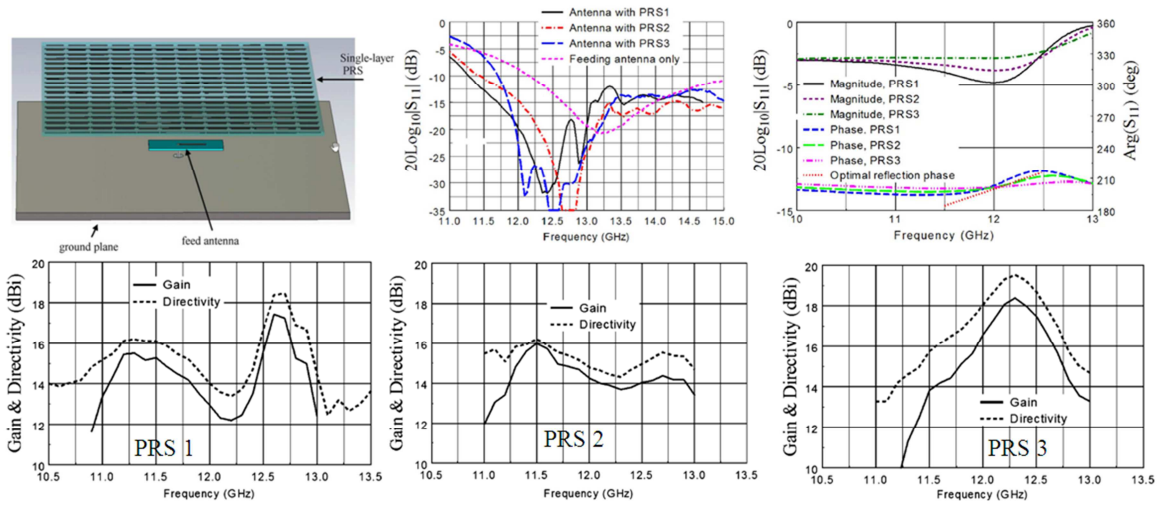

Figure 2.45: Configuration and characteristics of the wideband resonant cavity antenna based on the double-side dissimilar strip dipole PRS structure and the monopole source antenna [6].

In 2012, Ge et al. reported the study of a thin PRS consisting of two dissimilar dipole arrays on a dielectric slab as illustrated in Fig. 2.45 [6]. A notable characteristic is the positive gradient in a reflection phase. A monopole antenna was used as a primary source. Three operation modes were illustrated consisting of a double band, wide band and single band depending on the reflection-phase characteristics of a PRS structure. The measured 3-dB gain bandwidth of a wide band is 15.7% with a peak gain of 16.2 dBi for an aperture size of 108x108 mm^2.

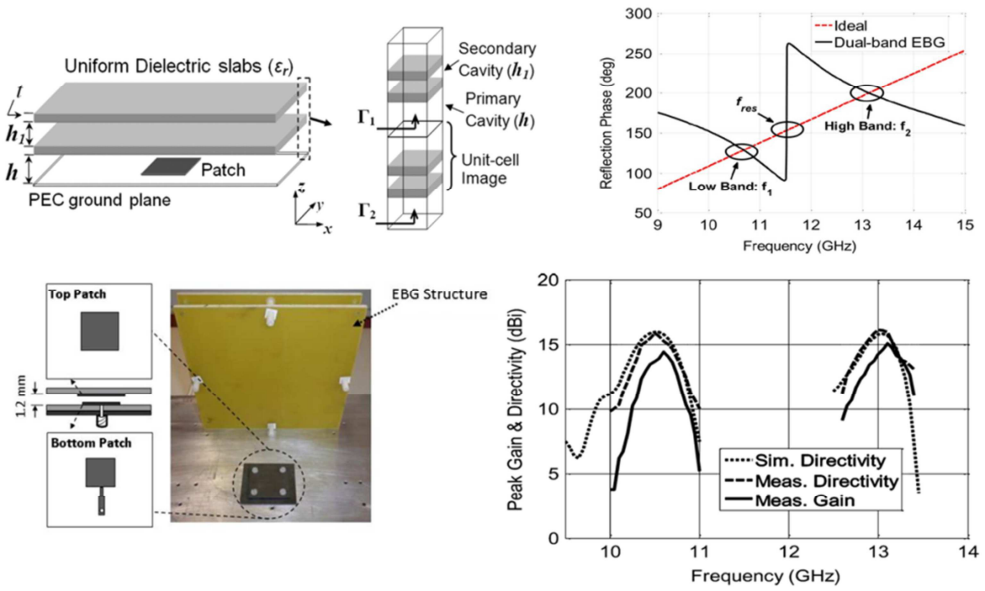

Figure 2.46: Configuration and characteristics of the double-band resonant cavity antenna based on the two-layer symmetric dielectric superstrate and the patch source antenna [127].

A dual band radiation has also been shown in an antenna using a two-layer 1D dielectric superstrate as shown in Fig. 2.46 [127]. The measured peak gains were 14.5 dBi and 15.1 dBi, respectively by using a single patch based excitation source. The inverted reflection phase was introduced to obtain two resonance conditions.

In 2013, Al-Tarifi et al. presented the investigation of a double slab based superstrate in a similar configuration but it was based on a simulation work [128]. Two dielectric layers of different thicknesses were used as shown in Fig. 2.47. The key features are dielectric thicknesses and air spacing between them as well as the dielectric property of that material. The antenna was excited by an open-end waveguide aperture and the dimensions of a superstrate were 60x60 mm^2 exhibiting a 3-dB radiation bandwidth of 19.3% at the centre frequency of 14.5 GHz.

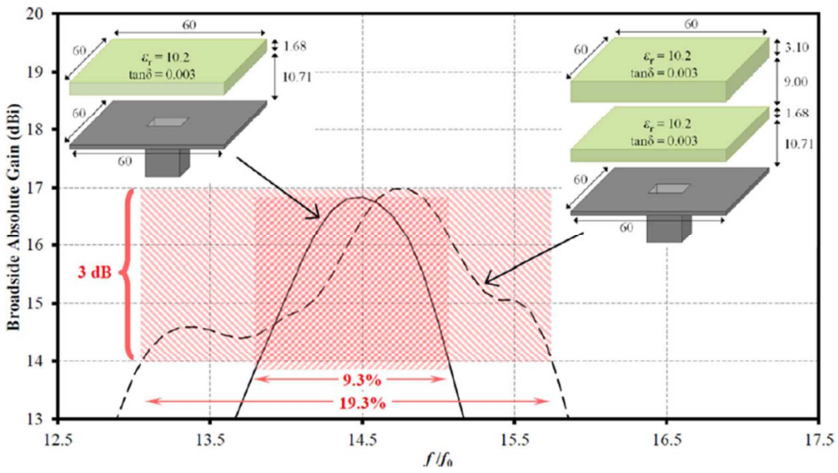

Figure 2.47: Configuration and characteristics of the wideband resonant cavity antenna based on the two-layer asymmetric dielectric superstrate and the open-end waveguide antenna [128].

Moreover, a wideband primary antenna has also been used in a broadband cavity antenna configuration. The microstrip-fed aperture-coupled patch antenna was applied into a resonant cavity antenna with a superstrate consisting of two asymmetric dielectric layers as shown in Fig. 2.48 [7]. The 3-dB radiation bandwidth was around 20.7% at the centre operation frequency of 15.5 GHz and a peak gain of 16.5 dBi. The impedance bandwidth was around 23%. It shown that the bandwidths of impedance and radiation are corresponding in operation.

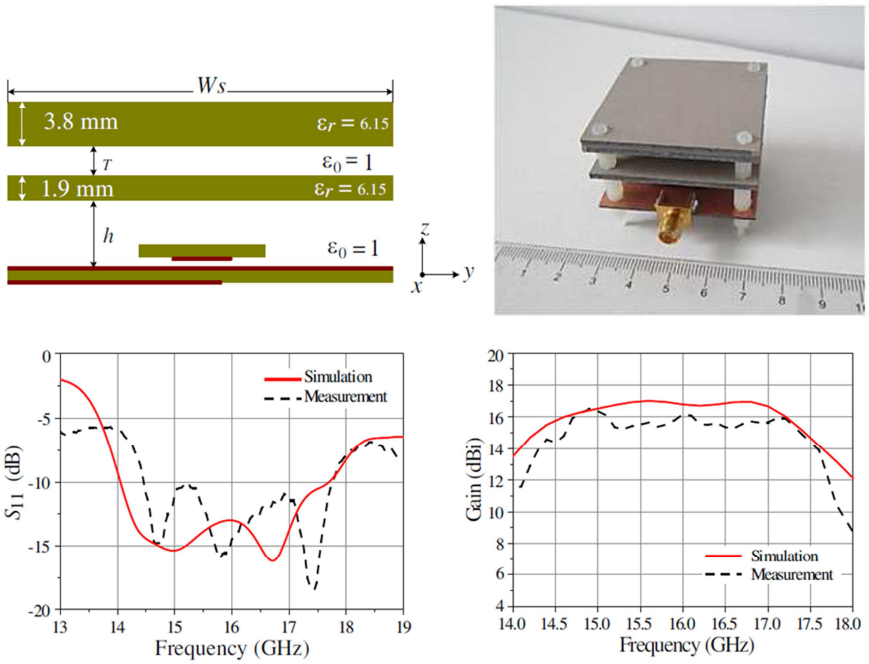

Figure 2.48: Configuration and characteristics of the wideband resonant cavity antennas based on the two asymmetric dielectric layers and the aperture-coupled patch source antenna [7]

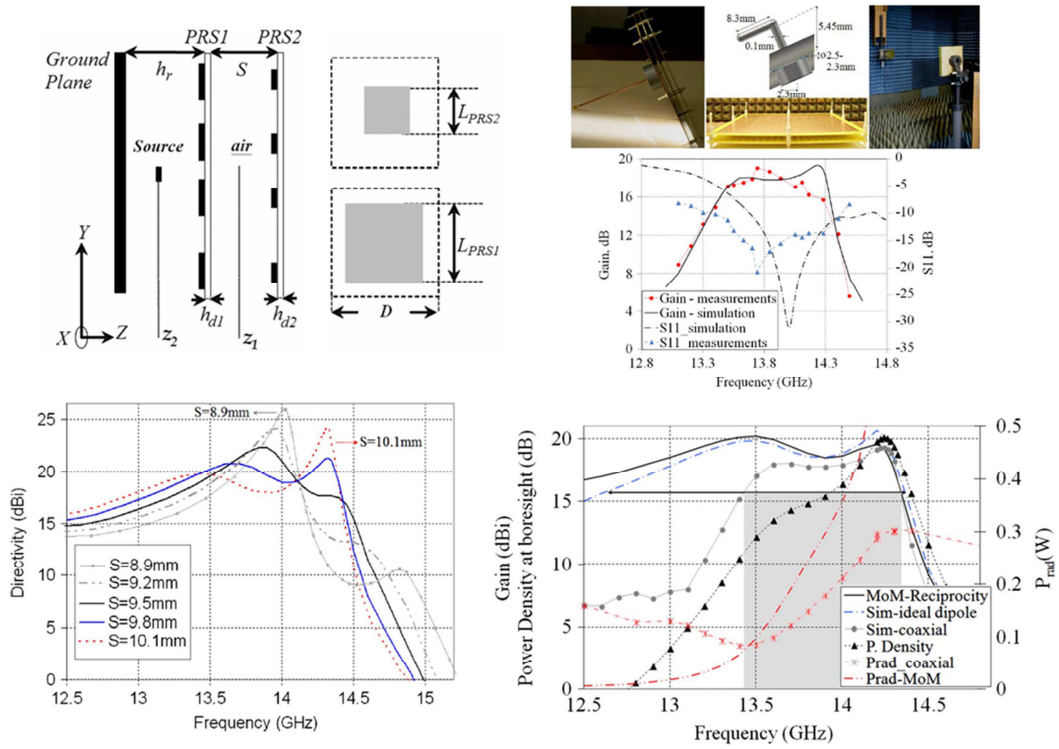

Figure 2.49: Configuration and characteristics of the broadband resonant cavity antenna based on the two-layer dissimilar patch PRS structure and the blended monopole source antenna [129].

In 2014, Meteo-Segura et al. described a RCA configuration based on two dissimilar patch-type FSS layers which was investigated by optimisation and analysis as shown in Fig. 2.49 [129]. The study of an inter-layer interaction between two FSS layers showed its effect on two radiation peaks which shift towards to the high frequency region as a separation between layers is reduced. The antenna performance was also affected by the source antenna and the relative size of a superstrate. The radiation bandwidth was reported of 6% with a peak gain of 17.44 dBi. In that, the large size of an antenna is 28x28cm^2 (~13λx13λ) at 14 GHz.

Recently, a complementary structure based two-layer superstrate has been studied consisting of an array of square patches on one side of a dielectric slab and the square aperture layer on the other side as shown in Fig. 2.50 [8]. The feature of a positive reflection phase gradient was discussed for wideband operation. The practical resonant cavity antenna was formed by a two-layer superstrate of 2.4λx2.4λ in area and a microstrip fed aperture coupled patch was used as an excitation source. The measured 3-dB gain bandwidth was 28% with a peak gain of 13.8 dBi. The total dimension of a practical antenna was 72x72x15 mm^3.

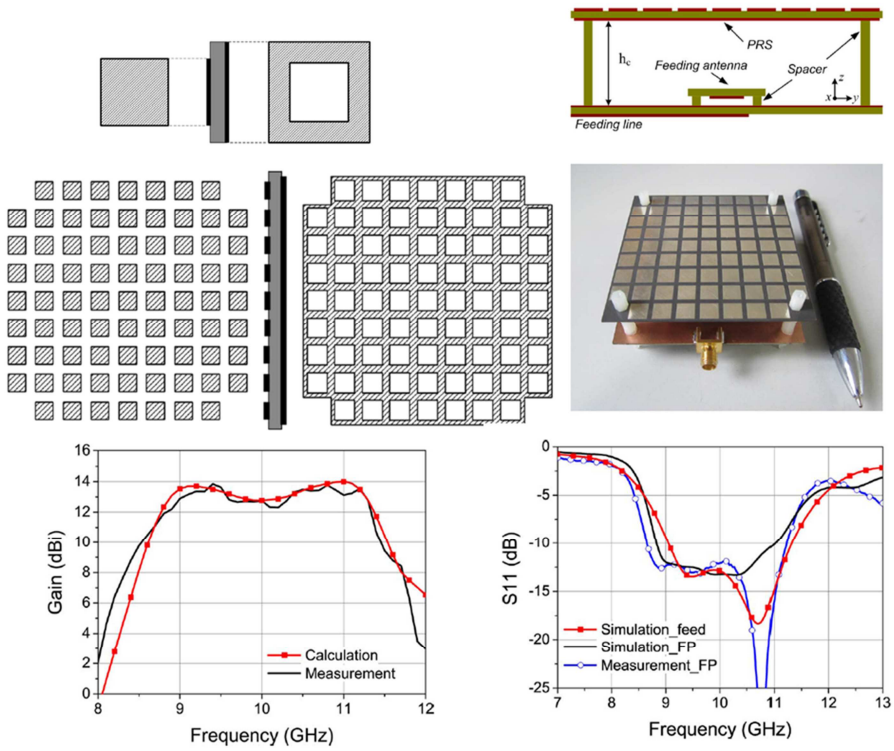

Figure 2.50: Configurations and characteristics wideband resonant cavity antennas based on the two-layer complementary pattern PRS structure, (a) the double-side of the patch and mesh array superstrate, and the aperture coupled patch source antenna [8].

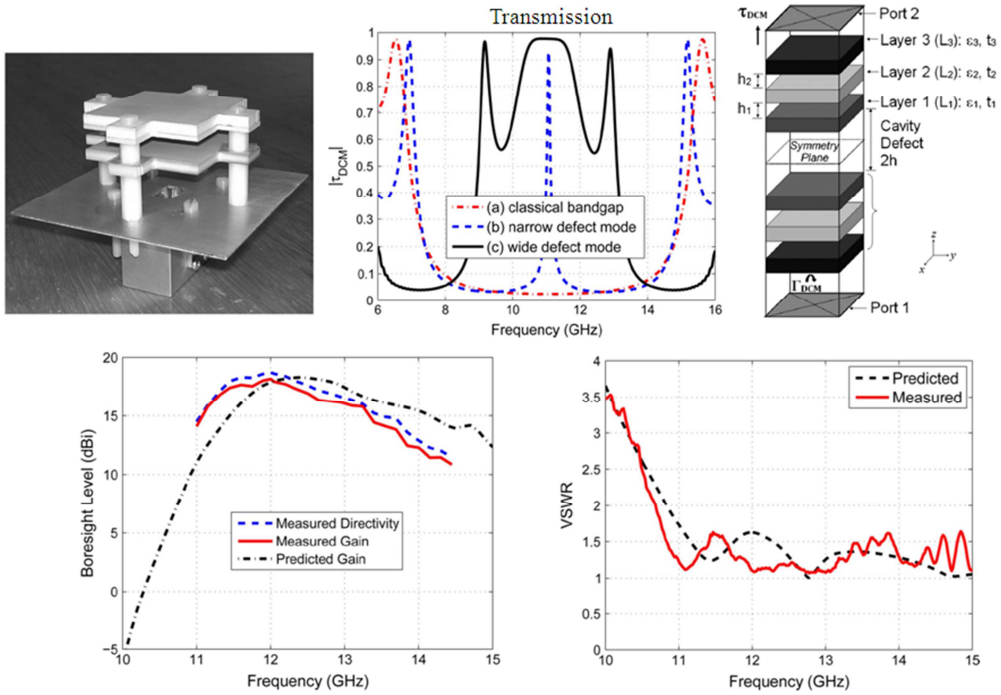

(b)

Figure 2.51: Configuration and characteristics of the wideband resonant cavity antennas based on the three asymmetric dielectric layers and the open-end waveguide antenna [9].

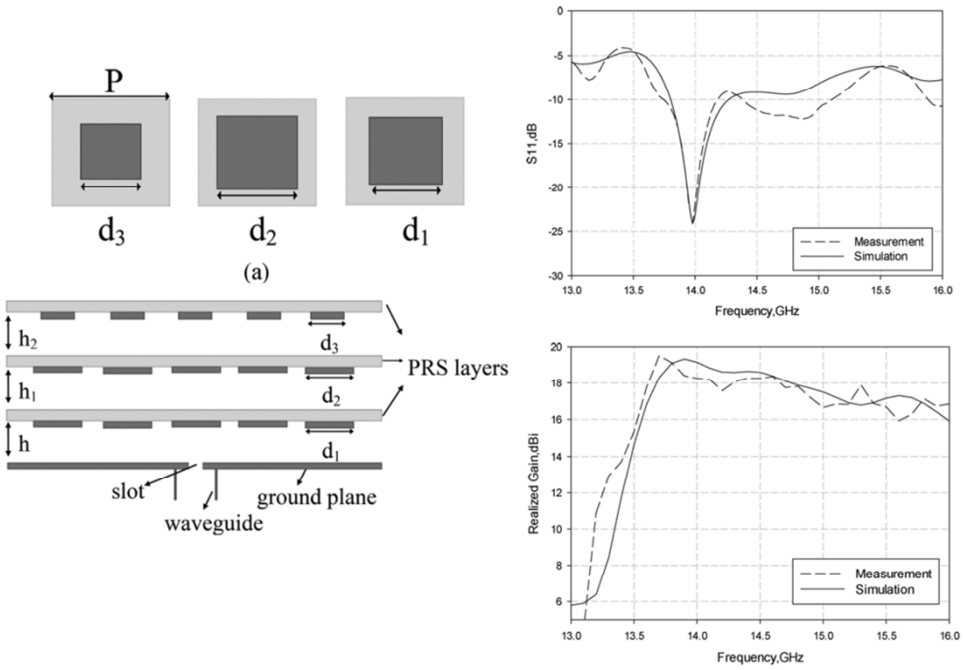

Figure 2.52: Configuration and characteristics of the broadband resonant cavity antenna based on the three-layer dissimilar patch PRS structure and the slot-loaded waveguide source antenna [10].

In use of dielectric materials, a superstrate based on three asymmetric dielectric layers was used with an open-end waveguide source in a resonant cavity antenna as shown in Fig. 2.51 [9]. The effects of a dielectric property, a thickness of each layer and a superstrate size on antenna performance, were studied. The 3-dB radiation bandwidth was 22% at the operation frequency of 11.1 GHz and the peak gain was 18.2 dBi. The superstrate size was around $1.5\lambda_0 x 1.5\lambda_0$. (40x40 mm^2) and the total superstrate thickness was roughly 0.52 λ_0 (14.05 mm). The considered point of fabrication is depending on specific dielectric properties and its thickness.

A broadband resonant cavity antenna based on a multilayer PRS superstrate as shown in Fig. 2.52 has also been investigated [10]. The PRS was a three-layer structure with dissimilar square patch arrays. The 3-dB radiation bandwidth was around 15% at the middle frequency of 14.5 GHz with a peak gain of 19.5 dBi. The overall area of the antenna was $80x80mm^2$ or $\sim 4\lambda x 4\lambda$ at 14.5 GHz. The total height of a superstrate structure was around 24.3 mm ($\sim 1.18\lambda$). The impedance bandwidth was not good due to the reflection characteristic of a slot-loaded waveguide source. The trade-off comes up with the air-filled superstrate thickness and radiation bandwidth.

2.5 Summary

In this Chapter, the literature related to the research work of the thesis has been discussed. The review work has focused on three areas of research; design and properties of metamaterials in electromagnetic spectrums, development of wideband patch antennas and antenna devices with a metamaterial-based ground plane, and the resonant cavity antennas. It has been shown that there has been significant interest in studies of metamaterials and their characteristics such as plasmas frequency, Fano resonance effects, extraordinary optical transmission, and absorbers. Metamaterials exhibit novel properties as phenomenal resonances which are not possible with the conventional materials. The novel designs of a superstrates in resonant cavity antennas have also been illustrated in performance and critical features. Significant improvements can be made in antenna performance by incorporating metamaterials into antenna devices.

CHAPTER 3 FANO RESONANCE IN A TWO-LAYER PATCH BASED METAMATERIALS

3.1 Introduction

This chapter describes the research work on the design and studies of an electromagnetic metamaterial exhibiting Fano resonance [45, 130-133]. For example, in a two-layer array [134, 135], the metamaterial constituent shows unusual properties based on an interaction of incident radiation with the ordinary properties of materials. The mechanism is based on a coupling effect of the reactive near-field between resonant elements adjacent to each other. In the physical arrangement, metamaterials based on the metallo-dielectric composite medium are formed in a periodic fashion that plays a fundamental role in the electromagnetic interaction in their materials. A unit-cell can be considered as a building block of a material allowing a convenient investigation of the material properties. The scattering response can reveal electromagnetic activities and also explain anomalous resonances in the engineered material. The desirable resonant frequency depends on dimensions of a unit-cell with respect to the operating wavelength.

The use of two coupled resonators in several metamaterials implies that unit-cells can produce a resonance effect. The resonant elements interact with incident radiation resulting in the near-field coupling effect. Here, the resonance configuration is based on two coupled layers of identical patch arrays which provide the advantages of the ease of design and analysis. The investigation of metamaterials is based on the responses of transmission and reflection coefficients. With the modification of physical parameters, tunability can be manipulated for the desirable frequency. Two dielectric materials are used to produce metallo-dielectric configurations. The modal properties of metamaterials are introduced by phenomenal resonances of the extraordinary transmission related to the trapped (absorbed) modes. The behaviour of resonance depends on the physical configuration and the ordinary properties of dielectric materials. In addition, a physical insight is considered in the attribute of the surface current configuration in illustration of the Fano-resonance effect. Also, the complex properties of their materials are presented as an electric and magnetic response. The designed configurations are produced using micromachining based fabrication techniques. Also, the verifications of the practical structures are made by measurement and comparison with the results of simulation.

3.2 Origin of the Fano resonance

The Fano effect originated from the studies of the ionisation of an atomic system in physics associated with the resonance scattering in terms of the interference phenomenon between a discrete (bound state) and a continuum (unbound state) spectrum [52]. The appearance of a spectral line-shape illustrates the intensity alternation and also the phase shifting effect is a significant condition to obtain a resonance process. The Fano resonance can be described by a line-shape function perturbed. The unique characteristic function results in the asymmetric profile is given as [52]

$$F(\epsilon) = \frac{(\epsilon+q)^2}{\epsilon^2+1} \tag{3.1}$$

$$\epsilon(\omega) = \frac{2(\omega-\omega_o)}{\delta} \tag{3.2}$$

The parameter, q, is a line-shape factor which indicates the degree of asymmetry of a resonance. The parameter, ϵ, is a reduced energy or a response as a function of a frequency. The parameter, ω_o and δ are a resonant frequency and a resonant bandwidth.

Fig. 3.1 shows the graphic plot of a normalised Fano function in a variation of the parameter q consisting of 0, -1, 1, and 100. The normalised frequency is a ratio of ω/ω_o. The amplitude plots are normalised with the scaled factor (σ) involved with the line-shape function that is defined by [54]

$$\sigma = \frac{1}{(1+q^2)} \tag{3.3}$$

The major attribute of an asymmetric line-shape is clearly seen in two cases in which the locations of a peak and a trough is around the resonant frequency. It is seen that the parameter q is able to influence on a resonant profile. The consideration of the parameter q is to be large ($q \gg 1$) leading to a symmetric line-shape as expressed as the Lorentzian function $L(\epsilon)$. Therefore, the mathematic formula in equation 3.1 is modified as

$$L(\epsilon) = \frac{1}{\epsilon^2+1} \tag{3.4}$$

In contrast, the anti-Lorentzian appears as the parameter q becomes a zero. As a consequence, the asymmetric degree of a shape-line profile can be influenced by the parameter q for which a small value offers the sharp transition of the coincident resonance. The parameter q with a sign also presents the order of the peak and dip attributes.

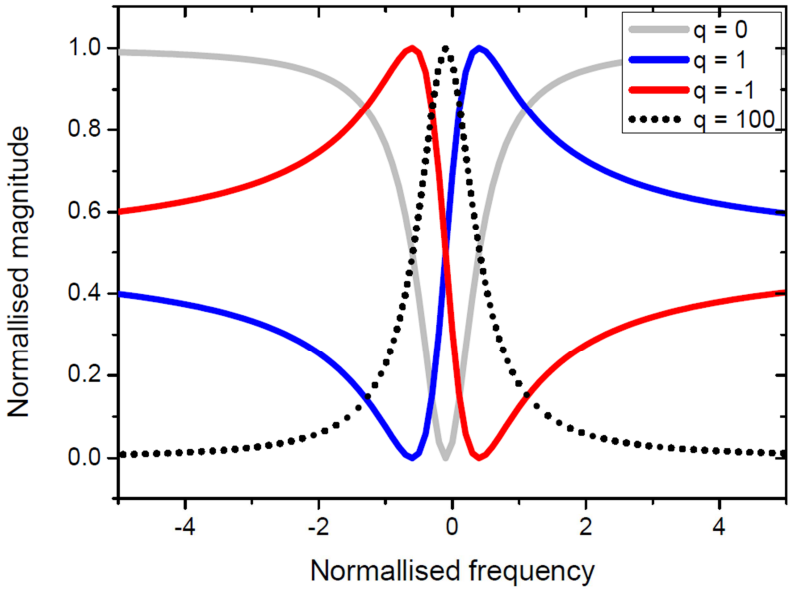

Figure 3.1: Behaviour of the asymmetric line-shape profile of the Fano function.

In conjunction with the electromagnetic interference, the light phenomenon of the Wood's anomalies [136] occurs in a metallic diffraction grating that the extraordinary illumination was observed but then rapidly diminished at the vicinity of a wavelength spectrum. The explanation [130] has associated the asymmetric behaviour with the electromagnetic surface wave mode as a surface plasmon polariton (SPP) [137]. The Fano resonance is connected with the hybridised plasmon modes found in the light-matter interaction in nanostructures [138, 139]. It is shown that the coupling of incident radiation causes a charge configuration along a material interface of nanostructures and the formation is referred to as the SPP behaviour. In association with the original Fano effect, there are two significant attributes consisting of the bright (super-radiance) mode and the dark (sub-radiance) mode. This effect can result in the asymmetric line-shape that the peak and dip (off-peak) locations are coincident at adjacent frequencies. In order to explain the mechanism of the plasmonic system, the resonant elements are electromagnetically induced by the incident far-field propagation. The radiative mode (peak) occurs in that process and this mode can influence the near-field coupling effect in short distance with the adjacent elements. This interaction results in the non-radiative (dip) mode which is a significant condition of the Fano effect in the spectral response. The surface wave is related to the charge distribution associated with a dipole moment. Hence, the occurrence of an anti-phase current configuration is dealt with the coupled SPP mode in plasmonic structures.

The electromagnetic theory of the Fano resonance in plasmonic metamaterials [140, 141] is presented to study the effect in connection with the general dispersive and lossy properties of the media. Here, the angular frequencies and intrinsic losses of the bright and dark modes are defined as ω_b and ω_d, and γ_b and γ_d, respectively. The parameters ω_b and ω_d indicate a resonant peak and dip. The parameters γ_b and γ_d determine a high and low damping of an asymmetric line-shape, respectively. The classical Fano function is modified to include a factor associated with the resonance contrast as briefly expressed as

$$F(\epsilon) = a\frac{(\epsilon+q)^2+b}{\epsilon^2+1} \tag{3.5}$$

$$q = \frac{\omega_d^2-\omega_b^2}{\gamma_b\omega_d} \tag{3.6}$$

$$\epsilon = \frac{\omega^2-2\omega_d^2+\omega_d\Delta}{\gamma_b\omega_d} \tag{3.7}$$

The term a represents a magnitude of the bright mode (peak) based on a symmetric lorentzian profile, while b is a modulation damping parameter by applying the intrinsic losses as expressed as

$$b = 4\frac{\gamma_d^2 q^2}{\Delta^2} \tag{3.8}$$

The term Δ is the phase difference of the asymmetric resonant frequency due to coupling between the dark and bright mode as

$$\Delta = \pm\frac{\omega_d^2-\omega_b^2}{\omega_d} \tag{3.9}$$

3.3 Fano-resonance in a two-layer metamaterial

3.3.1 Metamaterial design

By analogy with the grating configuration [45], the structure must possess two attributes of a resonant asymmetric profile consisting of the peak (radiative mode) and the dip (non-radiative mode). In the microwave regime, the configuration based on two layers of the grating strip arrays with a dielectric spacer is an example showing the coupled SPP behaviour. In addition, a square patch array can behave as a truncated grating strip and can be modified to produce a switched polarisation response. In this section, a two-layer metamaterial consisting of two identical patch arrays is designed and studied. The selection of a square patch array is considered in a geometric layout that is able to form the SPP-like behaviour in the microwave regime. Also, the benefit of using a square patch based design is less sensitive to polarisation due to its higher degree of symmetry than short wires.

Fig. 3.2 illustrates the physical layout of the metamaterial formed by a planar dielectric slab with electric permittivity (ε_r) and magnetic permeability (μ_r). The coupling mechanism of two symmetric layers based on identical arrays of square patch elements which are positioned on the top and bottom surface of the dielectric slab. The resonant frequency is determined by the period in a patch array and the physical dimensions of a metallic patch element. The primary investigation is started with the observation of resonance behaviour in two conditions: (1) the resonant patch in a coupled lattice and (2) the properties of dielectric materials.

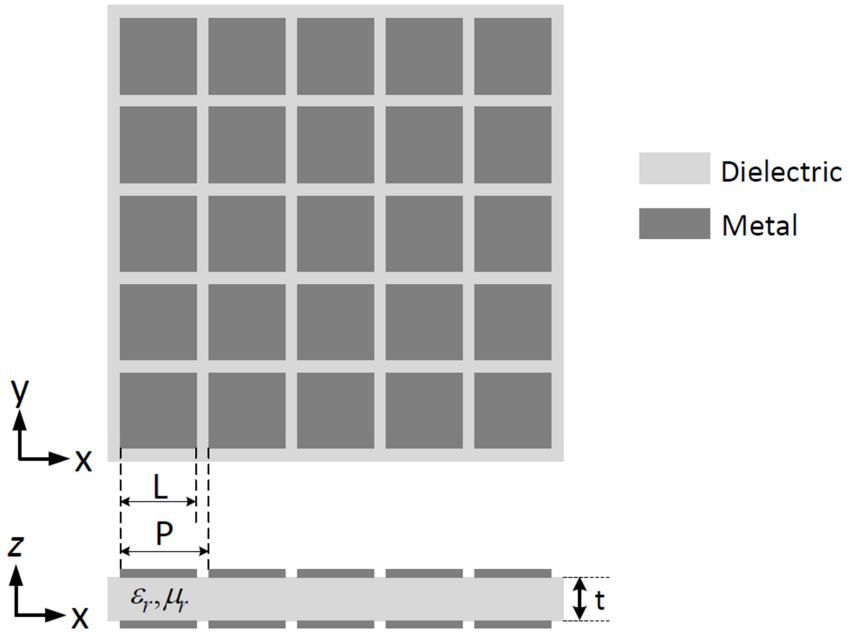

Figure 3.2: Geometry of the configuration of a patch based double layer metamaterial.

Initially, a lossless material with a unity dielectric constant (i.e. air) as an ideal dielectric material was used to study this type of metamaterials. Therefore, the material properties are referred to as $\varepsilon = \varepsilon_o$ and $\mu = \mu_o$, ε_o and μ_o are electric permittivity and magnetic permeability of a free space, respectively. The Fano-resonance metamaterials are characterised by a scattering response. The resonant frequency is targeted at 10 GHz. The corresponding wavelength (λ_o) is 30 mm which is used to determine the period (P) in a patch array to be approximately $\lambda_o/2$ in length, giving the grating frequency at ~20 GHz. The length (L) of a square patch determines the resonant frequency.

3.3.2 Characteristics of the Fano-resonance metamaterials

The basic characteristics of the Fano-resonance metamaterials are observed from the transmission and reflection coefficients. The investigation of the geometric two-layer metamaterials is performed by HFSS simulation as detailed in Appendix A. With the field interaction, the occurrence of the Fano effect is found at the designed frequency. Fig. 3.3 shows the Fano-resonance profile obtained for the design in which the dielectric medium is assume to be a lossless material with the unity dielectric constant. The dimensions of the unit-cell are 15x15 mm^2 corresponding to a half wavelength at 10 GHz. The dimensions of the copper patches are 13x13 mm^2. The dielectric thickness is 1.0 mm corresponding to 1/30 of the target wavelength. The electromagnetic response is characterised by studying both the magnitude and phase responses of transmission and reflection coefficients.

As a result, the profile of the resonance behaviour exhibits two modes in transmission. The points of the peak and dip attributes are located at 10 GHz and 11.2 GHz leading to a narrow frequency window due to strong electromagnetic coupling between the patch arrays. The asymmetric line-shape is the signature of the Fano resonance. In addition, the phase behaviour of the reflection and transmission shows a phase-shift of 180° across a resonant region. The two patch arrays are out of phase due to coupling effects of a harmonic oscillator system [53]. The occurrence of the first phase change is located at the frequency of the zero reflection magnitude because of the oscillation of patches under the external field excitation. While the second phase variation is related to the coupling field causing the zero-amplitude transmission. It is seen that the attribute of a resonance condition is associated with the effect of the extraordinary optical transmission in the opposite dip location [45].

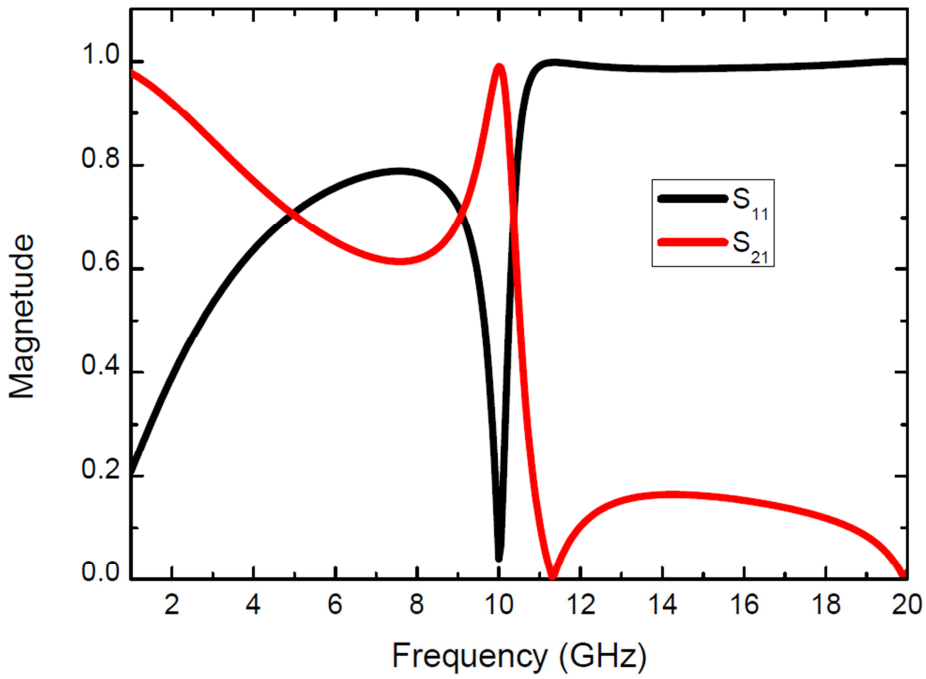

(a)

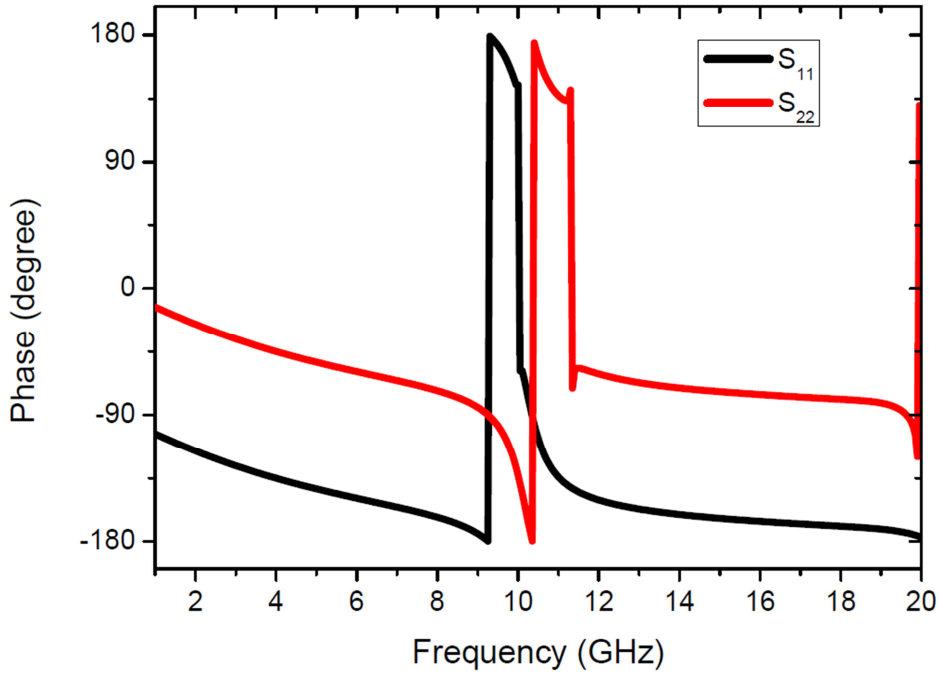

(b)

Figure 3.3: Simulation results for the transmission and reflection of the base-line two-layer metamaterials with a period of 15 mm and the patch length of 13 mm, (a) magnitude and (b) phase.

As discussed in the studies of a two-layer structure in [135], the effect of the Fano resonance and the Fabry-Perot resonance clearly shows different characteristics and the resonance profile in the electromagnetic property. It was found that the attribute of the trapped mode (absorbance) occurs only in the context of the Fano-resonance effect. Therefore, the asymmetric line-shape of Fano resonance can distinguish from the behaviour of Fabry-Perot resonance characterised by a symmetric profile. The characteristic of a trapped mode is the significant nature encountered in the frequency region in the vicinity of the transmission peak and refection peak (transmission dip). The thickness of a dielectric spacer in this work is a key factor in determining the near-field characteristics. While the study based on the Fabry-Perot approach [135], the layer separation was larger without causing coupled perturbation.

3.4 Investigation of Fano-resonance metamaterials

3.4.1 Properties of a one-layer square patch based array

For design of metamaterials with two or more layers of patch based arrays, it is necessary to carry out a study of the properties and characteristics of a one-layer patch array in detail. The response is referred to as a background for the one layer structure without the near-field coupling effect. Fig. 3.4 shows the transmission and reflection characteristics of a single layer square patch array. The period of the array (P) is 15 mm corresponding to a half wavelength at the frequency of 10 GHz. Four designs with different ratios of L/P values of 0.3, 0.5, 0.7 and 0.9 are investigated. Hence, the patch lengths (L) are 3.5 mm, 7.5 mm, 10.5 mm, and 13.5 mm, respectively. The results of simulation based on the Floquet theory in Fig. 3.4 show that the transmission and reflection behaviours have a significant dependence on the value of L/P. The grating frequencies in transmission are 19.68 GHz, 18.35 GHz, 18.76 GHz, and 19.96 GHz, respectively. The magnitude of transmission decreases significantly with frequency as the ratio of L/P or the value of L decreases and the corresponding reflection magnitude increases. For larger values (0.7 and 0.9) of L/P, the change is transmission and reflection is smoother, while it is much sharper for small values of L/P, 0.3 and 0.5, respectively. The effect of L/P on the grating frequency is further studied over a large range of L/P and the results are shown in Fig. 3.5. The dependence of grating frequency on L/P has a symmetric behaviour with respect to the value of 0.57. The range of the grating frequency is from 18.25 GHz and 20 GHz over a variation of the ratio of L/P from 0.2 to 0.95.

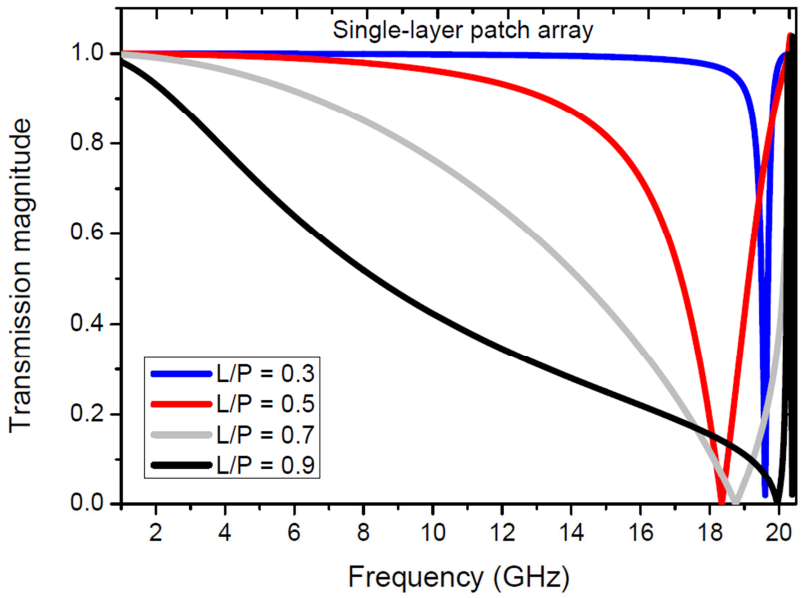

(a)

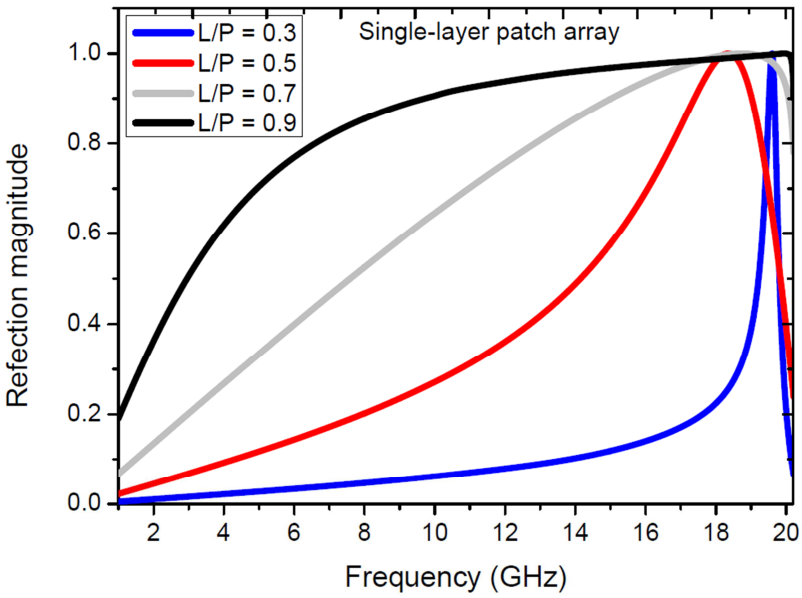

(b)

Figure 3.4: Simulation results of electromagnetic characteristics for a one-layer patch array for different ratios of L/P consisting of 0.3, 0.5, 0.7, and 0.9 (P = 15 mm), (a) transmission and (b) reflection.

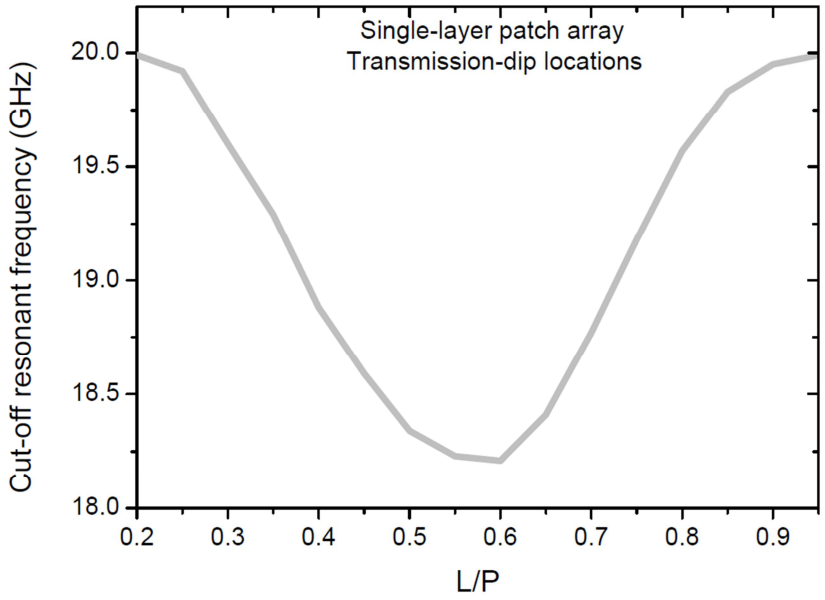

Figure 3.5: Simulation results for the location of the grating resonance as a function of the ratio L/P (P = 15 mm).

3.4.2 Effect of the L/P ratio in two-layer metamaterials

The configuration of the two-layer metamaterials is investigated for the period value of 15 mm and the free space separation of 1 mm between two square patch arrays which are aligned to each other. Fig. 3.6 shows the transmission and reflection behaviour of a two-layer design and that of the one-layer array in the material for L/P ratios 0.9, 0.5, and 0.3. This study illustrates the relationship between the resonance condition of the patch element and the grating response of an array configuration. For the L/P ratio of 0.9, the peak and dip of the Fano resonance occur at ~10 GHz and ~11 GHz as shown in Fig. 3.6(a). Away from the frequency region of the Fano resonance, the behaviour of the two layer material is similar to that of the single array. In the case of the L/P ratio of 0.5, the first resonance (peak) of the two-layer metamaterials occurs at ~18 GHz, in contrast to the trough of the single (array) around the same frequency as can be seen in Fig. 3.6(b). This resonance characteristic is graphically similar to the effect of the electromagnetically induced transmission (EIT) [59]. In the case of the L/P ratio of 0.3, the transmission characteristics of a single-layer and two-layer materials are shown in Fig. 3.6(c). There is no sharp resonance in the spectral frequency due to the influence of the grating response. It is concluded that the Fano-resonance interference is limited when the patch elements resonate at higher frequencies than the grating response. The results in Fig. 3.6 show that in order to obtain the Fano resonance in the two-layer metamaterials, the ratio of L/P should be selected to be in the range of $0.5 < L/P < 1$.

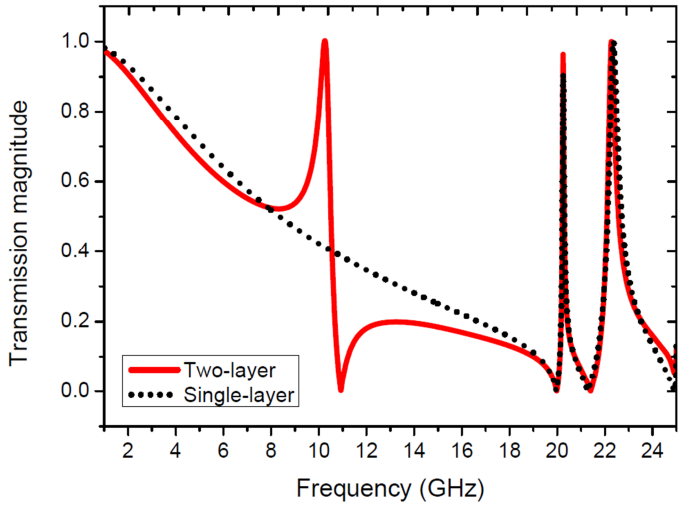

(a)

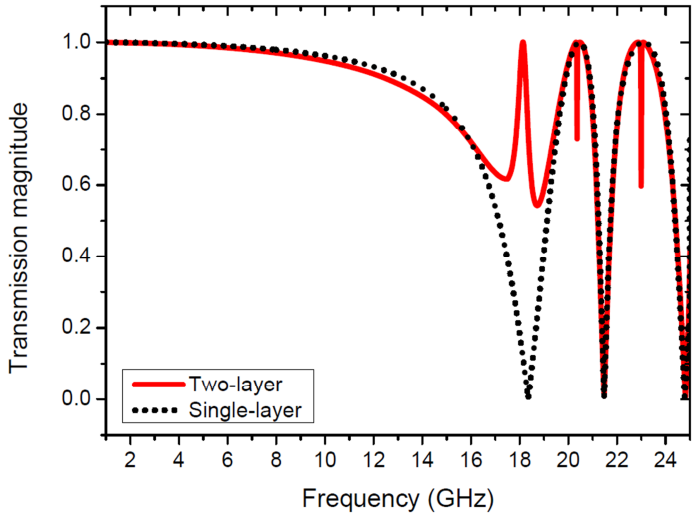

(b)

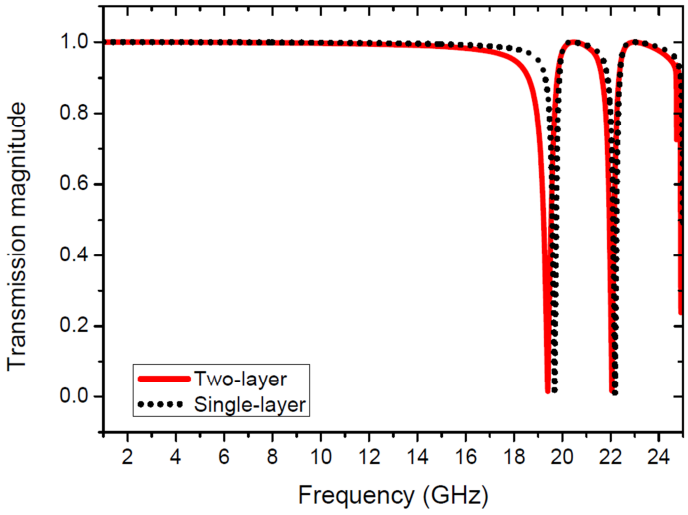

(c)

Figure 3.6: Simulation results for the defect mode in the metamaterials with different ratios of L/P, (a) 0.9, (b) 0.5, and (c) 0.3 (P = 15 mm).

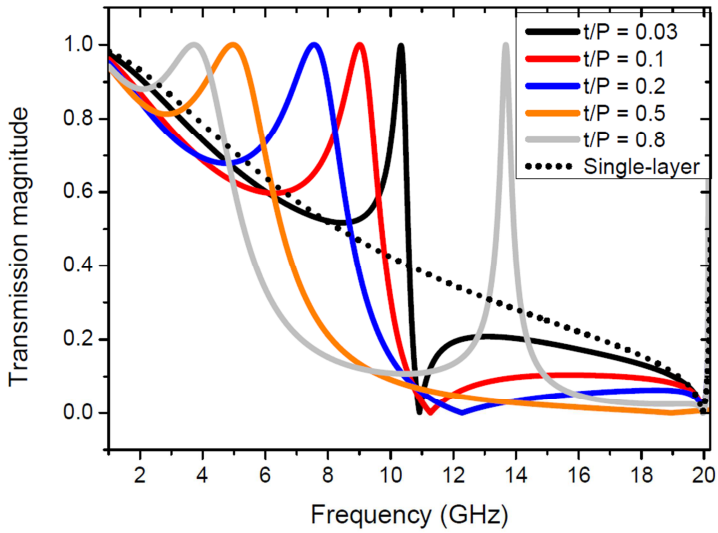

Figure 3.7: Simulation results for the Fano effect for various values of the inter-layer separation (t). (P = 15 mm), the single-layer design (background) the ratio L/P is 0.9.

3.4.3 Effect of the ratio t/P

The coupling level is connected to the separation between a pair of identical patch arrays. This condition also involves to the Fabry-Perot approach. Fig. 3.7 shows the effect of the inter-layer separation (t) (the thickness of an air dielectric) on the resonance behaviour in the two-layer metamaterials. The periodic value of P is maintained as a half wavelength of 15 mm corresponding to 10 GHz. The ratio of L/P is fixed as 0.9 (13.5 mm). In this study, a parametric variation of the ratio t/P consists of 0.05, 0.1, 0.5, and 0.8. The transmission responses are observed and compared with that of the single layer. The term of the frequency window is defined by a band between the locations of the peak and dip of the Fano resonance. As a result, the responses are observed that the frequency windows of the Fano resonance are extended by the increase in the ratio t/P. However, no frequency window can be defined for the t/P ratio between 0.5 and 0.8, no sharp dip is presented in the transmission response. As the ration of t/P (or t) increases the resonance becomes broader indicating decreased electromagnetic near-field coupling as a dielectric thickness is increased. For the ratio of t/P = 0.8, another resonance peak is observed at 13.7 GHz at which the Fabry-Perot approach agrees with the reflection phase of -163° (at 13.7 GHz).

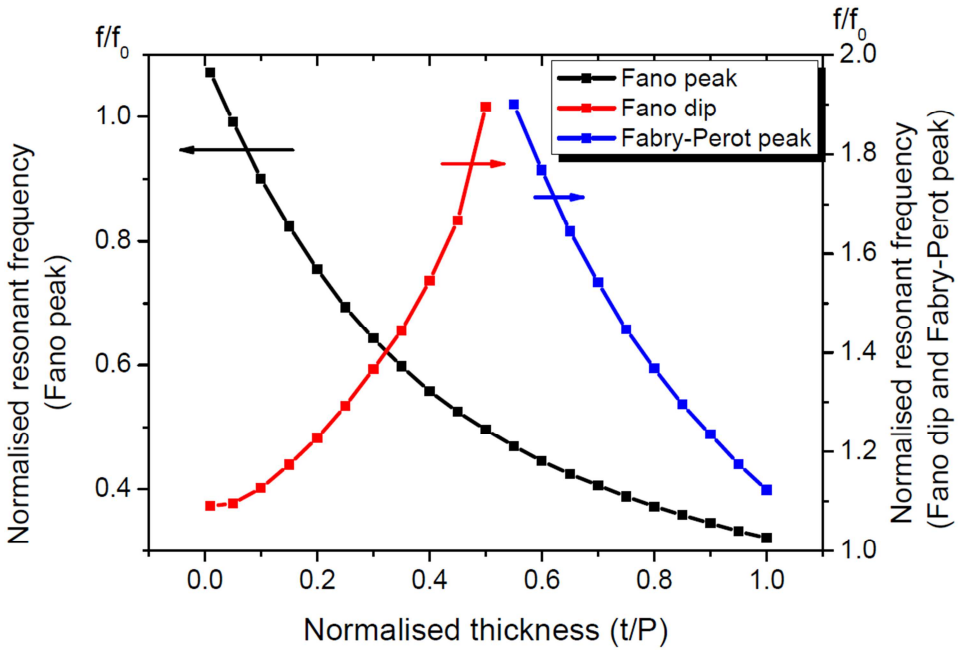

Figure 3.8: Simulation results for the relation of the Fano effect as a function of the different ratio t/P.

Fig. 3.8 describes the relation of the Fano effect based on the normalised inter-layer thickness t in connection with the ratio t/P in a range over 0.01–1.0. The normalised-frequency is dealt with respect to the frequency (f_0) of 10 GHz. Here, there are three attributes connected to this investigation consisting of the Fano peak, the Fano dip, and the Fabry-Perot peak as pictured in Fig. 3.7. It is seen that the association between the Fano dip and the Fabry-Perot peak is relied on a inter-layer distance as a function of wavelength due to the coupling level of the interfacial near-field [142]. The attribute of the Fano peak is associated with the extraordinary transmission and also considered as zero-order transmittance. In this case, two modes can be considered consisting of the coupled SPP mode along with the cavity mode in the similar context of the metallic grating structure [143]. As the ratio of t/P increases, the frequencies of the Fano peak (radiative mode) decrease, while the frequencies of the Fano dip (non-radiative mode) increase. It is shown that the Fano peaks at the normalised-frequency are relocated from ~1.1 to ~0.4 depending on a level of the coupled SPP strength.

3.4.4 Effect of the patch period (P)

In this section, a resonance condition of the Fano effect is studied as a period of the patch arrays is changed. The period is varied with respect to the wavelength (λ_o) at a fixed frequency (f_o) of 10 GHz. Fig. 3.9 shows the normalised peak and dip frequencies

of the Fano resonance as a function of P/λ_o for four different inter-layer distances (values of t/λ_o). In the previous investigation, the period in a design target was determined by $P = 0.5\lambda_o$ and it was shown that the ratios of L/P and t/P should be less than 0.5 to in order to achieve the Fano resonance. Here, the parametric study is performed for the ratio of P/λ_0 between 0.1 and 0.65. The difference in the coupling conditions is studied in a variation of the inter-layer separation (t) of 1.5 mm (0.05λ_0), 3 mm (0.1λ_0), 4.5 mm (0.15λ_0), and 6 mm (0.2λ_0). The ratio L/P is maintained as 0.9 in all of cases which means the radiative mode of the Fano resonance is not maintained at 10 GHz.

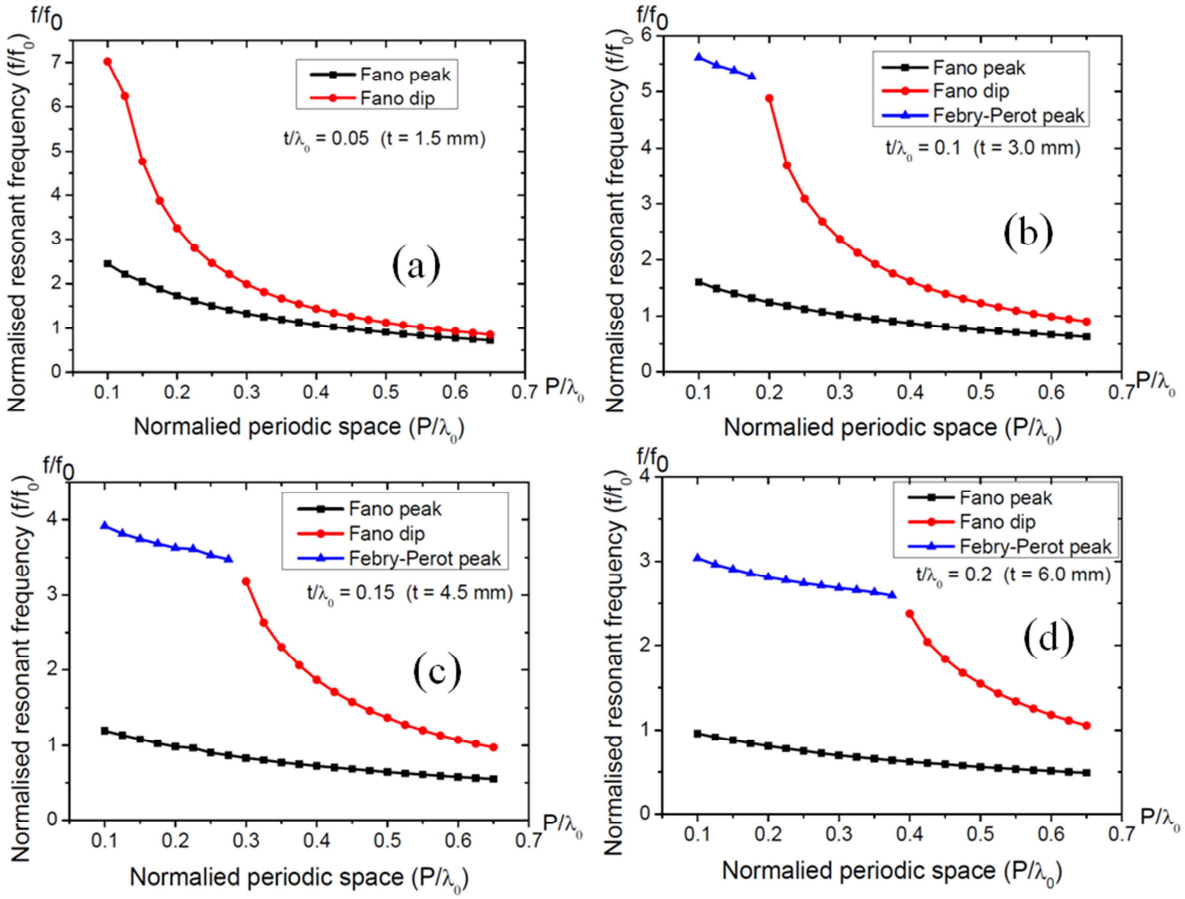

Figure 3.9: Simulation results of the resonance effect as a function of the ratio P/λ_0 in a variation of t/λ (a) 0.05, (b) 0.1, (c) 0.15, and (d) 0.2.

As shown before, the response of the Fano resonance as a period changed is associated with the grating frequency of a one-layer patch array. Hence, the variation of the period is able to control the grating frequency. As a period is decreased, the grating or cut-off wavelength (λ_c) shifts to the higher frequency. This behaviour can lead to broadening of the peak or radiative mode of the Fano resonance. Also, the trapped mode dominates

and it enhances the supper-radiation mode. It is shown that the ratio of P/λ_0 plays a role in the location of the dip and a condition of the transition state of the Fabry-Perot effect. There are three cases in which the Fabry-Perot effect occurs resulting in the ratio P/λ_0 of ~0.2, ~0.3, and ~0.4 with respect to the ratio t/λ_0 of 0.1, 0.15, and 0.2, respectively.

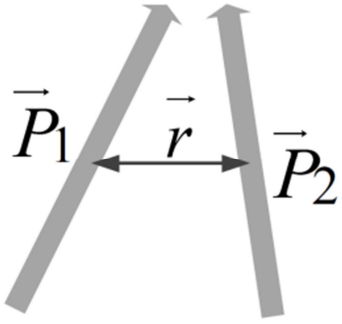

Figure 3.10: Configurations of the dipole-dipole interaction.

3.5 Anti-phase current configuration

The electromagnetic activity of materials can influence a polarisation based on an induced charge distribution creating an electric dipole or quadrupole effect as a class of the multi-pole configuration [144]. The orientations of the dipole and quadrupole are illustrated by a charge density with a displacement ($\vec{d}$) between two opposite sign charges ($\pm q$). The dipole moment can be presented as $\vec{p} = \pm q\vec{d}$ in a coupled opposite sign charges. In addition, the polarisation vector is given by $\vec{P} = N\vec{p}$ where N refers to as the number of electric dipoles per unit volume in medium. The behaviour of the dipole polarisation causes an electric dipole moment as a vector which is referred to as the lowest-mode multipole. The paired charge separation results in the polarised current density as

$$\vec{J}_P = \frac{\partial \vec{P}}{\partial t} \tag{3.10}$$

This term is included in the Maxwell's equation which is performed in HFSS simulation package. In consideration with a coupled dipole moment in space, the extension of the coupling phenomenon shows the interaction force. Fig. 3.10 illustrates the relation of coupling of two dipole moments between $\vec{P}_1$ and $\vec{P}_2$ which interact at the distance, $\vec{r}$ [29].

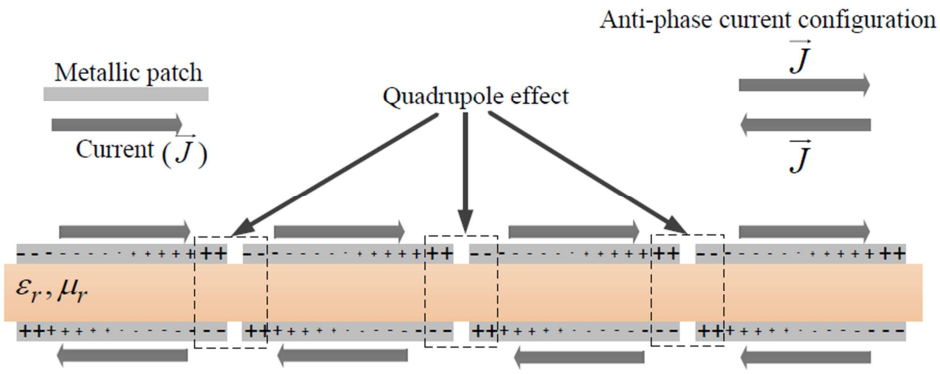

Figure 3.11: The quadrupole and anti-phase distribution in the two-layer metamaterials.

In this work, the observation of the electromagnetic behaviour on a pair of identical patch arrays can be illustrated in the same context as the coupled surface plasmon polaritons (SPPs) [45]. The effect on a charge and polarisation in coupled patches as a parallel configuration results in the coupled dipole moments under an excitation of the electromagnetic field. In that, the formation of charge distributions can influence each other which cause a field interaction leading the coupled interfacial surface wave.

Fig. 3.11 illustrates the understanding of a physical insight with assistance of a charge and current configuration. In the cross-sectional view, electric charges on the front patches are produced by incident field leading to the creation of the polarisation current $(\vec{J})$ behaved as a dipole moment. As the back patches are able to induce near-field energy from the front patches, the charge behaviour can cause an anti-phase current as a dipole-dipole interaction with the phase-changed behaviour in a reactive near-field distance. The presence of the quadrupole is occurred by electric charge arrangement near a space between the adjacent edges between four patches in two arrays. Therefore, the behaviour of a surface current distribution is referred to as a coupled SPP mode.

To understand the physical insight of the geometric structure of two patch arrays, surface current configuration associated with the Fano-resonance effect is studied. It is seen that the behaviour of surface current distribution on two patches is a mimic of the coupled SPPs. Similar to the effect in a dielectric grating excited by microwave radiation [145], the charge distribution in planar array configuration causing a surface electromagnetic wave as a SPP-like behaviour depends on an array period and a patch length as illustrated in Fig. 3.12. It is evident that surface current distributions at the selected frequencies of 8 GHz, 10 GHz and 11.2 GHz provide the anti-phase signature which correspond to a key feature of the characteristics of the Fano resonance are shown in Fig. 3.3.

The vector surface current is caused by the orientation of electric charges when it interacts with the incident wave in the top patch array (entrance side). The near-field coupling induces a similar current in the bottom patch array (exit side) and the coupling process on an anti-phase current configuration leads to the occurrence of coupled SPP modes. As seen in Fig. 3.12(a), the current density in bottom array is negligible at 8 GHz. But at 10 GHz, the top patch elements are able to oscillate and produce the coupled near-field with the bottom patch array. The current distribution on two patches illustrates the same magnitude but the current direction is different as an anti-phase as shown in Fig. 3.12(b). This attribute results in the radiative mode which the peak of the Fano resonance is revealed in a transmission response. As the frequency beyond 10 GHz (peak position), a vector current changes its direction. This mode also operates in a coupling of the oscillation excited by a reactive near-field and 180° out of phase. It shows that anti-phase current distribution with the same magnitude resulting in the non-radiative mode which a dip of the Fano resonance at 11.2 GHz as shown in Fig. 3.12(c). Hence, the characteristic of the trapped-mode resonance (absorbance) is established between two frequencies and it is the signature of Fano resonance.

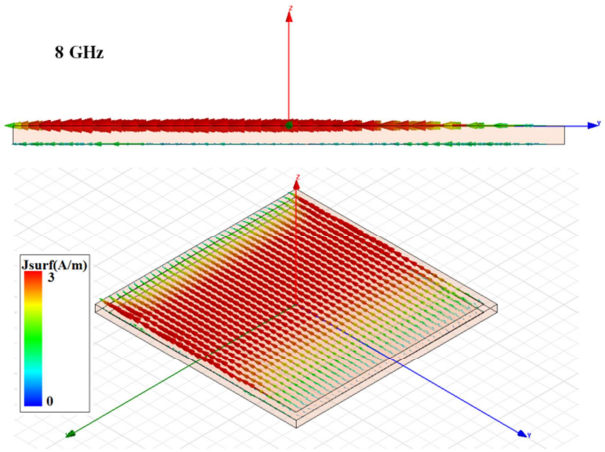

(a)

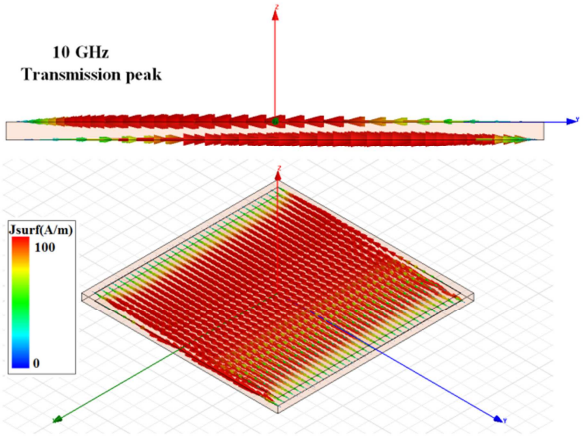

(b)

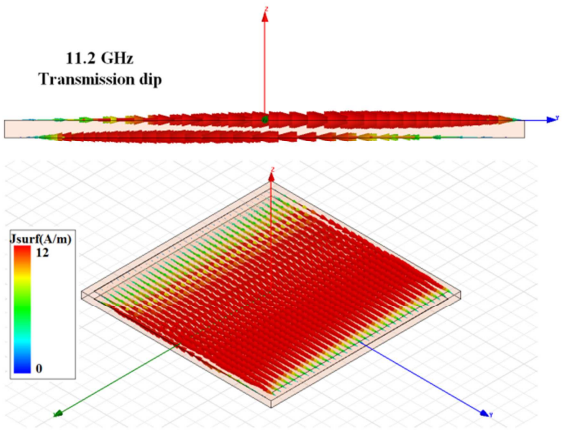

Figure 3.12: Simulation results for the current configuration of the Fano effect as a period of 15 mm and the patch length of 13 mm at (a) 8 GHz, (b) 10 GHz, and (c) 11.2 GHz.

3.6 Material characterisation of Fano-resonance metamaterials

With the dielectric material is excited by electromagnetic radiation based on a dipole-dipole coupling, the ordinary properties such as magnetic permeability and electric permittivity are affected and transformed to non-linear behaviour by the interference effect. In nature, the ordinary medium provides static material properties of electric permittivity and magnetic permeability with the ability to support the electromagnetic field. Here, the appearance of the Fano resonance is able to modify a complex function of material properties of the permittivity and permeability as defined as $\varepsilon = \varepsilon' + j\varepsilon''$ and $\mu = \mu' + j\mu''$, respectively. In [146], the plasma frequency is introduced in the microwave operation that involves a complex function of the material properties are expressed as

$$\varepsilon_r(\omega) = \frac{\varepsilon(\omega)}{\varepsilon_o(\omega)} = \left(1 - \frac{\omega_{pe}^2}{\omega(\omega + j\gamma_e)}\right) \tag{3.11}$$

$$\mu_r(\omega) = \frac{\mu(\omega)}{\mu_o(\omega)} = \left(1 - \frac{\omega_{pm}^2}{\omega(\omega + j\gamma_m)}\right) \tag{3.12}$$

where ω_{pe} and ω_{pm} are an electric and a magnetic plasma frequency, respectively. The material loss term describes a damping frequency in the electrical components, γ_{pe} and the magnetic component, γ_{pm}. In a lossless medium, the damping terms disappear from equations (3.10) and (3.11) and $\varepsilon_r(\omega)$ and $\mu_r(\omega)$ can be re-written as

$$\varepsilon_r(\omega) = 1 - \frac{\omega_{pe}^2}{\omega^2} \tag{3.13}$$

$$\mu_r(\omega) = 1 - \frac{\omega_{pm}^2}{\omega^2} \tag{3.14}$$

In connection with the complex index of refraction, the identical properties in the plasmas and damping frequencies can be expressed as $\omega_p = \omega_{pe} = \omega_{pm}$ and $\gamma = \gamma_e = \gamma_m$. By dealing with the electric permittivity and the magnetic permeability, the expression of the refraction index can be determined by

$$n(\omega) = \sqrt{\varepsilon_r(\omega)\mu_r(\omega)} \tag{3.15}$$

$$n(\omega) \approx 1 - \frac{\omega_p^2}{\omega^2} - j\frac{\gamma\omega_p^2}{\omega^3} \tag{3.16}$$

In addition, the complex impedance (z) is influenced by a complex function of the permittivity and permeability as expressed as

$$z = \sqrt{\frac{\mu(\omega)}{\varepsilon(\omega)}} \tag{3.17}$$

In association with the electromagnetic response, the retrieval method [147] of material characterisation to obtain permittivity and permeability is connected with the scattering or S parameters consisting of the reflection and transmission responses as described in Appendix B. The expression of refraction of index and impedance can be determined by [148]

$$n = \frac{1}{kd} cos^{-1}\left[\frac{1}{2S_{21}}(1 - S_{11}^2 + s_{21}^2)\right] \tag{3.18}$$

$$z = \sqrt{\left(\frac{(1+S_{11})^2 - S_{21}^2}{(1-S_{11})^2 - S_{21}^2}\right)} \tag{3.19}$$

The parameter, d, refers to a thickness of the two-layer structure and also the parameter, k, is a wave number. Therefore, the relations in (3.15) and (3.17) can be rewritten and the effective medium properties consisting of electric permittivity (ε) and magnetic permeability (μ) are determined by complex impedance and refractive index as $\varepsilon(\omega) = n/z$ and $\mu(\omega) = nz$.

Fig 3.13 shows the response of complex material properties of the Fano-resonance metamaterial consisting of electric permittivity and magnetic permeability. The lossless condition of an air-interior medium is considered in the Fano-resonance profile in which the locations of a peak and a dip are at 10 GHz and 11.2 GHz, respectively. The anomalous behaviour of electric permittivity and magnetic permeability are exhibited in a frequency window of the Fano effect. The condition of $\varepsilon_r(\omega) = 0$ is associated with the plasmas frequency that is located at the peak of the Fano line-shape as shown in Fig. 3.13(a). The effect shows the capability of the metamaterial to contribute the enhanced transmission. The complex function of magnetic permeability occurs in the frequency window between the peak and the dip of a Fano profile as illustrated in Fig. 3.13(b). The real part of magnetic permeability presents a near-zero value between the peak and the dip of the Fano-resonance profile leading to the resonant absorption.

It is found that a region between the peak and the dip of the Fano resonance effect can illustrate a complex function of electric permittivity and magnetic permeability. This feature can introduce the characteristics of frequency responses of electric permittivity and magnetic permeability as expressed as $\varepsilon(\omega) = \varepsilon_o(1 + \chi_e(\omega))$ and $\mu(\omega) = \mu_o(1 + \chi_m(\omega))$. The imaginary terms present electric and magnetic susceptibility leading to the appearance of loss in which the trapped mode occurs in that region. It is seen that the characteristics of a coupling as magnetic responses can be clearly observed in purely positive and negative values of a real part of the permeability. The corresponding

attributes of magnetic permeability behaviour is connected to two modes of the anti-phase current configuration at the peak and the dip locations of the Fano effect as seen in Fig. 3.11(b) and (c).

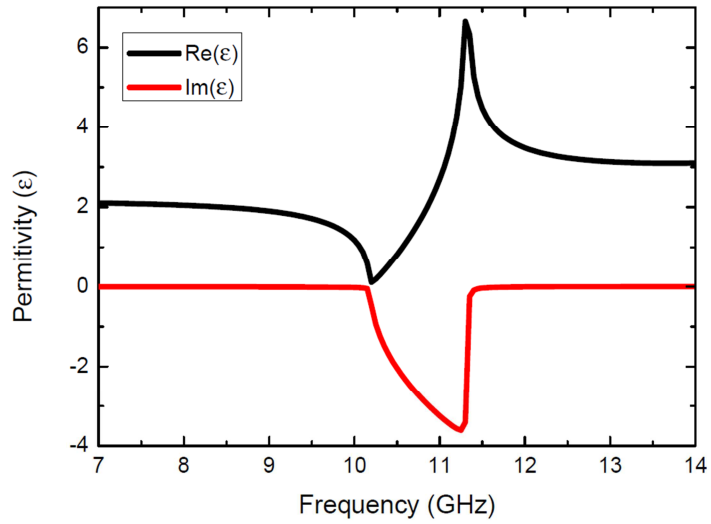

(a)

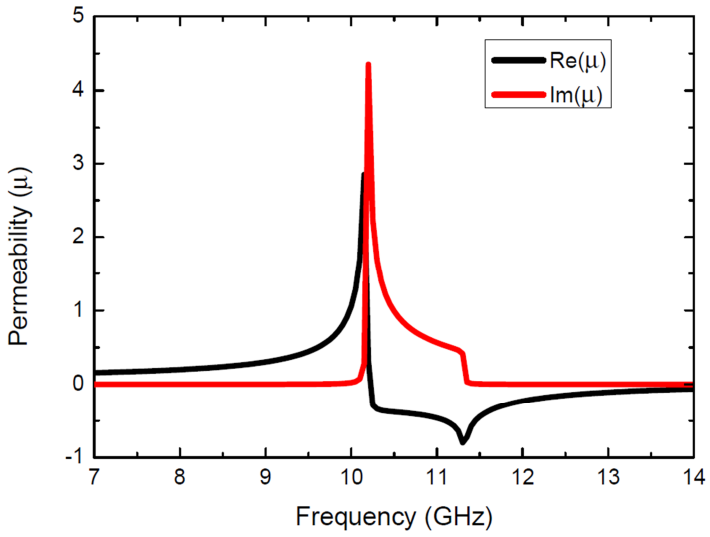

(b)

Figure 3.13: Simulation results for the complex properties of the metamaterial, (a) the electric permittivity and (b) the magnetic permeability.

3.7 FR4-based metamaterials

In this section, the study of the Fano-resonance metamaterials is carried out in use of the widely FR4 dielectric material which is a lossy material in the frequency range of interest. The presence of a resonance condition is demonstrated in the same way as for a

lossless material in the previous sections. The electric permittivity and loss tangent of the FR4 material are 4.1 and 0.02, respectively at 8~10 GHz [149]. The Fano-resonance metamaterials can be designed to operate at the target frequency of 15 GHz which is a part of the Ku band in satellite communications. The guided wavelength of the FR4 dielectric can be determined to be roughly ~10 mm (λ_g) by $\lambda_o/\sqrt{\varepsilon_r}$. Therefore, a half wavelength period for a patch array is 5 mm. The length of a square patch element is 4.5 mm. The FR4-based metamaterial is studied by a parametric variation of the thickness that is connected to the coupling level. The electromagnetic properties are studied in order to observe the Fano effect. The thicknesses of the FR4 dielectric board used in the design work are 0.2 mm, 0.8 mm, and 1.6 mm, respectively. Therefore, the normalised thicknesses (t/λ_0) in three case studies are $0.02\lambda_g$, $0.08\lambda_g$, and $0.16\lambda_g$, respectively.

Fig. 3.14 shows the characteristics of the coefficients of transmission, reflection, and absorption of the FR4-based metamaterial. The absorption is determined by $A = 1 - T^2 - R^2$. It can be observed that the peaks of transmission resonance occur at frequencies of 15.6 GHz, 13.84 GHz, and 11.65 GHz with respect to the FR4 thickness of 0.2, 0.8, and 1.6 mm, respectively. Due to the strong coupling effect, an asymmetric line-shape is clearly obtained in Fig. 3.14(a) which is for thinnest (0.2 mm) FR4 board, i.e. $\sim\lambda_g/100$. The lower peak transmission is a result of the effect of the finite dielectric loss in a FR4 material. The increase in FR4 thickness can influence the level of a coupling effect and a resonance condition. The behaviour results in a shift of the transmission peak towards the low frequency side and a broader resonance. It results from the reduced coupling of the near-field effect and the level of the resonance transmission increases as a result of less field strength in the FR4 material. Also, the distinctive attribute of the resonant absorption is maximum absorptance of 0.5 associated with the thinnest FR4 thickness of 0.2 mm. The resonant absorption becomes weaker as a FR4 thickness increases. The resultant absorption rate of 50% (0.5) can be considered in the impedance characteristics in terms of energy conversion efficiency determined by P_{out}/P_{in}. It is shown that the matched impedance condition is obtained when two wave impedances in a free space (~377Ω) at the entrance side (source) and the exit side (load) interact with impedance of the metamaterial. The characteristic impedance of the sharp Fano resonance in the thinnest FR4-based metamaterial becomes extremely small (near-zero) due to the strong magnetic response associated with the current distribution.

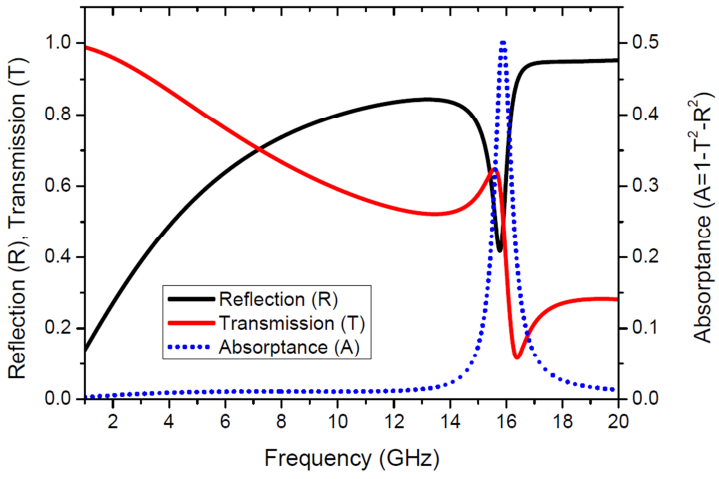

(a)

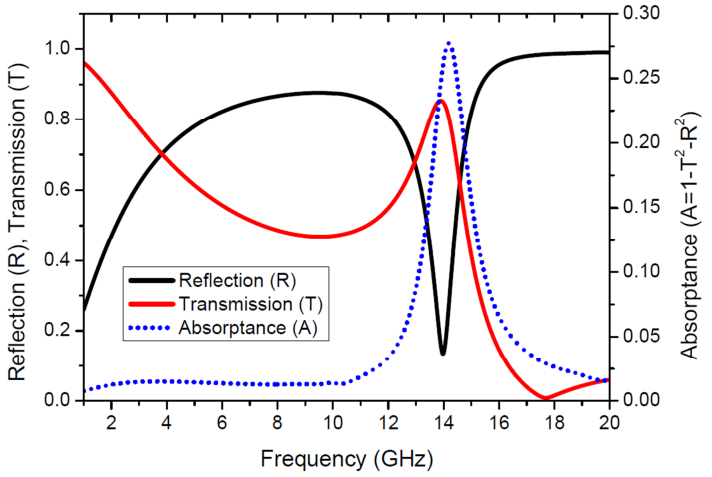

(b)

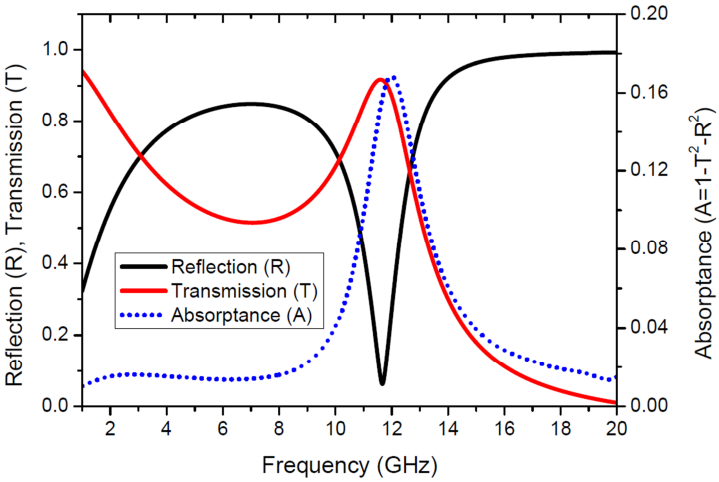

(c)

Figure 3.14: Simulation results for the electromagnetic response for the FR4-based metamaterial in a variation of the thickness, (a) 0.2 mm, (b) 0.8 mm, and (c) 1.6 mm.

3.8 LCP thin film based metamaterials

The employment of an LCP thin-film based dielectric material is investigated to study the Fano resonance effect due to its low dielectric loss and availability in thin film form. The LCP thin film (Ultralam 3850, Rogers) with a thickness of 100 μm is used as a dielectric spacer between a pair of copper based patch arrays. The electric permittivity and loss tangent for the LCP film are 2.9 and 0.0025, [150]. The target operating frequency is 10 GHz which leads to the guided wavelength (λ_g) of 17.6 mm so the equivalent film thickness in wavelength is λ/176. The array period of 8.6 mm is about a half wavelength. The dimensions of a square copper patch are 8.5x8.5 mm^2.

Fig. 3.15 shows the characteristics of transmission, reflection, and absorption for period values of 8.6 mm, 9.0 mm, and 10.4 mm, respectively. It can be seen that sharp Fano resonances are obtained. The locations of the transmission resonance peaks are at 10.07 GHz, 10.08 GHz, and 9.97 GHz, respectively. In contrast, the transmission dips are located at 10.36 GHz, 10.26 GHz, and 10.16 GHz, respectively. As a result, the appearance of the resonant absorption in all cases is at ~10.1 GHz and the magnitudes of absorptance are 48%, 49%, and 47%, respectively. These results illustrate the effect of period values in patch arrays which influence on the characteristics of wave impedance in the thin LCP film based metamaterials. When the value of a period is larger, the Fano resonance becomes weak as shown in Fig. 3.15(c).

Fig. 3.16 illustrates a physical insight of the surface current distribution as a vector profile on the top and bottom copper patch elements at two frequencies of 9.9 GHz and 10.4 GHz corresponding to a transmission peak and dip of the resonance characteristics in Fig. 3.15(b). The behaviour of the anti-phase current configuration based on a charge arrangement is evidently observed on the top and bottom patches in opposite direction at 9.9 GHz in Fig. 3.16(a). Also, that current behaviour is turned in direction at 10.4 GHz in Fig. 3.16(b). The current behaviour is similar to that in Fig. 3.12 and it is the result of dipole-dipole interaction between patches.

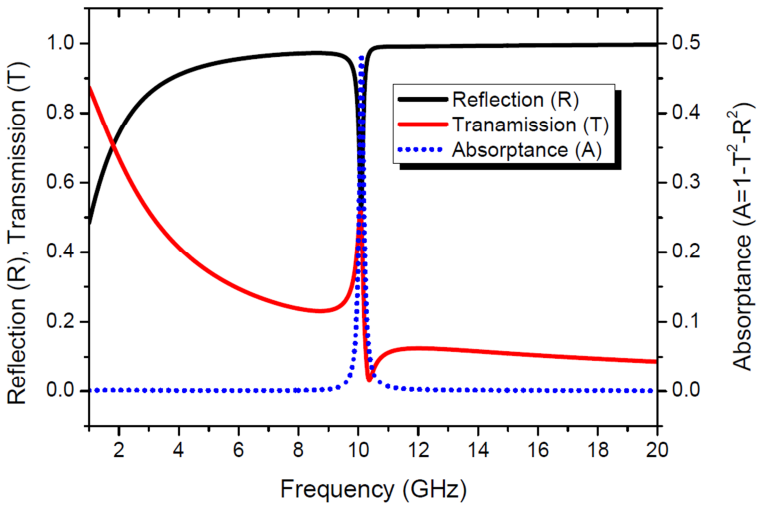

(a)

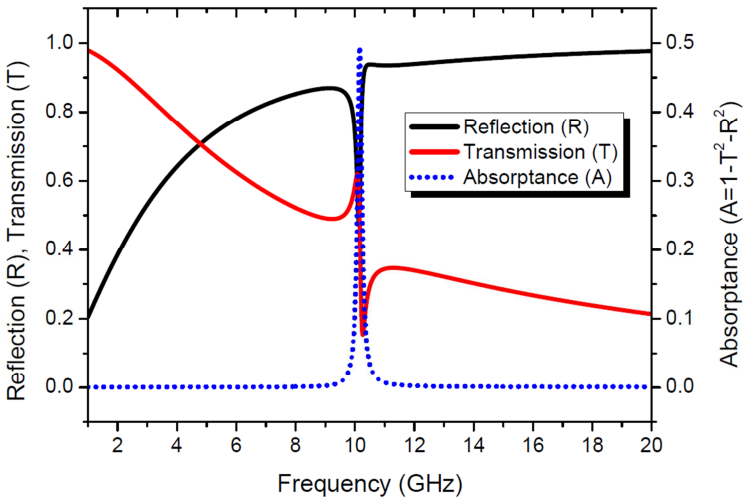

(b)

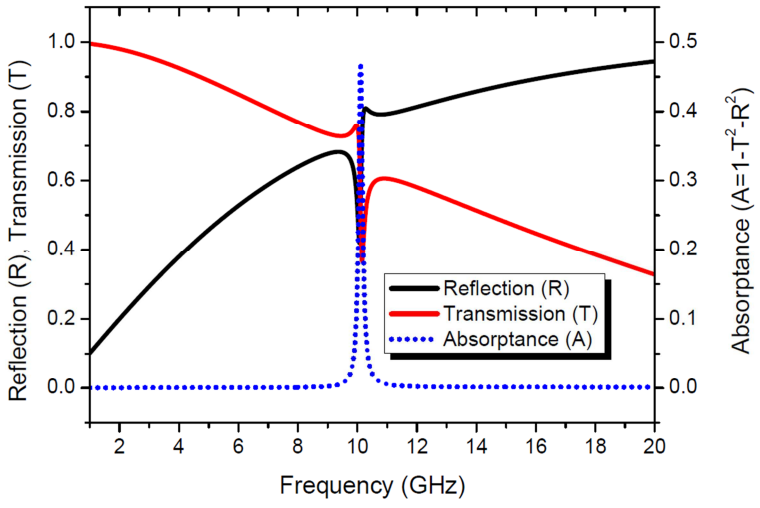

(c)

Figure 3.15: Simulation results for the electromagnetic response for LCP-based metamaterials in a variation of the period, (a) 8.6 mm, (b) 9.0 mm, and (c) 10.4 mm.

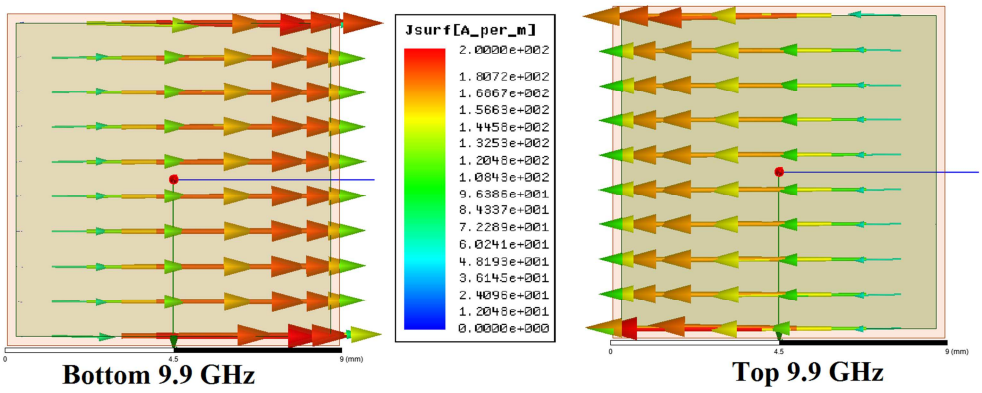

(a)

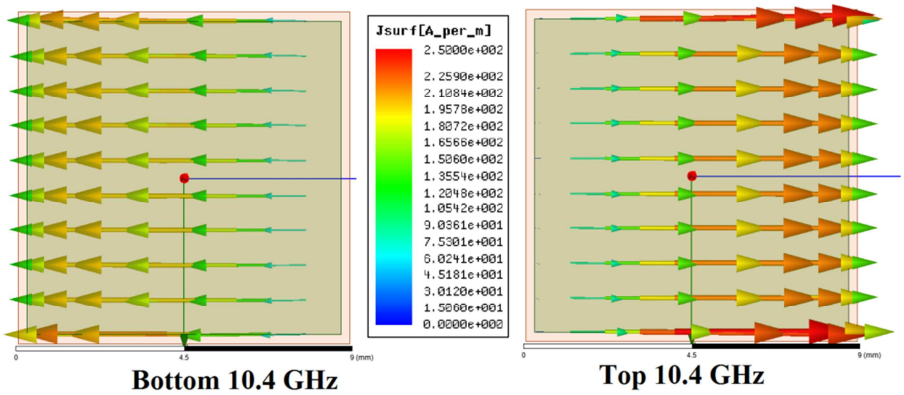

(b)

Figure 3.16: Simulation results for the surface current configuration on a pair of coupled patches at the resonance mode of 9.9 GHz and 10.4 GHz.

Fig. 3.17 also illustrates the field distributions which relate to the electromagnetic behaviour of the anti-phase current configurations at 9.9 GHz and 10.4 GHz. The results show that the electric field distribution is along a direction of the electric field excitation as expected. The characteristics of the magnetic moment based on an electric quadrupole at the edges of patch elements in two layers can be created in a region between four adjacent patch pairs. The formation of the four electric poles can interact with each other resulting in the strong electric field as seen in Fig. 3.17(a) and (c). The strong magnetic field distribution is also generated due to the coupling behaviour of the electric dipoles on top and bottom patches as illustrated in Fig. 3.17(b) and (d).

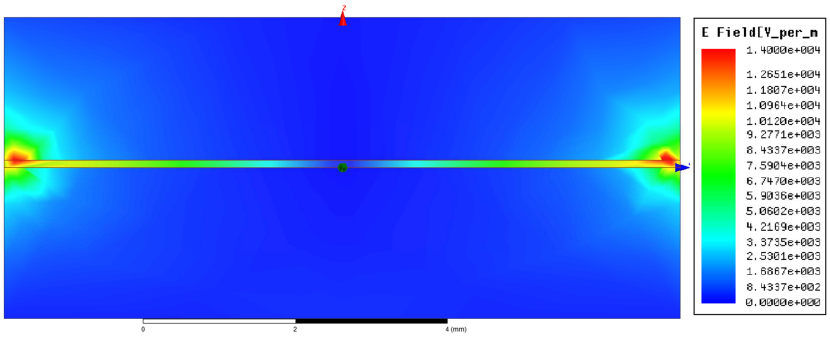

E-field distribution 9.9 GHz

(a)

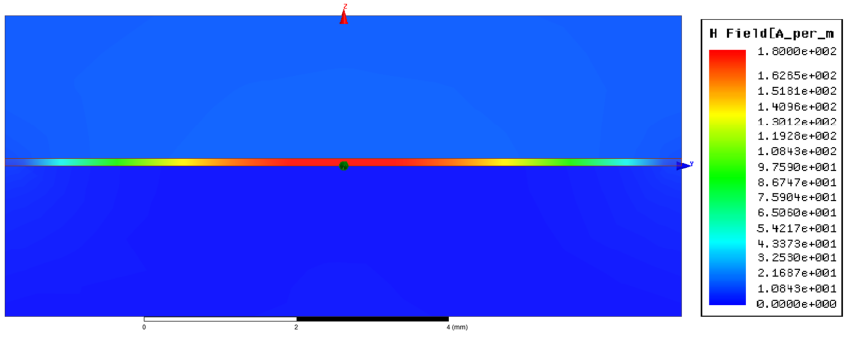

H-field distribution 9.9 GHz

(b)

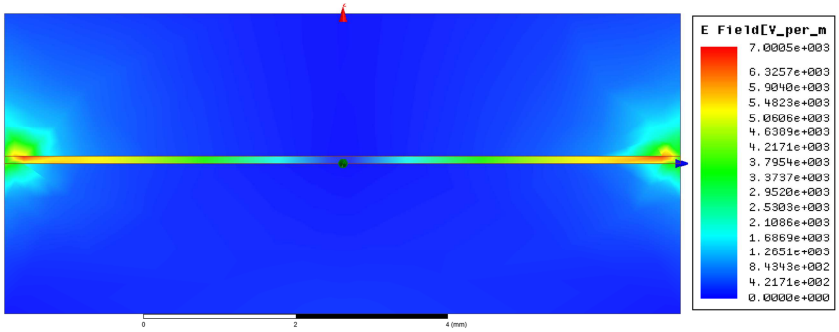

E-field distribution 10.4 GHz

(c)

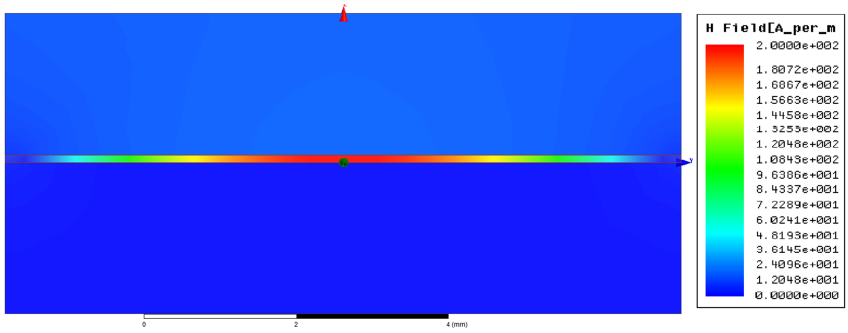

H-field distribution 10.4 GHz

(d)

Figure 3.17: Simulation results for the field distribution of the LCP-based metamaterial, (a) E field and (b) H field at 9.9 GHz (Fano peak), (c) E field and (d) H field at 10.4 GHz (Fano dip).

3.9 LCP based metamaterial as near-perfect absorbers

This section describes the design of near-perfect absorbers which are similar as a high impedance surface (HIS) structure. It is shown that the existing HIS configurations play a major role in a total reflector with a zero reflection phase. But this design is focused on a zero reflection magnitude which is behaved as a perfect absorber. The microwave absorption based on a SPP-like behaviour is obtained in association with the Fano-resonance metamaterial. With the identical configuration as discussed in Section 3.8 but replacing the bottom patch array with a blank copper layer, the resultant structure can be developed to an effective absorber by applying the electromagnetic image theory [151]. Each patch array can be reflected on a perfect electric conductor (PEC) to create a mirror image of the same patch array. The resonance condition is determined by a physical structure and good reflection property is also obtained by good impedance matching considering the design of a patch array and a spacer thickness for the LCP film material. In operation, the perfect metal surface behaves as an electromagnetic reflector and also a barrier to block the field transmission. It can cause ideally a zero transmission leading to the creation of the high (infinity) impedance in considering as a transmission line model due to the resonance condition. In addition, the wave impedance is associated with the ratio of the transverse components of electric and magnetic fields in the front interface. Therefore, the behaviour of the resonant metamaterial absorber is analysed using wave impedance to achieve a matched condition. In association with the electromagnetic mirror, the appearance of the image current distribution on a conducting plane is equivalent to the fictitious patch array [152]. Fig. 3.18 illustrates the geometric layout of the near perfect absorber.

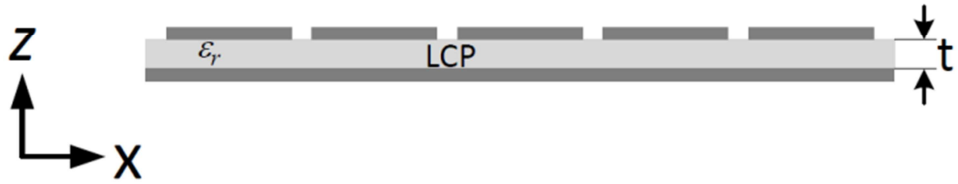

Figure 3.18: Geometry of the perfect resonant absorber based on the Fano-resonance metamaterial.

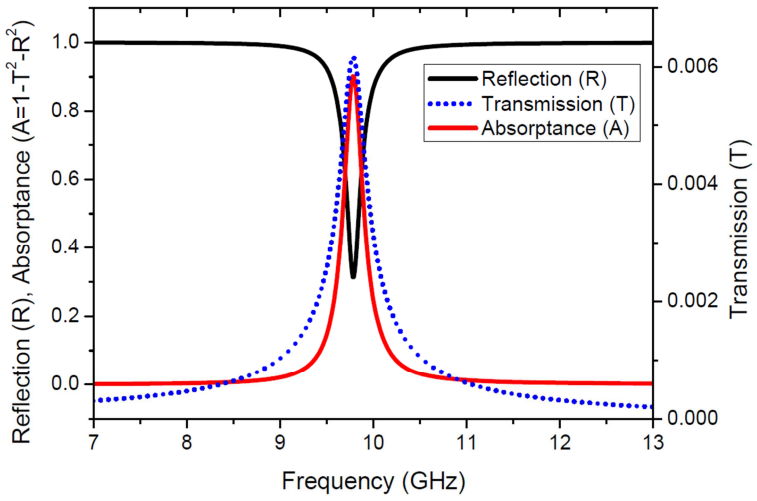

(a)

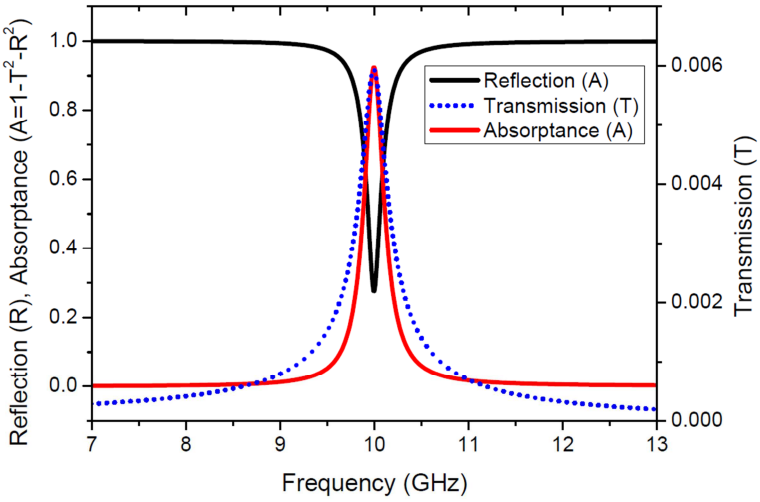

(b)

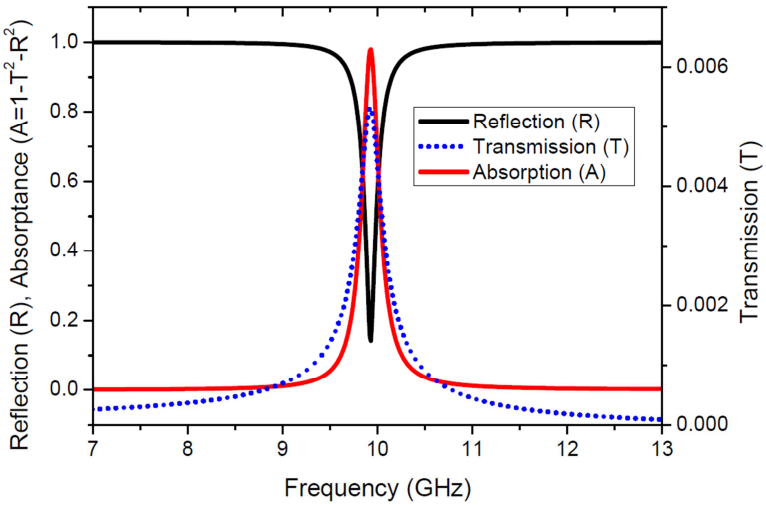

(c)

Figure 3.19: Simulation results for the resonant metamaterial absorber in a variation of the period (P), (a) 8.6 mm, (b) 9 mm, and (c) 10.4 mm.

Fig. 3.19 shows the electromagnetic characteristics of resonant absorbers for varied period values of 8.6 mm, 9.0 mm, and 10.4 mm, respectively. The levels of a peak absorption are 90%, 90%, and 98%, respectively, whereas the values in transmission properties are nearly zero (0.005~0.0065%). The effect of the small resonant transmission is influenced by a induced current and a charge configuration on a mirror conductor due to the scattering process. In accordance to a condition of the resonant transmission, the reflection is minimised at the resonant frequency which is able to trap the incident field. This behaviour can result in the resonant impedance matching. The observed levels of the minimum reflection magnitude are 31.4%, 27.6%, and 14.2% corresponding to period values of 8.6 mm, 9.0 mm, and 10.4 mm, respectively. The reflection magnitude shows the ability of the electromagnetic wave-impedance matching. In this work, a change in reflection coefficient is due to the variation of periods in a patch array. The patch dimension dominates the resonant frequency in this design.

Fig. 3.20 demonstrates a configuration of the surface current distribution in magnitude and vector profile at the responding frequency of 10 GHz. It is shown that the presence of an image current on the conducting plane is related to a patch source. The coincidence of the current density is observed in the same magnitude but a 180° phase difference is seen. Therefore, the anti-phase current configuration can be obtained causing the resonant effect similar to that shown in Fig. 3.16.

Fig. 3.21 illustrates electric and magnetic field distribution at the absorption frequency of 10 GHz. The results show the field distribution along a direction of the incident electric field. Due to the patch-array equivalence on a complete metal surface, the arrangement of the four electric poles provides a strong electric field near the edge of a pair of patch elements. The response of strong magnetic field is also obtained in a space between layers due to the anti-phase current configuration. This behaviour of the electromagnetic activity is similar to that shown in Fig. 3.17.

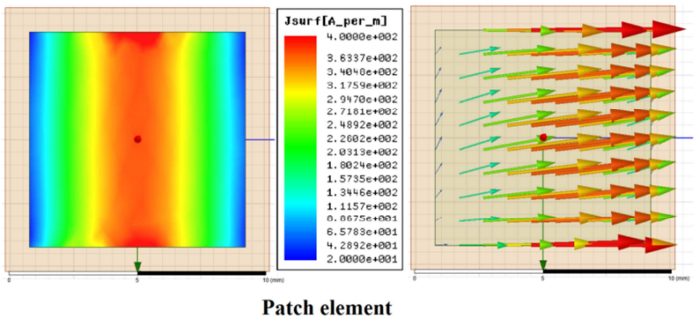

(a)

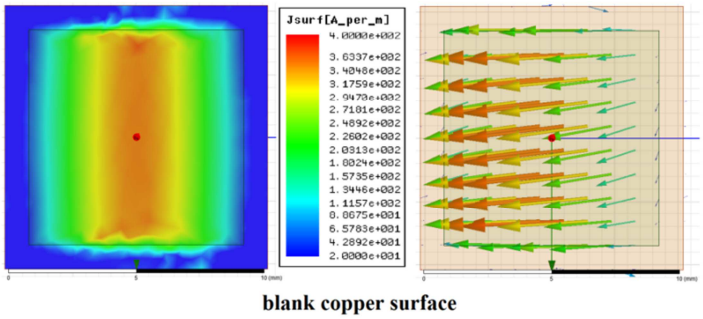

(b)

Figure 3.20: Simulation results for the behaviour of the surface current on two copper elements in the unit-cell including (a) the top patch element and (b) the perfect conductor at 10 GHz.

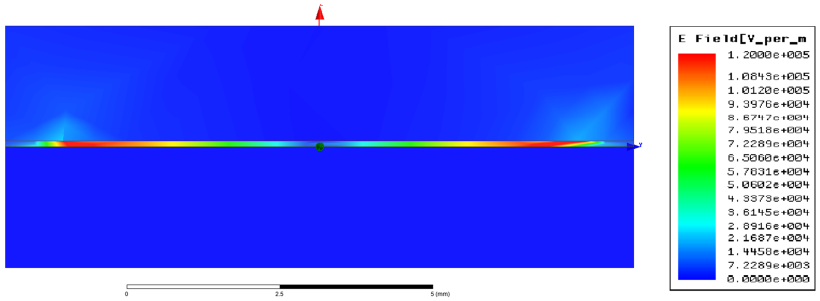

(a)

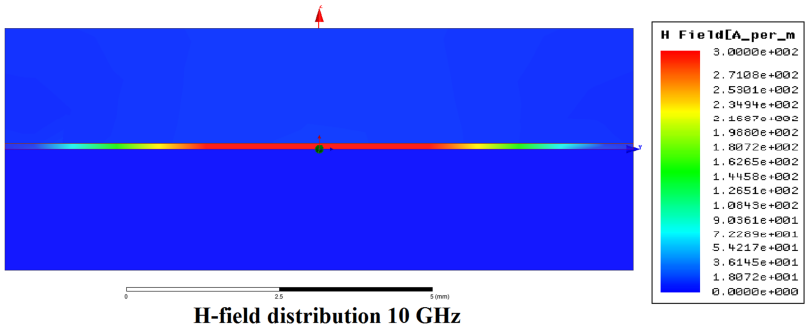

(b)

Figure 3.21: Simulation results for the field distribution (a) the electric-field and (b) the magnetic-field d at 10 GHz for the near-perfect resonant absorber based on a LCP material.

3.10 Metamaterial fabrication

The metamaterial designs are fabricated using a surface micromachining technique. Three design configurations as described in the previous sections are implemented; an FR4 spacer, an LCP film, and a patch array with a blank copper layer on each side of an LCP film. A liquid photoresist (AZ9260) for thick film, high resolution application was used. The thicknesses of the FR4 board and the LCP thin film are 1.6 mm and 100 μm, respectively, the thicknesses of a double cladding copper are 35 μm and 18 μm, respectively. The alignment marks are drilled holes and are used to match the patch-array patterns on both sides of a dielectric material.

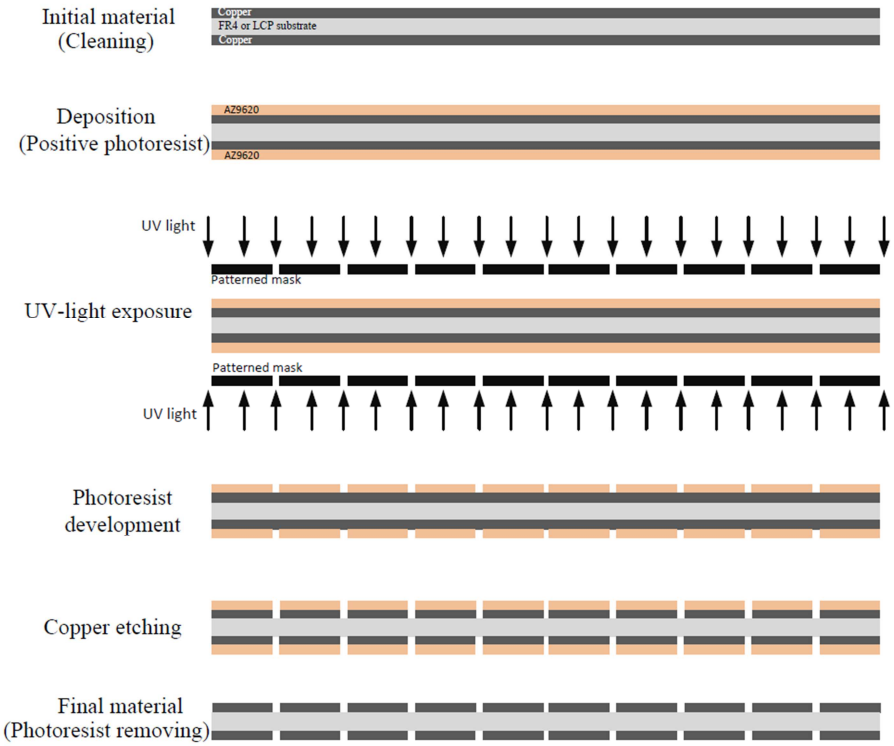

Figure 3.22: Schematic of the fabrication steps for the FR4 based two-layer Fano-resonance metamaterials.

Fig. 3.22 shows the schematic diagram of fabrication steps. Firstly, the dielectric material with a cladding copper was cleaned in diluted DCON-99 liquid. Then, the positive AZ9260 photoresist was deposited on each side of substrate using a spin-coating method. The thickness of a photoresist layer was 10 μm at a spinning speed of 2400 rpm for 60 seconds. The dielectric substrate was based on a hotplate at 100°C for three minutes. After that, the photoresist coated substrate was removed from the hotplate and left to cool down at room temperature for ~30 minutes. The UV exposure was performed using a thin film based photomask at an energy dose of 500 mJ. Next,

the AZ 400K developer diluted with pure water at a ratio of 1:4 was used to remove the exposed regions of a photoresist layer. The exposed copper was then etched away using a ferric chloride solution. The final stop is removed a photoresist film. Hence, the copper layout is produced by the pattern of a patch array. The process is repeated for another side of a dielectric substrate to fabricate the second patch array as necessary. Then, two aligned identical square copper patch arrays one on each side of the dielectric material was obtained to complete fabrication of the two-layer metamaterials.

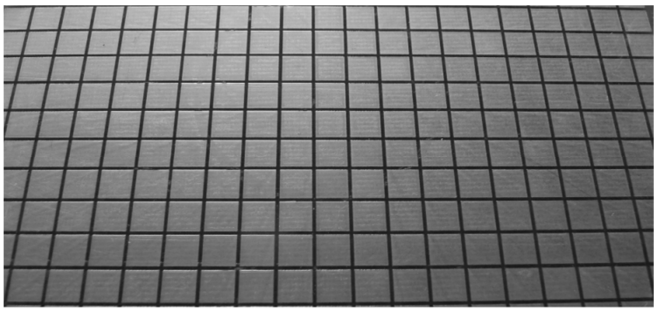

Figure 3.23: A photograph of the FR4 metamaterial.

Fig. 3.23 shows a fabricated FR4-based metamaterial, each copper patch array consists of 21x21 elements arranged in mirror symmetry with respect to the dielectric spacer. The period of a patch array is 5 mm, the total array size is 105x105 mm^2 corresponding to 4.2λ x 4.2λ at the frequency of 12 GHz.

Fig. 3.24 shows pictures of two fabricated LCP thin-film based metamaterials. The patch dimensions are the same as 8.5x8.5 mm^2, but one having a period of 8.6 mm and the other one of 9.0 mm. The square patch arrays consist of 12x12 elements on each side of a thin LCP film substrate. The total dimensions are 103.2x103.2 mm^2 and 108x108 mm^2 which are ~3.44λx3.44λ and ~3.6λx3.6λ at 10 GHz, respectively.

Fig. 3.25 shows the fabricated structure of a resonant metamaterial absorber based on the LCP thin-film. In this design, only one side of the cladding copper layer was patterned to form a patch array since a copper layer on the other side of substrate is used as a PEC layer. The array size is 11x11 cells and the period is 10.4 mm. The patch dimensions are 8.5x8.5 mm^2. The total array dimensions are 114.4x114.4 mm^2 corresponding to ~3.8λx3.8λ at the frequency of 10 GHz.

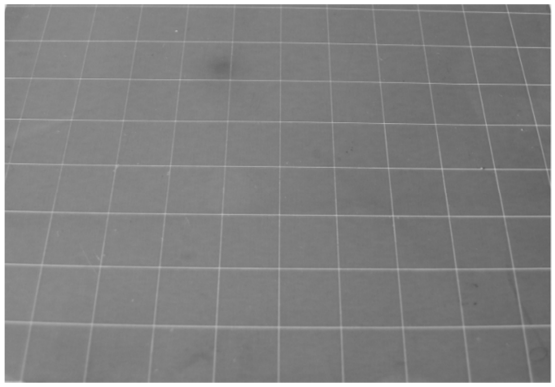

(a)

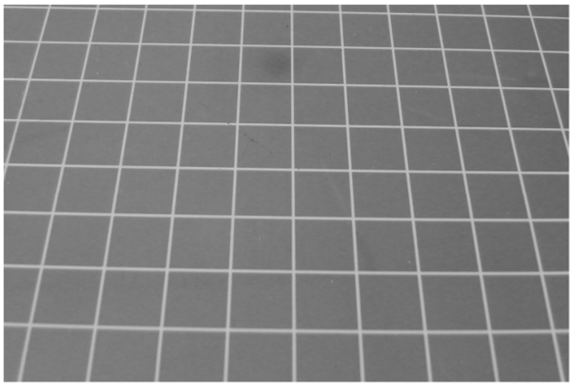

(b)

Figure 3.24: Photograph of the LCP-film based metamaterials for two different periodes, (a) 8.6 mm and (b) 9.0 mm.

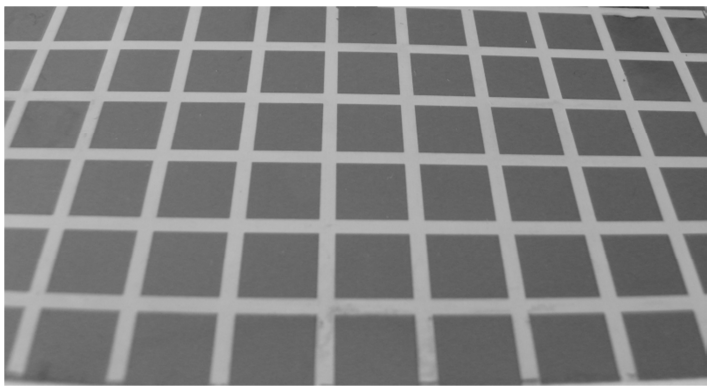

Figure 3.25: A photograph of the near-perfect resonant absorber of the LCP-film metamaterial with the period of 10.4 mm and patch of 8.5x8.5 mm^2.

3.11 Characterisation and measurement

3.11.1 Measurement configuration

The fabricated Fano-resonance metamaterials were characterised by a microwave measurement of electromagnetic properties. Fig. 3.26 shows the measurement setup. The sample was a metamaterial under test (MUT) and the measurement was made in an anechoic environment to avoid the effect of multiple reflections. A vector network analyser (HP8510) was used to characterise the electromagnetic property in which the properties of transmittance and reflectance are obtained in S-parameters, S_{21} and S_{11}, respectively. The transmitter is a horn antenna (Flann^{TM} model 16240-20) and the receiver is another horn antenna from Microwave Instruments Limited (type No.WI6146). A far field arrangement was used in the measurement, the separation between two antennas was 30 cm or 10λ at 10 GHz. The MUT was placed in the middle of the path between two horn antennas.

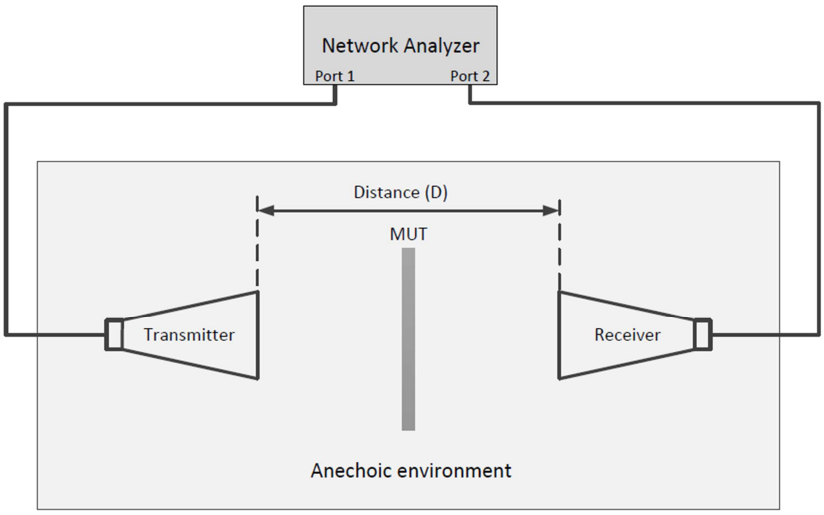

Figure 3.26: Configuration of the measurement setting for the electromagnetic characterisation.

It is important to perform the full two-port calibration of a VNA instrument before starting measurement. This was carried out using standard loads for the analyser. In transmission measurement, the measured signal with MUT in place is normalised to the results without MUT to obtain the transmission coefficient. The reflection measurement is conducted using the setup shown in Fig. 3.27. The measured signal from the MUT is normalised to a signal when a copper sheet was in place of the MUT in order to obtain the reflection coefficient. The reflectivity of the copper sheet is assumed to be unity.

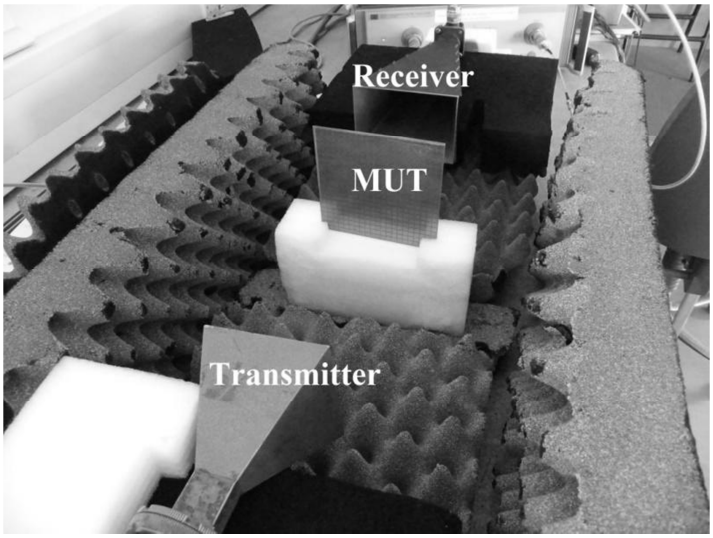

Figure 3.27: The environment and setup for reflection measurement.

In the free-space measurement setup, there are three conditions for consideration consisting of (1) the relative object size of the MUT, (2) the arrangement of absorber walls along a path length, and (3) the distance between a transmitter (receiver) and a MUT. The actual object size of the MUT is 3.5λ~4λ in this experiment that is sufficient in the terms of ensuring less diffraction interference associated with the edge effect. Absorber walls are used in all directions. A distance of 5λ between the MUT and the horn transmitter was used so that a wave front of the horn antenna is close to a plane wave when interacting with the MUT object.

3.11.2 Characteristics of FR4-based metamaterials

Fig. 3.28 shows the reflection and transmission characteristics over the frequency range from 1 GHz to 20 GHz. The measurement frequency range was 7−13 GHz limited by the operation band of the horn antennas. The smoothing function of a VNA instrument is applied to obtain a better signal profile. The resonance frequency of the FR4-based metamaterials was measured to be 11.7 GHz corresponding to the results of simulation. It can be seen that good agreement between the measured results and simulation has been obtained. The peak transmission is about 92%.

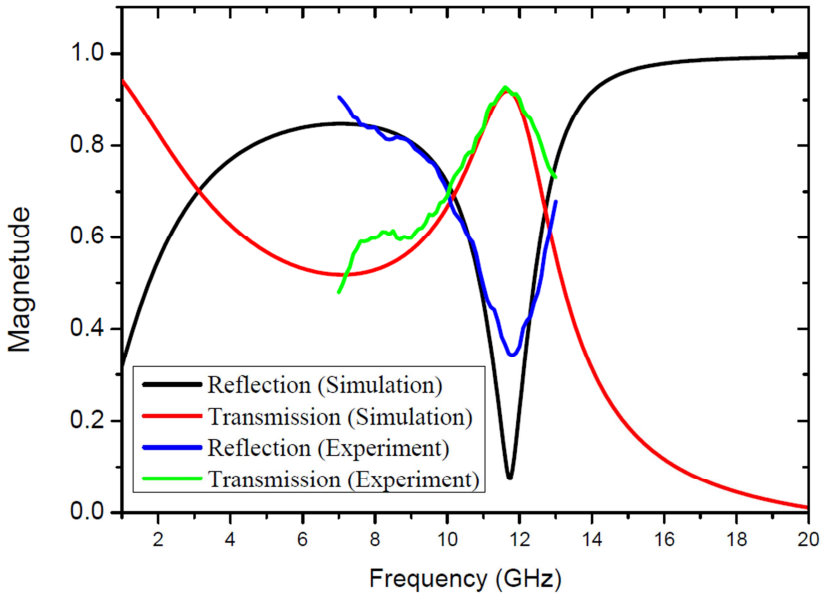

Figure 3.28: The measured and simulated results of the FR4 based metamaterial.

3.11.3 Characteristics of LCP-based metamaterials

Fig. 3.29 shows the characteristics of reflection and transmission of the LCP-based metamaterials with a period of 8.6 mm and patch dimensions of 8.5 mm. The measurement was made over the frequency range of 9–11 GHz. The reflection dip and transmission peak are observed in the simulation and measurement corresponding to the frequencies of 10.1 GHz and 10.25 GHz, respectively resulting in a difference of only 150 MHz.

Fig. 3.30 also shows the characteristics of reflection and the transmission of a LCP based metamaterial with a period of 9.0 mm. The transmission peak and dip in the measured results are at the frequency of 10.5 GHz and 10.6 GHz, respectively. The difference between the simulation and measurement of the transmission peak is 400 MHz.

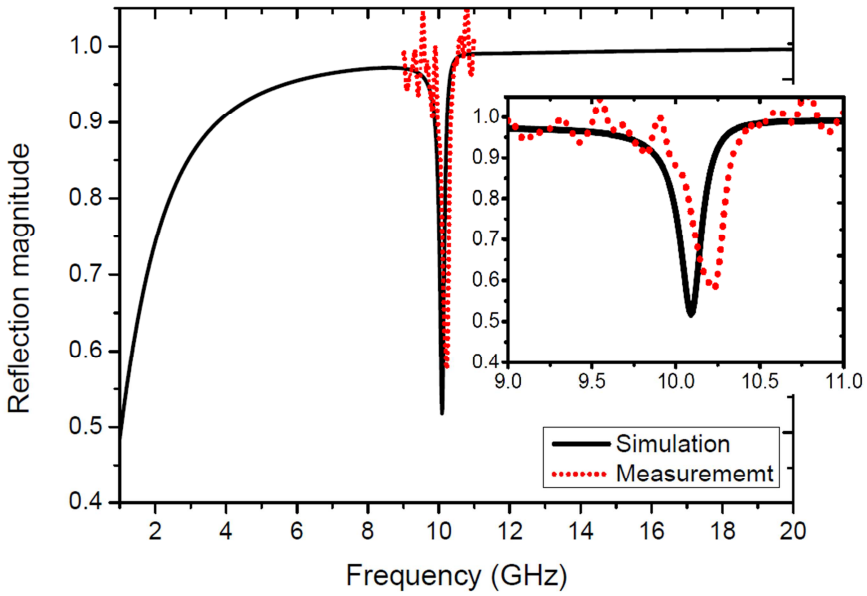

(a)

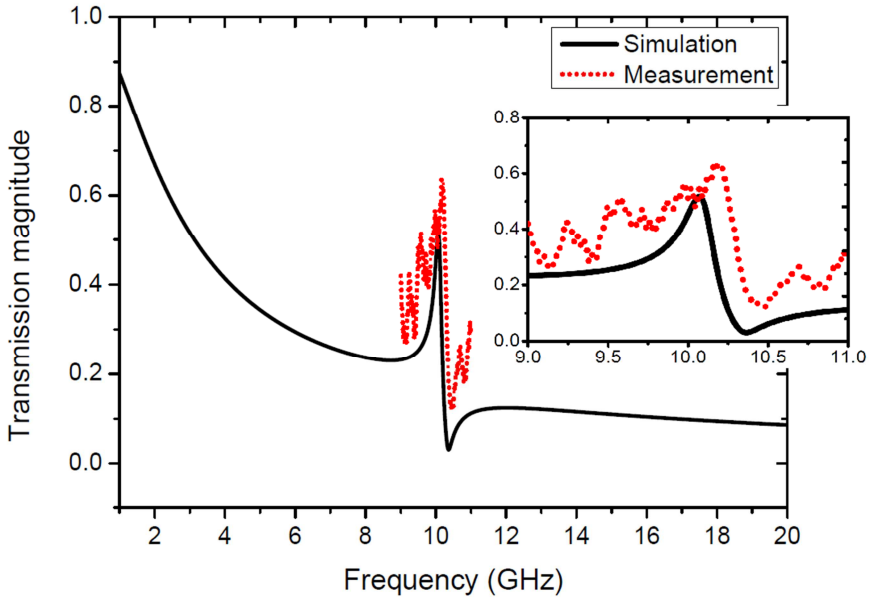

(b)

Figure 3.29: The measured and simulated results of an LCP based metamaterial with a period of 8.6 mm, (a) reflection and (b) transmission.

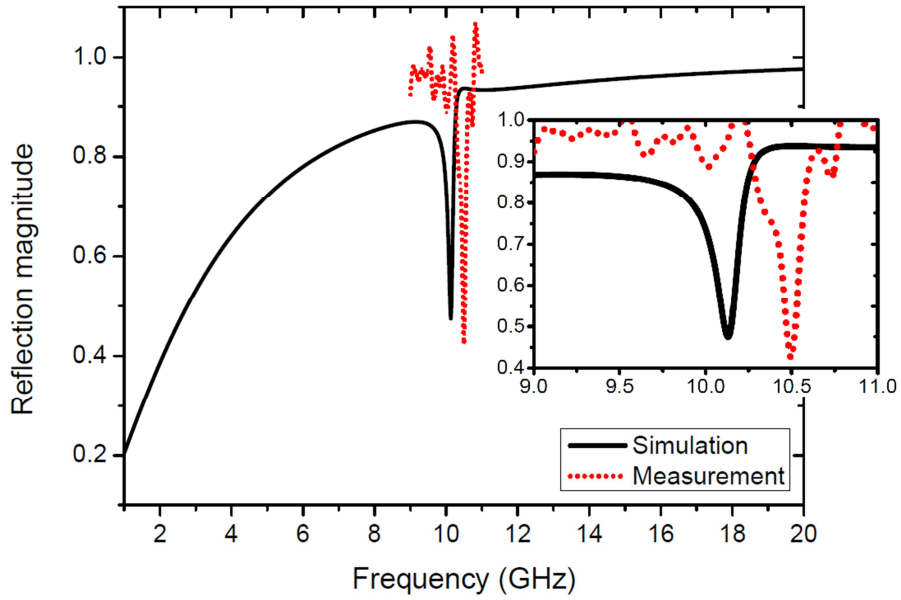

(a)

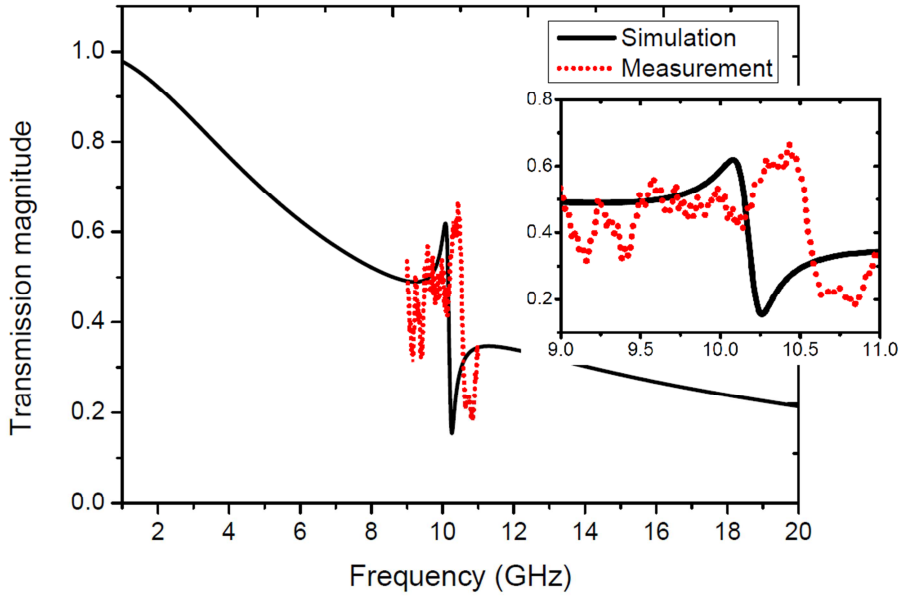

(b)

Figure 3.30: The measured and simulated results of the LCP based metamaterial with a period value of 9.0 mm, (a) reflection and (b) transmission.

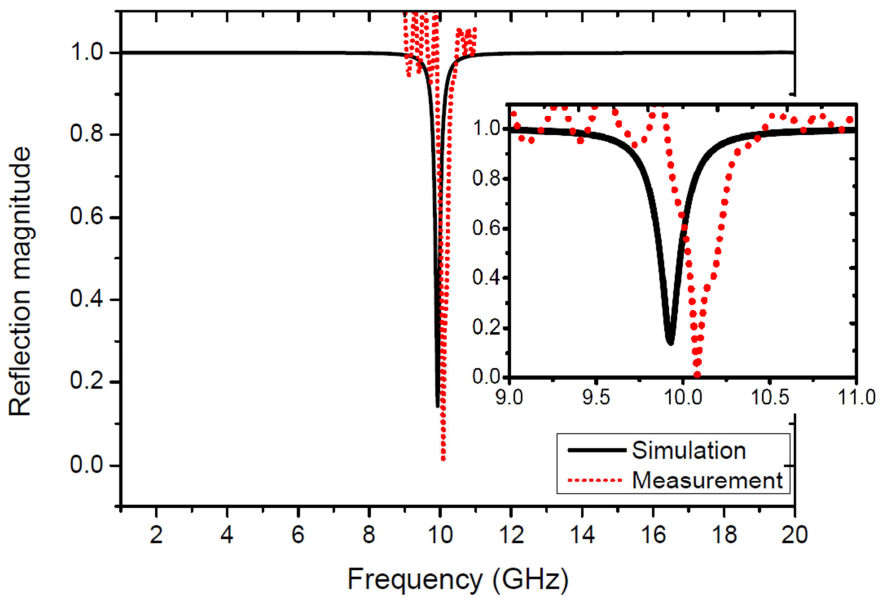

(a)

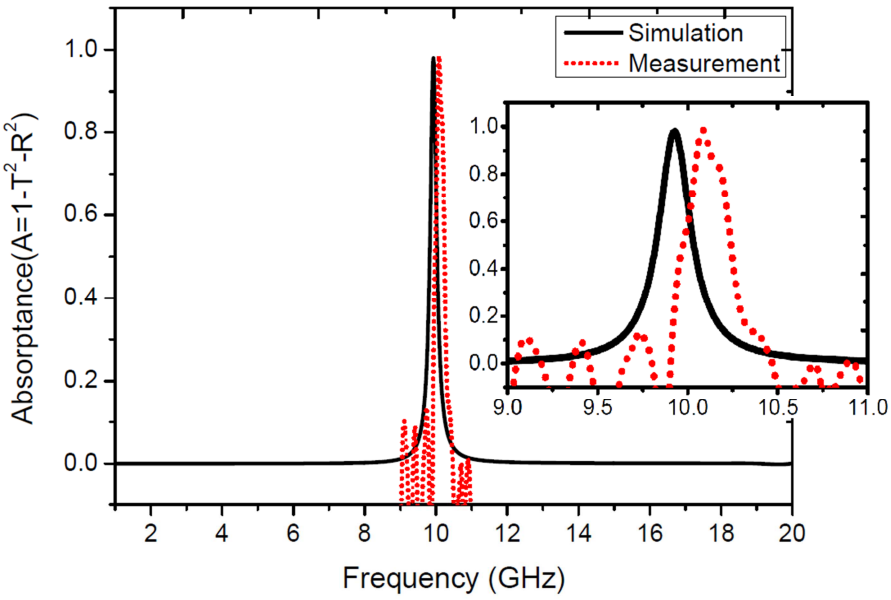

(b)

Figure 3.31: The measured and simulated results of a LCP based metamaterial absorber with total absorption; the period of the arrays is 10.4 mm, (a) reflection and (b) absorptance.

3.11.4 Characteristics of the resonant metamaterial absorber

Figure 3.31 shows the characteristics of reflection (R) and absorption compared with the simulation results. As a result, resonance frequencies of 10.05 GHz and 9.95 GHz are observed corresponding measurement and simulation, respectively. The absorption result is obtained by $A = 1 - T^2 - R^2$. It is shown that the measured absorption is reported at the peak of 100%.

Table 3.1: Summary of the fabricated metamaterials.

Metamaterials	Resonant frequency (GHz)			Peak transmission (%)		
	Meas.	Simul.	Difference (%)	Meas.	Simul.	Difference (%)
Fano-FR4	11.7	11.7	0	92	92	0
Fano-LCP 1	10.25	10.1	1.5	62	52	19.2
Fano-LCP 2	10.5	10.2	3.0	68	62	9.7
LCP absorber	10.05	9.95	1.0	-	-	-

Table 3.2: Summary of the design and measured gaps between patches.

LCP based metamaterials	Patch separation (μm)		Patch length (mm)		Period (mm)	
	Design	Fabrication	Design	Fabrication	Design	Fabrication
Fano-FR4	500	569	4.5	4.38	5.0	4.95
Fano-LCP 1	100	157	8.5	8.36	8.6	8.52
Fano-LCP 2	500	540	8.5	8.36	9.0	8.9
LCP absorber	1,900	1,918	8.5	8.34	10.4	10.26

3.11.5 Discussion of the results

The three fabricated metamaterials were studied by transmission and reflection measurements. The resultant characteristics of the fabricated metamaterials show the behaviour of the Fano-resonance effect as predicted in the design and simulation work. Table 3.1 shows a summary of the measured and simulation results of the resonant frequency and peak transmission of the fabricated metamaterials. As can be seen in Table 3.1, an excellent agreement has been obtained between the results of measurement and simulation for the FR4 based metamaterial. Since the FR4 substrate is much thicker than the LCP film material, the Fano resonance is much broader as shown in the previous sections and, therefore, the frequency and peak transmission are less sensitive to the design parameters. For the LCP based samples, the difference between the measured and simulated results in resonance frequency is between 1% and 3%.

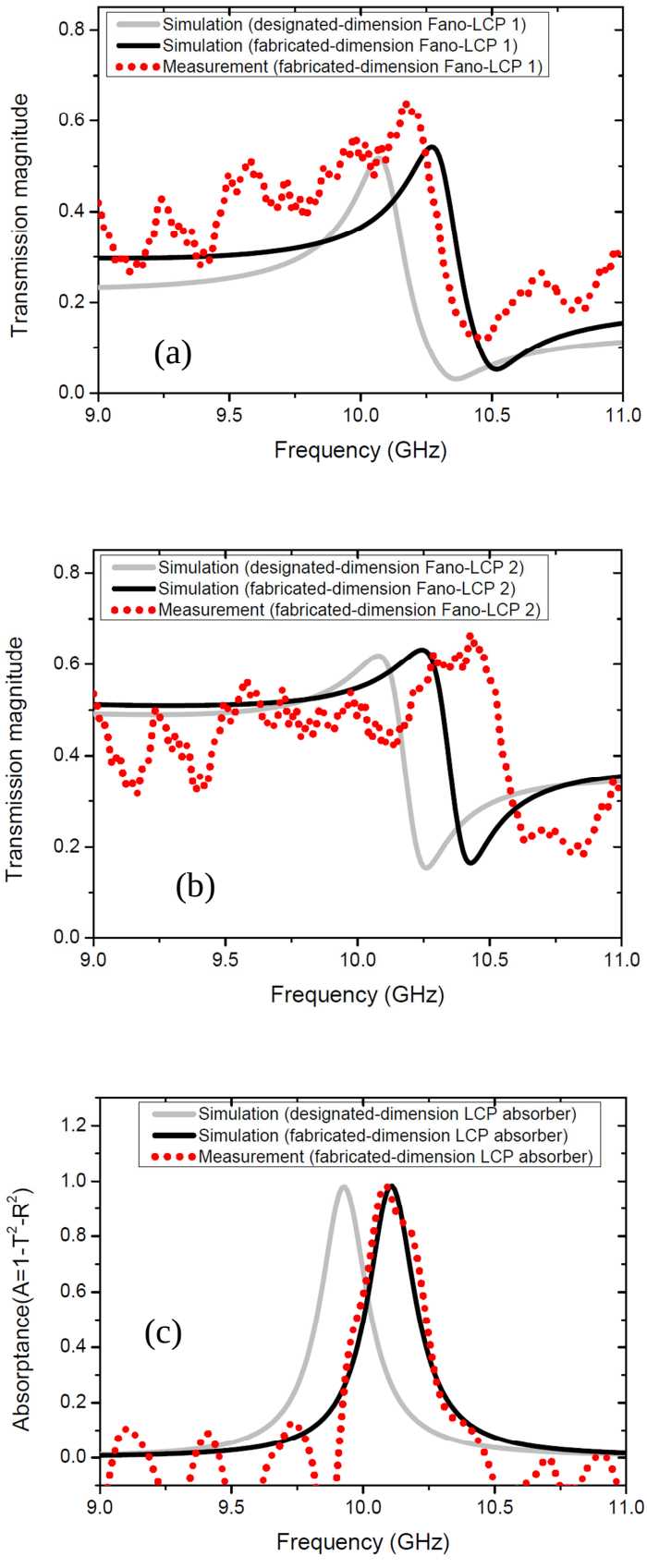

Figure 3.32: The investigated results in the physical effect between the design and fabricated dimensions of three samples, (a) Fano-LCP 1, (b) Fano-LCP 2, and (c) LCP absorber.

For the peak transmission, the measured values are higher than that of the simulation work. In order to determine if the difference is caused by the physical change in patch dimensions during fabrication and, hence, the geometric parameters between two adjacent patches, the gap spacing and the patch element were measured using an optical microscope. The values from measurement and design are given in Table 3.2. It is not surprising to see that the error is the largest for a small design value of 100 μm for sample Fano-LCP 1. The measured value for the sample after fabrication is 157 μm. The error is mostly caused by the wet etching process; it is a well-known effect in the field of microfabrication.

Fig. 3.33 illustrates the responses of simulation and measurements, the measured dimensions in Table 3.2 were used in a simulation work. The simulated results of the fabricated samples according to the measured dimensions show that the actual patch length and period give the features with better agreement with the experimental results. The appearance of the Fano-resonance transmission as seen in Fig. 3.33(a) and (b) is close to the measured transmission magnitude. As can be seen in Fig. 3.33(c), the results of resonant absorption of the near perfect LCP absorber are in excellent agreement between simulation and measurements.

3.12 Summary

This chapter presented results of the studies on the Fano resonance in a two-layer metamaterial consisting of two identical patch arrays. It has been discovered that sharp Fano resonance can be obtained in such materials with a thin dielectric spacer. The effects of period, patch dimensions, and thickness of the dielectric spacer on resonant frequencies have been studied in detail. The surface current configurations show the characteristic signature of the Fano resonance in metamaterials. The experimental study was carried out using samples fabricated using copper clad FR4 and thin film LCP materials. Transmission and reflection measurements were made to characterise the samples. It has been shown that the measured results are in good agreement with simulation. In addition, the LCP based structures consisting of a square patch array on the front surface and a blank copper clad layer on the back surface have been designed and fabricated for use as metamaterial based absorbers. A near perfect absorber performance has been obtained. Part of the results in this chapter has been published in [153].

CHAPTER 4 DEVELOPMENT OF A MICROMACHINNED AND CPW FED APERTURE COUPLED BROADBAND PATCH ANTENNA

4.1 Introduction

This chapter describes the research work on development of a broadband patch antenna for resonant cavity antenna applications. The patch antenna is designed to be a broadband source which is used for the work in Chapter 5 in the development of a broadband resonant cavity antenna. It is challenging to design a wideband patch antenna with high directivity and a wide impedance bandwidth. The feasibility depends on a physical design of an antenna configuration. In design of wide bandwidth antennas, the practical technique exploiting multiple resonances has been introduced as discussed in the literature review work in Chapter 2.

This chapter describes the coplanar waveguide (CPW) and aperture coupled design found to the best impedance match over a wideband. A short-end CPW transmission line is implemented to feed an aperture element. The matching technique is applied to develop a broadband input impedance characteristic which deals with the feeding geometry over the target frequency band in operation. The double-tuned matching method is performed. The resonant patch is suspended above the coupling aperture. This configuration can provide input impedance with wideband behaviour and also enhances the radiation characteristics. The antenna configuration is an air-backed cavity design using an air gap between the resonant patch and the coupling aperture leading to no dielectric loss. The investigation illustrates a design method and the effect of the electromagnetic interaction such as mutual interference. In addition, antenna construction using a polymer rim structure shaped by laser machinery is developed along with microfabrication approaches for high precision fabrication of the CPW fed antenna structure. The results of design and simulation, fabrication and measurements are described. The background principles of antenna characteristics and the fundamentals of patch antennas are described in Appendix C and D.

4.2 Fundamentals of the CPW geometry

The coplanar waveguide (CPW) is a type of transmission-line which was introduced by C. P. Wen in 1969 [154]. The description and analysis of the CPW configuration have been addressed in several features and also used in many applications. The configuration offers a physical structure of the signal track and the ground reference in the same layer. The configuration is ideal for monolithic microwave integrated circuits (MMIC). The two-port structure or the CPW through line is used to determine the effective dielectric constant and the guided wavelength which are used to design the electromagnetic components. Here, the CPW on a dielectric substrate of the finite thickness is considered and applied for a wideband antenna application. Fig. 4.1 shows the 2D view of the CPW structure in which the signal track and ground are located on the dielectric material with the finite thickness (H) and the electric permittivity of ε_r. The geometric parameters of the CPW transmission-line consist of a width of the signal track (W_f) in the middle and coupling gaps (G) between the feed-line and the infinite ground spaces. The analysis of the properties is based on a equivalent capacitance approach.

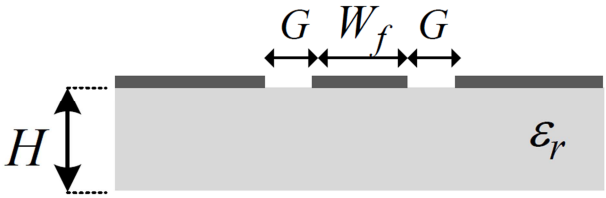

Figure 4.1: A cross section of the CPW structure.

The characteristic impedance of the CPW transmission-line is associated with the behaviour of a capacitance as [154]

$$C_{CPW} = C_1 + C_{air} \tag{4.1}$$

where $C_1 = 2\varepsilon_o(\varepsilon_r - 1)\frac{K(k_1)}{K(k_1')}$ and $C_{air} = 4\varepsilon_o \frac{K(k_0)}{K(k_0')}$.

The terms of $K(k_1)$, $K(k_0)$, $K(k_1')$ and $K(k_0')$ are presented as complete elliptic integrals. The parameters of k_1, k_0, k_1' and k_0' are connected with widths of the gap and the CPW feed-line given by

$$k_1 = \frac{sinh\left(\frac{\pi W_f}{4H}\right)}{\sinh\left\{\frac{\left[\pi\left(W_f+2G\right)\right]}{4H}\right\}} \quad , \quad k_1' = \sqrt{1-k_1^2}\,.$$

$$k_0 = \frac{W_f}{W_f+2G} \quad \text{, and} \quad k_0' = \sqrt{1-k_0^2}\,.$$

Therefore, the expression of total capacitance in (4.1) can be rewritten by

$$C_{CPW} = 2\varepsilon_o(\varepsilon_r - 1)\frac{K(k_1)}{K(k_1')} + 4\varepsilon_o\frac{K(k_0)}{K(k_0')} \tag{4.2}$$

Also, the term of the capacitance ratio leads to the effective dielectric constant as

$$\varepsilon_{eff} = \frac{C_{CPW}}{C_{air}} = 1 + \frac{\varepsilon_r - 1}{2} \cdot \frac{K(k_1)}{K(k_1')}\frac{K(k_0)}{K(k_0')} \tag{4.3}$$

To determine the characteristics impedance, the expression can be yielded as

$$Z_o = \frac{1}{cC_{air}\sqrt{\varepsilon_{eff}}} = \frac{30\pi}{\sqrt{\varepsilon_{eff}}}\frac{K(k_0')}{K(k_0)} \tag{4.4}$$

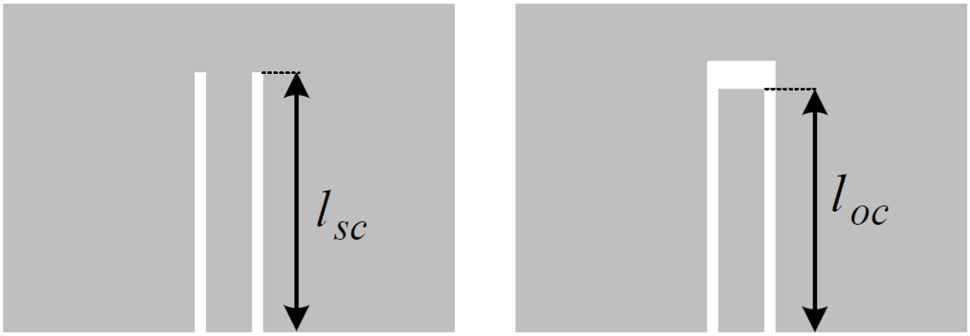

Figure 4.2: Layout of the one-port CPW discontinuities for the short-end and the open-end designs.

Fig. 4.2 illustrates the modification of the CPW discontinuities as a one-port structure which can be modelled in two types including the short-end and open-end layouts. The behaviour of input impedance can be expressed as a purely inductive and capacitive load and also varied as a periodic function associated with the electrical length. The type of the one-port CPW structures is able to integrate with the aperture radiators to form the antenna configuration.

Firstly, the analysis of the open-ended or open circuit CPW structure is considered in capacitance which relate to the extension length l_{oc} as

$$C_{oc} = \frac{tan(\beta l_{oc})}{\omega Z_o} \tag{4.5}$$

where β is the phase constant as $\frac{2\pi\sqrt{\varepsilon_{eff}}}{\lambda}$ and $\omega = 2\pi f$.

In a case of a small length extension, the open-circuit capacitance can be rewritten as

$$C_{oc} = \left(\frac{\beta}{\omega Z_0}\right) l_{oc} \tag{4.6}$$

Also, the capacitance C per unit length for a lossless CPW is expressed by

$$C = \frac{C_{oc}}{l_{oc}} = \frac{\beta}{\omega Z_0} \tag{4.7}$$

Secondly, impedance of the short-ended or short circuit CPW can be expressed on inductance due to the physical condition to provide magnetic energy at the termination which is depended on the length extension as l_{sc} at the reference plane. The expression of the short-ended inductance can be obtained by

$$L_{sc} = \left(\frac{2}{\pi}\right)\varepsilon_0\varepsilon_{eff}(a+b)Z_0^2\left\{1 - \frac{1}{[cosh(60\pi^2/Z_0\sqrt{\varepsilon_{eff}})]}\right\} \quad (4.8)$$

where $2a = W_f$ and $2b = W_f + 2G$. In addition, the inductance L per unit length for a lossless CPW is expressed by

$$L = \frac{L_{sc}}{l_{sc}} = \frac{\beta Z_0}{\omega} \quad (4.9)$$

4.3 Fundamentals of the aperture radiator

The aperture or slot element is a type of radiating structures which provides bi-directional radiation. The theory of aperture antennas has been addressed for the physical mechanism based on the Babinet's principle [155]. As seen in Fig. 4.3, the narrow aperture is surrounded by an infinite metallic plate and the feeding position is at the centre of the aperture. Different feeding methods can be used for an aperture element such as a waveguide and a planar transmission-line. The current can behaviourally travel around a perimeter of the aperture element. The E-field distribution is also induced in the aperture geometry. In mechanism, the narrow aperture element is represented as a complementary dipole that the radiation characteristics can behave in a similar way. Therefore, the antenna parameters of an aperture including impedance and resonance condition can be modified based on that of the dipole antennas. The relation of two types of the antenna structure can be considered in impedance of antennas in that the expression can be written by

$$Z_{dipole}Z_{aperture} = \frac{\eta^2}{4} \quad (4.10)$$

where η is the intrinsic impedance of free space.

The characteristics of the aperture structure can be determined by a resonance condition. With the feeding point in the middle as shown in Fig. 4.3, the structure of the aperture can be considered as a dual dipole elements. In an equivalence of a dipole, the electrical length in each section is able to resonate as a half wavelength. This behaviour results in the total length of the aperture of one wavelength. The aperture width is also specified as a small fraction of a wavelength [155].

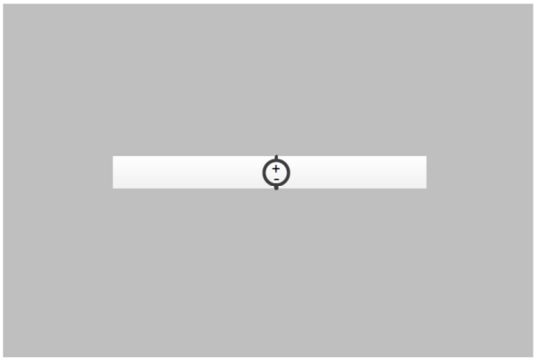

Figure 4.3: Geometry of the layout of the narrow aperture radiator.

4.4 Broadband patch antenna configuration and design method

4.4.1 CPW fed and aperture coupled patch antenna

The development of the broadband aperture-coupled patch antenna is designed and verified in order to contribute to the resonant cavity antenna work in Chapter 5. The patch antenna is treated as a driven element. There are two key design techniques based on a series-resonance aperture and double-tuned matching method [156], respectively. The short-end CPW structure is capable of wideband performance as a coupling element for radiating apertures [157-162]. In addition, the influence of a finite ground-plane size on radiation performance has been studied previously based on the geometric theory of diffraction (GTD) [163]. Fig. 4.4 shows the physical layout of the aperture-coupled patch antenna with the short-end CPW feeding. The structural configuration consists of the ground plane and the radiating patch separated by an air gap defined by the thickness of the PMMA rim and the thin LCP film. The ground-plane layer is positioned on top of the FR4 dielectric substrate with the thickness, H. The driven element is a narrow aperture excited by the short-end CPW line on a ground-plane layer.

The structure of a CPW feed-line is composed of a signal track which is in between two spacing gaps. The parameters, W_f and G, are a width and a gap of the CPW geometry. The length of the CPW structure is defined by L_f which determines input impedance. The aperture element is equally separated in two parts. The parameter L_s and W_s are the length and width of an aperture element. The polymer based rim is used to define an air gap thickness and to support the thin LCP film substrate. The top layer is the patch element fabricated on a thin LCP film. The air gap defined by H_g is between the thin dielectric film and the ground-plane layer. The parameters, L_p and W_p, are the length and width of the rectangular patch element.

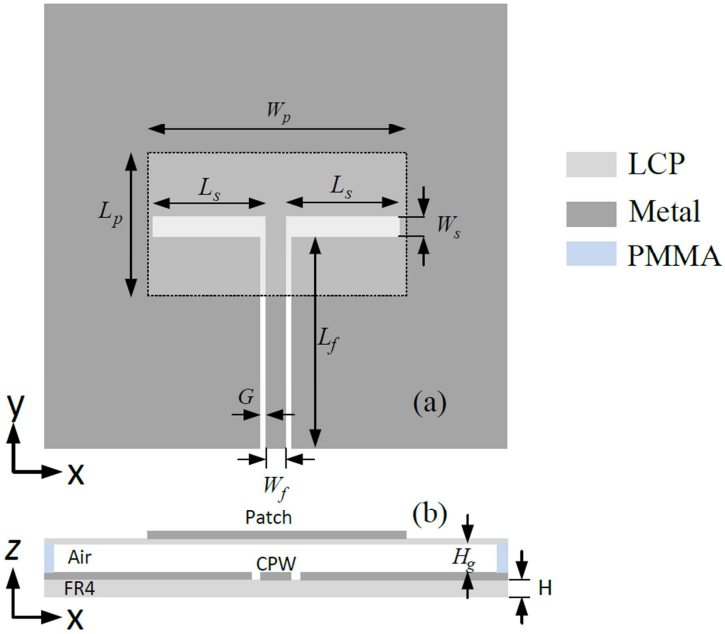

Figure 4.4: Geometry of the physical configuration of the short-end CPW-fed aperture coupled patch antenna, (a) top view and (b) cross section.

4.4.2 Design method

There are three elements involved in this antenna configuration which can be considered in a design process. The aperture element behaves as a driven radiator. The second element is the CPW structure that is performed as a feed-line and also behaves as a circuit element for matching. The characteristic of the capacitance or inductance can be obtained depending on an electrical length of the CPW transmission line. The resonant patch is a parasitic element to operate with the driven radiator by the near-field coupling effect. Therefore, the design methodology can be divided into three steps to complete the antenna configuration.

- Firstly, the narrow aperture is investigated by applying the short-end feeding. The input impedance is characterised by simulation to study the resonance behaviour. The characteristics of the radiation and impedance are also observed in context of the edge effect of diffraction. The observation is connected to the ground-plane sizes. The aperture study will be described in section 4.5.1.

- Secondly, the CPW feed-line with the short-end is a physical part connecting with the input port and the aperture load. The length of a CPW line determines its electrical properties as a function of wavelength. Hence, this element plays a vital role in the impedance matching technique. The double-tuned matching approach based on the Wheeler's method is able to deal with the edge bands of the aperture resonance by the intrinsic impedance of a CPW structure. The configuration and the matching effect will be discussed in sections 4.5.2 and 4.5.3.

- Finally, the radiation patch which is suspended above the aperture element is considered. The air-gap thickness is determined in the mutual effect influenced by impedance interference between the driven aperture and the resonant patch. In order to obtain broad bandwidth, the mutual impedance is manipulated by optimising the self-impedance of the aperture and patch element. The edge effect is also studied to observe the radiation characteristics. The design details will be addressed in section 4.6.

4.4.3 Configuration of the HFSS Simulation

The investigation is performed by electromagnetic simulation using the HFSS software tool. The simulation approach is based on the finite element method (FEM) as a powerful technique to analyse the electromagnetic problem. The overview of the analytical technique was introduced in Appendix A. Here, the HFSS tool is used to model an antenna design. Fig. 4.5 shows the configuration of the antenna simulation in the HFSS tool. The antenna configuration is composed of three antenna components including a patch, a CPW feed-line, and an aperture. The antenna structure is formed on an FR4 dielectric substrate and the radiating patch element is on a thin LCP film stacked with a PMMA (polymer) rim. The microwave excitation is applied at the lumped port at the terminal of the CPW feed-line which is connected to the signal track and the ground plane. The model of the antenna configuration is put in the radiation box which is defined by an air medium. The radiation box is a confined simulation environment which is truncated from the infinite space.

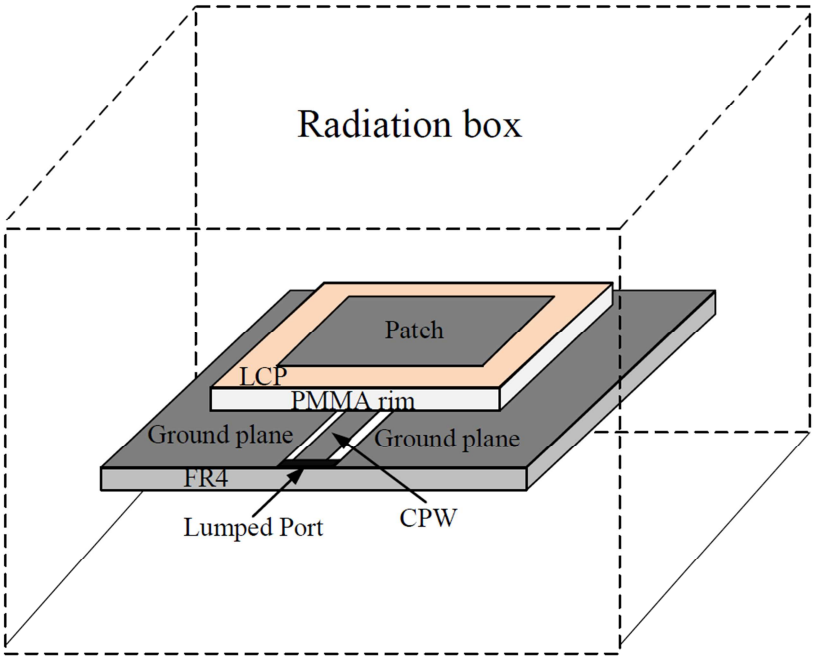

Figure 4.5: Configurations of the antenna simulation in the HFSS tool.

In this work, the solution type of the HFSS simulation is set as a driven mode. The lumped port is based on 50-Ω impedance applied to a terminal of the CPW feed-line. The design of an antenna structure is drawn in the larger radiation boundary. The space of the radiation box is defined by quarter wavelength dimensions at the target frequency between the simulated structure and the boundary of the radiation box. For an accurate response and efficient simulation speed, spacing is made larger in the expected direction of the radiation which is one and half wavelengths. The target frequency is 10 GHz in the centre band is defined in a simulation work. The adaptive solution consists of the maximum number of passes and the maximum of delta S which are 10 and 0.002, respectively. In the frequency sweep, the simulation type is a discrete mode and the observing frequency range is set from 7 GHz to 13 GHz in a step size of 100 MHz to cover the target band. The simulating results are associated with the characteristics of the reflection parameter referred to as the return loss of an antenna parameter. The impedance characteristics can also be obtained to observe input impedance that influences the matching condition. In addition, the radiation performance can be examined based on the far-field propagation in 2D or 3D coordinates.

4.5 Design of the CPW-fed aperture radiators

4.5.1 Effect of the aperture on the finite ground plane

In order to understand the radiation characteristics, the effect of ground-plane dimensions on the radiation patterns of an aperture element is investigated. The infinite size of a ground plane is assumed in the theoretical analysis of an aperture element. Due to the surface electromagnetic wave, the behavior of the radiation is influenced by the edge effect based on the diffraction. The responses of the finite-size ground plane have been shown in a microstrip-fed and cavity-backed slot antenna [164], a patch antenna [165] and a dipole antenna at a higher frequency of 77 GHz [166].

Here, the study of the aperture on the input impedance and the radiation characteristics is carried out by simulation. The aperture element is positioned in a variation of the finite size square ground planes. The ground planes of five different sizes are 20x20 mm^2, 30x30 mm^2, 45x45 mm^2, 60x60 mm^2, and 75x75 mm^2. The normalised scales with respect to the free-space wavelength at 10 GHz are determined as $0.67x0.67\lambda^2$, $1.0x1.0\lambda^2$, $1.5x1.5\lambda^2$, $2.0x2.0\lambda^2$, and $2.5x2.5\lambda^2$, respectively.

Fig. 4.6 illustrates the response in normalised impedance on the Smith chart in response of the aperture radiator. The plots present in the different ground-plane sizes over an operation range between 8 GHz–12 GHz. The resonance condition as a zero reactance is observed with a slight variation between 9.5~10 GHz. The attribute of impedance behaviour starts from the capacitive region and then moves to the inductive zone. The results of the resonance condition exhibit a small difference in the resistance. The near perfect matching impedance is observed in the case of the finite ground plane of 20x20 mm^2 as a smallest finite-size study case. For the other cases, the corresponding value of the resistance decreases slightly when the finite ground-plane size is increased to more than one wavelength. In addition, the plots also imply the effect on the bandwidth based on the impedance behaviour. The SWR (standing wave ratio) circle shows the bandwidth limitation of the antenna characteristics due to the resistance in a conductor and it is fundamentally related to cross sectional area of a conductor.

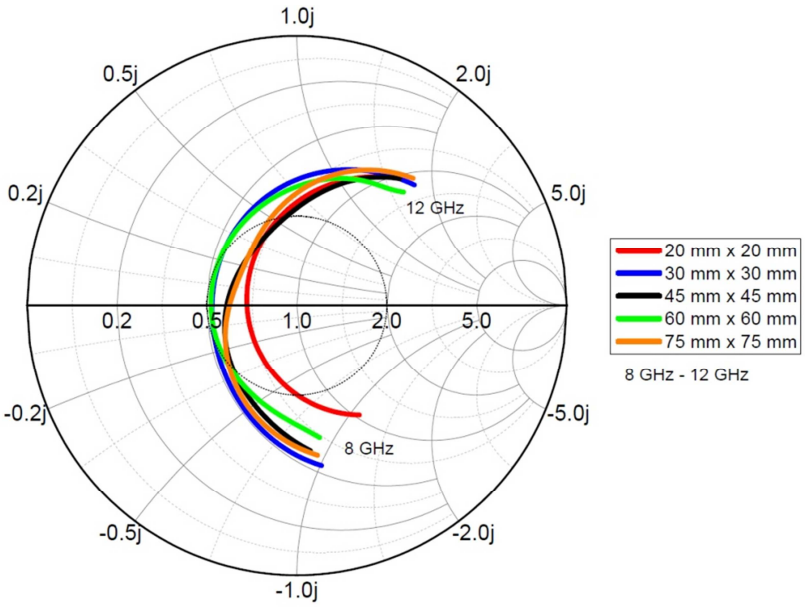

Figure 4.6: Simulation results of the normalised input impedances of the aperture radiator for different ground plane sizes.

Fig. 4.7 shows the radiation pattern of the aperture radiator at 10 GHz in a variation of the finite ground-plane sizes in 2D and 3D patterns for the purpose in comparison. It can be seen that when the finite ground-plane dimensions are less than one wavelength, the radiation is bi-directional similar to that of the dipole element radiation (zero order beam). A near symmetric pattern is obtained with respect to the ground plane and the directivity peak is around 4 dBi. In addition, the radiation patterns in the E- and H-plane have similar attributes. Apart from that, the radiation patterns in the case of the finite ground-plane size more than one wavelength show deviation (tilted) from the normal of the ground plane due to the effect of diffraction from the edge of a ground plane. For the largest ground-plane size of 75x75 mm^2, higher order diffraction produce a zero order beam at each side of the plane.

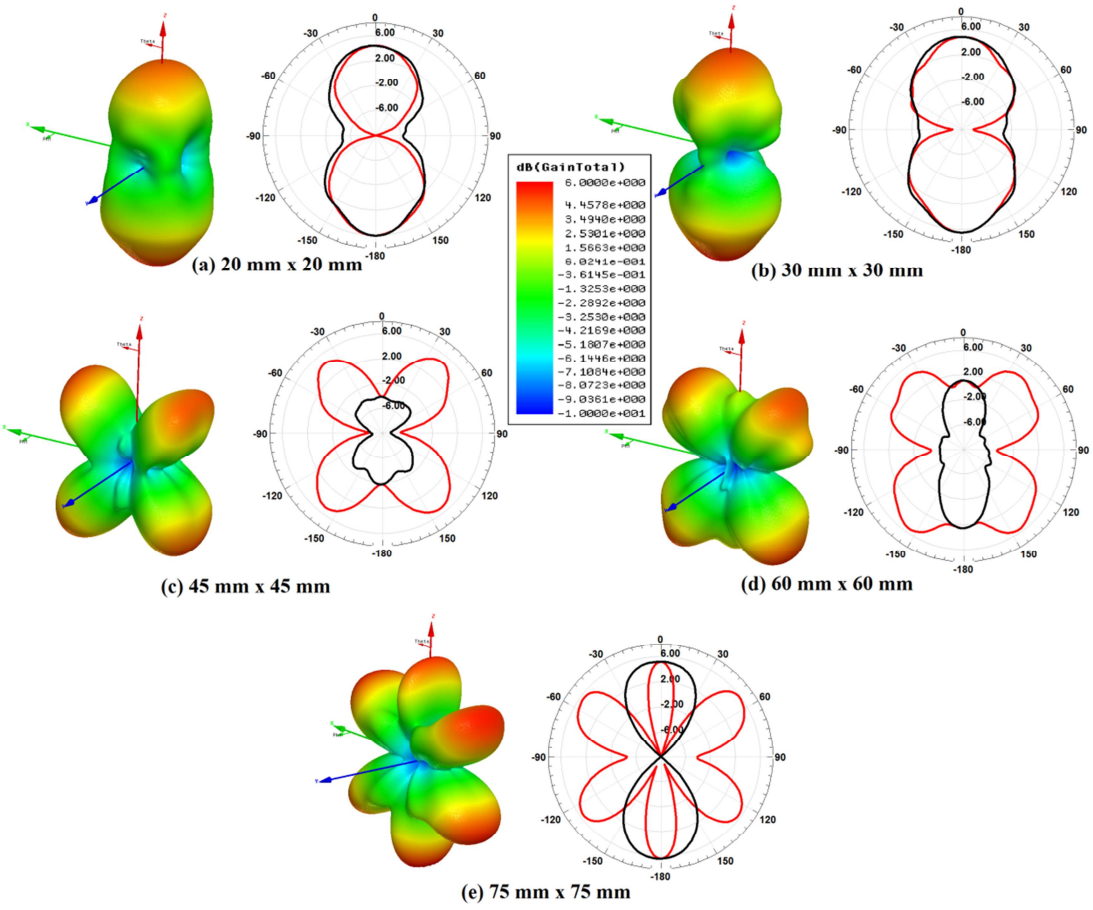

Figure 4.7: Simulation results at 10 GHz for the effect of the finite-size aperture radiator on the radiation characteristics (all in the same scale).

4.5.2 Configuration of the CPW-fed aperture radiator

The driven aperture is associated with the magnetic dipole behaving as a field radiator. The CPW feed-line is used to integrate to the aperture element as a short-end condition in order to interface with the signal connector. The broadband impedance matching can also be performed in a geometrical approach. The concept of the double-tuned matching technique is given and implemented. The investigation of the capability of the matching technique is illustrated.

Fig. 4.8 shows the physical layout of an aperture radiator integrated with the short-end CPW feed-line. The driven aperture can radiate the electromagnetic field to couple to a resonant patch in the final design step. The symmetrically feeding point is considered and this leads to two sections of the aperture element. The length of each aperture section L_s is associated with the resonance condition as a half target wavelength. The aperture impedance is based on the parameters W_s and L_s. In connection with the

relation of equation (4.10), the aperture impedance is related to the complementary structure as a dipole strip. Hence, the expression of the dipole strip impedance can be approximated by [167]

$$Z_{dipole} = R(z) - j\left[120\left(ln\frac{2L_s}{W_s} - 1\right)\cot(z) - X(z)\right] \quad (4.11)$$

$$R(z) = -0.4787 + 7.3246(z) + 0.3963z(z)^2 + 15.613(z)^3 \quad (4.12)$$

$$X(z) = -0.4456 + 17.00826(z) + 8.6793z(z)^2 + 9.6031(z)^3 \quad (4.13)$$

where $z = kL_s/2$ and $k = 2\pi/\lambda$.

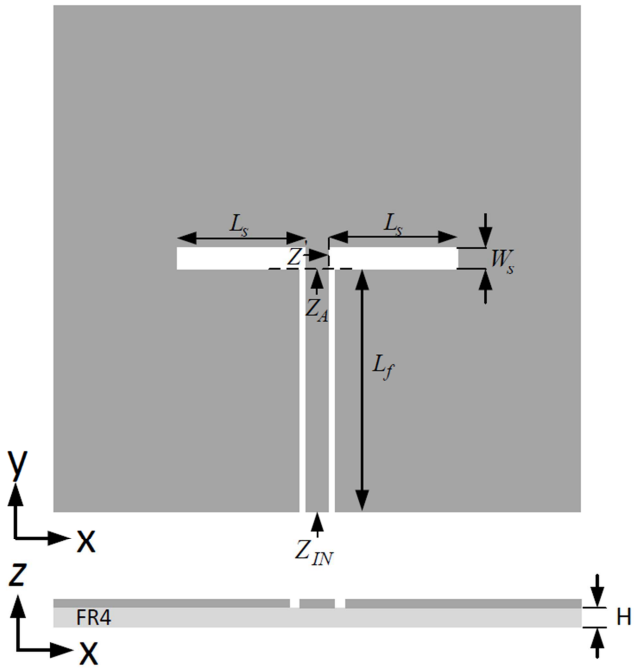

Figure 4.8: Geometry of the physical structure of the narrow aperture radiator.

The impedance (Z_A) of the aperture element is examined at the boundary of the reference plane which is the position between the CPW feed-line and the identical aperture elements where they are joined. Therefore, the analysis of input impedance can be considered in parallel elements of which the total impedance of an aperture is expressed as

$$Z' = -jZ_{aperture}\tan(\beta L_s) \quad (4.14)$$

$$Z_A = \frac{Z'}{2} = -j\frac{Z_{aperture}}{2}tan(\beta L_s) \quad (4.15)$$

Here, the design parameters are related to the target wavelength and the properties of a substrate material. A FR4 dielectric with a single-side copper is used as a substrate to support an aperture and a CPW structure. The electric permittivity (ε_r) and the loss tangent ($\tan\delta$) of the FR4 material are 4.1 and 0.02, respectively. The dielectric thickness is 1.6 mm. At the target frequency of 10 GHz, the guided wavelength (λ_g) of the FR4 material is approximately 15 mm given by $\lambda_o/\sqrt{\varepsilon_r}$. The parameters of the aperture element result in the length (L_s) as a resonance condition and the width (W_s) as a fraction of the wavelength. With the 50-Ω impedance, the parameters of the CPW feed-line; the width (W_f) and the gap (G) in Fig. 4.10, are determined. The dimensions of the CPW structure is used to calculate effective permittivity (ε_{eff}) and a quarter guided wavelength. All of parameters are listed in Table 4.1.

Table 4.1: The dimensions of the CPW fed aperture radiator in millimetres.

L_s	W_s	W_f	G	ε_{eff}	$0.25\lambda_g$
7.8	1.7	1.4	0.2	2.47	4.8

4.5.3 Broadband matching technique

In order to deal with the wide impedance bandwidth, the technique of the double-tuned impedance matching [156, 168] is applied into a configuration of the CPW-fed aperture radiator in this work. Technically, there are two ways to implement this method based on the lumped and distributed approaches [169, 170].

Here, the matching technique is based on an impedance transformer that is associated with the physical structure of a transmission line. The electrical length of the transmission line (L_f) can be cut at the particular distance [171]. This effect can lead to the reflection coefficient of a transmission line structure with the aperture load which can be determined as

$$\Gamma(L_f) = \Gamma_{Load} e^{-2j\beta L_f} \tag{4.16}$$

In connection with the Wheeler's method [166], the bandwidth expression for a double tuning resonance can be determined by

$$B = \frac{1}{Q}\frac{2\sqrt{\Gamma}}{1-\Gamma} = \frac{1}{Q}\sqrt{VSWR^2 - 1} \tag{4.17}$$

$$B = \frac{f_H - f_L}{\sqrt{f_H f_L}} \tag{4.18}$$

where VSWR is a voltage standing wave ratio and $f_o = \sqrt{f_H f_L}$ for the zero reflection. The parameters of f_H and f_L are defined as the high and low frequency of the edge band, respectively.

The calculation of the Q factor is a significant factor in dealing with the bandwidth [172] and also the modification of antenna dimensions can give the double-tuned impedance. The matching point can be considered by the Foster reactance as a function of the angular frequency which is illustrated as antenna impedance (Z_A) by [173]

$$Z_A = R_A^{rad} + R_A^{loss} + j\left(\omega L_A - \frac{1}{\omega C_A}\right) = R_A + jX_A \tag{4.19}$$

$$R_A = R_A^{rad} + R_A^{loss} \tag{4.20}$$

$$X_A = \omega L_A - \frac{1}{\omega C_A} \tag{4.21}$$

where R_A^{rad} and R_A^{loss} are radiation and loss resistance of an antenna. The parameter X_A is the characteristics of antenna reactance composed of the inductance (L_A) and the capacitance (C_A). Also, the evaluation of the Q factor based on an equivalent circuit under a lossless condition is expressed as [173]

$$Q = \frac{\omega\frac{dX_A}{d\omega} \pm X_A}{2R_A^{rad}} \tag{4.22}$$

Therefore, the reactance part of the load impedance is considered and modified by the compensation of the conjugated reactance in the front section.

In this context, the analysis of the transmission line is based on a classical inductance-capacitance (L-C) model in a lossless condition. With the response of the reflection phase, the property of reoccurrence is obtained at multiples of 90° or 180°. In addition, a guided wavelength is varied as a function of frequency and this leads to the independent modification of impedance. Hence, the behavior of a travelling phase response allows the transmission line to function as an L-C network in the wideband impedance matching. In control of the impedance behavior, the complex aperture impedance in the operation range can be compensated by the intrinsic CPW characteristics as conjugated impedance. The variation of the CPW length can dominate as a periodic function of a wavelength. Therefore, the edge band is manipulated at the low and high frequencies whereas the middle band is maintained by a resonance condition with the minimum reflection.

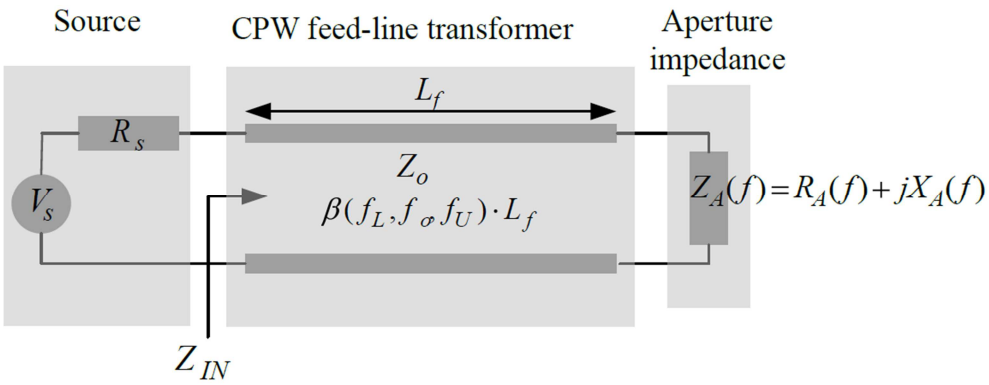

Figure 4.9: Model of the impedance matching equivalent circuit of the aperture impedance.

Fig. 4.9 illustrates the diagram of a matching transformer in connection with the transmission line with the distance L_f as considered in [174]. Under relevant conditions [164], two non-resonant frequencies in the edge band of the target frequency are considered to be the lower and upper frequencies as $f_L = f_o - \Delta f$ and $f_U = f_o + \Delta f$. The aperture impedance at the frequencies f_L and f_U can be observed in the different types of reactance $jX(f_L)$ and $jX(f_U)$. As illustrated in section 4.5.1, the aperture reactance is presented as a capacitance and inductance at the lower and upper region, respectively. Therefore, the transmission line section behaves as an L-C network to match the load impedance (aperture radiator) and the source impedance in order to broaden the impedance bandwidth. The input impedance of the CPW feed-line connected with the load impedance as an aperture radiator is expressed as a function of the frequency as

$$Z_{IN}(Lf, \omega) = Z_o \frac{Z_A(\omega) + jZ_o \tan(\beta Lf)}{Z_o + jZ_A(\omega) tan(\beta Lf)} \tag{4.23}$$

where the antenna impedance is $Z_A(f_L) = R_A(f_L) - jX_C(f_L)$ and $Z_A(f_U) = R_A(f_U) + jX_L(f_U)$.

With the distributed approach, the electrical length of the CPW feed-line is tailored in correspondence to the resonant wavelength in the multiple of $\lambda_o/2$. The resultant reactance of the CPW feed-line can behave as an inductance and capacitance at the conditions of the lower frequency $(f_L < f_o)$ and the upper frequency $(f_U > f_o)$, respectively. The impedance compensation is performed at both sides of the resonant frequency with the values of the reactive elements as $\pm j\Delta X$. By the multiples of the electrical length at the centre frequency, a location of the middle frequency can be preserved. It is shown that the conjugate matching based on the structural transmission line acts as a reflective equalizer.

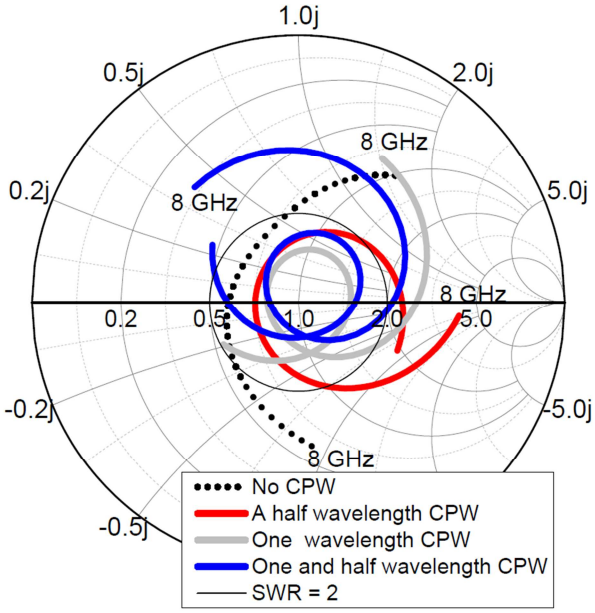

Figure 4.10: Simulation results for the response of the double turning impedance matching of the aperture radiator.

Fig. 4.10 shows the response of input impedance on the Smith chart for the CPW fed aperture radiator. Three cases of the electrical length of the CPW transmission line (L_f) are demonstrated in the multiples of a half wavelength. In comparison, the relocation of the input impedance is illustrated that the one-wavelength CPW feed-line of 18.8 mm provides a good impedance matching and a wide bandwidth. The location of impedance at the low and high frequencies is clearly observed in the opposite reactance space on the Smith chart as compared without the feed-line (No CPW). It is seen that the impedance behaviour of the CPW fed aperture can form a loop around the match within the 2.0 SWR circle from 8.9 GHz to 12 GHz. The enhancement of the impedance bandwidth is around 30% at the centre frequency of 10 GHz, whereas the aperture radiator without the conjugate impedance matching provides a bandwidth of only 15% (9~10.5 GHz). The total size of the antenna with the CPW feed-line can be fitted into the area of 45 mm x 45 mm.

Fig. 4.11 shows a component of the resultant impedance consisting of resistance and reactance. The resistance plot presents a double resonance as a function of the electrical length of the CPW feed-line between 8 GHz and 12 GHz. As a half-wavelength multiple of the CPW length, the middle band is able to preserve the reactance of the input impedance at 10 GHz. The lower frequency of 8 GHz indicates a longer guided wavelength around $1.25\lambda_o$, while the upper frequency of 12 GHz reveals a shorter guided wavelength of $\sim 0.83\lambda_o$. As a condition of the CPW length, the series of reactance components are given and manipulated to match the aperture reactance within the frequency band.

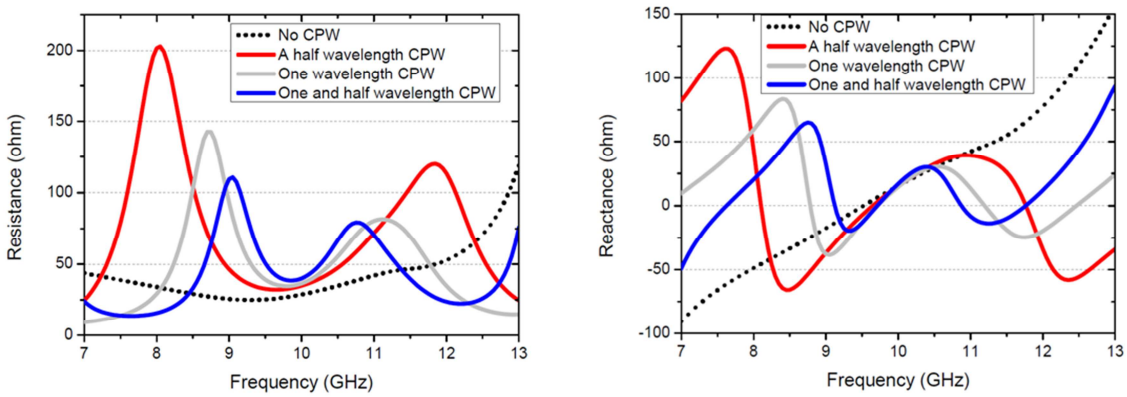

Figure 4.11: Simulation results for the input impedance of the double turning matching of the aperture radiator, (a) resistance and (b) reactance.

Fig. 4.12 also shows the attributes of the reflection coefficient (S_{11}) of the CPW-fed aperture radiator in a variation of the CPW length between zero and λ_g. It clearly shows the evolution of the bandwidth extension between $0.5\lambda_g$ and λ_g of the CPW length resulting in the appearance of a double dips at ~9.5 GHz and ~11.5 GHz. On the other hand, in the cases of CPW lengths of $0.25\lambda_g$ and $0.75\lambda_g$, better single matching can be observed especially in a case of $0.75\lambda_g$ at ~10.5 GHz. It is concluded that the use of the one-wavelength transmission-line with the short-end is the most effective method for matching the one-wavelength aperture radiator in achieving the wide impedance bandwidth.

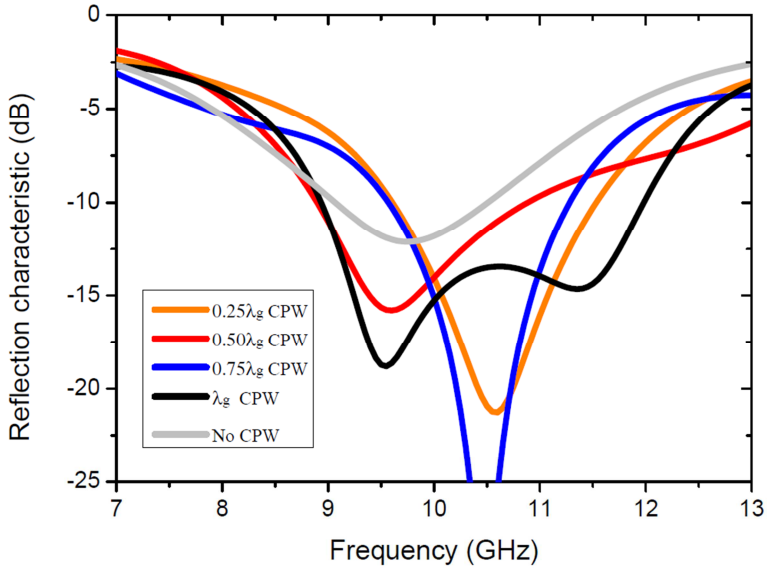

Figure 4.12: Simulation results for the characteristics of the reflection of the aperture radiator by varying the length of the CPW feed-line including $0.25\lambda_g$, $0.5\lambda_g$, $0.75\lambda_g$, and λ_g.

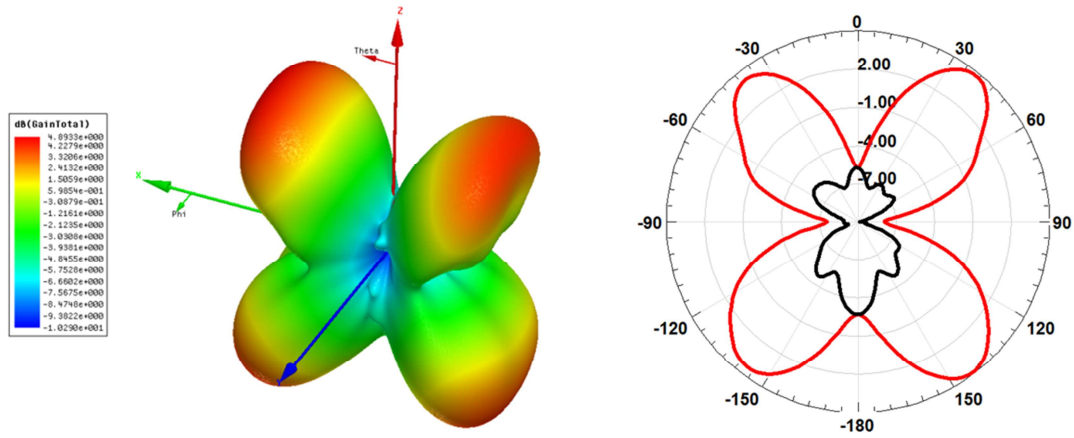

Figure 4.13: Simulation results for the 3D and 2D radiation patterns of the CPW fed aperture radiator on the ground plane size of 45 x 45 mm^2.

Fig. 4.13 shows the characteristics of the 2D and 3D radiation patterns of the CPW-fed aperture radiator with good impedance matching at the target frequency of 10 GHz. As seen in the above, the edge effect can dominate the radiation characteristic due to the finite ground-plane size. The pair of the radiation peaks illustrate the direction at the angle of 0±40° and 180±40°. The far-field radiation pattern in the E-plane pattern corresponds to the appearance of the E field in the aperture element. In contrast, the H-plane pattern gives small radiation.

4.6 Design of the CPW-fed aperture-coupled patch antenna

In this section, the CPW-fed aperture is combined with a resonant patch to produce a wideband antenna device. As shown in Fig. 4.4, the resonant patch element is above the driven aperture positioned in the ground plane on the FR4 dielectric substrate. The coupling of the patch element and the aperture will result in wideband operation of the resultant patch antenna. The investigation on the aperture-coupled patch antenna is influenced by the effect of the input impedance due to the mutual coupling between the elements. The edge effect based on the theory of diffraction is also observed in a variation of the finite ground-plane size. The impedance optimisation of the resonant elements can improve the bandwidth and radiation performance. In addition, the air-gap structure is introduced to the antenna mechanism for eliminating the material loss. By applying the micromachining technique, the air-medium based structure can be produced using a laser machined polymer (PMMA) rim. A square polymer rim with the dimensions of approximately λxλ is necessary in order to avoid the fringing effect on the radiation of the patch element.

4.6.1 Effect of the CPW-fed aperture-coupled patch

The air-gap based design has been used in the aperture-coupled patch antenna as illustrated in [175] and [176]. In this work the initial air-gap height is specified around 0.1λ which is obtained by the optimisation of a parametric variation for wideband operation. The possibility of producing a polymer based rim by the laser micromachining method is able to control the width of a rim frame to be 2 mm. The total dimension of the polymeric rim is 40x40x3 mm^3 at the frequency of 10 GHz. For the air gap of 3 mm, the length (L_p) and width (W_p) of the patch element are determined as 10 mm and 20 mm, respectively. Due to the interaction of the two resonators positioned within a small distance by the air gap, a mutual coupling effect is introduced in the antenna device [177]. In this circumstance, the effect of a driven aperture loaded by a parasitic patch is solved by impedance optimisation. The mutual coupling behaviour can be studied by dealing with self-impedance of the aperture and the patch in a similar method as performed for the patch stack configuration [175].

Fig. 4.14 illustrates the response of the input impedance on the Smith chart. The plots consist of the aperture-coupled patch antenna for non-optimised and the optimised impedance. The frequency response is observed between 7 GHz and 13 GHz and the

expected SWR circle is given. The optimisation deals with only the width of the aperture element. The aperture width of the initial structure and the optimised version are 1.7 mm and 1 mm, respectively. The observed attribute of the response shows the creation of two loops to determine the desirable operation. In comparison, the good impedance behaviour of the optimised structure is illustrated with an appearance of the loci in a SWR circle. But as seen in the non-optimised version, the wideband impedance bandwidth gives poor matching in the target of the operation band and the response is clearly affected by the mutual effect.

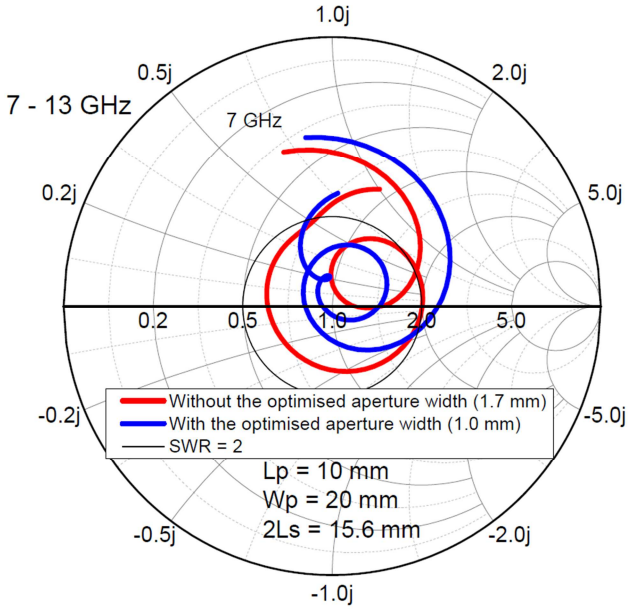

Figure 4.14: Simulation results of the input impedance of the aperture coupled patch in the optimisation of the aperture width.

In order to consider the optimised antenna configuration, the narrow aperture is made with a smaller width than the initial dimension that is able to relocate two loops in the 2.0 SWR circle. The narrow aperture width is represented as high impedance. As a result, the modification of an aperture width can deal with the mutual impedance due to the ability to dominate the induced current.

4.6.2 Effect of the mutual impedance

Fig. 4.15 and 4.16 show how impedance behaviour is influenced by the mutual effect on the Smith chart in a variation of the width of a patch and aperture element. The plots exhibit the response of impedance in the frequency range over 7–13 GHz. It is seen that the appearance of the loci is caused by impedance behaviour between the aperture and the resonant patch element.

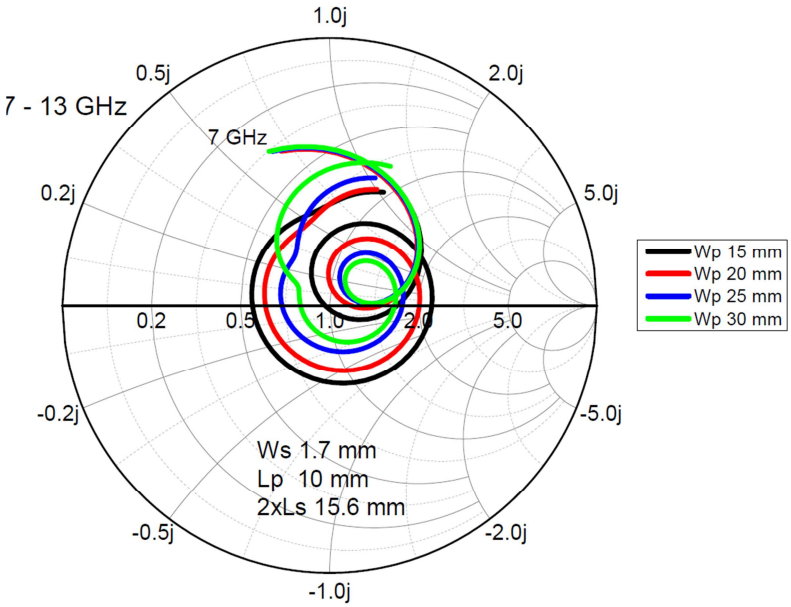

Figure 4.15: Simulation results of the input impedance of the aperture coupled patch in a variation of the patch width.

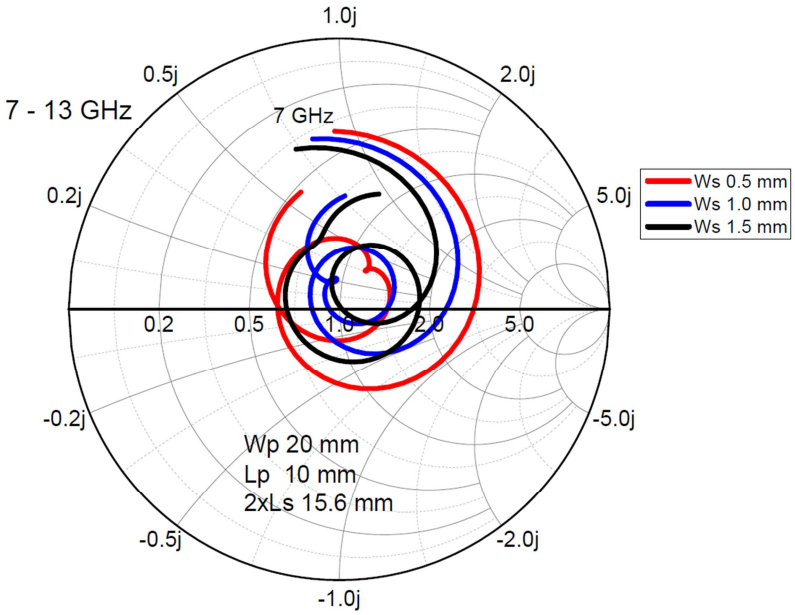

Figure 4.16: Simulation results of the input impedance of the aperture coupled patch in a variation of the aperture width.

Fig. 4.15 illustrates the effect of the patch impedance that acts as a parasitic element. The major change can be observed only in the first loop, whereas the second loop is dominated by the aperture element and is influenced by the small variation in the decrease of reactance. As the patch impedance is increased by enlarging the width (W_p), the first loop is directly affected by moving the locus which passes through the perfect

matching point to the inductive space due to less capacitance and also the resonance location is modified. This action influences mutual impedance in the higher frequency region that causes the mismatching issue to the upper band of the aperture response. Fig. 4.16 demonstrates the effect of the aperture width (W_s) that can dominate impedance of the driven element. The significant change can affect the second loop by increasing the resistance. The location of that loop is moved to pass through the perfect matching point. The minor effect of modifying the aperture structure can manipulate the first loop because the patch is a parasitic element in control of the characteristics of the aperture resistance. It is concluded that the response of the self-impedance in the aperture and patch element can take account of the mutual effect and also the impedance bandwidth can be improved by the optimisation of their physical widths.

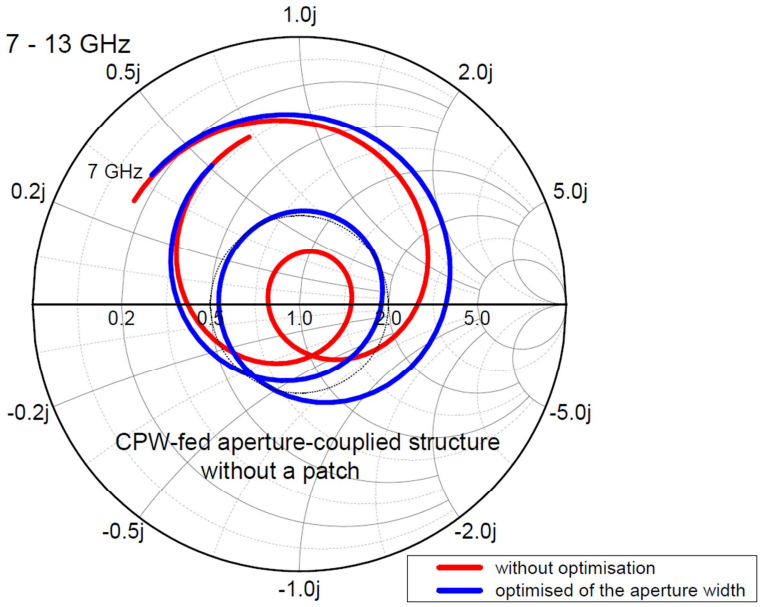

Figure 4.17: Simulation results of the input impedance of the aperture radiator with and without the optimisation of the width of the aperture radiator.

Fig. 4.17 depicts the characteristics of the input impedance of the aperture radiator without the patch element. The plots illustrate the effect of the aperture width between 1.7 mm and 1 mm. The resultant impedance plays an important role in the reflection coefficient over the band. As seen in the impedance behaviour, it can be clearly seen that the major element affecting the impedance effect is the aperture structure. The patch modification is avoided because the increase of the patch width causes the spurious radiation. In the impedance behaviour, the response is concerned with the reflection coefficient tolerance |Γ| as explained in [168].

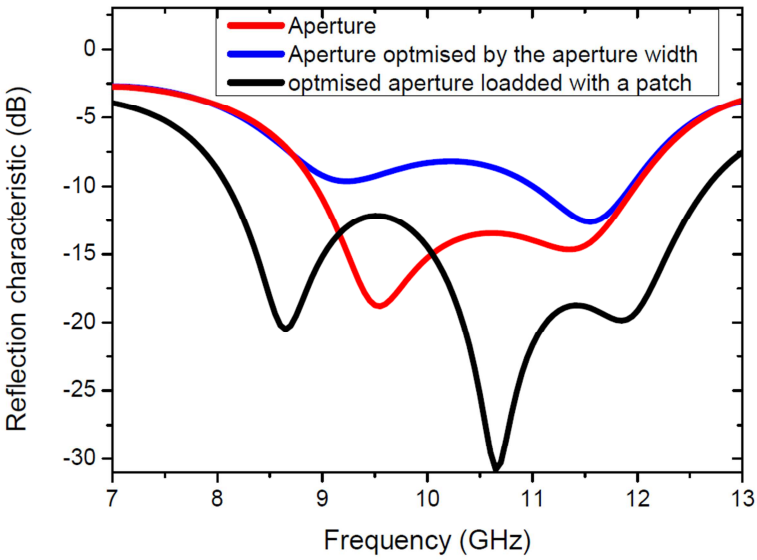

Figure 4.18: Simulation results for the comparison of the reflection characteristics between the aperture radiator with and without the patch element.

Fig. 4.18 also exhibits the attributes of the reflection characteristics for three cases. The reflection coefficients are obtained for the initial aperture radiator design, the optimised aperture radiator, and the optimised aperture coupled patch. It is clearly evident that the resonance of the patch element is captured and merged in the middle operation band in which the overall impedance bandwidth is extremely large around 46% to cover the X-band frequency (8 GHz–12 GHz).

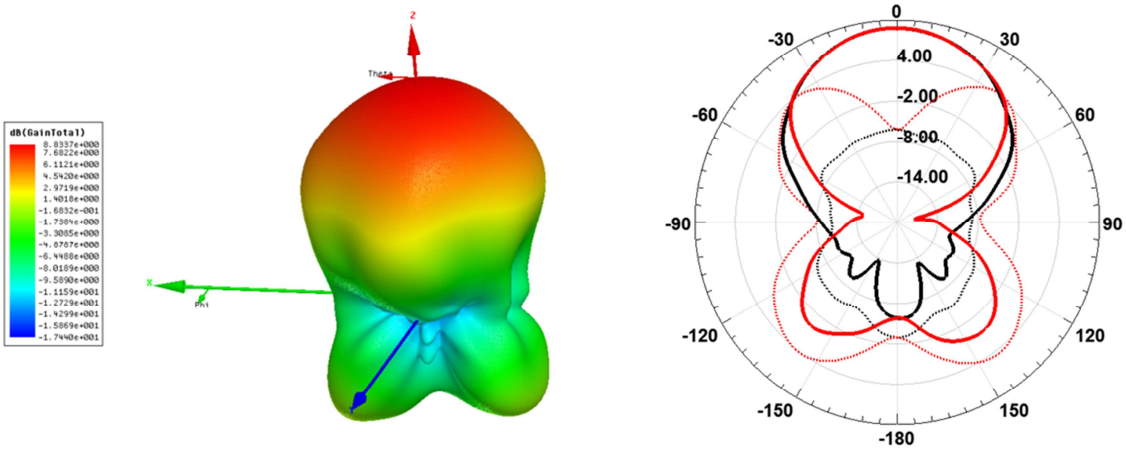

Figure 4.19: Simulation results for the 3D and 2D radiation patterns of the wideband aperture-coupled patch.

Fig. 4.19 illustrates the radiation characteristics of the aperture coupled patch antenna at the observed frequency of 10 GHz. The radiation patterns are depicted in the 3D and 2D diagrams. The radiation characteristics show significant enhancement in antenna directivity. In the 2D pattern, the comparison between the aperture radiator with and without the patch element exhibits the improved radiation patterns in a broadside direction with the peak of 9.3 dBi in which the original radiation is about -6 dBi. Also, the reduction of a back radiation produces a front-to-back ratio of ~14.5 dBi.

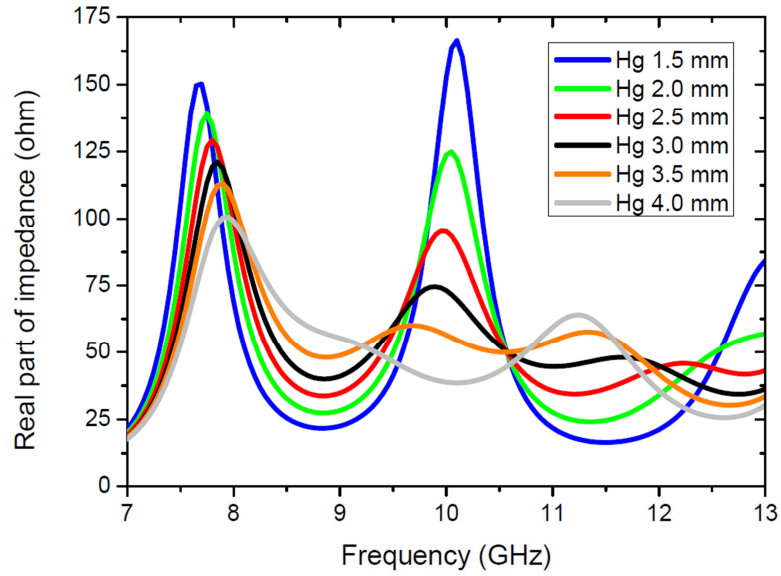

(a)

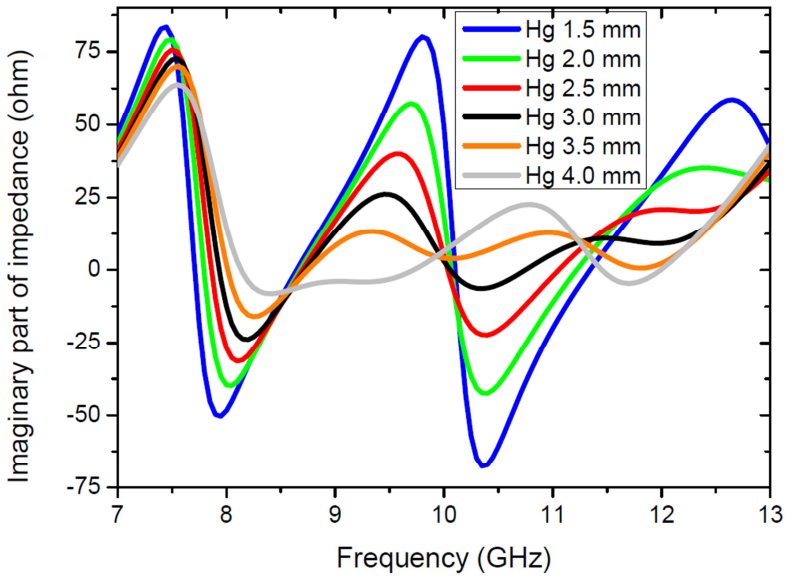

(b)

Figure 4.20: Simulation results for the effect of the air gap on the impedance for the Hg values (Fig. 4.4) of 1.5 mm, 2.0 mm, 2.5 mm, 3.0 mm, 3.5 mm and 4.0 mm, (a) resistance and (b) reactance.

4.6.3 Effect of the air-gap thickness

Fig. 4.20 demonstrates the input impedance in a variation of the air-gap separation (H_g). The resistance and reactance are plotted for air gap values of 1.5 mm, 2.0 mm, 2.5 mm, 3.0 mm, 3.5 mm and 4.0 mm. In this study, the dependence of the coupling effect on the air gap is discussed. As described in section 4.6.1, the initial air-gap distance of 3 mm (0.1λ) is performed in the antenna design. As the value of an air-gap decreases, the impedance values at 8 GHz and 10.5 GHz become larger and this leads to a mismatching condition in the antenna impedance. It is shown that a smaller air-gap results in a stronger coupling effect to govern the aperture impedance that the patch impedance is unable to compensate the mutual reactance (strong capacitance).

4.6.4 Effect of the finite ground-plane size

With the occurrence of the edge effect in the aperture radiator, the configuration of the aperture-coupled patch antenna is considered and studied for the characteristics of the impedance and radiation. To take into account of the effect of the finite ground-plane size, the reflection coefficient and directivity are obtained for various ground-plane sizes between 1.5λx1.5λ and 2λx2λ at the frequency of 10 GHz. The actual dimensions for the configuration described in Section 4.5 are 45x45 mm^2, 50x50 mm^2, 55x55 mm^2 and 60x60 mm^2.

Fig. 4.21 shows the simulation results of antenna performance consisting of the characteristics of the reflection and radiation. As can be seen in Fig. 4.21(a), the ground plane size does not have a strong effect on the magnitude of the reflection coefficient and the impedance bandwidth. The responses around 10 GHz in the middle band region is less affected.

Fig. 4.21(b) illustrates the results of the characteristics of the radiation bandwidth as a function of the frequency. It is clearly seen that the directivity decreases significantly as the ground-plane size increases. This result is caused by the radiation characteristics of the driven aperture associated with the edge effect of diffraction as discussed in section 4.7.1. The peak radiation moves slightly toward the high frequency region as the ground-plane size increase. At the frequency of 10.5 GHz, the radiation peak is around 9.3 dBi for the ground plane size of 45x45 mm^2, whereas it is about 6.8 dBi for the ground plane size of 60x60 mm^2 and thus it is a reduction of ~2.5 dBi.

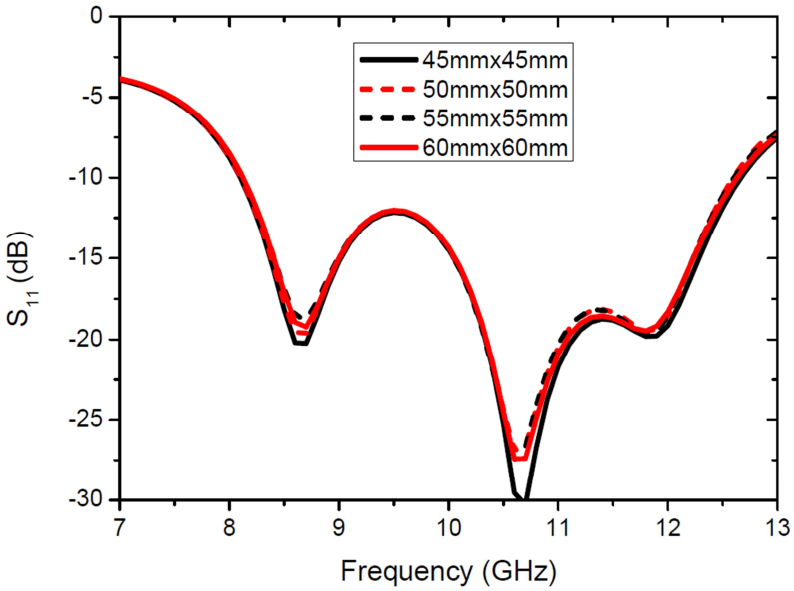

(a)

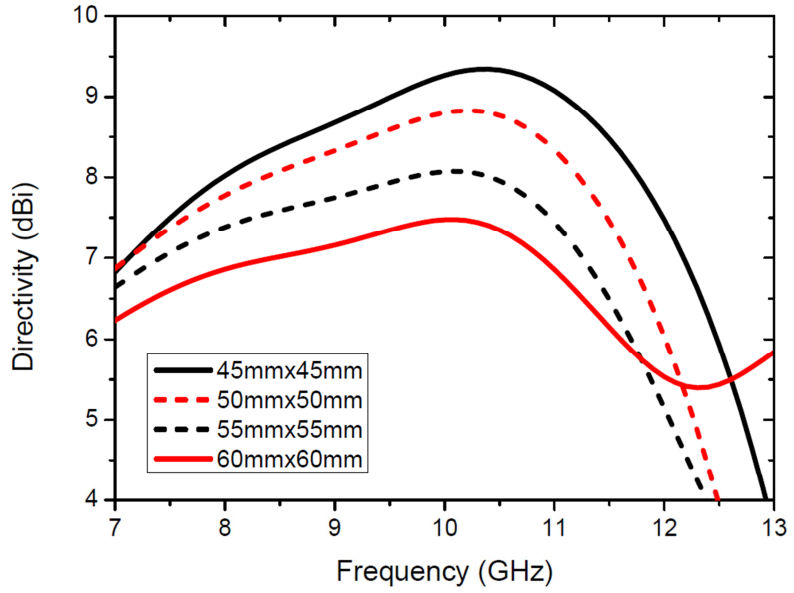

(b)

Figure 4.21: Simulation results of the characteristics of an aperture coupled patch antenna for a variation of ground plane dimensions, (a) reflection coefficients and (b) directivity.

4.7 Antenna fabrication

Microfabrication and micromachining methods have been widely used in development of microelectronic devices and microelectromachanical devices [178-180]. Here, it is a potential technique to produce the wideband patch antenna device. The substrate materials include a commercial copper clad FR4 board (Roth Elektronik, RE01-LF, RS Components) and a thin film LCP material (Ultralam 3850, Rogers Corporation). The thickness of the copper layers on the FR4 board is 35 μm and it is 18 μm on the LCP substrate. The PMMA (polymethylmethcrylate) material is used to fabricate the rim shaped spacer for an air cavity in the antenna design [181]. The properties of the materials are listed in Table 4.2.

The physical elements of the antenna configuration can be divided into three parts consisting of the patch element, the CPW-fed aperture, and the PMMA rim. An antenna assembly is obtained by all of their elements together. The manufacturing steps of microfabrication are shown in Fig. 4.22. It is seen that the patch element and the CPW-fed aperture have the same manufacturing steps including: step (2) for the deposition of a thin photo resist film (AZ9260) on a dielectric materials (FR4 and LCP), step (3) to pattern the photo resist layer using UV exposure, step (4) for the development of a patterned photo resist film, and step (5) for etching the exposed areas of the copper layer.

In step (6), the polymer rim spacer is made by a laser micromachining method. The PMMA material is the most suitable polymer for carbon dioxide (CO_2) laser machining based the effect of the laser ablation. The laser based method is a modern fabrication technique to shape a 3D structure especially for dielectric materials [182-184]. These elements are then assembled using an SU8 based bonding method to produce a wideband antenna. The PMMA rim is assembled with the LCP film and the copper surface of the FR4 substrate by the bonding steps (7 and 8), respectively. The antenna structure will be used in the work described in Chapter 5 in construction of broadband resonant cavity antenna devices.

Table 4.2: Electrical properties of dielectric materials at ~10 GHz.

	FR4 [149]	LCP [150]	PMMA [181]
ε_r	4.1	2.9	2.6
tanδ	0.02	0.0025	0.008

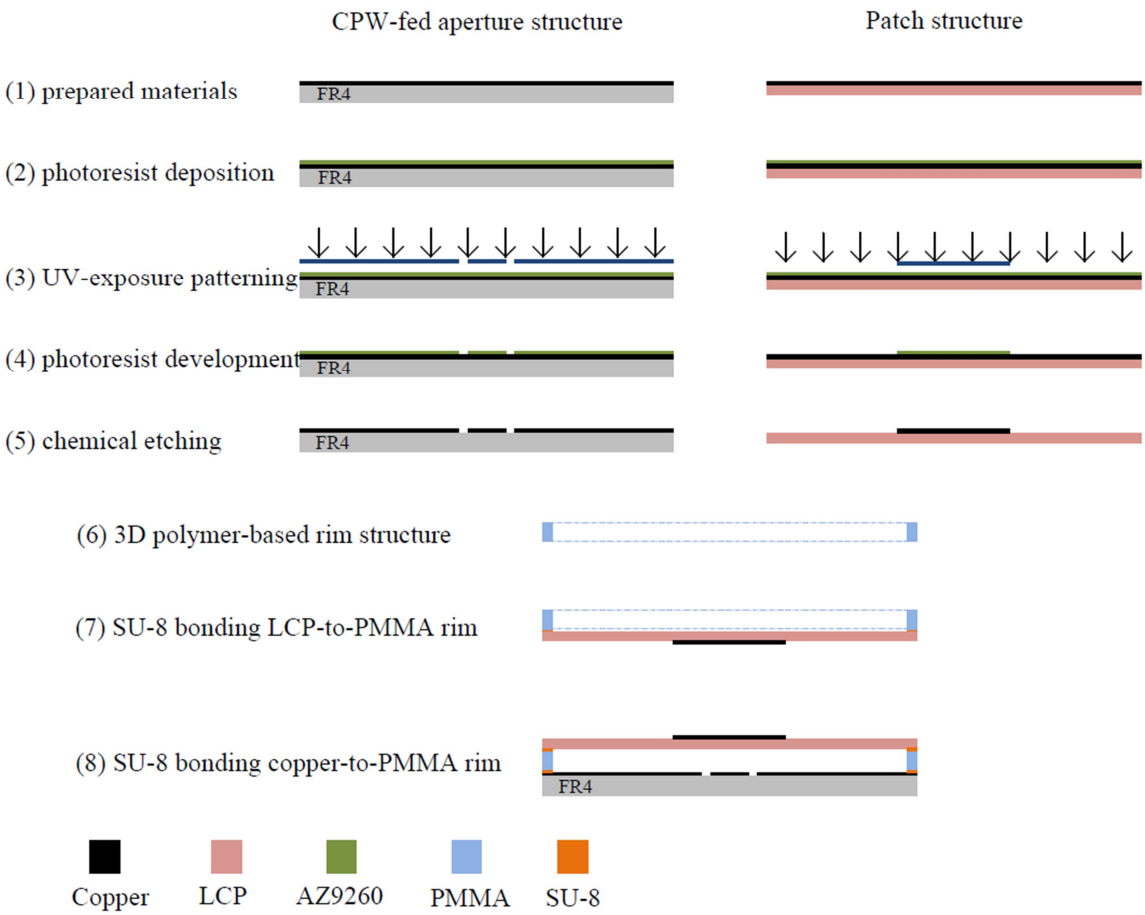

Figure 4.22: Schematic of the fabrication steps for the CPW-fed aperture-coupled patch antenna.

4.7.1 Photoresist deposition

The FR4 and LCP materials were cut into the required sizes. Then, holes (0.2-mm diameter) were drilled at the corners of the square substrate as alignment marks required in the UV exposure process to be described in section 4.7.2. The copper clad FR4 and LCP substrates were cleaned in diluted (5:1) Decon-99 liquid. The substrates were then dried using compressed dry nitrogen. The positive photoresist AZ9260 was deposited on the copper surface of a FR4 substrate using a spin coating based method. The thickness of the photoresist layer was about 10 μm at the spinning speed of 2400 rpm for 60 seconds. After this, soft baking at the temperature of 100°C was carried out on a hotplate for 3 minutes and then the substrate was removed from the hotplate and allowed to cool to room temperature for 30 minutes. Deposition of the photoresist on the LCP substrate was performed using the same method.

4.7.2 UV exposure

The process of the UV exposure was for transferring the geometric layouts on a mask to the photoresist layer. In this work, high resolution (64,000 dpi) film masks were used. Before UV exposure, the mask containing the design pattern was aligned to the photoresist layer on a substrate. The UV exposure work was carried out on a mask aligner. The layout scale was patterned with the ratio of 1:1 and the UV energy dose was specified at 500 mJ/cm^2 which was the same as described in section 3.10.

4.7.3 Development and chemical etching

In order to obtain the design pattern on the copper layer, photoresists development and copper etching were performed to remove a region of the photoresist film exposed to the UV light. The development solution for the AZ9260 photoresist was diluted with AZ400K solution of which the deionised water was added as the ratio of 1:4. The development time is 90 seconds. The exposed photoresist was removed completely with no damage to the unexposed region. Wet chemical etching was performed to the exposed copper using a Ferric chloride ($FeCl_3$) based etching solution. The etching time was around 7 minutes for the CPW-fed aperture structure and 10 minutes for the patch element. After copper etching, the photoresist layer was removed using acetone to complete the fabrication process for the respective elements on an FR4 or a thin film LCP substrate. Fig. 4.23 shows an optical image of the resultant structure of the CPW-fed aperture radiator on the FR4 substrate. A SMA connector was mounted at the terminal of the CPW transmission line for interfacing with a connecting cable to a network analyser for characterisation and measurements.

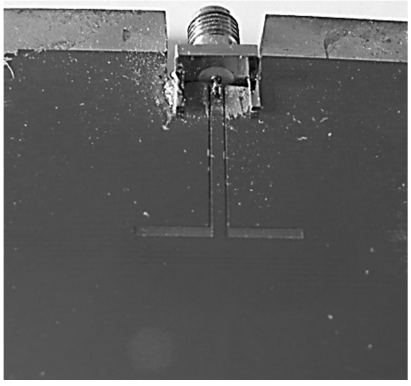

Figure 4.23: A photograph of an assembled CPW fed aperture with a SMA connector.

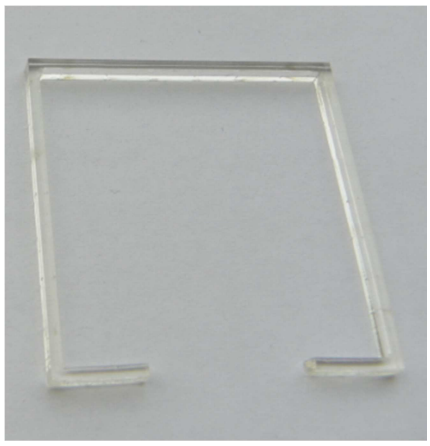

Figure 4.24: A photograph of the assembled antenna of a PMMA rim.

4.7.4 Laser micromachining for fabricating rim structures

The fabrication of a polymer-based rim spacer is carried out using a laser-based method. The machining of a dielectric material by pulsed laser radiation depends on the material properties and the laser parameters [185]. The polymer based rim structure for supporting the thin LCP film substrate was fabricated using a CO_2 laser based micromachining method. A PMMA material was used to produce the polymer rim. This material is robust, low cost and widely available. The laser power and scanning speed are operating parameters that were carefully controlled. The commercial PMMA material is available in a wide range of thicknesses. A PMMA sheet of thickness of 3 mm was selected as it provides the required thickness for construction of the wideband patch antenna. In operation, the schematic layout of the rim structure was drawn by the CAD tool. The laser power and scanning speed are 40 W and 114 mm/s. Fig. 4.24 shows an optical image of a PMMA based rim produced by the CO_2 laser micromachining method. The split ring design is to eliminate dielectric loss on the CPW feed-line by positioning the opening part of the PMMA rim in line with the CPW structure.

4.7.5 Antenna assembly

A SU8 based bonding method was used to assembly the LCP substrate with the patch, the PMMA rim, and the FR4 substrate to produce a patch antenna device. SU8 is a UV sensitive material which can be used as photoresist material, usually a permanent photoresist since it is difficult to remove it from a substrate after UV exposure. It is also used to fabricate 3D structures for microsystem applications. A viscous liquid SU8 (SU8-100) material is applied in the PMMA rim by a contact imprinting method [186]. A thin film SU8 layer of about 10 μm of thickness was produced on a glass wafer. The

polymer rim was then pressed against the glass wafer to take up the SU8 material for bonding. The PMMA rim with the SU8 material was then placed on a hotplate at 100°C for 5 seconds to allow the solvent to evaporate to increase the viscosity of the SU8 material. In the next step, the PMMA rim was aligned to the patch on the LCP substrate and the bonding process was completed by applying a load of 500 g for 30 minutes. Fig. 4.25 shows an optical image of a bonded PMMA rim on the LCP thin film substrate.

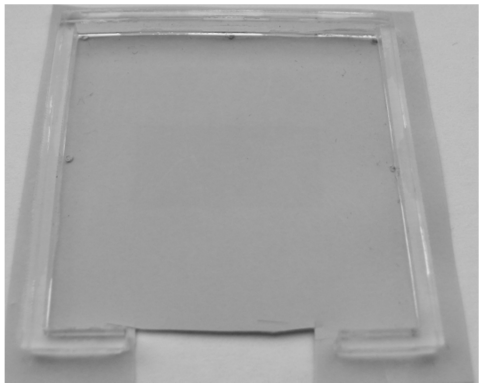

Figure 4.25: A photograph of the assembled antenna of a PMMA rim and LCP film.

The same SU8 imprinting and the bonding process was repeated for the other side of the PMMA rim to bond it to the FR4 substrate with the CPW feed-line and the coupling aperture. Fig. 4.26 shows an optical image of a complete structure of the CPW-fed aperture patch antenna.

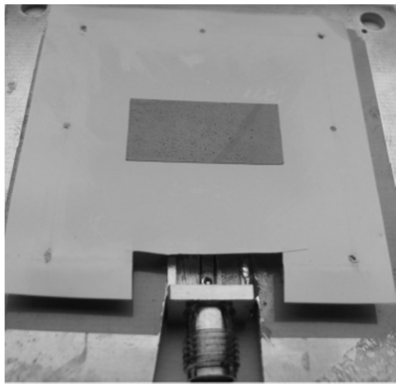

Figure 4.26: A photograph of the assembled antenna of a CPW-fed aperture coupled patch.

4.8 Measurements

In this section, the verification of the fabricated wideband antenna device was conducted using the same vector network analyser (HP 8510) and the horn antennas described in Chapter 3. The electromagnetic characteristics of the wideband antenna performance are obtained including the reflection coefficient, the radiation gain, and the radiation patterns. The results will show that the fabricated patch antenna structure in this chapter provides a wide impedance bandwidth and high radiation gain. In order to obtain the gain of the antenna device, the gain-transfer or gain-comparison method is used to obtain the far-field radiation behaviour [187].

4.8.1 The gain transfer measurement method

This section introduces a principle and method of the gain transfer technique for measurements of the radiation characteristics of antenna structures. This method only requires one antenna with the known characteristics called a gain standard or a reference antenna. The transmission antenna is not necessary to have known gain characteristics. The measurement process is performed in the receiving mode to obtain measurement results. The received powers, P_{AUT} and P_{GS}, are obtained from the antenna under test (AUT) and the gain-standard horn antenna (G_{GS}), respectively in the same arrangement of the far-field distance (L) and the transmitting power (P_0) from the transmitting antenna. In principle, the gain calculation of the AUT (G_{AUT}) antenna is fundamentally based on the Friis transmission equation as a gain transfer function. The free-space path loss is determined as $FL\ (dB) = 20log_{10}\left(\frac{4\pi L}{\lambda}\right)$. Therefore, two measurements can lead to the following equations in dB: $P_{AUT} = P_o + G_T + FL + G_{AUT}$ and $P_{GS} = P_o + G_T + FL + G_{GS}$. To deduce the gain of the AUT antenna, both equations are mathematically manipulated to eliminate the transmitting gain (G_T) and it can be shown that

$$G_{AUT} = P_{AUT} - P_{GS} + G_{GS}. \tag{4.24}$$

Fig. 4.27 shows the configuration of the measurement setup to obtain the antenna characteristics. The measurements were carried out in the anechoic chamber environment to remove the effect of multipath ray reflection. The vector network analyser (HP 8510) was calibrated for the full two-port mode. The standard gain antenna was a broadband horn antenna (Flann^{TM}16240-20). The operation band is over 8–12 GHz with an average gain of 20 dBi. A horn antenna with the gain of 15 dBi from Microwave Instruments Limited was used as the RF transmitter. The alignment between

the transmitter and receiver was set using a line-of-sight link. The distance between them was 30 cm (10λ at 10 GHz) corresponding to the far-field propagation.

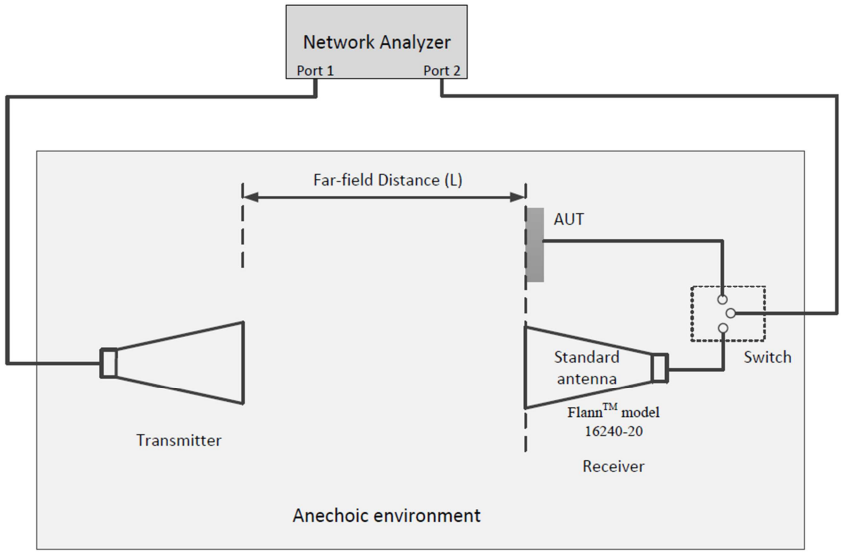

Figure 4.27: Schematic of the set-up for antenna measurements.

4.8.2 Characteristics of the aperture radiator

Fig. 4.28 shows the reflection characteristics (S_{11}) of the fabricated structure of the short-end CPW-fed aperture radiator. The measured impedance bandwidth was around 34% at the middle frequency of ~10 GHz. The lower and upper frequencies were 8.4 GHz and 11.8 GHz, respectively. Two frequency dips were clearly observed which were designed to broaden the bandwidth. A broad agreement between the results of simulation and measurement has been obtained, though the measured characteristic shows reflection around 10.5 GHz. It is shown that the impedance of the aperture radiator gives the pure resistance of 50 Ω which points to good matching with the source impedance at the second dip of frequencies.

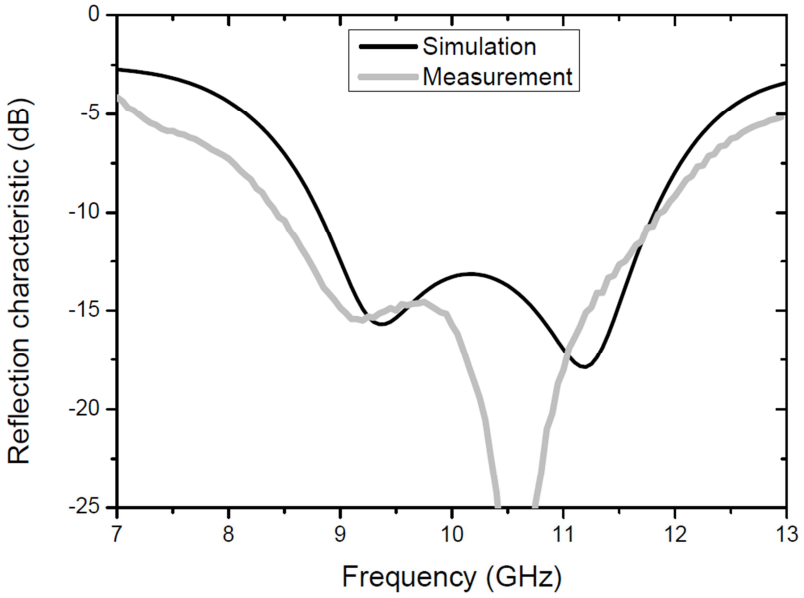

Figure 4.28: The measured and simulation results of reflection characteristics of the aperture.

4.8.3 Characteristics of the aperture coupled patch antenna

Fig. 4.29(a) shows the reflection characteristics (S_{11}) of the fabricated structure of the CPW-fed aperture-coupled patch antenna over 7–13 GHz. The overall impedance bandwidth of the -10 dB reflection property is between 8.4 GHz and 12.5 GHz or 41% at the middle frequency of 10 GHz. The reflection characteristics can obviously be seen with triple dips over the operation band. It can be seen that the measured characteristics agrees with the results of simulation. However, the attribute of the middle dip is weak in comparison with that of the simulated results. This may be effect of the SMA connector which was not included in the model of the simulation work. Fig. 4.29(b) shows the measured results of the antenna gain as a function of frequency over 7 GHz – 13 GHz. It is evident that a wide gain bandwidth is achieved with a peak gain of 8.5 dBi and the 1-dBi and 3-dBi ripple bandwidth of around 30% (8.5–11.5 GHz) and 43% (8–12.3 GHz), respectively. The significant difference below 8 GHz may be caused by the fact that the gain horn antennas were operated beyond their operation bandwidth. The horn transmitter (Flann^{TM}16240-20) has the specification that it can operate exactly over the frequency range of 8.2–12.5 GHz. But the observed frequency range in the AUT measurement was from 7 GHz which is out of the lower frequency limit of the horn antenna. Therefore, it shows a large discrepancy between the results of measurement and simulation below 8.5 GHz.

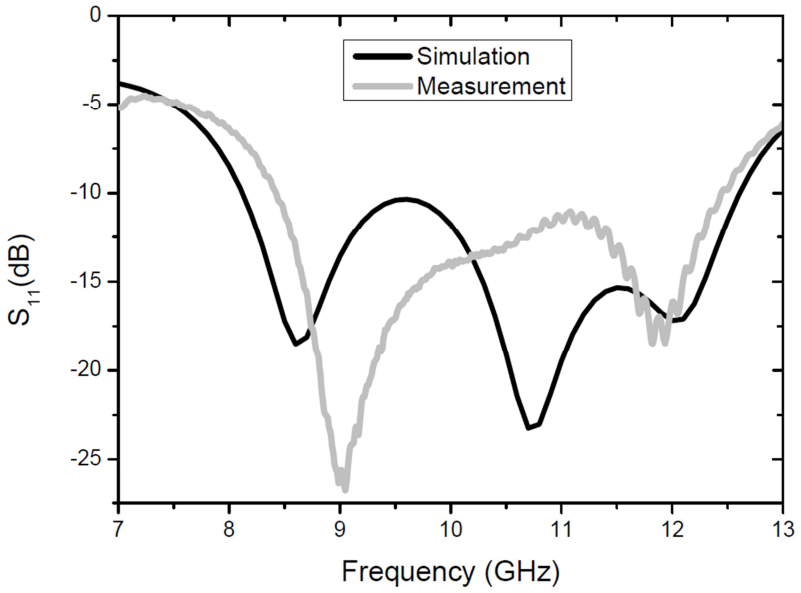

(a)

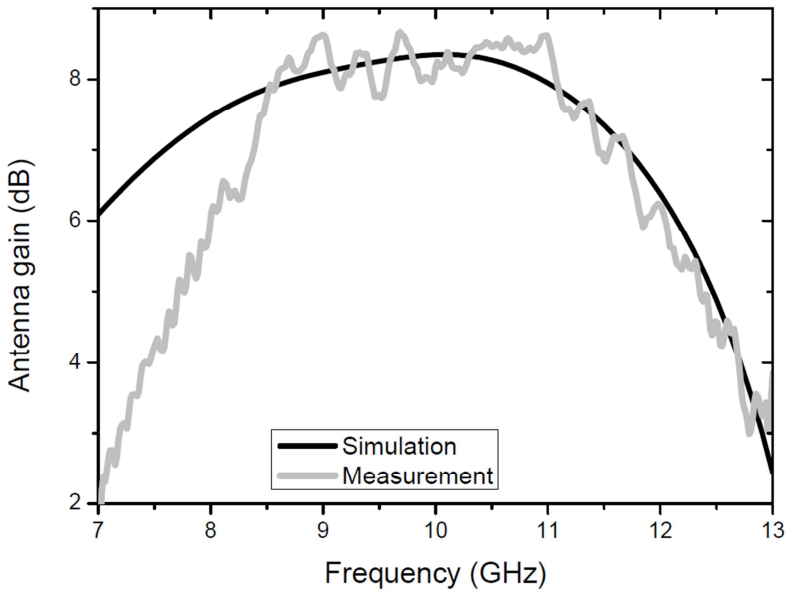

(b)

Figure 4.29: The measured and simulation results of the fabricated antenna, (a) reflection characteristics and (b) radiation characteristics.

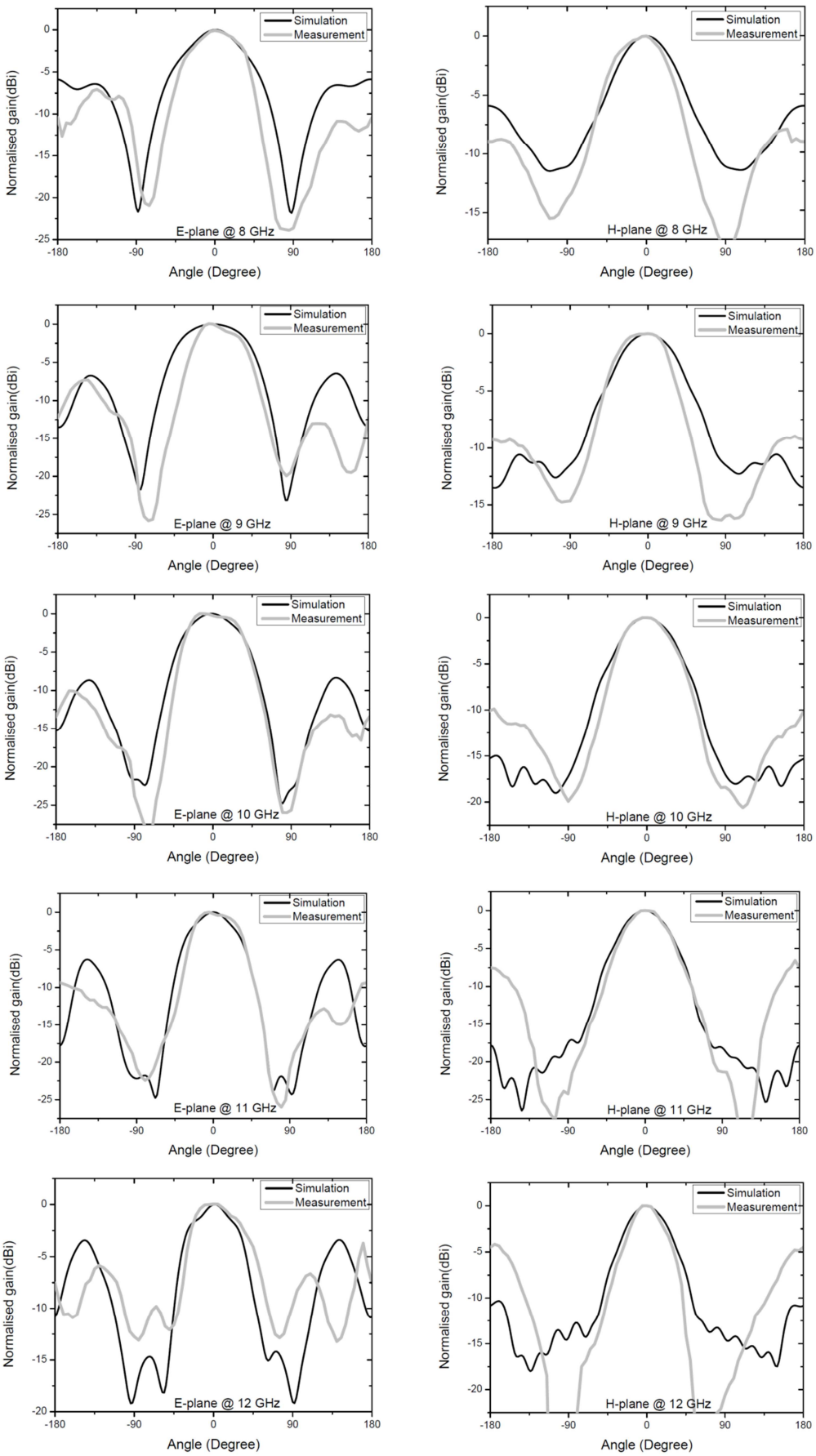

Figure 4.30: E- and H-plane far-field radiation patterns of the antenna at five different frequencies of 8 GHz, 9 GHz, 10 GHz, 11 GHz and 12 GHz, respectively.

Fig. 4.30 shows the far-field characteristics of the normalised radiation patterns in the H- and E- plane at the frequencies of 8 GHz, 9 GHz, 10 GHz, 11 GHz, and 12 GHz, respectively. The plots were obtained in the scan angle range of 0±180° at a step size of 5°. In comparison, the measured patterns of the radiation characteristics show good agreement with the results of the full-wave EM simulation. The E-plane patterns have a major lobe and two backside lobes, whereas the H-plane patterns have only one major front lobe and a minor back lobe. The front-to-back ratio of the directional antenna between the angle at 0° and ±180° is in the range of 7.5~12.5 dBi in both E- and H-plane. The HPBW values were determined to be 40° and 30° for the E- and H-plane, respectively. A discrepancy in the radiation pattern can be observed in the back-side region (±90° to ±180°) of the H-plane, especially at 11 GHz and 12 GHz. In particular, the unmatched angle was found around ±90° at which the gain decreases. Also, the angles of ±180° provide a different magnitude. It is possible that the differences are caused by the AUT holder. The AUT might not be properly positioned at the centre of the rotating point due to the inaccuracy of the alignment method. As the AUT is moved from the 0° angle, the location of the AUT is off from the initial position. Because of this the measurement results of the radiation pattern are not in perfect agreement with the simulation work.

4.9 Summary

In this chapter, the wideband patch antenna has been designed, constructed and assessed by reflection and radiation measurements. The CPW-fed and aperture-coupled design with a suspended patch has been studied. Wideband characteristics are obtained using coupled triple resonance based on the distributed matching method with a single typical patch element. The dimensions of the antenna elements are determined associated with the edge effect based diffraction analysis and numerical simulation. The effect of finite substrate on radiation characteristics of the aperture is investigated. The behavior of the short-end CPW feeding design with the aperture has been studied in detail for design of a wideband patch antenna. The polymeric rim spacer is technically produced by a laser micromachining method that allows convenient fabrication and accuracy of millimetre thick polymer structures compared with the SU8 based structures produced using a surface micromachining method. A 3-mm thick PMMA rim is used in construction of the wideband patch antenna. Liquid SU8 is used as a bonding medium in assembly of the patch antenna. The dimensions of the practical antenna are 45x45x4.6 mm^3. The

impedance bandwidth of the fabricated antenna is measured to be as large as 41%. The measured peak gain is 8.5 dBi, and the 3-dB and 1-dB ripple radiation bandwidths are as large as 43% and 30%, respectively. The measured bandwidth shows an improvement by a factor of two over the previous work [188]. The wideband antenna will be used as a primary source in the development of the broadband resonant cavity antenna described in Chapter 5.

CHAPTER 5 SYNTHESIS AND IMPLEMENTATION OF BROADBAND RESONANT CAVITY ANTENNAS

5.1 Introduction

In this chapter, the aim is to design and implement a broadband resonant cavity antenna (RCA) based on the study works of the two-layer metamaterials and the wideband patch antenna described in Chapter 3 and 4, respectively. A two-layer metamaterial is used as a superstrate or a partially reflective surface (PRS) and the Fano-resonance effect in the metamaterial is employed to achieve broadband performance. The effect of the resonant transmission of the metamaterial is investigated for applications as a superstrate for RCA devices. The electromagnetic image theory is also applied in design and modelling of the resonant cavity antenna. Broadband RCA structures are produced in 3D configurations. The primary broadband source antenna that has been developed successfully as described in Chapter 4 is used to provide the field energy into a cavity structure. Due to the radiation characteristics of the primary source, the resonant cavity antenna with broadband behaviour is studied based on an optimisation of the cavity height. The edge effects of the finite size of the metamaterial superstrate on the bandwidth and radiation characteristics are investigated. The two-layer metamaterials based superstrate designs are fabricated, one consisting of two patch arrays on LCP thin film substrates assembled using a micromachined PMMA rim spacer and the other one is based on two patch arrays each fabricated on one side of an FR4 board. The results of reflection and radiation measurements are described and it is shown that broadband RCA devices are realised.

5.2 Principle of resonant cavity antennas

The resonant cavity antenna (RCA) is based on a parallel plate configuration with a separation of approximately half wavelength at the design frequency. The planar structures are a total reflector as a ground plane and a partially reflective surface (PRS) as a superstrate. The pair of the reflectors is separated by a dielectric medium which is usually air or free space. This type of antenna structures is capable of providing high gain and narrow beam characteristics. There are several other names that have been used to describe a RCA device including EBG antennas, Fabry-Perot cavity antennas,

resonator antennas, and 2D leaky-wave antennas as reported in the literature. In connection to the terminology of RCA configuration, their names are associated with the structure of a PRS superstrate and the methods and models used in the theoretical analysis. The theoretical analysis in [106] and [189] has been characterised with the various PRS structures consisting of the multilayer dielectric materials, patch arrays and periodic apertures, and the periodic metallic strips or rod gratings as shown in Fig. 5.1.

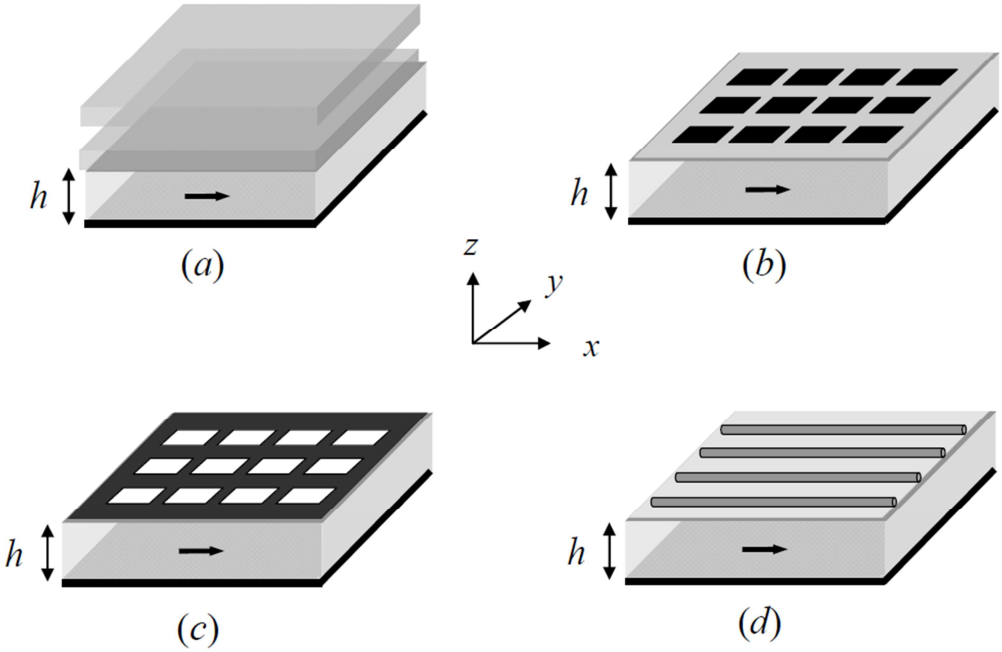

Figure 5.1: Configurations of the resonant cavity antenna [186].

The theory for a RCA configuration is based on various fundamental approaches including the ray-optic tracking method based on a phase interaction between infinite-size reflectors. Also, the transmission line model or the transverse equivalent network (TEN) is associated with the leaky-wave propagation. The electromagnetic bandgap (EBG) analysis is based on the characteristics of the wave propagation and interaction through a layered medium interface of two different media assisted with the Fresnel equations. However, most of them are related to the cavity distance and also the phase interaction. In this thesis, the theoretical details are briefly explained in terms of the physical parameters and the radiation characteristics.

In the original RCA work [106], various metal based a PRS structures were incorporated with the conducting ground plane that was excited by an open-end waveguide as a primary source. The key operational behaviour and parameters were studied using reflection coefficients.

The two factors associated with the RCA operation are a phase interaction determining a resonance condition of the cavity structure in that the reflection magnitude affects antenna directivity. In behaviour, the appearance of the multi-ray inside a cavity structure is shown in Fig. 5.2. In the ray theory, the multi-reflection is caused in between at the internal surfaces of a ground plane and a PRS surface. As it is generally known, the total reflective surface as a ground plane gives the unity magnitude and the phase response of 180° or π. Hence, the term of the electric field can be expressed as [106],

$$E = \sum_{n=0}^{\infty}\left\{F(\alpha)\cdot E_o \Gamma^n \sqrt{1-\Gamma^2 e^{j\Theta_n}}\right\} \tag{5.1}$$

where $F(\alpha)$ is a radiation pattern of the primary source, Θ_n is a phase difference, and $\Gamma e^{j\theta_{PRS}}$ is a reflection coefficient. The phase difference between the rays can be determined by

$$\Theta_n = n\beta = n\left(-\frac{4\pi}{\lambda} l cos\delta - \pi + 2\theta_{\mathrm{PRS}}\right) \tag{5.2}$$

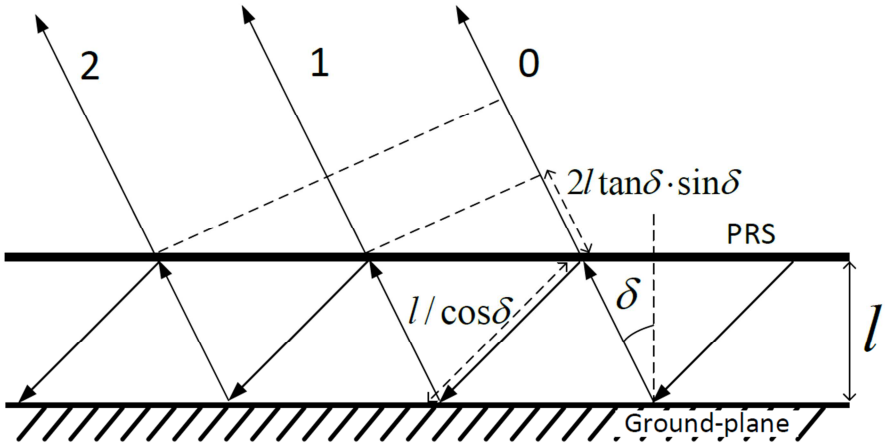

Figure 5.2: Behaviour of multi-reflection and transmission in the resonant cavity antenna.

The magnitude of reflection can be considered for $\Gamma < 1$ that can lead to the modification for a summation of the multi-reflection as

$$\sum_{n=0}^{\infty}\left(\Gamma e^{j\beta}\right)^n = \frac{1}{1-\Gamma e^{j\beta}} \tag{5.3}$$

Therefore, the electric field in (5.1) can be rewritten as

$$|E| = |E_o| F(\alpha)\sqrt{\frac{1-\Gamma^2}{1+\Gamma^2-2\Gamma cos\beta}} \tag{5.4}$$

The transmitted power is formed by the collective interference of the rays. Hence, the power of the radiation pattern is given by

$$P(\alpha) = \frac{1-\Gamma^2}{1+\Gamma^2-2\Gamma cos\left(\theta_{PRS}-\pi-\frac{4\pi}{\lambda}lcos\delta\right)}(F(\alpha))^2 \quad (5.5)$$

The maximum power can be obtained as an angle of the incidence is $\delta = 0°$

$$\theta_{PRS} + \pi - \frac{4\pi}{\lambda}l = 2N\pi \quad (5.6)$$

where N= 0, 1, 2, 3, etc. As known in the collective interference, the interaction of the phase response occurs at the in-phase condition. At the target frequency or wavelength (λ_o), the resonance distance (l_r) can be determined as

$$l_r = \left(\frac{\theta_{PRS}}{\pi} - 1\right)\frac{\lambda_o}{4} + N\frac{\lambda_o}{2} \quad (5.7)$$

In order to improve the antenna performance, the enhancement of a radiation gain is connected with the reflection magnitude. Therefore, the maximum power of a cavity structure can be approximated as

$$G = \frac{1+|\Gamma|}{1-|\Gamma|} \quad (5.8)$$

In addition, the operational bandwidth (B) relating to the frequency range which depends on a cavity distance. The term of the radiation bandwidth can be obtained by

$$B = \frac{\lambda}{2\pi L_r}\frac{1-\Gamma}{\sqrt{\Gamma}} \quad (5.9)$$

It is seen that the potential parameter is based on the reflection coefficient of a PRS structure. In practice, the 2D periodic plane referred to as a frequency selective surface (FSS) is suitable for designing a PRS structure due to the flexibility in tailoring of the reflection coefficient. Also, the beneficial factor of the FSS structure is that it can be produced on any substrate thickness only by the availability of the dielectric materials.

5.3 Resonant cavity antenna with Fano-resonance metamaterial superstrate

In the study of the Fano-resonance metamaterials in Chapter 3, the transmission and reflection resonances based on two identical patch arrays were discovered which are associated with the extraordinary transmission. The employment of the Fano-resonance metamaterials in a resonant cavity antenna (RCA) is a new design concept in the enhancement of the radiation bandwidth. Fig. 5.3 shows a schematic of the broadband resonant cavity antenna which is formed by a planar parallel structure between the Fano-resonance metamaterial superstrate with the PEC ground-plane, and the source antenna positioned inside the cavity. With the resonant transmission of the Fano-resonance metamaterials, there are two advantages in the RCA design consisting of (1)

the behaviour of zero-order transmittance and (2) the π-phase shifting of the reflection coefficient as discrete phase behaviour. The antenna mechanism depends on two conditions of the radiative Fano effect and the Fabry-Perot approach that are involved in the design method. In this chapter, the characteristics of the radiation behaviour are investigated based on a cavity resonance distance (height), the interaction with the actual source antenna, and the superstrate size of the RCA configuration.

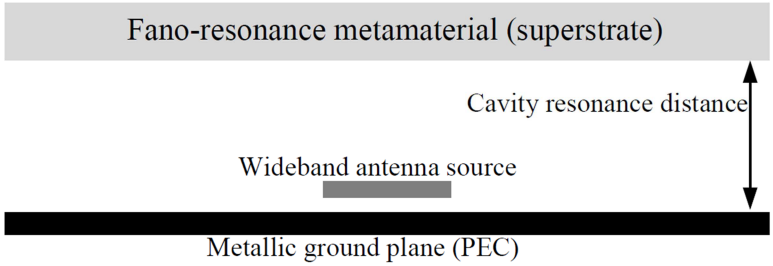

Figure 5.3: Scheme of the resonant cavity antenna consisting of the Fano-resonance metamaterial superstrate

The radiation bandwidth of an RCA is determined by two characteristics. The first characteristic is two cavity modes based on the Fabry-Perot effect that creates a double band and this leads to a lower and upper bound of the radiation bandwidth. The second characteristic is an inherently radiative mode of the Fano effect of the two-layer metamaterial at the middle band. The effect of the relative finite size of a patch array can influence the resonant transmission when the two-layer metamaterial interacts with the actual radiation of a source antenna. Therefore, the design methodology can be divided into three steps to complete the RCA configuration.

- Firstly, the two-layer metamaterial is investigated by dealing with the reflection in terms of the period and the patch length in a lattice structure. The resonant Fano transmission with the radiation-enhanced property is characterised at the desirable frequency. The characteristics of the Q factor are also observed in the context of the dielectric thickness between two patch arrays. The study of the two-layer metamaterial will be described in section 5.4.

- Secondly, the cavity structure is arranged by using a couple of the two-layer metamaterials to study the Fabry-Perot effect. The resonant distance (height) of an air space between two two-layer metamaterials is determined. This geometry plays a

significant role in the radiation bandwidth. An electromagnetic mirror in the image theory is used to study the cavity effect in transmission at a plane wave. A PEC surface as an equivalent image is placed to form a resonant cavity antenna. The characteristics of the radiation bandwidth and the resonance condition will be discussed in section 5.5

- Finally, the source antenna, the CPW-fed aperture-coupled patch, is incorporated into the RCA configuration. In order to deal with the spherical wave front of the actual source antenna, the cavity distance is varied and optimised for a good response of correspondence between the radiation and impedance bandwidth over a desirable frequency range. The edge effect in the RCA structure is also controlled by optimising a finite size of the two-layer metamaterial. In addition, the characteristics of the surface current on the patch array and the electric field distribution in a cavity space are observed by studying the radiation behaviour in a variation of the superstrate size. The design details will be described in section 5.6 and 5.7

5.4 Two-layer metamaterials

The two-layer metamaterial design studied in Chapter 3 is applied to the RCA device as a superstrate. However, the periodic spacing of the patch arrays is a quarter wavelengths which are found to provide suitable characteristics for development of broadband RCA devices. The characteristics of the PRS design differ from the previous work that exhibits the positive reflection-phase gradient for wideband operation of a RCA device [6-10,120,128,129].

5.4.1 Physical structures

Fig. 5.4 shows the schematic illustration of the two-layer metamaterials that consists of a pair of periodic surfaces with the identical patch arrays. The properties of the dielectric material consist of the electric permittivity (ε_r) and magnetic permeability (μ_r). The thickness of the dielectric medium is referred to as Hr. The period of the patch array is denoted by P and the edge dimension of the square patch is L. Two dielectric materials are considered to study the cases of a lossless cavity medium (air) and a lossy material (FR4), respectively. The effect of the field interference can influence the cavity medium to create the resonance process as described in Chapter 3.

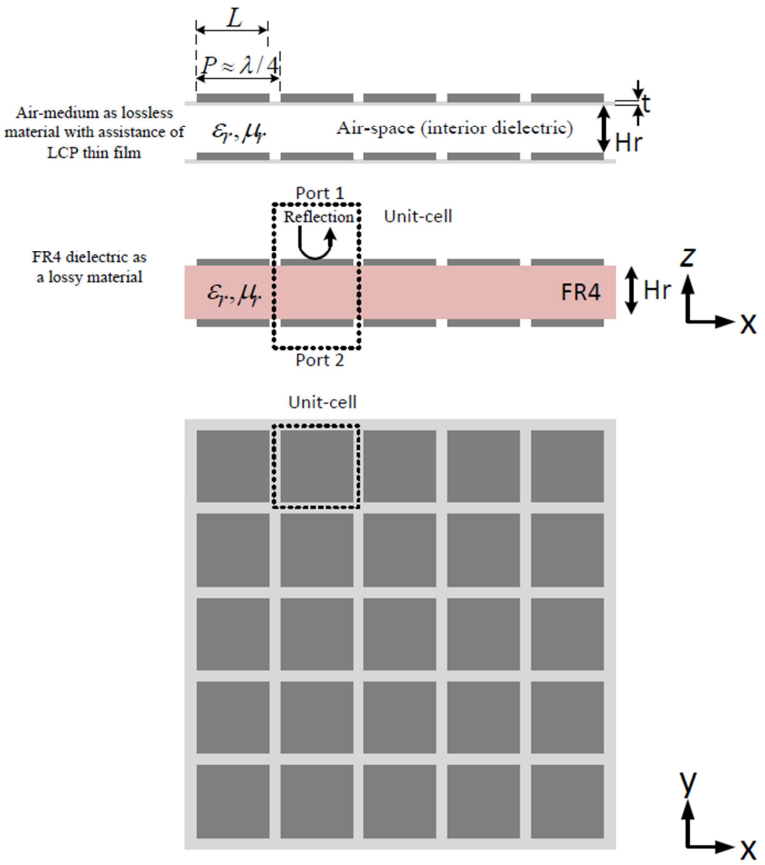

Figure 5.4: Geometry of the two-layer metamaterials with a pair of identical patch arrays separated by a dielectric medium (air and FR4).

As shown in Chapter 3, the investigation can be carried out using the Ansoft^{TM} HFSS simulation tool which is based on a full-wave electromagnetic analysis assisted with the finite element method. The unit-cell is positioned in a boundary box which is defined by the infinitive condition of the Floquet theory. The plane-wave excitation is applied to port 1 at the top the boundary box and the transmitted signal is monitored at port 2 at the bottom of the boundary box. The details of the simulation method have been provided in Appendix A. The analysis of the characteristics of wave propagation and interaction is conducted in terms of transmission and reflection responses. The scattering process of the incident field interacted with the interface of a unit-cell is considered in both phase and magnitude.

The related phase change and the scattering parameters of the patch array are considered in order to understand the effect on the response of the metamaterial superstrate. The characteristics on the Q factor are investigated due to the interest in resonant bandwidth. The period of the square patch array is a quarter wavelength which is optimised to obtain the resonant transmission as a relevant parameter.

With the optimisation of the metamaterial structure, the characteristic of the reflection phase of the periodic surface is tailored by the physical length of square patch elements. Hence, the air based dielectric medium is firstly considered in the metamaterial structure due to the flexibility in control of the thickness through fabrication. In practice, the actual air-medium structure is produced using a micromachined polymer rim. Also, the arrangement of a metallic patch array is patterned on the LCP thin-film with the thickness of 100 μm (t). The effect of the thin-film substrate is considered as a part of the dielectric medium. However, the thickness of the LCP film is an extremely small compared to the separation between two arrays for investigation ($t \ll Hr$). Therefore, the effective permittivity of a dielectric medium can be approximated to be that of an air. The operation at the target frequency of 10 GHz results in the guided wavelength of 30 mm, the periodic spacing in array is specified as 7 mm approximately a quarter wavelength. To study the effect of separation or spacing between the periodic patch layers, five values of the separation are used ranging from 1 mm to 5 mm corresponding to a range between 0.03λ–0.16λ within an interfacial near-field zone. The path length phase response in between the two-layer structure and the reflection phase of the one-layer patch array are obtained at 10 GHz and summarised in Table 5.1.

Table 5.1: Patch lengths related phase and reflection phase for difference spacer thickness at 10 GHz. The period of the patch arrays is 7 mm.

Hr (mm)	$\Delta\phi$	φ_{PRS} @10 GHz	L (mm)
1	12°	-168°	6.95
2	24°	-156°	6.77
3	36°	-144°	6.45
4	48°	-132°	6.0
5	60°	-120°	5.3

5.4.2 Characteristics of the two-layer metamaterials

The investigation of the resonance effect of the two-layer metamaterials is performed by electromagnetic simulation. The unit-cell element is modelled and defined as before (Fig. 5.4). The electromagnetic behaviours are studied for both of the one-layer and two-layer configurations.

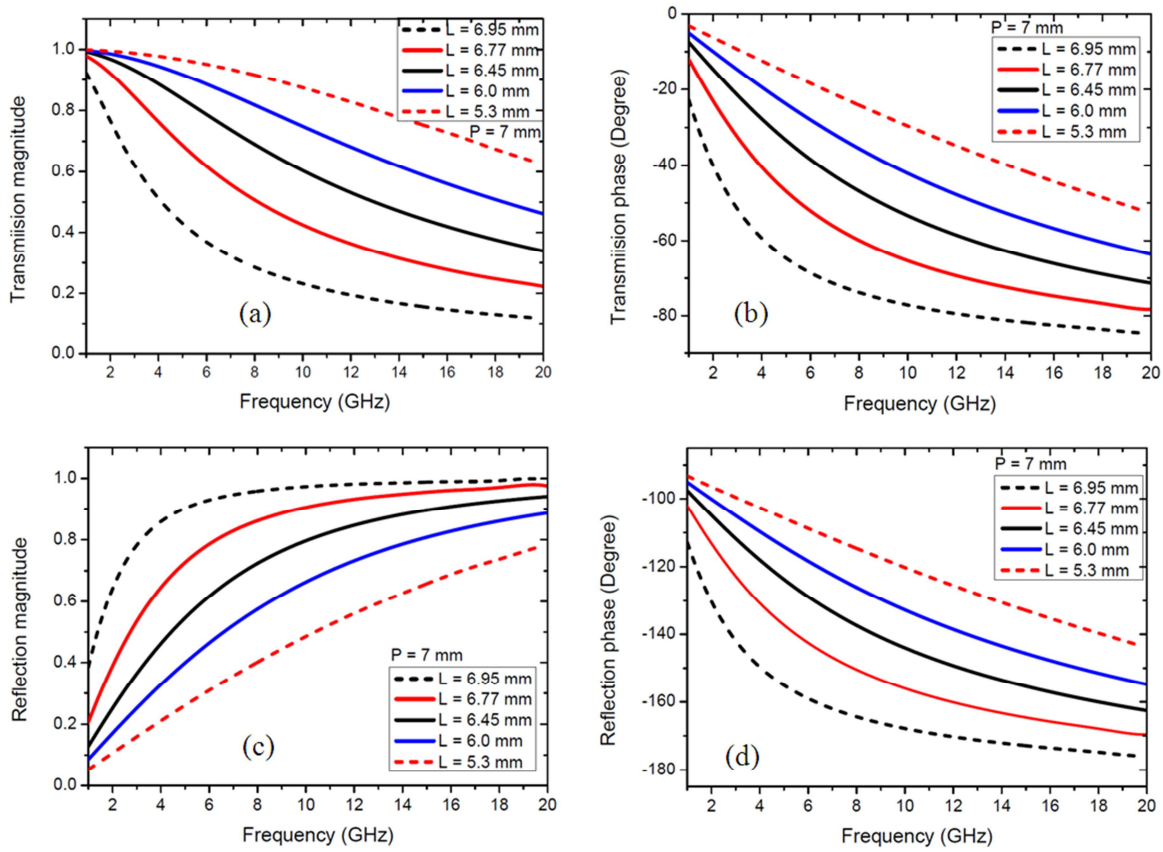

Figure 5.5: Simulation results for a single patch array design, (a) transmission magnitude, (b) transmission phase, (c) reflection magnitude, and (d) reflection phase.

Fig. 5.5 shows the simulation results of the transmission and reflection coefficients for the single-layer patch array. The period of the array is maintained as 7 mm. The different lengths of the square patch elements are 6.95 mm, 6.77 mm, 6.45 mm, 6.0 mm, and 5.3 mm. All responses of the transmission magnitude give similar attributes but it is higher when the patch is larger connecting to a smaller array separation. The reflection responses are in opposite and the reflection magnitude is greater for the array with larger patches. The phase changes on the reflection of the patch array at 10 GHz correspond to the values in Table 5.1. The reflection magnitudes from the largest patch to the smallest one are 0.97, 0.91, 0.8, 0.66, and 0.49. The phase difference between the transmission and reflection is obtained to be around 90°.

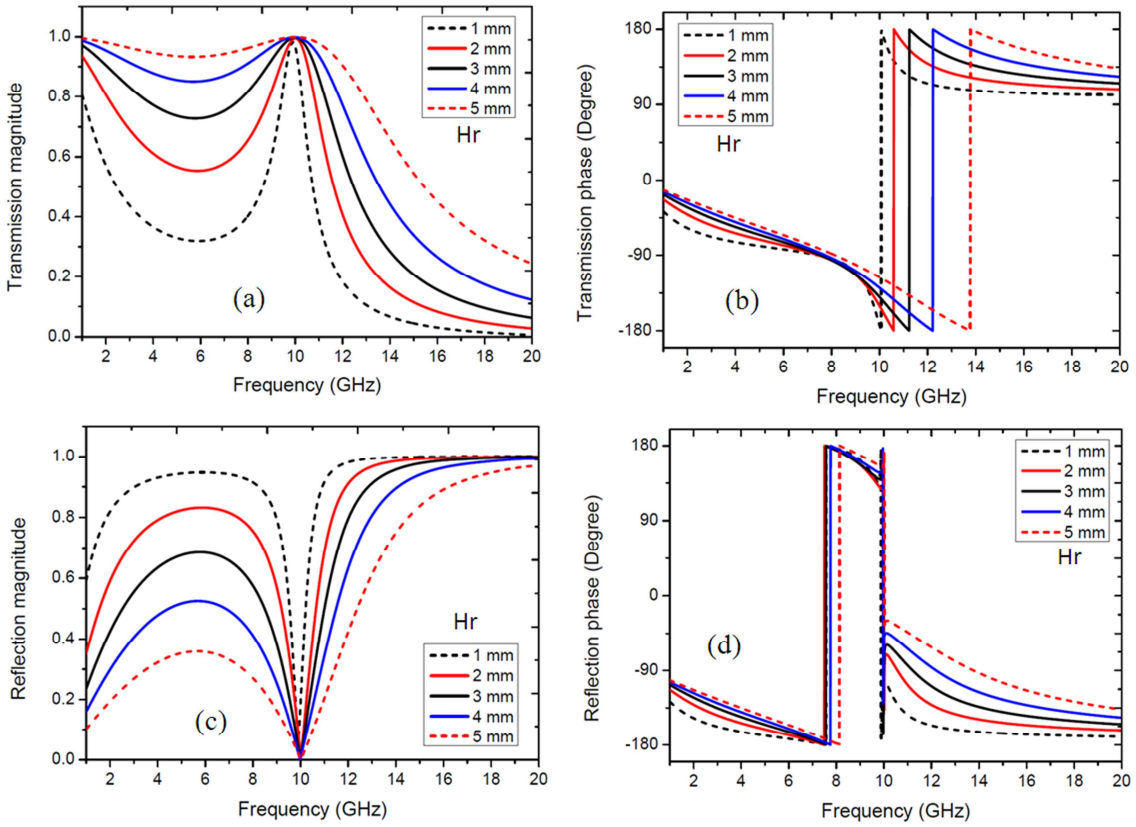

Figure 5.6: Simulation results for a two-layer patch array design, (a) transmission magnitude, (b) transmission phase, (c) reflection magnitude, and (d) reflection phase.

The same study is repeated for the two-layer configuration with the same patch-array characteristics. Fig. 5.6 shows the simulation results of the characteristics of the transmission and reflection coefficients of the two-layer metamaterials. The corresponding values of spacing between the two arrays are 1 mm, 2 mm, 3 mm, 4 mm, and 5 mm for patch length of 6.95 mm, 6.77 mm, 6.45 mm, 6.0 mm, and 5.3 mm. The results illustrate the magnitude and phase responses which show the resonance effect. The resonant frequency is the same all at 10 GHz as designed. It is shown that the phase change in reflection at the transmission peak is 180°. Also, the behaviour of the pole reflection phases at ~8 GHz behaves as a conventional PRS.

It can be seen that the strength of the resonance reduces as a separation between the two arrays increases due to the effect of reduced electromagnetic coupling as have been shown in Chapter 3. The Q factor of the resonance is also influenced by the reflection magnitudes from the two interfaces, the Q factor can be determined as [42]

$$Q = 2\pi \frac{Hr}{\lambda} \frac{\sqrt{\rho_1 \rho_2}}{(1-\rho_1 \rho_2)} \tag{5.11}$$

Since the two patch arrays are identical and, therefore, reflection magnitudes are the same and equation (5.11) can be rewritten as

$$Q = 2\pi \frac{Hr}{\lambda} \frac{\rho}{(1-\rho^2)} \tag{5.12}$$

5.5 Design and modelling of two-layer metamaterials for antenna applications

In this section, the properties of the two-layer metamaterial designs are studied for use as a superstrate for broadband resonant cavity antenna applications. The study is carried out using the image theory [151]. In accordance to the mechanism of the actual RCA configuration, the partially reflective surface (PRS) forms a cavity with the total reflective metal surface as a perfect electric conductor (PEC) at a specific resonance distance. The PEC interface is an electromagnetic mirror with which the equivalent object of the two-layer metamaterial appears at the same distance from the PEC in the electromagnetic image theory. This configuration can be considered in the same way as an electromagnetic band-gap (EBG) structure. In order to determine the transmission response, a plane wave source was excited in the cavity by the two-port configuration and the passband is determined to indicate the capability of the radiation bandwidth.

Fig. 5.7 shows the schematics of the cavity configuration based on image approach and the associated unit-cell which has a spacing of $2H_c$ between two objects of the two-layer metamaterials and its image. The excitations, as presented by Port 1 and Port 2, are installed at the top and the bottom boundaries of a unit-cell box. Based on the electromagnetic image theory, the perfect metallic surface is also applied to the unit cell and placed in the middle of the distance, $2H_c$, between two two-layer metamaterials.

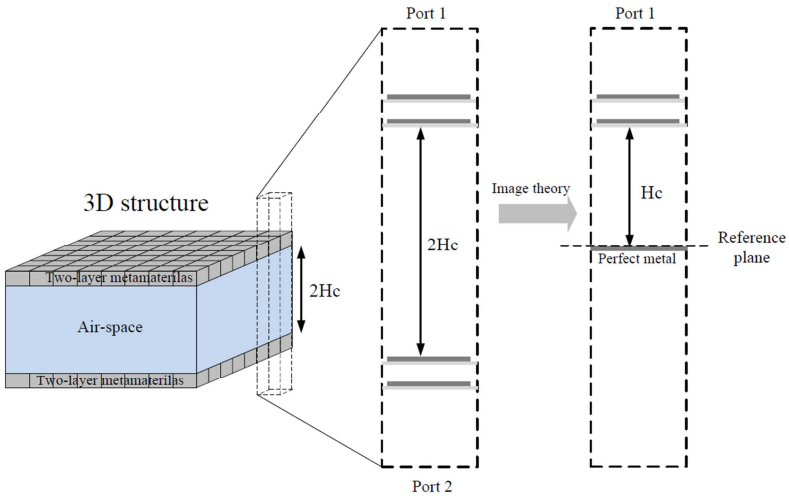

Figure 5.7: Configurations of the cavity structure and unite cell for analysis of antenna application based on image theory.

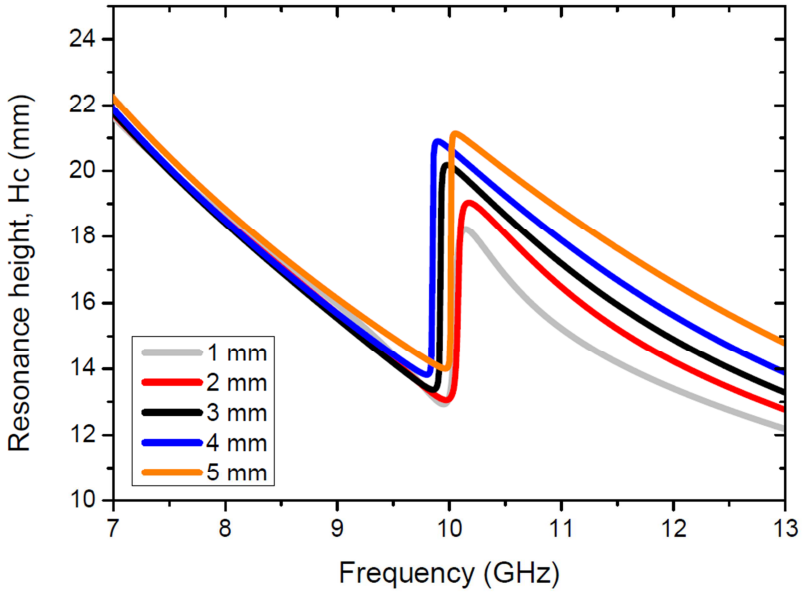

Figure 5.8: Calculated results for the resonance distance of the cavity for different thicknesses of the air spacer of the metamaterial superstrate.

For a given wavelength, λ_0, the minimum cavity height, H_c, for cavity resonance can be determined from the cavity resonance condition expressed in equation (5.6) as $H_c = l$ to be

$$H_c = \frac{\lambda_o}{4}\left(\frac{\varphi_m}{\pi} + 1\right) \tag{5.13}$$

where φ_m is a phase change in reflection from the metamaterial PRS. Based on the results of the studies of the two-layer metamaterials in the previous section, H_c can be obtained for a wavelength or frequency range of interest which in this work the

frequency range is between 8 GHz and 12 GHz. Fig. 5.8 shows the results of calculation of the cavity distance (H_c) at resonance based on equation (5.13) for the metamaterial PRS with five different values of H_r. The sharp change at 10 GHz is associated with the resonant behaviour of the two-layer metamaterial superstrate that the term φ_m expresses the phase shift of 180° in all designs. The resonance heights beyond 10 GHz are different due to the dependence of the reflection phase of the superstrate on the thicknesses (Hr) of the two-layer metamaterials. It can be seen that the value of H_c can be in the range of 13–21 mm over the frequency range. For broadband RCA applications, the suitable value for H_c is determined in the study of the radiation characteristics in RCA synthesis work described in section 5.6.

Fig. 5.9 illustrates the characteristics of the transmission response of the cavity configuration for three different thicknesses of H_r, the unit-cell was shown in Fig. 5.7. The two cases of the thicknesses of H_r of 1 mm and 5 mm are not included due to the narrow resonance bandwidth and less reflection magnitude, respectively, as stated in previous sections. The three PRS designs corresponding to the Hr values of 2 mm, 3 mm, and 4 mm were selected for study based on large bandwidth of the passband with the ripple resonance behaviour. The transmission responses are investigated for the Hc values between 15 mm and 20 mm. It can be seen in Fig. 5.9 that there are three peaks in the passband over the frequency range of 7 GHz and 12 GHz. As Hc increases the passband shifts to the lower frequency side. This effect is due to the increase in the path length related cavity phase change. It is evident that the middle resonant frequency of the cavity maintains at the frequency of 10 GHz which is caused by the intrinsic resonant transmission in the two-layer metamaterials without any effect of the cavity distance.

The ripple behaviour in transmission has a strong dependence on the cavity distance (height) for a given value of Hc. The ripple effect is the smallest at the cavity height of 16 mm, 17 mm, and 18 mm in Fig. 5.9 (a), (b) and (c), respectively. The results in Fig. 5.9 also show that the ripple is larger when the value of Hr is smaller. This is due to the strong dependence of the reflection magnitude on Hr as shown in Fig. 5.5. A higher Q factors result in strong interference in the cavity leading to the stronger ripple effect as shown Fig. 5.9 (a). Since low ripple effect is desirable for superstrate application in RCA devices, therefore, the two-layer metamaterial with the air spacer thickness of 4 mm between patch arrays is selected for RCA synthesis work.

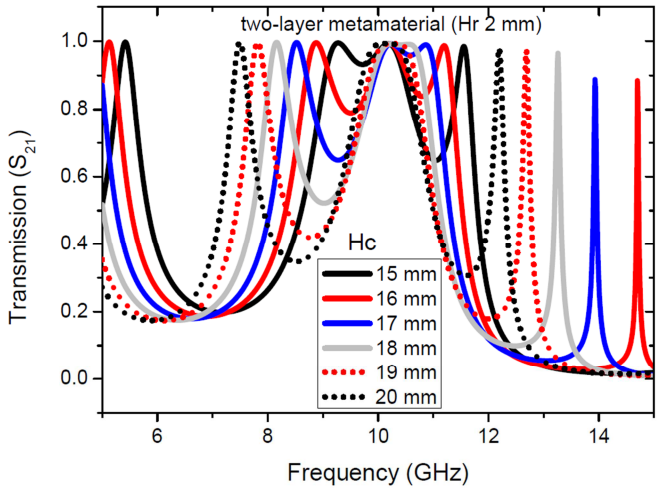

(a)

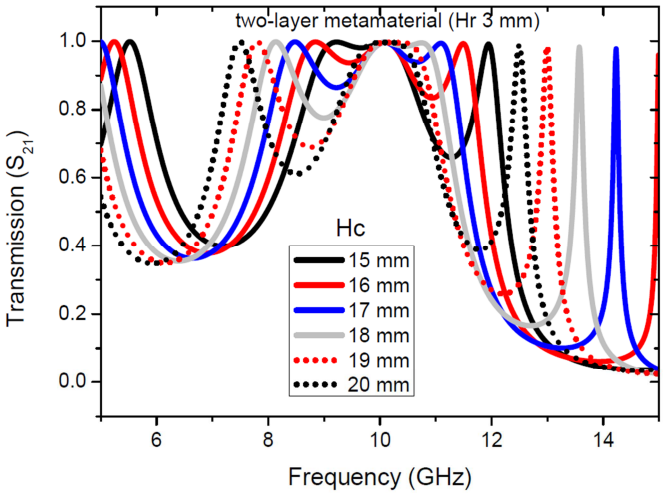

(b)

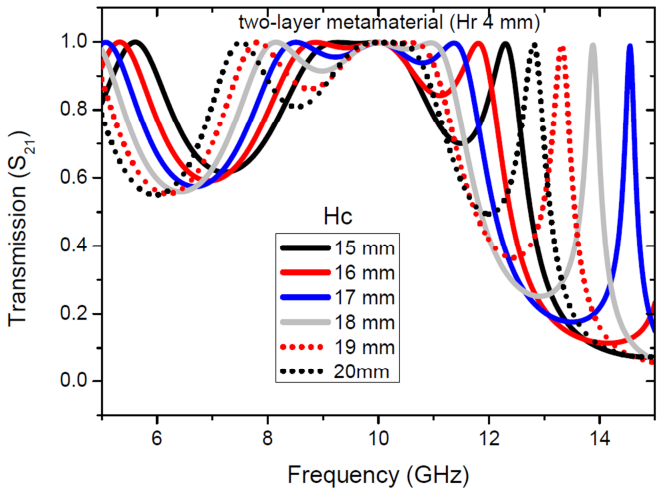

(c)

Figure 5.9: Simulation results for the transmission response of the resonant cavity for Hc values in applying the two-layer metamaterials with Hr values of, (a) 2 mm, (b) 3 mm, and (c) 4 mm.

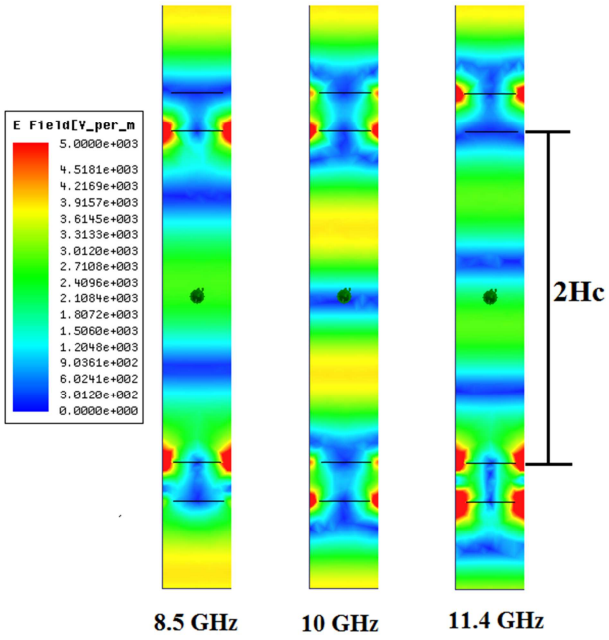

Figure 5.10: Simulation results for the electric field distribution in a cavity structure at frequencies of the transmission peaks at 8.5 GHz, 10 GHz, and 11.4 GHz (all in the same scale).

Figure 5.10 illustrates the characteristics of the electric field distribution inside a unit cell of the cavity structure in order to understand the radiation mechanism. The electric field distribution is observed at the peak frequencies of the transmission response as shown in Fig. 5.9(c) with the distance (Hc) of 17 mm. The air cavity spacing is then 34 mm between two two-layer metamaterials. As a result, three peaks appear over a desirable transmission band consisting of 8.5 GHz, 10 GHz, and 11.4 GHz. The electric field behaviour based on the Fabry-Perot effect illustrates a lower and higher cavity mode at the frequencies of 8.5 GHz and 11.4 GHz, respectively. The electromagnetic image approach can deal with the attribute of the resonant transmission of the two-layer metamaterials performed at the frequency of 10 GHz. The zero electric-field position is at the middle of the cavity since it is the creation of PEC plane.

5.6 Broadband resonant cavity antennas

5.6.1 Design of RCA configurations

The configuration of the RCA in this work is described. The RCA device is based on the combination of the wideband aperture-couple patch antenna investigated in Chapter 4 as a primary source and the two-layer metamaterial as a superstrate as discussed in the

previous sections. Fig. 5.11 shows the geometric structure of the resonant cavity antenna in top and cross-sectional views. As shown in Chapter 4, the short-end CPW and the aperture-coupled structure are surrounded by the ground plane with a suspended patch above the aperture. The cavity height, denoted by Hc, is a separation between the ground plane of the patch antenna and the bottom surface of the metamaterial superstrate. The design details of the source antenna were provided in Chapter 4. The separation between two patch arrays of the air-based superstrate is denoted by Hr. Table 5.2 provides a summary of the dimensions of the wideband aperture-coupled patch antenna and the metamaterial superstrate. The properties of the dielectric materials (LCP, FR4, and PMMA) using in the RCA device in terms of electric permittivity and loss tangent are listed in Table 4.2. In the initial design the finite array size of the two-layer metamaterial is specified to be 5x5 patches with a period of 7 mm (35x35 mm^2) which the corresponding dimension is wavelength at 10 GHz (30 mm) are 1.16λx1.16λ.

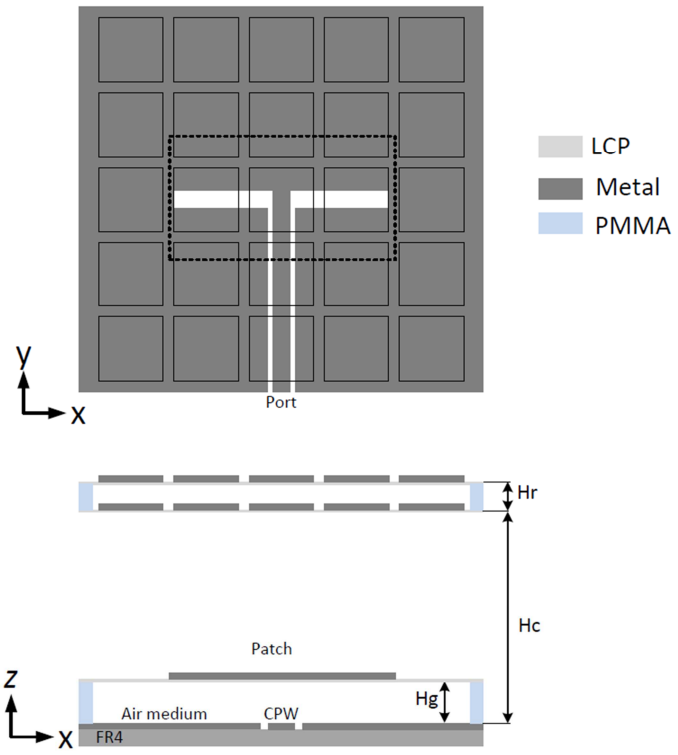

Figure 5.11: Geometry of the physical structure of the RCA configuration with the air spacer based metamaterial superstrate.

Table 5.2: Dimensions of the aperture-couple patch antenna in millimetres.

Lp	Wp	Ls	Ws	Wf	G	Hg	Hr	P	L
10	20	7.8	1.0	1.4	0.2	3	4	7	6

The characteristics of impedance and radiation behaviour are studied for bandwidth enhancement. The electromagnetic characteristics of the RCA configuration are obtained using the Ansoft^{TM} HFSS based on the method described in section 4.4.3. The characteristics of the current distribution and the far-field radiation are observed for the RCA antenna. This aim is to achieve high directivity and wide radiation bandwidth. The optimisation of an antenna configuration is also considered in terms of broad, low ripple bandwidth.

Fig. 5.12 shows the results the reflection coefficients of the RCA configuration for the cavity height (H_c) of 17 mm, 18 mm, 19 mm, and 20 mm. In comparison, the characteristics all show a similar impedance bandwidth, but there is difference in the strengths of the resonant dips. All of the characteristics have four resonance dips over the frequency range of 7 GHz and 13 GHz. The multiple resonances produce a broad impedance bandwidth (-10 dB) that is in exceed of 45% around the middle frequency of 10 GHz. The impedance bandwidth is largely the same as that of the source antenna and thus less affected by the appearance of the superstrate above it.

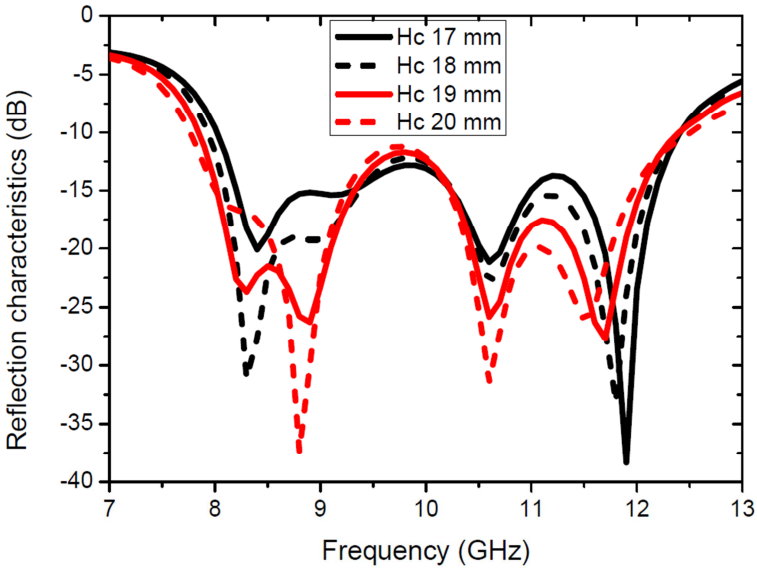

Figure 5.12: Simulation results for the reflection coefficients of the RCA configuration at different cavity heights.

Fig. 5.13 shows the simulation results of the characteristics of the broadside directivity as a function of the frequency for the different cavity heights. The highest directivity occurs at the frequency of ~10.5 GHz. The ripple behaviour is influenced by the locations of the three peaks. It is seen that the radiation bandwidth is between 8 and

12.5 GHz depending on the cavity height (H_c). Low ripple performance can be obtained over 8~12 GHz at the cavity height of 19 mm and 20 mm. The 1-dB-ripple bandwidth is around 45% at the middle band frequency of 10 GHz and the peak value of the directivity is 13.5 dBi. As expected the characteristics of the radiation bandwidth is similar to the impedance bandwidth with the multiple resonances as shown in Fig. 5.12. A cavity height of 20 mm is selected to form the RCA configuration due to the best bandwidth.

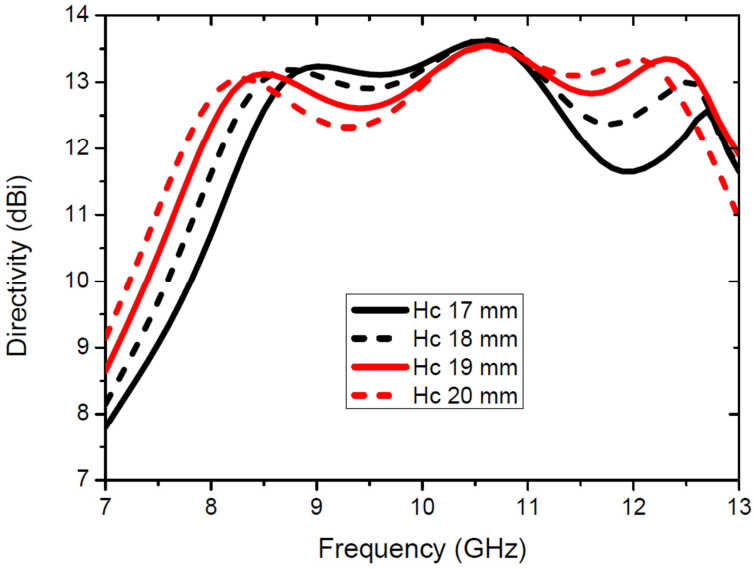

Figure 5.13: Simulation results for the antenna directivity of the RCA design.

Fig. 5.14 shows the simulation results of the characteristics of the far-field radiation patterns in H- and E-plane at the frequencies of 8 GHz, 9 GHz, 10 GHz, 11 GHz, and 12 GHz. The results show the directive characteristics with narrow beam behaviour at all of the observing frequencies. The angle widths of a HPBW are in a ranges from 34° to 40° (H-plane) and 24° to 40° (E-plane). In fact, the cavity height (H_c) in the RCA device is established for a resonant cavity at the operating frequency of ~8 GHz. This value is larger than that at the higher frequencies of a resonant cavity. In addition, the results of the strong side-lobes at the upper frequency of 12 GHz are found to be around 10 dBi and 8 dBi in the H- and E-plane, respectively. Also, the front-to-back ratios are around 13.5 dBi and 28.5 dBi at the frequencies of 9 GHz and 12 GHz, respectively.

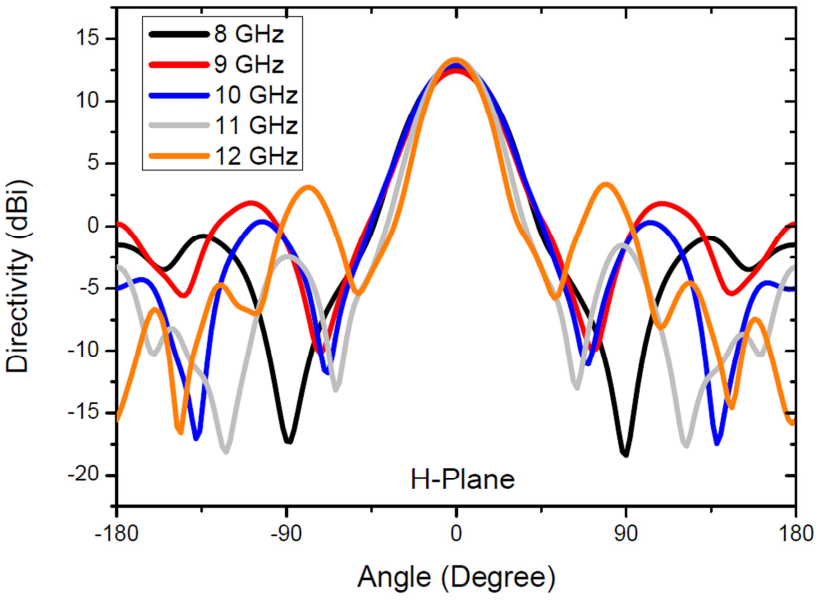

(a)

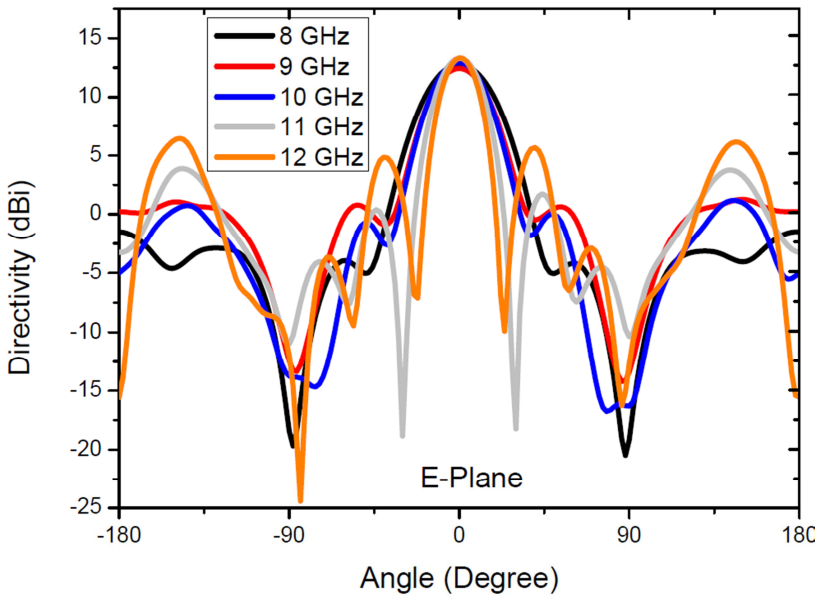

(b)

Figure 5.14: Simulation results for the radiation patterns of the RCA design at the frequencies of 8 GHz, 9 GHz, 10 GHz, 11 GHz, and 12 GHz, (a) H-plane and (b) E-plane.

5.6.2 Effect of the finite-size PRS

The geometric theory of diffraction (GTD) is considered in the study of a finite-size RCA device in terms of dimensions of the two-layer metamaterial superstrate. It was shown in Chapter 4 that the ground-plane size has a significant effect on the performance of a radiation element, an aperture in that case. In this section the effect of the superstrate size (radiation aperture) as defined by the array size of the periodic patch layer, is investigated. The term of the radiation aperture is referred to as the total dimensions (area) of the PRS.

As described in the previous study of the cavity structure in section 5.5, the unit-cell based modelling method was used assuming an infinite array size and the excitation was an incident plane wave. The diffraction effect of the RCA is caused by the interaction between the radiation from the actual source antenna and the finite-size metamaterial superstrate. It is shown that the radiation of the source antenna has a spherical wave-front which is different from the plane wave source used in the unit-cell based study. The effect of the physical dimensions is investigated in a variation of the array size in order to obtain good radiation bandwidth.

Fig. 5.15 shows the simulation results of the antenna directivity and the reflection characteristics in various sizes of the patch array consisting of 3x3, 4x4, 5x5, 6x6, 7x7, 8x8, and 9x9 of patch elements. The array sizes can affect the radiation bandwidth as shown in Fig. 5.15(a). The effect on the reflection coefficient have influenced on the impedance bandwidth since the lower and upper bounds of the -10 dB minimal band is maintained as shown in Fig. 5.15(b). The effect of the resonant transmission of the two-layer metamaterial is shown by the appearance of two bands especially in the cases of 3x3, 8x8, and 9x9 arrays in that two peaks are at the frequencies around 8 GHz and 11 GHz. For the other array size, the effect is less and thus wideband performance can be obtained. The best wideband performance is achieved from the 5x5 array based design. The small array size of 3x3 cells produces less enhancement in the directivity. A similar effect of the finite-size superstrate has also been reported in the previous RCA design based on a dielectric EBG superstrate [9, 114].

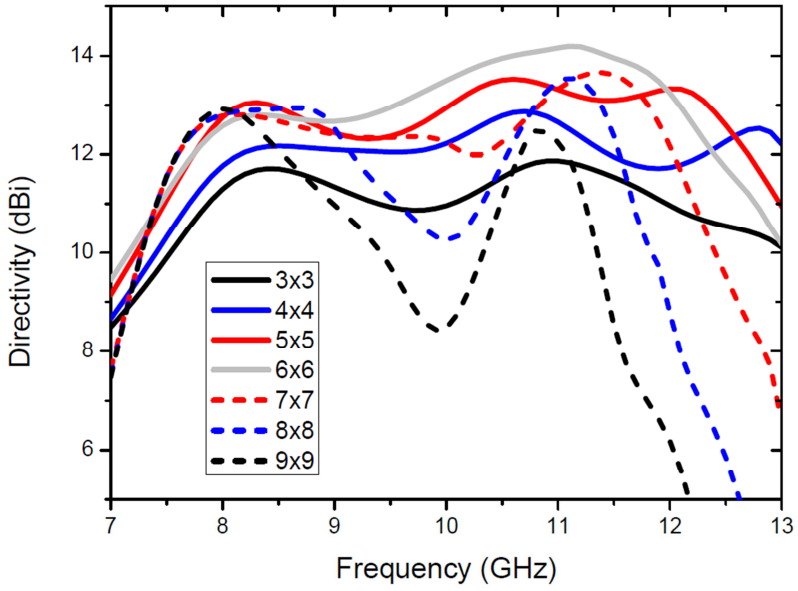

(a)

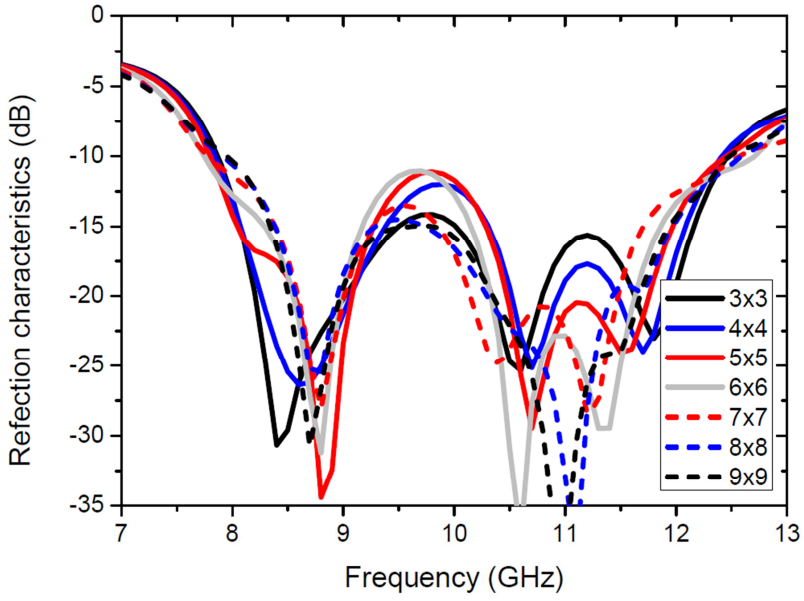

(b)

Figure 5.15: Comparison of (a) broadside directivity and (b) reflection characteristics of the RCA design for different patch arrays in the finite-size PRS.

The results of the study show that the finite-size PRS has a significant impact on the radiation behaviour of the RCA devices. Table 5.3 shows a summary of the dimensions of the finite-size superstrate which have been studied in RCA devices. The designs with 5x5 and 6x6 cell arrays provide good broadband performance corresponding to PRS dimensions of 1.2λ~1.4λ.

Table 5.3: Summary of the dimensions in comparison with a wavelength of 30 mm.

3x3	4x4	5x5	6x6	7x7	8x8	9x9
$21x21mm^2$	$28x28mm^2$	$35x35mm^2$	$42x42mm^2$	$49x49mm^2$	$562x56mm^2$	$63x63mm^2$
(0.7λx0.7λ)	(~0.9λx0.9λ)	(~1.2λx1.2λ)	(1.4λx1.4λ)	(~1.6λx1.6λ)	(~1.9λx1.9λ)	(2.1λx2.1λ)

In the leaky-wave analysis [190-192], it has been shown that the broadside radiation can be affected by the beam-splitting condition caused by the intrinsic characteristics of the PRS. This behaviour occurs when the frequency is beyond the region of the resonance frequency of a cavity. The radiation is unable to radiate in the broadside direction. It is shown that the resonant cavity is represented as a critical boundary for the maximum directivity or gain depending on the radiation aperture. The investigation in the finite-size PRS is carried out by studying the broadside characteristics and the radiation bandwidth for different sizes of the PRS structure.

Fig. 5.16 shows the radiation patterns in E- and H-plane for the different array sizes in the superstrate at 10 GHz. This is the frequency at which the dependence of the directivity on superstrate size is the most significant as shown in Fig. 5.15. The beam-splitting effect is associated with the edge effect. The behaviour is caused by the wave front pattern of the primary source. The majority of the beam plays a role only at the central area of the metamaterial superstrate. The variation of the finite-size arrays can illustrate the characteristics of the radiation pattern. As can be observed in the evolution of the side lobe behaviour for all array sizes, the side lobes become more significant in the case of the 7x7 or 9x9 in the superstrate while the directivity of the broadside beam becomes lower. The split beams in Fig. 5.16(a) for the 9x9 array size are in the directions of ±25° from broadside direction.

To understand the electric field distribution underlining the beam-splitting behaviour, the electric field distribution in the patches of the superstrate has been studied. Fig. 5.17 shows the results of the surface current distribution in three cases for PRS sizes of 5x5, 7x7, and 9x9 cell arrays at the frequency of 10 GHz. It is shown that the appearance of the strong and uniform surface current at the centre area of the patch array is similar in all cases. However, the weak distribution of the surface current is also observed in the outer surrounding area when the array size becomes large especially for 7x7 and 9x9 arrays. The non-uniform current distribution in the case of the 9x9 array causes the

beam-splitting effect in the radiation pattern. Therefore, consideration of finite-size superstrate is important in order to avoid the beam splitting effect.

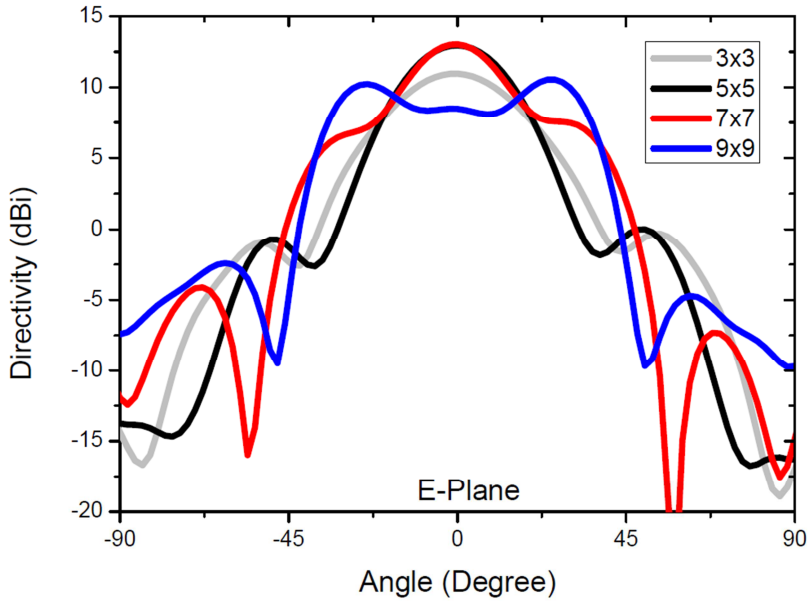

(a)

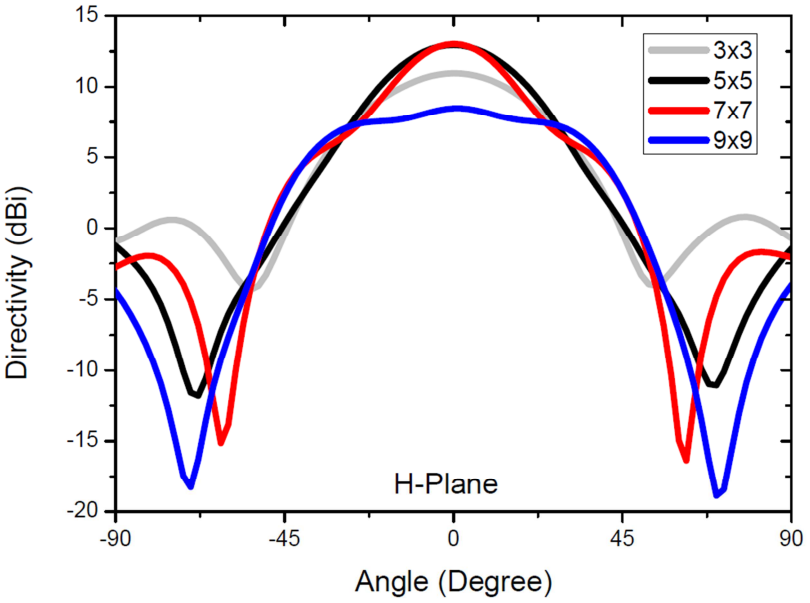

(b)

Figure 5.16: Radiation characteristics for (a) H-plane and (b) E-plane for finite-size PRS designs at 10 GHz.

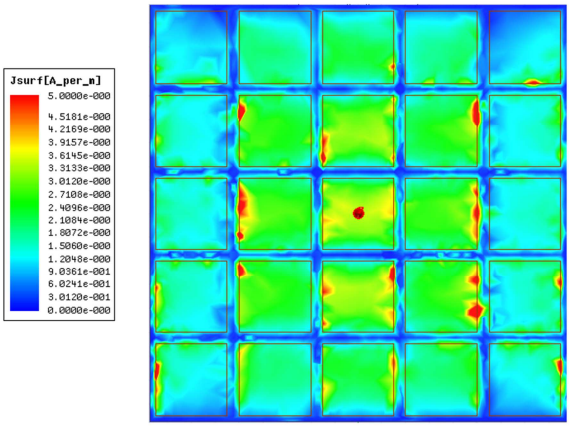

(a)

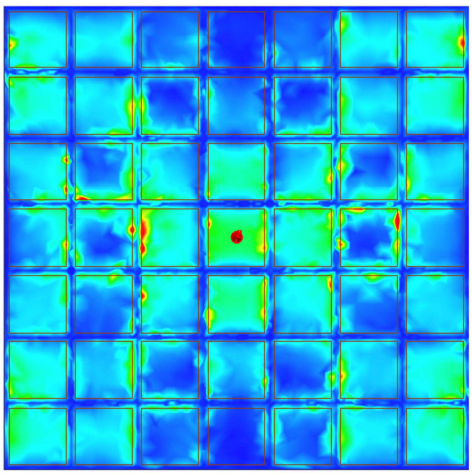

(b)

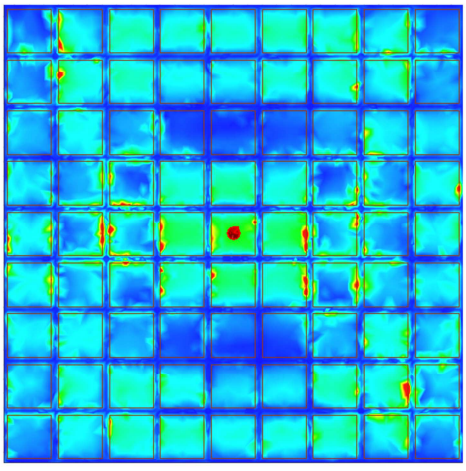

(c)

Figure 5.17: Simulation results for the surface current distribution on PRS in a variation of the patch array sizes, (a) 5x5, (b) 7x7, and (c) 9x9 (all in the same scale).

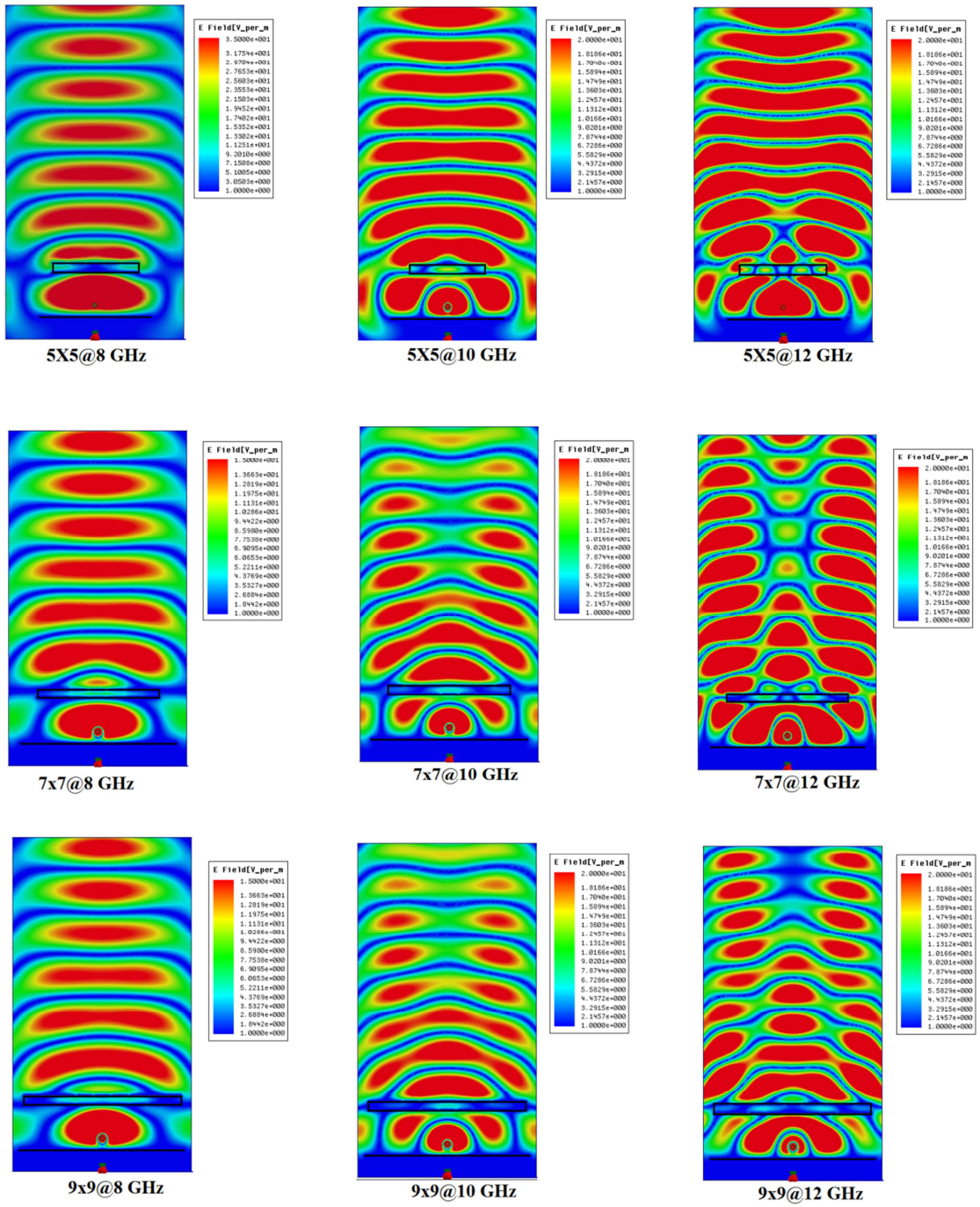

Figure 5.18: Simulation results for the electric field distribution in a variation of the array sizes of the superstrate at the observed frequencies of 8 GHz, 10 GHz, and 12 GHz.

In order to understand the beam splitting effect further, the electrical field distribution in the patch array in the cross-sectional view is studied using an electric line source to provide a primary field. Fig. 5.18 shows the results of electric field distribution for array sizes of 5x5, 7x7, and 9x9 at the selected frequencies of 8 GHz, 10 GHz, and 12 GHz. The field pattern is radiated as a spherical wave-front. In observation of the radiation characteristics, the field propagates to the broadside direction in all cases at the frequency of 8 GHz. Also for the 5x5 case, it also exhibits broadside radiation at other two frequencies of 10 GHz and 12 GHz, whereas in the case of 7x7 and 9x9 arrays, the field splits and propagates into two directions. Thus, this study confirms that the beam-splitting pattern is caused by the characteristics of the wave-front.

5.7 Resonant cavity antenna using FR4 based metamaterial superstrate

The applicability of the FR4-based metamaterial as a superstrate in the RCA device is investigated. The FR4 dielectric is a widely used material in microwave devices but is a lossy material in the frequency range (8–12 GHz) of interest in this work. The electric permittivity and the loss tangent are 4.1 and 0.02 over this frequency range. The effect on the characteristics of the radiation and impedance bandwidth is studied in the same way as in the previous sections for the air-spacer based two-layer metamaterial superstrate. In the subject of wideband operation, the property and thickness of the FR4 material are considered in the work. The patch arrays of the two layer metamaterial superstrate are on each side of an FR4 dielectric slab (substrate) arranged in mirror symmetry. In the investigation, the antenna performance is studied based on modelling and analysis of the impedance and radiation characteristics of the RCA device. The effect of finite superstrate size is also investigated.

Fig. 5.19 shows the physical configuration of the RCA device in the same structure as shown in Fig. 5.11 but an FR4 spacer is used in the metamaterial superstrate. In this design, a commercially available FR4 material is used and a thickness of 3.2 mm is obtained by combining two 1.6 mm thick FR4 slabs. The thickness is approximately equal to $0.2\lambda_g$, λ_g is the guided wavelength in FR4 at 10 GHz which is given by $\lambda_o/\sqrt{\varepsilon_r}$ and can be calculated to be 14.8 mm. Therefore, the path length related phase change as a single-layer patch in the FR4 spacer can be obtained to be ~77.8°. The array period and the square patch length are 6 mm and 4 mm, respectively. To obtain a good response for broadband performance, the finite-size PRS structure is determined to ~1.2λ x 1.2λ consisting of 6x6 patch cells.

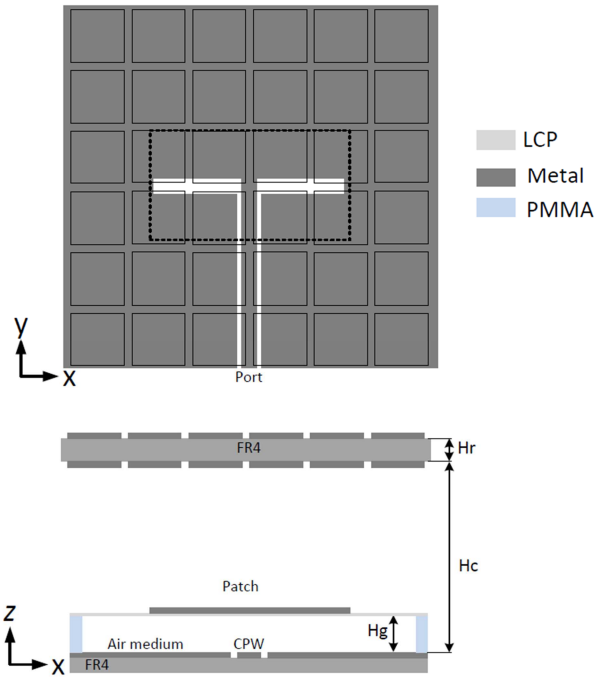

Figure 5.19: Geometry of a RCA configuration using a FR4 based metamaterial superstrate.

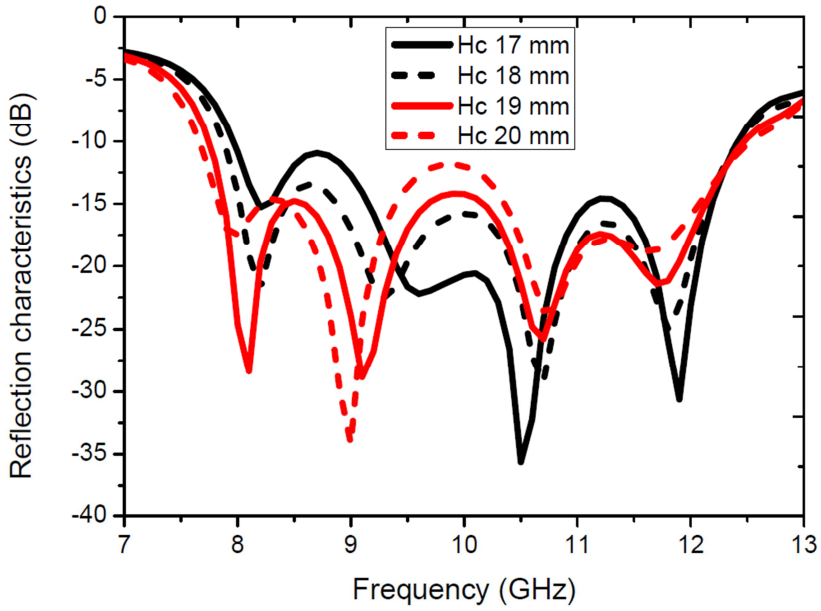

Figure 5.20: Simulation results for the reflection coefficients of the RCA configuration using FR4 based superstrate for different values of Hc.

Fig. 5.20 shows the simulation results of the reflection coefficients of the RCA device with the FR4-based superstrate for H_c values of 17 mm, 18 mm, 19 mm, and 20 mm. The characteristics of broadband impedance bandwidth show good matching. The impedance bandwidth is about 50% and is similar to that of the previous design incorporating the air spacer based metamaterial superstrate. The lower and upper frequencies of the -10 dB bandwidth are located at the frequency of 7.5 GHz and 12.5 GHz, respectively. It can be seen that the wideband performance results from the multi-resonance effect. The cavity resonance occurs at ~9 GHz.

Fig. 5.21 shows the simulation results of directivity of the broadside radiation of the RCA design for the FR4-based superstrate. The characteristics of the radiation are also investigated for the cavity height between 17 mm and 20 mm. A similar radiation bandwidth as that of the RCA configuration using the air spacer based superstrate is achieved. The middle frequency is still maintained at around 10 GHz. The flat-ripple attribute of the radiation characteristics shows that the best performance can be obtained for the cavity height of 19 mm. The 1-dB-ripple radiation bandwidth is about 50% covering the frequency range of 7.8~12.8 GHz and the maximum directivity is 13.5 dBi. It is seen that the behaviour of the broadband resonant cavity antenna can be obtained by using an FR4-based metamaterial superstrate.

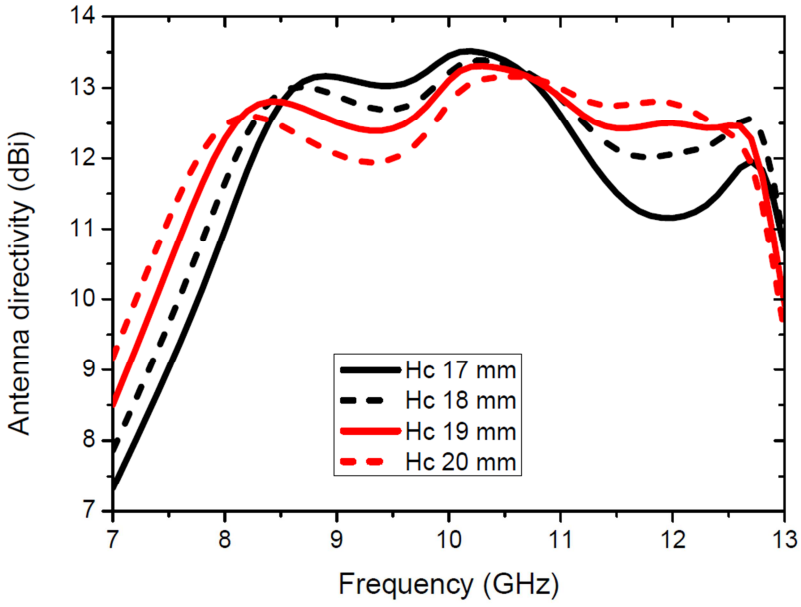

Figure 5.21: Simulation results for the antenna directivity of the RCA configuration using the FR4 based superstrate in a variation of the cavity height Hc.

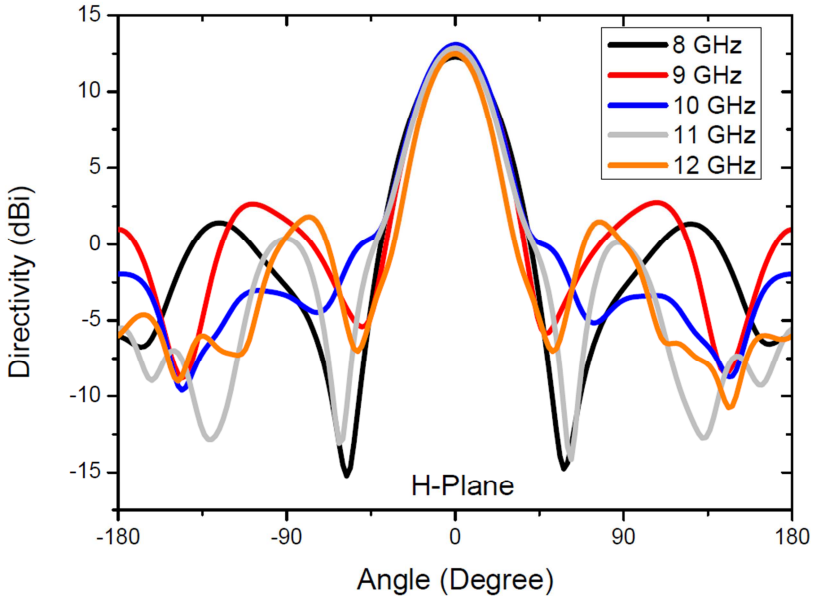

(a)

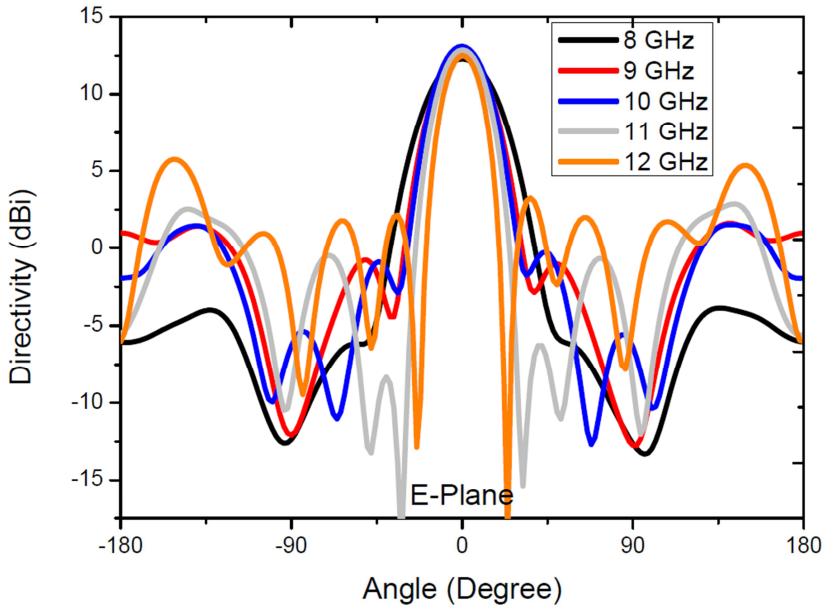

(b)

Figure 5.22: The radiation patterns of the RCA configuration using the FR4 based superstrate at the frequencies of 8 GH, 9 GHz, 10 GHz, 11 GHz, and 12 GHz, (a) H-plane and (b) E-plane.

Fig. 5.22 shows the simulation results of the radiation patterns of the RCA device with the FR4-based superstrate. The cavity height is 19 mm and the superstrate consists of an array of 6x6 cells. The results are obtained at the selected frequencies over the target band at 8 GHz, 9 GHz, 10 GHz, 11 GHz, and 12 GHz. High directivity and narrow beamwidth are obtained. The HPBW values of the H- and E-plane radiation are 30~36° and 20~36° over the frequency range of 8~12 GHz. The feature of the SLL is around 10 dBi. In comparison with the RCA device with the air-based superstrate in Fig. 5.14, the beams of the radiation pattern of using the RCA device with the FR4-based superstrate are narrower by around ~4°.

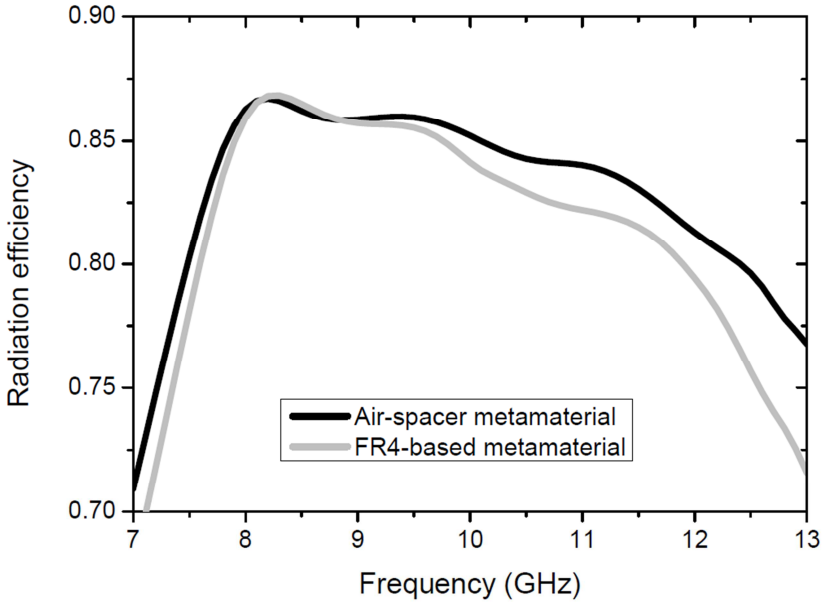

Figure 5.23: The radiation efficiency of the broadband RCA devices using the air spacer based metamaterial superstrate and FR4 based superstrate.

Fig. 5.23 shows the simulated results of the radiation efficiency of the RCA devices over the operation band for the air spacer and FR4 based metamaterial superstrates. Both RCA devices have the same patch antenna design as a primary source. As expected, the radiation efficiency is better for the RCA device with the air spacer based superstrate than the one with the FR4 based superstrate due to the dielectric loss in a FR4 material. This can result in the advantage of the air spacer based superstrate design over the choice of FR4 as a dielectric material in between two patch arrays in the metamaterial superstrate.

5.8 Fabrication of RCA devices

In this section, the development of fabrication and assembly methods for practical implementation of RCA devices are presented. The fabrication process is similar to that described in Chapter 3 and 4. However, additional processes were developed for assembly of the RCA devices. Fig. 5.24 shows a schematic illustration of the process steps on fabrication and assembly of two types of the RCA device, one incorporating the air spacer based metamaterial superstrate and another based on the FR4 based superstrate.

The process starts with the material preparation of the thin LCP film and FR4 substrates. After cleaning based on the method described in chapter 3, the copper layers were coated with a layer of AZ9260 positive photoresist with a thickness of 10 μm. After prebaking, UV exposure was applied to transform the design layout on the photomask into the AZ9260 film. The AZ9260 film was then developed to expose the regions of the copper layer by the wet etching in $FeCl_3$ based solution at room temperature. A copper patch array is obtained by removing the AZ9260 film. Since in both types of the superstrate, two arrays each on a separate substrate were required the fabrication process is repeated to produce the second array on another thin LCP film or FR4 substrate.

For the air spacer based superstrate design, the 4-mm-thick PMMA rim was fabricated using the laser micromachining method described in Chapter 4. In the assembly process of the metamaterial superstrate, the two LCP substrates were bonded to each side of the PMMA rim using the liquid SU8 as an adhesive material. The two FR4 substrates were bonded together between the dielectric surfaces also using the SU8 based bonding approach. The superstrate was assembled with a source antenna by a nylon nut and bolt. Plastic screws (Nylon 6-6, RS Components) were used to secure the superstrate structure to the FR4 substrate of the source antenna using pre-drilled alignment holes located at the 4 corners of superstrate and FR4 board of the source antenna.

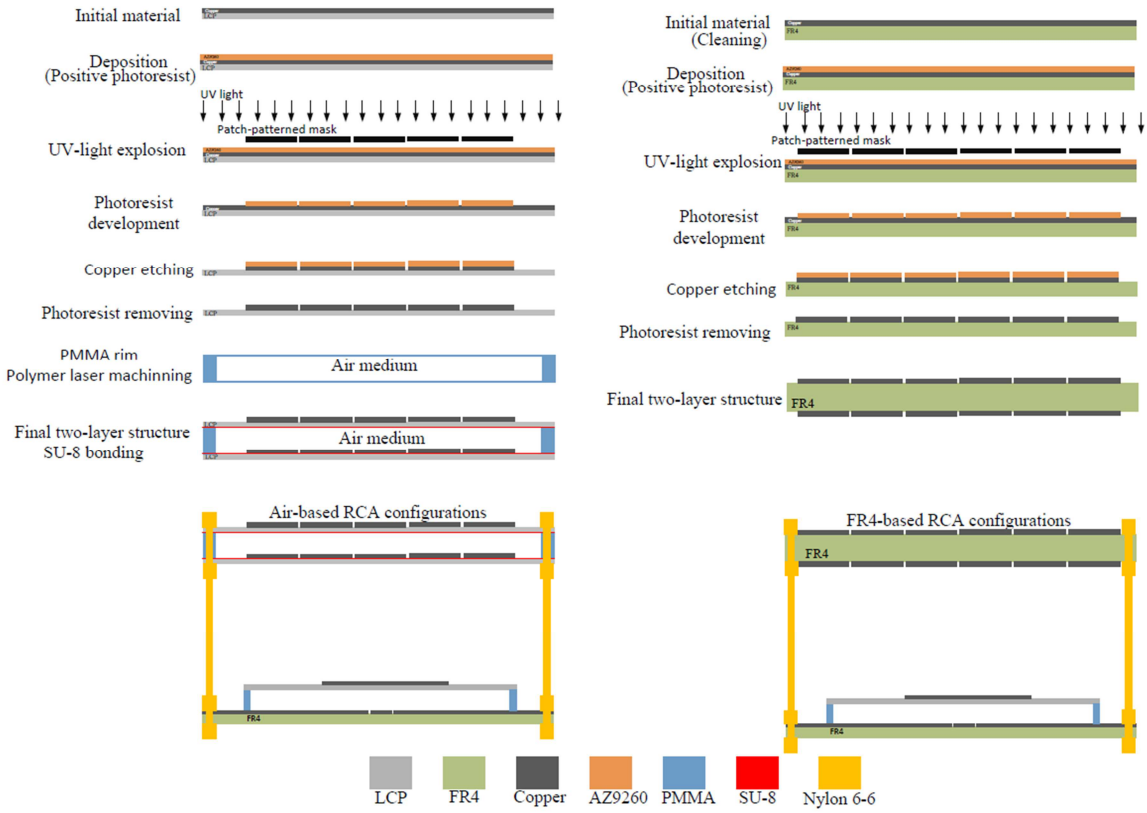

Figure 5.24: Schematic illustration of the fabrication steps of the RCA configurations consisting of the air spacer based and FR4 metamaterial superstrate, respectively.

Fig. 5.25(a) shows a picture of the laser machined PMMA rim and the assembled RCA device. The outer dimensions of the PMMA rim are 50 mm x 50 mm and the width of the rim is 5 mm. The thickness of the rim is 4 mm. Fig. 5.25(b) shows the assembled RCA device, the superstrate is the air spacer based two-layer metamaterial. The superstrate was based on the design consisting of an array of 5x5 cells for the best optimised performance. The length and diameter of the nylon screws are 30 mm and 4 mm, respectively. The cavity height can be controlled by adjusting the position of the nuts securing the assembly. The dimensions of the FR4 substrate of the source antenna are 50 mm x 50 mm.

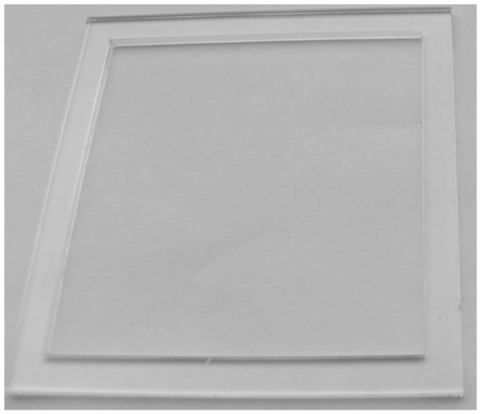

(a)

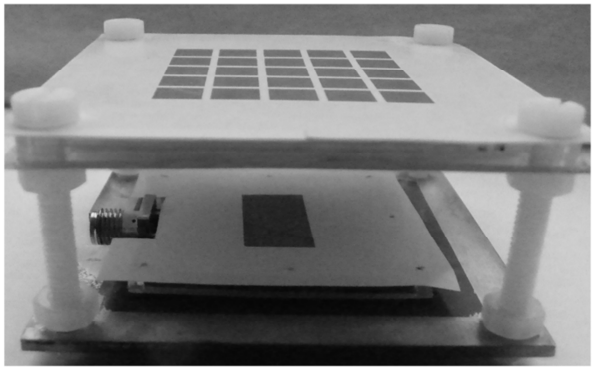

(b)

Figure 5.25: Photographs of (a) a micromachined PMMA rim and (b) an assembled RCA device using an air spacer based metamaterial superstrate.

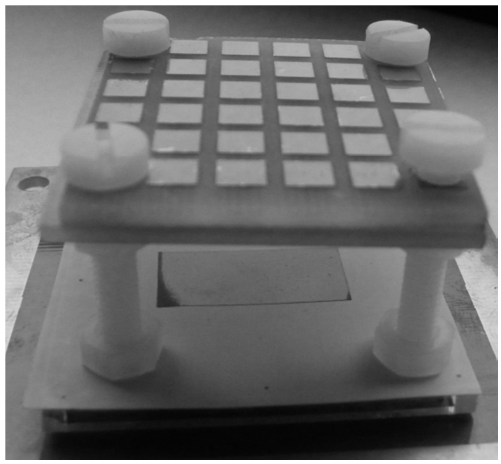

Figure 5.26: A photograph of the assembled RCA device incorporating the FR4 based superstrate design.

Fig. 5.26 shows a picture of the RCA device using the FR4 based metamaterial superstrate. In order to avoid the edge effect, an FR4 based metamaterial superstrate with dimensions of 36mm x 36mm was used containing a 6x6 array of patches, but the 4 corner patches on each side are sacrificed for mounting holes. The cavity height is 19 mm.

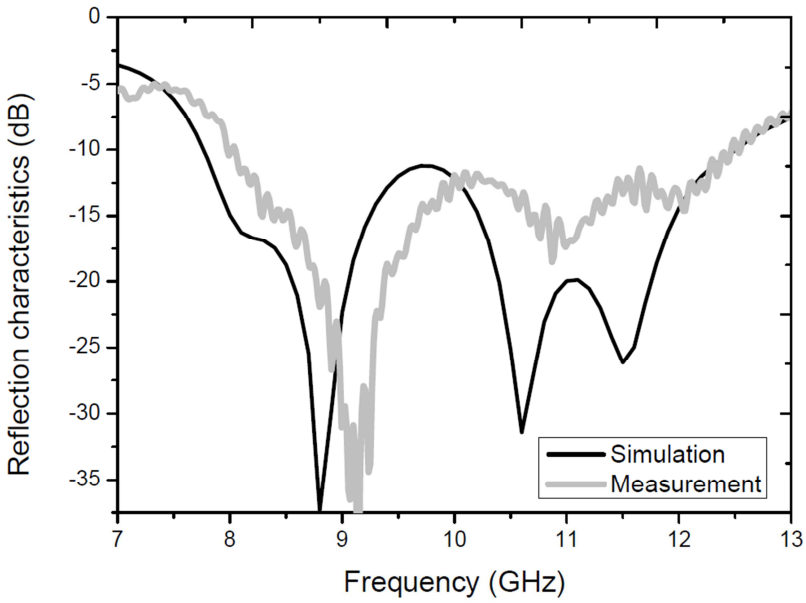

Figure 5.27: The results in measurement and simulation of reflection characteristics of the RCA device using the air spacer base superstrate.

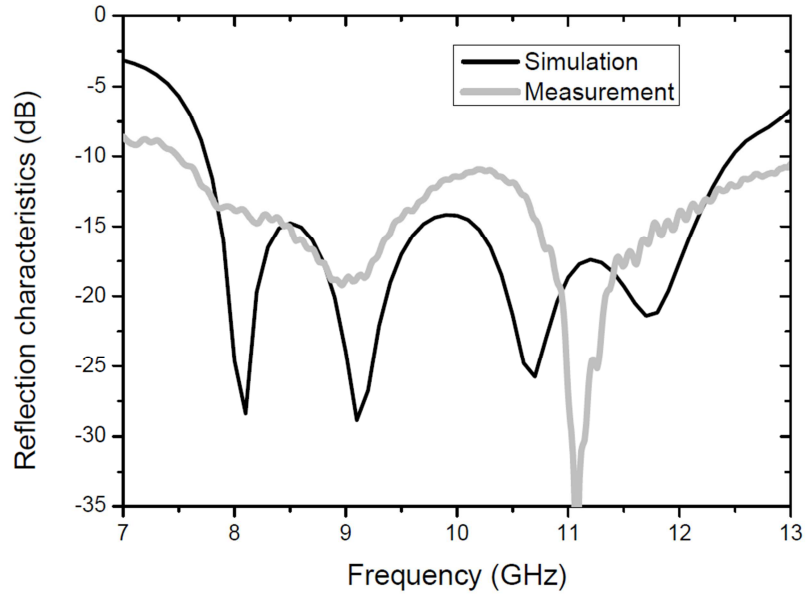

Figure 5.28: The results in measurement and simulation of reflection characteristics of the RCA device using the FR4 based metamaterial superstrate.

5.9 Measurements and characterisation

The verification of the antenna performance was carried out by measurements of the electromagnetic characteristics. The reflection and the radiation behaviours were characterised to confirm the capability of broadband operation based on the measurement methods described in Chapter 4.

5.9.1 Reflection characteristics

Fig. 5.27 shows the reflection characteristics of the RCA device using the air spacer based two-layer metamaterial superstrate over the frequency range of 7–13 GHz. It can be seen that the -10 dB impedance bandwidth is between 8.3 GHz and 12.3 GHz. The percentage bandwidth is thus 40% for the middle frequency of 10 GHz. In comparison, a good agreement in bandwidth is obtained between the measurement and simulation results. The dip locations of the reflection characteristics are coincident with the measured results of the primary source which are at ~9 GHz, ~11 GHz, and ~12 GHz as shown in Fig. 4.29(a) in Chapter 4. The appearance of the cavity response can be noticed around 8.5 GHz.

Fig. 5.28 shows the reflection characteristics of the RCA device using the FR4 based superstrate as shown in Fig. 5.26 over the frequency range of 7–13 GHz. The measured impedance bandwidth is between 7.5 GHz and 13 GHz or ~55% at the frequency of 10 GHz. The measured bandwidth is larger than the result of simulation since the measured reflection characteristic shows a broader response. The locations of the dips are also observed to be around 8 GHz, 9 GHz, 11 GHz, and 12 GHz, similar to those in Fig. 5.27.

5.9.2 Measurements of antenna gain

Fig. 5.29 shows the radiation characteristics of the antenna gain for the RCA device with the air spacer based superstrate measured over the frequency range of 7–13 GHz. The maximum broadside gain is ~13 dBi. The measured 1-dB ripple radiation bandwidth is 40% covering the frequency range of 8 GHz to 12 GHz. For the 3-dB ripple condition, the radiation bandwidth is as wide as ~47% over the frequency region of 7.5~12.2 GHz.

Fig. 5.30 shows the characteristics of the radiation for the RCA device with the FR4 based metamaterial superstrate. The measured peak gain at the broadside direction is 12.5 dBi. The 1-dB ripple radiation bandwidth of 45% is achieved between 7.7 GHz and 12.2 GHz at the middle frequency of 10 GHz. For the 3-dB ripple radiation bandwidth, the operation band is ~51% between 7.4 GHz and 12.5 GHz, whereas the 3-dB-ripple radiation bandwidth from simulation is ~53% from 7.6 GHz to 12.9 GHz.

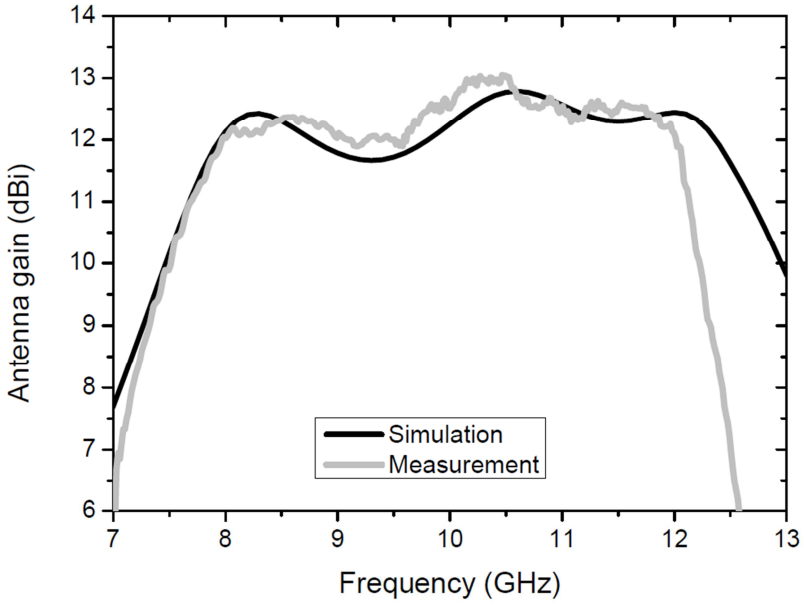

Figure 5.29: The results in measurement and simulation of radiation characteristics of the RCA device for the air spacer based superstrate.

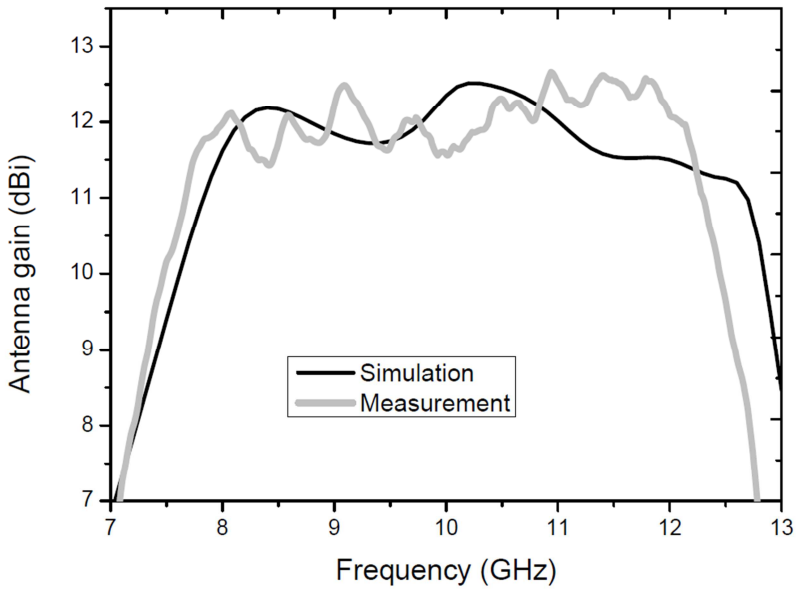

Figure 5.30: The results in measurement and simulation of the radiation characteristics of the RCA device for the FR4 superstrate.

A discrepancy between measurement and simulation is observed that the sharp drop beyond 12 GHz may be caused by the upper operation frequency of the standard gain horn antennas used in the measurement system. The random is associated with the accuracy of the measurement system.

The results show that a smooth ripple band has been obtained over the target frequency range of operation for both antenna configurations. Broadband performance with enhanced gain or directivity has been achieved. It can be considered in the characteristics of the gain-bandwidth product (GBP) addressed in [193] as

$$GBP = G_{max} \times \%BW \tag{5.14}$$

$$G_{max} = 10^{\frac{G_{max(dB)}}{10}} \tag{5.15}$$

where G_{max} is a liner maximum antenna gain. The GBP values are 938 and 907 with respect of using the air spacer based superstrate and the FR4 based metamaterial superstrate, respectively.

5.9.3 Characteristics of the radiation patterns

Figs. 5.31 and 5.32 show the characteristics of the normalised radiation patterns of the two broadband RCA devices. The results were obtained for the frequencies of 8 GHz, 9 GHz, 10 GHz, 11 GHz, and 12 GHz within a range of the operation frequency. The measurements were carried out in both E- and H-plane over a full circle of 360° (or ±180°) at a step size of 5°. In comparison, the characteristics of the radiation patterns agree well with the results of simulation as good directivity and narrow beamwidth. The results for H-plane show a more close agreement. Furthermore, the attributes of the side lobes show that the number of side lobes increases as frequency. The side-lobe levels (SLLs) are less than -12 dB in all of the frequencies. However, the back radiations of the H-plane at 11 GHz and 12 GHz are different with a similar attribute of the measured radiation patterns of the source antenna in Chapter 4.

The characteristics of the narrow-beam response show significant enhancement over that of the source antenna as shown in Chapter 4. The half-power beamwidth (HPBW) parameters for the observed frequencies are summarised in Table 5.4 and 5.5. The values in brackets are from the results of the simulation. In general there is a good agreement between results of measurements and simulations.

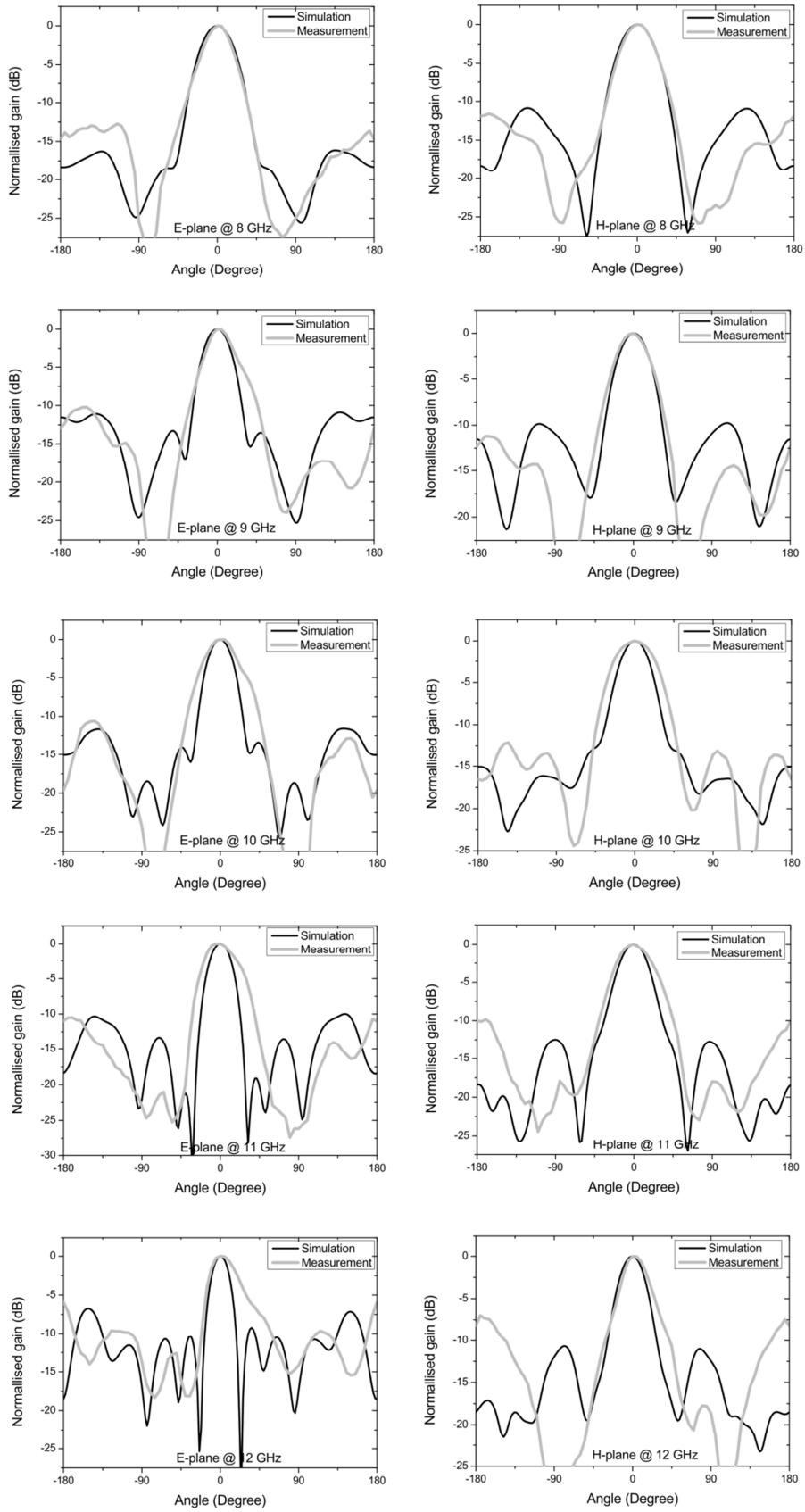

Figure 5.31: The E- and H-plane far-field radiation patterns of the RCA device using the air spacer based superstrate at five different frequencies of 8 GHz, 9 GHz, 10 GHz, 11 GHz and 12 GHz.

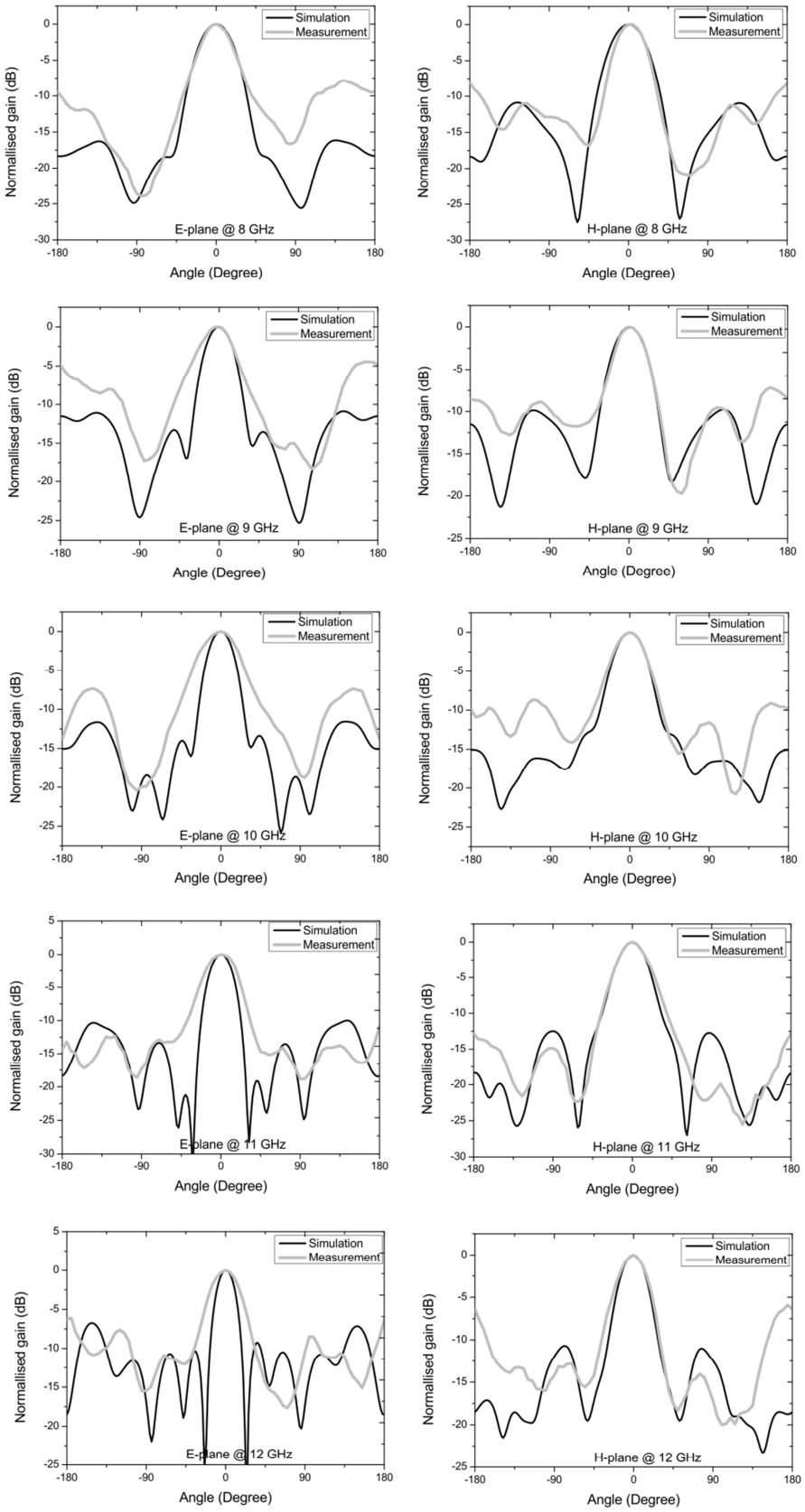

Figure 5.32: E- and H-plane far-field radiation patterns of the RCA device using the FR4 based superstrate at five different frequencies of 8 GHz, 9 GHz, 10 GHz, 11 GHz and 12 GHz.

Table 5.4: Summary of the 3-dB beamwidth (HPBW) of the air-based RCA device.

	8 GHz	9 GHz	10 GHz	11 GHz	12 GHz
E-plane	35° (40°)	32.5° (32°)	40° (30°)	42° (28°)	29° (22°)
H-plane	40° (42°)	32° (38°)	55° (36°)	50° (36°)	32° (29°)

Table 5.5: Summary of the 3-dB beamwidth (HPBW) of the FR4-based RCA device.

	8 GHz	9 GHz	10 GHz	11 GHz	12 GHz
E-plane	35° (40°)	32° (32°)	47° (30°)	35° (28°)	35° (22°)
H-plane	35° (42°)	32° (38°)	32° (36°)	32° (36°)	32° (29°)

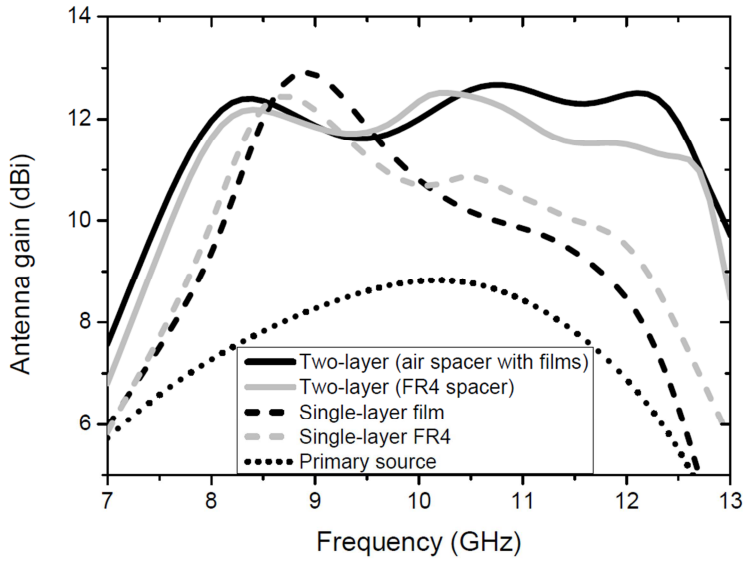

Figure 5.33: The simulation results of antenna gain of the RCA devices with the air spacer and FR4 based metamaterial superstrate structures in comparison with the RCA devices using a single-layer patch-array superstrate and a primary source.

5.10 Discussion

The RCA devices are discussed in terms of the radiation bandwidth with the directivity and gain, and the characteristics of the radiation patterns. The effect of the finite-size superstrate is considered in connection with antenna performance. The effects of the superstrates based on the one-layer patch array and the two-layer identical patch arrays, are studied and compared for the purpose of wide radiation bandwidth as shown in Fig. 5.33. In order to compare the radiation performance of the RCA devices, the simulation results show antenna gain for the wideband source antenna and the performance of the two RCA devices using the LCP film and the FR4 based substrate designs. It is evident that the radiation bandwidth of the two-layer metamaterial based superstrate design is much better than that of the single-layer based version.

However, due the effect of gain-bandwidth product, the bandwidth is larger for the RCA devices in this work, the antenna gain of 13 dBi is not as high as those of some RCA designs, for 16.2 dBi [6], 16.5 dBi [7], 13.8 dBi [8], 18.2 dBi [9], and 19.5 dBi [10]. In RCA devices, the finite-size RCA and the material-loss property play a significant role in the characteristics of the radiation performance based on the trade-off parameter between gain and bandwidth. In addition, the side lobes are strong in the back direction due to the property of the driven aperture on the FR4 material that decreases the primary radiation performance.

In this thesis, the RCA mechanism is based on the hybrid behaviour of the radiative Fano resonance in the two-layer metamaterials and the double cavity mode in the Fabry-Perot configuration. The novel two-layer metamaterial exhibits the property of transmission. Such characteristics are unavailable in the one-layer (FSS) based PRS which only produce a single mode of the Fabry-Perot effect as shown in a conventional resonant cavity antenna. Also, the two-layer identical patch array is a simple design and is a unique structure in the RCA application that is different from the previous RCA designs based on two-layer dissimilar arrays.

The good attribute of the enhanced antenna gain for the achieved radiation bandwidth is the low ripple performance over the operation band. The small antenna footprint has been discussed in the effective size of the RCA devices. The conditions of the metamaterial superstrate design in the RCA devices have been studied and verified in antenna characteristics. Table 5.6 summarises the design parameters and the measured

performance of the two types of the dielectric medium in the two-layer metamaterial superstrates. The peak gain of the RCA device with the air medium is slightly better than the device with the FR4-based superstrate. This is due to the effect of the dielectric loss in the FR4-based superstrate which is significant at high frequencies [194].

Table 5.6: Summary of the antenna dimensions and performance.

Interior medium	Physical parameters			Antenna performance		
	Hr	Hc (mm)	Superstrate dimensions (mm^2)	Impedance bandwidth	Measured 1-dB ripple Radiation bandwidth	Measured peak gain (dBi) (Simulated err.)
Air-spacer based design	4 mm ($0.13\lambda_g$)	20 ($0.67\lambda_0$)	35 x 35	40%	40%	~ 13.0 (err. ~1.5%)
FR4	3.2 mm ($0.22\lambda_g$)	19 ($0.63\lambda_0$)	36 x 36	55%	45%	~ 12.5 (err. ~1%)

λ_g is the guided wavelength at 10 GHz.

The sizes of the two RCA devices are similar around 1.2λ x 1.2λ at 10 GHz. As has been discussed, the size of the RCA structure has an influence on an antenna gain. In the recent RCA works as addressed [9, 10], it has been shown that relatively high gain and wideband can be obtained in RCA devices using three layers (thickness of the superstrate more than a half wavelength) of the dissimilar dielectric slabs or FSSs based superstrate, respectively. This point shows the possibility of a broadband high-gain RCA device with a small footprint.

In studying effect of the cavity height (distance), the two Hc values were optimised to be 20 mm and 19 mm for the air- and FR4-based superstrates, respectively. The cavity heights lead to the resonant frequency at the lower bound (~8 GHz) of the radiation bandwidth.

Table 5.7: Comparison of the structures and radiation performance of RCA devices.

	Superstrate designs	Superstrate dimensions	Cavity height	Gain peaks	Radiation bandwidth
This thesis	Identical patch arrays	35x35x4.2 mm^3 1.16λx1.16λx0.14λ	20 mm	13 dBi	47% (4.7 GHz)
Ref. 8	Complementary FSS arrays	72x72x0.79 mm^3 2.4λx2.4λx0.027λ	15 mm	13.8 dBi	28% (2.8 GHz)

The dimensions and performance of the RCA devices in this thesis are compared to the recent broadband RCA in Ref. 8 which was designed to operate in the same frequency band at the centre frequency of 10 GHz. The superstrate in the work is also based on a two-layer superstrate and the source is an aperture couple patch antenna. Table 5.7 shows a comparison of the superstrate design, the RCA dimensions and the radiation performance of the RCA devices. In [8], the two-layer FSS superstrate is based on a patch pattern on one side of a dielectric substrate and a complementary mesh pattern on the other side of the substrate. It is evident that the RCA device in this thesis has advantages in terms of the antenna size and the radiation bandwidth. The cavity height and peak gain are similar. But the bandwidth in the thesis work is larger by more than 50% as compared with the value reported in [8].

5.11 Summary

In this chapter, the development of the broadband RCA devices has been described. The RCA devices are based on a superstrate design using the patch based two-layer metamaterial and the wideband patch antenna studied in Chapter 4 as a primary source. The modified patch array with a period of approximately quarter wavelength as opposed to the half-wavelength design studied in Chapter 3 has been investigated and found to be suitable for creating two-layer metamaterials for used as superstrates to develop broadband RCA devices. The effects of the resonant transmission (radiative mode) associated with the extraordinary transmission in such metamaterials have been studied for different thicknesses of the dielectric spacer. The properties for superstrate applications have been investigated in the transmission response based on the electromagnetic image theory using the Fabry-Perot cavity. It was found that a gap of 4 mm between the two arrays each on an LCP film substrate in the air spacer based design

produces the best performance in terms of bandwidth and low ripple performance. In the antenna synthesis work for an RCA device, the metamaterial superstrate was combined with the primary source. The effect of the cavity height was investigated and then optimised for broadband performance. The size of the superstrate was subsequently studied in order to obtain broadband behaviour. The FR4 based two-layer metamaterial superstrate was also designed and incorporated into the RCA device successfully for broadband operation. Both designs were implemented successfully. The 3-dB radiation bandwidth and peak gain are 47% and 13 dBi for the RCA with the air spacer based superstrate, while they are 51% and 12.5 dBi for the device with the FR4 based superstrate, respectively. The bandwidth figures are much larger than that of similar devices in the previous work which is 28% [8], while the gain is slightly lower than corresponding value of 13.8 dBi. The RCA devices in this work are much more compact with the total dimensions of only 1.5λx1.5λx0.14λ as compared to the smallest RCA device of 2.4λx2.4λx0.027λ reported in the literature [8].

CHAPTER 6 CONCLUSIONS AND FUTURE WORKS

6.1 Conclusions

A thorough study of the Fano resonance effects in the metamaterial consisting of two identical patch arrays has been carried out as described in Chapter 3, it has been found that the sharp Fano resonances can be obtained in such metamaterial that exhibits a characteristic of the asymmetric line-shape profile. The geometry based on two identical patch arrays with a dielectric spacer is able to demonstrate the effect of the surface plasmon polaritons (SPPs) in that the two-layer structure can behave like a coupled grating configuration. The attributes of the resonance effect are associated with the extraordinary electromagnetic transmission based on the coupled SPP-like behaviour. The Fano resonance originates from the trapped mode effect showing the anti-phase current distribution in a pair of patches as a unit cell. The effects of geometrical parameters such as the period, the patch dimensions and the thickness of the dielectric spacers in the material have been studied. The period of 15 mm (half wavelength) and the square patch of 13 mm x 13 mm give the Fano resonance effect at the frequency of 10 GHz. Sharp resonances can be obtained using a sub-millimetre thick dielectric spacer. The resultant materials can be used for ultrathin resonator applications. The two-layer patch based Fano-resonance material has been demonstrated using both FR4 and liquid crystal polymer (LCP) based dielectric spacers. Two identical patch arrays were fabricated on each side of the copper clad FR4 and LCP substrates. A strong resonance effect was observed in the LCP based materials resulting from significant electromagnetic coupling between the two arrays since the LCP thickness is only 100 μm. A good agreement was obtained between the experiments and the simulation results. The strong absorption effect in the LCP based metamaterials has been investigated for potential applications as near perfect ultrathin absorbers. It has been shown that 98 percent absorption can be achieved in the LCP based material with a patch array on the front surface and the blank copper layer (PEC) on the back surface. In addition, the properties of electric permittivity and magnetic permeability associated with the Fano resonance effects have been studied. The metamaterial exhibits a negative permeability over the frequency window of the Fano resonance as well as zero permittivity at the resonance peak.

Design and fabrication methods have been developed for wideband antenna devices. The aim was to advance a wideband patch antenna as a primary source for the resonant cavity antenna described in Chapter 5. The CPW-fed aperture-coupled patch antenna design has been studied in order to develop a wideband patch antenna since it is capable of wideband performance as compared with other designs. The systematic approach was used to analyse the impedance and the radiation characteristics of the aperture element and the coupling with the patch element. For wideband operation, the short-end CPW was used as the feeding structure for the aperture-coupled patch antenna device in dealing with double-tuned impedance matching techniques. The dimensions of CPW, aperture and patch elements were optimised to ensure close coupling of the three resonances to obtain a wideband device as well the air gap between the patch and the ground plane on the FR4 substrate. The edge effects of finite-size ground plane on radiation patterns have been studied to determine a suitable substrate size for desirable radiation patterns.

The optimised design has been implemented. The short-end CPW based feeding structure and the coupling aperture were fabricated on a single side copper clad FR4 substrate using a microfabrication method. The laser micromachined PMMA rim was used as the spacer between the patch in an LCP substrate and the ground plane on the FR4 substrate. The laser based fabrication method for the PMMA rim is much simpler than the SU8 based approach used in the previous work. The SU8 based thermal bonding method was developed for assembly of the patch on the LCP substrate, the PMMA rim and the FR4 substrate. Drilled holes were used as the alignment marks for assembly of the patch antenna device. The measured result showed that the -10 dB impedance bandwidth of 46 percent has been achieved. This is an improvement by more than a factor of two as compared to that of the similar devices reported in the previous work. The 3-dB radiation bandwidth of 43 percent was obtained with a peak gain of 8.5 dBi. It is believed that both of the impedance and the radiation bandwidth are the best performance obtained for the patch antenna device. The antenna size was around 1.5λ x 1.5λ at the frequency of 10 GHz.

Design and synthesis methods have been developed for broadband resonant cavity antennas using a metamaterial based superstrate and the wideband patch antenna as a primary source. The two-layer metamaterial has been designed based on the work described in Chapter 3. However, the quarter wavelength based period has been used to

obtain two-layer patch based metamaterials for RCA applications. It has been found that such materials with broad radiative Fano resonance behaviour provide good characteristics of magnitude and phase of reflection for using as superstrates for RCA devices. Both air spacer and FR4 based two-layer metamaterials have been designed; the air spacer based metamaterials consists of two LCP film substrates each with a patch array and separated by a PMMA rim. In the FR4 based two-layer metamaterials, the two patch arrays are formed an each side of the FR4 substrate. The behaviours of the metamaterials for superstrate applications were investigated by studying the transmission characteristics for an incident plane wave based on the electromagnetic image theory. The synthesis work on the design of broadband RCA device was carried out using the Ansoft HFSS software package. The effects of cavity height and superstrate size have been studied in order to obtain low ripple effects and broad radiation bandwidths and good radiation patterns.

In the implementation of broadband RCA devices, the air spacer based two layer metamaterial superstrate was constructed using a laser machined 4-mm-thick PMMA rim. The two LCP film substrates each with a patch array were assembled with the PMMA rim using the SU8 based bonding method. For the FR4 based metamaterial superstrate, the two patch arrays were fabricated on one side of each FR4 substrate and then combined to form the metamaterial superstrate. The superstrate was then assembled and secured to the wideband patch antenna device using nylon bolts and nuts. The cavity height can be adjusted by moving position of nuts along the four nylon bolts. The sizes of RCA devices are about 45x45x44 mm^3 or $1.5x1.5x0.8\lambda^3$. The performance of RCA devices was evaluated by reflection and radiation measurements. The 1-dBi ripple radiation bandwidth is ~40% at 10 GHz with a maximum peak gain is ~13 dBi for the air spacer based superstrate. The RCA device with the FR4 based superstrate showed a reduction of gain peak by 0.5 dBi due to the effects of the dielectric loss in the FR4 materials.

6.2 Future works

The thesis work has focussed on the studies of RCA devices for broadband applications. In future works, the metamaterial substrate can be studied for dual band and multi-band applications. This may be achieved by a modification of two-layer metamaterials to produce the necessary characteristics in reflection magnitude and phase for developing RCA devices in dual band and multi-band applications. It will be interesting to

investigate alternative RCA devices using other types of antenna devices as the primary source. It is also possible to replace the blank ground plane of the patch antenna with a metamaterial based counterpart or to integrate a metamaterial structure with the existing ground plane to supress the edge effect of diffraction for enhancing the features of RCA performance, for example, directivity.

The wideband patch antenna developed in this thesis can be used as the primary source with other superstrate designs to develop alternative RCA devices for high gain and/or broadband applications. There is also a scope to extend the single patch based design to a multi-patch version for high gain applications.

For further study of the two-layer metamaterials, other shapes of elements can be investigated in terms of both Fano resonance effects and the associated complex electrical permittivity and magnetic permeability. The further work on the design of the LCP based two-layer metamaterials could lead to perfect thin film absorbers by modifying the front and back reflectors for improving impedance matching. The work on two-layer metamaterials can be extended to multilayer structures for a better performance and more novel properties.

In fabrication and assembly of more reliable joining methods than the SU8 based approach, the area can be further investigated to produce high-robustness antenna devices for using in the practical solutions.

APPENDIX A : UNIT-CELL SIMULATION

Numerical simulation based on the electromagnetic theory was used to design and study the characteristics of metamaterials. There are several simulation tools which are available in an electromagnetic research community. The varieties of the analytical methods are introduced based on the Maxwell's equations through the partial difference or integral equation based approaches. The numerical methods consist of finite element method (FEM), finite-difference time-domain (FDTD), moment of method (MoM), or a mixture of the algorithms. Also, GUI (Graphical User Interface) systems and adaptive solvers are different which are taken into account such as 3D capabilities and meshing techniques for accurate results.

In the thesis, a design process is performed using the commercial software package Ansoft HFSS^{TM} which is a general purpose tool of the full-wave electromagnetic solver based on the finite-element method (FEM) for 3D structures. The HFSS software is a widely used tool. It has a powerful and accurate solver and a user-friendly interface. The theoretical analysis is based on Maxwell's equations implemented through a set of the partial differential equation. The technique of the finite element mesh is particularly suitable for 3D structures or objects. In FEM, the problem space is physically divided into many small objects with a suitable mesh system. The scattering parameter is numerically calculated through an electromagnetic environment based on how components or structures perform in the field energy and influence of other nearby components. For simplicity and efficient simulation work, the investigation is based on a single unit-cell with the periodic boundary conditions (PBC) which can represent electromagnetic properties of the infinite lattice. The PBC is based on geometry of a small part of a large configuration. The unit-cell interacts with its mirror images in a two-dimensional coordinate. The scattering response of the metamaterial configuration is analysed based on the Floquet's theorem. This method deals with the uniform periodic structure via a harmonic function of the mathematical series of expansion [195].

Fig. A.1 shows the configuration of a unit-cell simulation on the HFSS tool. Here, the unit-cell based on a pair of patch elements is considered by the electromagnetic interaction with an ordinary dielectric material as a spacer. In HFSS simulation, the unit

cell of the investigated structure is positioned into a boundary box. The presence of the Master and Slave boundary referred to as an infinite condition is specified by surrounding side-walls of the boundary box that is equivalent to function in a similar way to an electric or magnetic conductor. The coupled surfaces on the top and bottom of the boundary box are applied by the Floquet ports as Port 1 and Port 2. The Floquet port is used by assuming that planar-periodic structure is infinite. The field excitation is performed by the plane-wave radiation at the normal incidence.

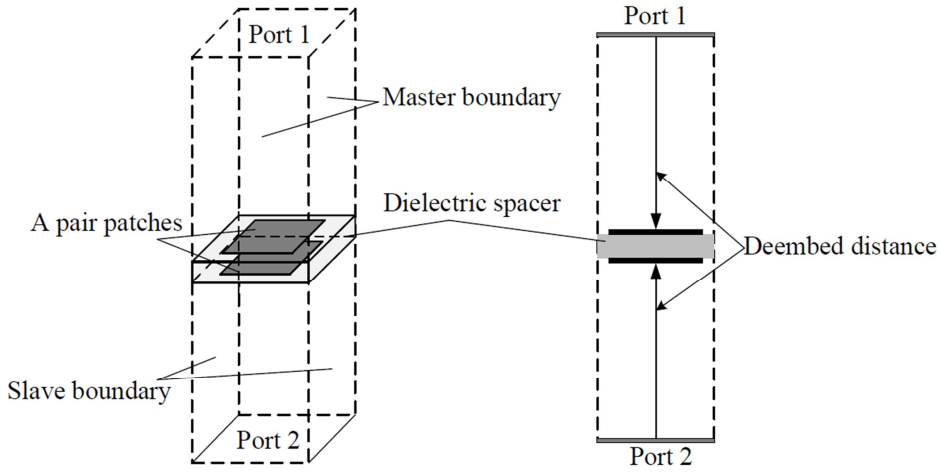

Figure A.1: Configuration of the Floquet-mode simulation of a unit-cell in HFSS.

In this thesis, process steps of the HFSS simulation include firstly creating a physical structure by drawing a model of a unit cell with the PBC system in the solution type as a driven mode. For the two ports of the excitation, the de-embed distance from the exciting port is also taken to the interface of the unit cell which deals with the accuracy of a phase response. Next, the simulation environment is defined by the solution setup in which the target frequency is set at 10 GHz as the mid-band frequency. The setup of the adaption solution refers to the maximum number of passes and the maximum of delta S (the convergence of the S parameter) which are 10 and 0.002, respectively. The value is the stopping criteria for the solution setup. In frequency sweep, the simulation type is a discrete mode and the frequency range is from 1 GHz to 20 GHz at a step size of 10 MHz to cover the desirable band. The simulation results are associated with the characteristics of the reflectance and transmittance of the unit-cell structure given by the S parameters in a linear and log scale. To observe the field plot, the components of the electric (E) and magnetic (H) fields are graphically available in field overlay and also the effect on the current distribution can be obtained.

APPENDIX B : THE MATLAB CODE FOR MATERIAL PROPERTIES

This section shows the retrieval method for a material characterisation [147].

```
% Set a constant for a speed of light
c=3e8;

% Load the S parameters as individual (CSV format data from the HFSS tool)
load S11_mag
load S21_mag
load S21_phase
load S11_phase

f=S11_mag(:,1)*1e9;          % Set a frequency range from a CSV file
k_0=2*pi*f/c;                % Calculate a wave number
d=1e-3;                      % Set a thickness of a unit-cell

% Reconstruct the complex values of S11 and S21
S11=S11_mag(:,2).*exp(i.*S11_phase(:,2));
S21=S21_mag(:,2).*exp(i.*S21_phase(:,2));

% Calculate the impedance (z)
z=sqrt( ( (1+S11).^2 - S21.^2 )./( (1-S11).^2 - S21.^2) );

% Calculate a value of a propagation and consider a passive medium
eink0d=S21./(1-S11.*((z-1)./(z+1)));
for p=1:length(S11)
   if abs(eink0d(p))>1
      z(p)=-z(p);
      eink0d(p)=S21(p)./(1-S11(p).*((z(p)-1)./(z(p)+1)));
   end
end

n = -i.*log(eink0d)./k_0./d;   % Calculation the refractive index (n)
ep = n./z                      % Calculation the permittivity (ε)
mu = n.*z                      % Calculation the permeability (μ)
```

APPENDIX C : PRINCIPLE OF THE ANTENNA CHARACTERISTICS

The performance of antennas is described by various parameters as can be understood by IEEE Standard Definition of Terms for Antennas (IEEE Std. 145-1993). In this section, some of the antenna parameters are briefly explained to facilitate discussion of the antenna development work in this thesis. The theory of antenna engineering [155] has been used in the study. The radiation component is dominated by the three electric-field components $(E_r, E_\theta, E_\emptyset)$ at the observing point. In general, the radiation characteristics consist of the directional and the omnidirectional patterns depending on the antenna configurations. The terms of the E- and H-plane patterns are defined as a component of the electric-field and the magnetic-field vector, respectively. In addition, the distance (R) around an antenna is significant in describing the field distribution related to the antenna dimension (D) and the wavelength (λ). There are three zones including a reactive near-field $\left(R < 0.62\sqrt{D^3/\lambda}\right)$, a radiating near-field $\left(0.62\sqrt{D^3/\lambda} < R < 2D^2/\lambda\right)$, and a far-field region $(R > 2D^2/\lambda)$. Based on the theory of the electromagnetic wave propagation, the average power density of the radiation can be expressed as

$$W_{av}(x, y, z) = \frac{1}{2} Re[E \times H^*] \tag{C.1}$$

Also, the term of radiation density in the far-field region is referred to as the radiated power with respect to the solid angle which can be written as [150]

$$P_{rad} = \oiint_S \ W_{av} \cdot \hat{n} da = \frac{1}{2} \oiint_S \ Re(E \times H^*) \cdot ds \tag{C.2}$$

In consideration of the isotropic radiator or the ideal source, the total power which can be radiated in all directions is given by

$$P_{rad} = 4\pi r^2 W_0 \tag{C.3}$$

where W_0 is the radiation density of the isotropic radiator. The radiation intensity that is a far-field parameter can be expressed as

$$U = r^2 W_{rad} \tag{C.4}$$

where W_{rad} is the radiated power density. Also, the radiation intensity is related to the electric field in the far-field zone depending on the coordinates as given by

$$U(\theta, \phi) = \frac{r^2}{2\eta} |E(r, \theta, \phi)|^2 \tag{C.5}$$

where η is the intrinsic impedance of the medium and $E(r, \theta, \phi)$ is the far-field electric field intensity presented as $E^o(\theta, \phi)\frac{e^{-jkr}}{r}$. The radiation intensity of an isotropic radiator can be expressed as [W/unit solid angle]

$$U_o = \frac{P_{rad}}{4\pi} \tag{C.6}$$

Significantly, the term of the antenna directivity is defined as a ratio of the radiation intensity in the given direction (U) to the radiation intensity in an isotropic radiator (U_o). Therefore, the directivity is defined as [dimensionless]

$$D = \frac{U}{U_o} = \frac{4\pi U}{P_{rad}} \tag{C.7}$$

The general expression of the antenna directivity can be considered based on the radiation-pattern function $\left(F(\theta,\phi)\right)$ and is written as

$$D(\theta,\phi) = 4\pi \frac{F(\theta,\phi)}{\int_0^{2\pi}\int_0^{\pi} F(\theta,\phi) sin\theta d\theta d\phi} \tag{C.8}$$

To illustrate this, the antenna efficiency (e_o), a parameter indicates the amount of loss at the terminals of the antenna structure. It can be defined as

$$e_o = e_r \cdot e_{.c} \cdot e_d \tag{C.9}$$

The terms of e_c and e_d are associated with the conduction and dielectric efficiency, respectively, whereas e_r refers to the reflection efficiency or mismatch defined by $(1 - |\Gamma|^2)$, Γ is the reflection efficiency in connection with the antenna input impedance (Z_{in}) and the characteristic impedance of the transmission line (Z_o). It can be defined as

$$\Gamma = \frac{Z_{in} - Z_o}{Z_{in} + Z_o} \tag{C.10}$$

The terms of e_c and e_d are associated with efficiencies of a conduction and dielectric, respectively. In particular, the consideration of the conduction and dielectric efficiency is represented in antenna radiation efficiency (e_{cd}) and this can be expressed as

$$e_{cd} = e_c \cdot e_d \tag{C.11}$$

In addition, the relative gain is a parameter of antenna performance which is related to the directivity in operation. The definition is considered by a ratio of the radiation intensity $\left(U(\theta,\phi)\right)$ to the radiated power (P_{rad}) in the lossless isotropic source which can be expressed as

$$G(\theta,\phi) = \frac{4\pi \cdot U(\theta,\phi)}{P_{in}} \tag{C.12}$$

The radiation efficiency of an antenna is related to the radiated power and the input power as expressed as $P_{rad} = e_{cd} \cdot P_{in}$. The effect of the radiation efficiency can be related to the absolute gain and can be determined as

$$G(\theta,\phi)_{abs} = e_{cd} \cdot \frac{4\pi \cdot U(\theta,\phi)}{P_{rad}} = e_{cd} \cdot D(\theta,\phi) \tag{C.13}$$

APPENDIX D: FUNDAMENTALS OF PATCH ANTENNAS

The concept of a patch or microstrip antenna was introduced by G.A. Deschamps in 1953 for an extension of a transmission line in accordance to the radiating elements in [155, 196, 197]. The physical layout is formed by a part of the strip patch as a metallic element with the feeding mechanism. The geometric dimensions of a patch element is a key to the resonant frequency which include the patch shapes such as a square, rectangular, circular, triangular, and annular or square loop. In general, the simple configuration of a patch antenna is formed by the parallel-plate structure of the patch element and the metallic ground plane. They are separated by a dielectric materials (ε_r) with the thickness of a fraction of the operating wavelength. The excitation is fed by a coaxial cable or probe as a sample as shown in Fig. D.1.

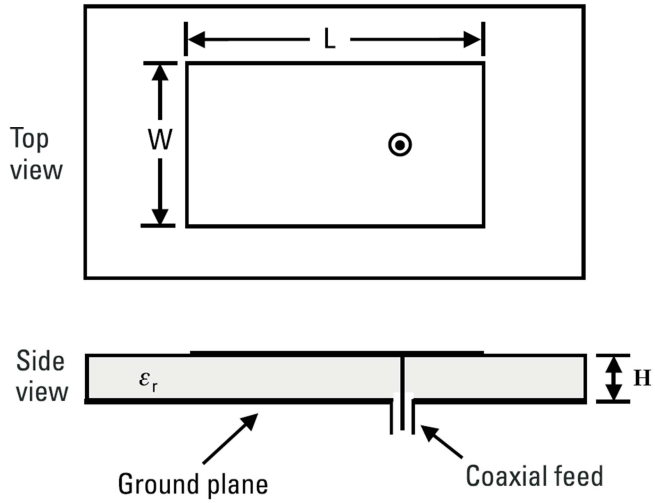

Figure D.1: A typical configuration of the patch antenna [151].

In accordance with the field travel at the interface of the dielectric-air media, the effective dielectric constant is considered for $W/H > 1$ as [197]

$$\varepsilon_{eff} = \frac{\varepsilon_{r+1}}{2} + \frac{\varepsilon_r - 1}{2}\left[1 + \frac{H}{W}\right]^{-0.5} \tag{D.1}$$

The theoretical analysis based on the transmission line model is illustrated in the approximation of physical parameters for the rectangular patch antenna. Due to the fringing effect, the effective length is extended from the end of the physical length of a patch element on each side as expressed as

$$L_{eff} = L + 2\Delta L \tag{D.2}$$

where $\Delta L = 0.412H\frac{(\varepsilon_{eff}+0.3)\left(\frac{W}{H}+0.264\right)}{(\varepsilon_{eff}-0.258)\left(\frac{W}{H}+0.8\right)}$.

The patch element is operated by the resonance condition based on the dominant $TM0_{010}$ mode, the resonant frequency can be determined as

$$f_r = \frac{1}{2L_{eff}\sqrt{\varepsilon_{eff}}\sqrt{\mu_o \varepsilon_o}} \tag{D.3}$$

For the radiation efficiency, the physical width of a patch element is also associated with the characteristic impedance as can be calculated approximately by

$$W = \frac{c_o}{2f_r}\sqrt{\frac{2}{\varepsilon_r+1}} \tag{D.4}$$

The presence of a fringing field causes radiating slots on two sides of the patch edges that can refer to the equivalent admittance as $Y_1 = G_1 + jB_1$ and $Y_2 = G_2 + jB_2$. Due to the finite width (W) and the symmetric patch shape, the expression can be given by

$$G_1 = G_2 = \frac{W}{120\lambda_o}\left[1 - \frac{1}{24}(k_o H)^2\right] \quad \text{for} \quad \frac{H}{\lambda_o} < \frac{1}{10} \tag{D.5}$$

$$B_1 = B_2 = \frac{W}{120\lambda_o}[1 - 0.636ln(k_o H)] \quad \frac{H}{\lambda_o} < \frac{1}{10} \tag{D.6}$$

With the distance between two radiating slots of ~λ/2, the resonant input resistance is also determined by transferred admittance as

$$\tilde{Y}_2 = \tilde{G}_2 + j\tilde{B}_2 = G_1 - jB_1 \tag{D.6}$$

This relation leads to the total input admittance at the resonant frequency which is obtained in the real part due to the zero reactance as expressed by

$$Y_{in} = Y_1 + \tilde{Y}_2 = 2G_1 \tag{D.7}$$

Alternatively, the total input impedance at the resonant frequency is also given by

$$Z_{in} = \frac{1}{Y_{in}} = \frac{1}{2G_1} \tag{D.8}$$

In connection with the mutual effect, the total resonant input impedance is given by

$$Z_{in} = \frac{1}{Y_{in}} = \frac{1}{2(G_1 \pm G_{12})} \tag{D.9}$$

where the plus (+) and minus (–) signs indicate a odd and even mode between the radiating slot. The mutual conductance is defined as

$$G_{12} = \frac{1}{|V_o|^2} Re \int\int_S E_1 \times H_2^* \cdot ds \tag{D.10}$$

where E_1 and H_2 are the electric field by the first slot and the magnetic field by the second slot, respectively. The mutual conductance is calculated as

$$G_{12} = \frac{1}{120\pi^2}\int_0^{\pi}\left[\frac{sin\left(\frac{k_o W}{2}cos\theta\right)}{cos\theta}\right]J_0(k_0 Lsin\theta)sin^3\theta d\theta \tag{D.11}$$

where J_0 is the Bessel function of the first kind of zero order.

In electromagnetics, the cavity model is applied to a configuration of the patch antenna by considering the field in the dielectric region between the patch element and the ground plane. This method can give an accurate analysis and also determine the resonant frequencies in higher modes. The formation of a cavity is bounded by the electric conductor on the top and bottom, and the magnetic wall along the perimeter of the patch element. The field configuration in a cavity can be obtained by the vector potential approach which gives the wave equation of

$$\nabla^2 A_x + k^2 A_x = 0 \tag{D.12}$$

In accordance to the boundary conditions, the electric and magnetic field in a cavity are connected to the vector potential A_x by

$$E_x = -j\frac{1}{\omega\mu\varepsilon}\left(\frac{\partial^2}{\partial x^2} + k^2\right)A_x \qquad H_x = 0 \tag{D.13}$$

$$E_y = -j\frac{1}{\omega\mu\varepsilon}\frac{\partial^2 A_x}{\partial x \partial y} \qquad H_y = -\frac{1}{\mu}\frac{\partial A_x}{\partial z} \tag{D.14}$$

$$E_z = -j\frac{1}{\omega\mu\varepsilon}\frac{\partial^2 A_x}{\partial x \partial z} \qquad H_z = -\frac{1}{\mu}\frac{\partial A_x}{\partial y} \tag{D.15}$$

Also, the wave numbers referring to k_x, k_y, k_z are represented as

$$k_x = \left(\frac{m\pi}{H}\right), \quad m = 0,1,2, \ldots \tag{D.16}$$

$$k_y = \left(\frac{n\pi}{L}\right), \quad n = 0,1,2, \ldots \tag{D.17}$$

$$k_z = \left(\frac{p\pi}{W}\right), \quad p = 0,1,2, \ldots \tag{D.18}$$

Therefore, the parameters of m, n and p represent the number of the half-cycle field variations along the x, y, x directions. The resonant frequency can be obtained by

$$f_r(m,n,p) = \frac{1}{2\pi\sqrt{\mu\varepsilon}}\sqrt{\left(\frac{m\pi}{H}\right)^2 + \left(\frac{n\pi}{L}\right)^2 + \left(\frac{p\pi}{W}\right)^2} \tag{D.19}$$

The directivity of a patch antenna for a single radiating slot can be expressed as

$$D_o = \left(\frac{2\pi W}{\lambda_o}\right)\frac{1}{I_1} \tag{D.20}$$

where $$I_1 = \int_0^{\pi}\left[\frac{\sin\left(\frac{k_o W}{2}\cos\theta\right)}{\cos\theta}\right]\sin^3\theta d\theta$$

In case of two radiating slots, the expression can be illustrated by

$$D_2 = \left(\frac{2\pi W}{\lambda_o}\right)\frac{\pi}{I_2} \tag{D.21}$$

$$I_2 = \int_0^{\pi}\int_0^{\pi}\left[\frac{\sin\left(\frac{k_0 W}{2}\cos\theta\right)}{\cos\theta}\right]^2 \sin^2\theta\, cos^2\left(\frac{k_0 L_e}{2}\sin\theta\sin\phi\right)d\theta d\phi \tag{D.22}$$

In addition, the Q factor which deals with antenna losses including radiation loss (Q_{rad}), conductor loss (Q_c), dielectric loss (Q_d), and surface-wave loss (Q_{sw}), is given by

$$\frac{1}{Q_t} = \frac{1}{Q_{rad}} + \frac{1}{Q_c} + \frac{1}{Q_d} + \frac{1}{Q_{sw}} \tag{D.23}$$

Due to the thin dielectric substrate, the surface-wave loss can be ignored. The approximation of other loses are expressed as

$$Q_c = H\sqrt{\pi f \mu \sigma} \tag{D.24}$$

$$Q_d = \frac{1}{\tan \delta} \tag{D.25}$$

$$Q_{rad} = \frac{\omega \varepsilon_r LW}{2HG_{rad}} \tag{D.26}$$

where G_{rad} is the radiation conductance, the term of tan δ or a loss tangent is $(\omega\varepsilon'' + \sigma)/\omega\varepsilon'$. In connection with the Q factor, the bandwidth based on a VSWR parameter associated with the impedance matching is given by

$$BW = \frac{VSWR-1}{Q_t\sqrt{VSWR}} \tag{D.27}$$

The radiation efficiency is defined as a ratio of the radiated power and the input power and in the case of the patch antenna it can be obtained as

$$e_{cdsw} = \frac{Q_t}{Q_{rad}} \tag{D.28}$$

The far-field radiation pattern of a rectangular patch is illustrated in operation of the TM_{10} mode is propagated in the E and H plans. The normalised radiation pattern can be written as [196]

$$E_{\theta n} = \frac{sin\left(\frac{kWsin\theta sin\phi}{2}\right)}{\frac{kWsin\theta sin\phi}{2}} cos\left(\frac{kL}{2} sin\theta cos\phi\right) cos\phi \tag{D.29}$$

$$E_{\phi n} = \frac{sin\left(\frac{kWsin\theta sin\phi}{2}\right)}{\frac{kWsin\theta sin\phi}{2}} cos\left(\frac{kL}{2} sin\theta cos\phi\right) cos\theta sin\phi \tag{D.30}$$

Fig. D.2 shows various designs of the feeding mechanism that have been developed for patch antennas. The feeding structures include microstrip line (Fig. D.2(a), electromagnetic coupling (Fig. D.2(b)), aperture coupling (Fig. D.2(c)), and coplanar waveguide (Fig. D.2(d)). Each feeding method provides different input impedance that depends on a physical design and a matching technique. In detail, the conventional coaxial probe is used to feed electric energy directly to a patch element as shown in Fig. D.1. In geometry, a conducting pin is vertically drilled via a dielectric substrate and positioned inside a patch element. The feeding point location on the patch can affect input impedance and a conducting probe also gives the inductance effect. Its disadvantage is that the structure is a non-planar configuration due to the position of a connecting component only beneath the patch element. Secondly, the use of the microstrip transmission line to connect to the edge of a patch element is shown in Fig.

D.2(a). The physical benefit is that the feed-line structure can be easily fabricated on a dielectric substrate together with a patch element. Also, the antenna impedance matching can be achieved by using a microstrip-line based feeding technique. However, the microstrip line produces spurious wave that can affect the radiation characteristics [197].

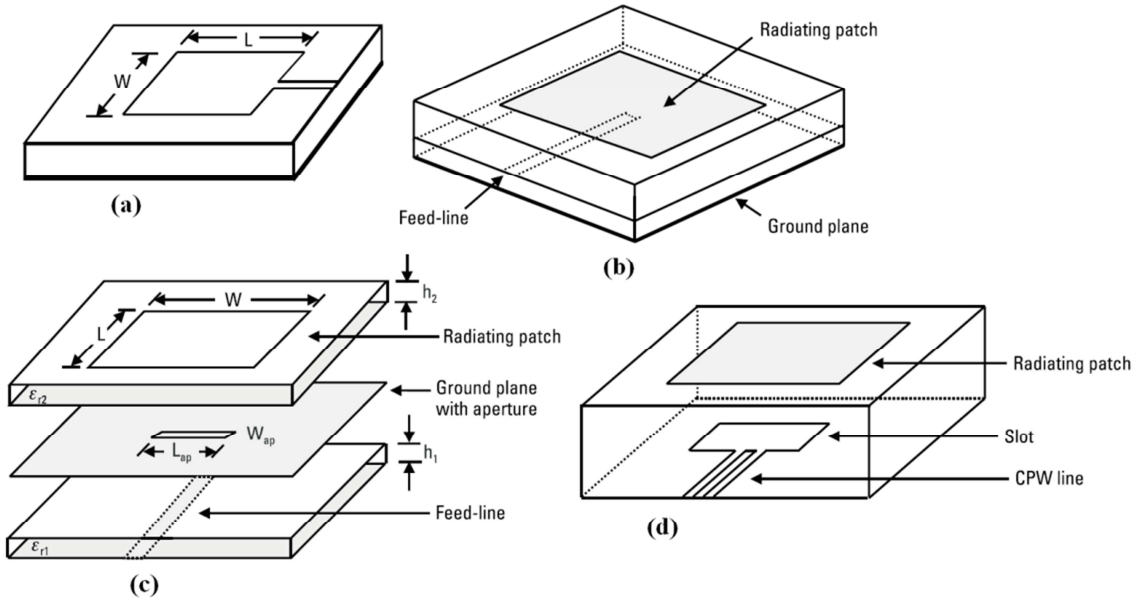

Figure D.2: Illustration of feeding method for patch antennas [197].

On the other hand, a coupling in a non-connected feeding configuration is illustrated in Figs. D.2(b), (c) and (d) in which there is no electrical connection between the feed-line structure and the patch element. As for the benefits, the choices of a dielectric material can be considered and also an air gap is feasible which offers the wideband operation due to the low dielectric constant. The gap provides a capacitance effect in which the compensation of impedance can be obtained at the low frequency. The first configuration is that the proximity coupling as seen in Fig. D.2(b) shows the feed-line is located in between the ground plane and the patch element. In the second as configuration as shown in Fig. D.2(c), the aperture coupled patch is fed by a microstrip line at the bottom surface of the dielectric substrate. Fig. D.2(d) shows the use of a coplanar waveguide (CPW) structure that is fabricated on the ground plane. The back radiation can be produced in the aperture-based coupling due to its inherent characteristic [197].

REFERENCES

[1] "Mars reconnaissance orbiter mission plan," JPL D-22239 Revision C (General Release), Oct., (2006)

[2] J. Taylor, D. K. Lee, and S. Shambayati, "Mar reconnaissance orbiter telecommunications," JPL, Pasafena, California, Sep., (2006)

[3] C. A. Balanis, "Antenna technology: past, present and future antenna," IEEE International Workshop on Technology (iWAT), pp. 5–7, (2012)

[4] K. Wu, Y. J. Cheng, and W. Hong, "Substrate-integrated millimetre-wave and terahertz antenna technology," Proc. IEEE, vol. 100, no. 7, Jul., pp. 2219–2232, (2012)

[5] D. R. Jackson, P. Burghignoli, G. Lovat, F. Capolino, C. Ji, D. R. Wilton, and A. A. Oliner, "The fundamental physics of directive beaming at microwave and pptical frequencies and the role of leaky waves," Proc. IEEE, vol. 99, no. 10, Oct., pp. 1780–1805, (2011)

[6] Y. Ge, K. P. Esselle, and T. S. Bird, "The use of simple thin partially reflective surfaces with positive reflection phase gradients to design wideband, low-profile EBG resonator antennas," IEEE Trans. Antennas Propag., vol. 60, no. 2, pp. 743–750, (2012)

[7] N. Wang, C. Zhang, Q. Zeng, N. Wang, and J. Xu, "New dielctric 1-D EBG structure for the design of wideband resonator antennas," Progress n Electromagnetics Research, vol. 141, pp. 233-248, (2013)

[8] N. Wang, Q. Liu, C. Wu, L. Talbi, Q. Zeng, and J. Xu, "Wideband Fabry-Perot resonator antenna with two complementary FSS layers," IEEE Trans. o Antennas Propag., vol. 62, May, pp.2463–2471, (2014)

[9] R.M. Hashmi, B.A. Zeb, K.P. Esselle, "Wideband high-gain EBG resonator antennas with small footprints and all-dielectric superstructures," IEEE Trans. on Antennas Propag., vol. 62, no. 6, pp. 2970-2977, (2014)

[10] K. Konstantinidis, A. P. Feresidis, and P. S. Hall, "Multilayer partially reflective surfaces for broadband Fabry-Perot cavity antennas," IEEE Trans. Antennas Propag., vol. 62, no. 2, pp. 3474–3481, (2014)

[11] Y. Liu and X. Zhang "Metamaterials: a new frontier of science and technology," Chem. Soc. Rev., 40, pp. 2494–2507, (2011)

[12] A. N. Lagarkov, V. N. Kisel, and A. K. Sarychev, “Loss and gain in metamaterials,” J. Opt. Soc. Am. B 27, pp. 648–659, (2010)

[13] W. Withayachumnankul and D. Abbott, “Metamaterials in the terahertz regime,” IEEE Photon. J., vol. 1, no. 2, Aug., pp. 99–108, (2009)

[14] C. M. Soukoulis and M. Wegener, “Past achievements and future challenges in the development of three-dimensional photonic metamaterials,” Nature Photonic, 5, pp. 523–530, (2011)

[15] N. Engheta and R. W. Ziolkowski, “A positive future for double negative metamaterials,” IEEE Microw. Theory Tech, vol. 53, Apr., pp. 1535–1556, (2005)

[16] A. Alù, N. Engheta, A. Erentok, and R. W. Ziolkowski, “Single-negative, double-negative and low-index metamaterials and their electromagnetic application,” IEEE Antennas Propag. Mag., vol. 49, no. 1, Feb., pp. 23–36, (2007)

[17] R. W. Ziolkowski, P. Jin, and C.-C. Lin, “Metamaterial-inspired engineering of antennas,” Proc. IEEE, vol. 99, no. 10, Oct., pp. 1720–1731, (2011)

[18] V. G. Veselago, “The electrodynamics of substances with simultaneously negative values of ε and μ,” Sov. Phys. Usp. 10, 509, (1968)

[19] J. B. Pendry, “Negative refraction makes a perfect lens,” Phys. Rev. Lett. 85, 3966, (2000)

[20] D. R. Smith, W. J. Padilla, D. C. Vier, S. C. Nemat-Nasser, and S. Schultz, “Composite medium with simultaneously negative permeability and permittivity,” Phys. Rev. Lett. 84, 4184, (2000)

[21] D. R. Smith, J. B. Pendry, and M. C. K. Wiltshire, “Metamaterials and negative refractive index,” Science 305, 788, (2004)

[20] D. Schurig, J. Mock, B. Justice, S. Cummer, J. Pendry, A. Starr, and D. Smith, “Metamaterial electromagnetic cloak at microwave frequencies,” Science 314, 977, (2006)

[23] D. Schurig, J. J. Mock, and D. R. Smith, “Electric-field-coupled resonators for negative permittivity metamaterials,” Appl. Phys. Lett. 88, 041109, (2006)

[24] W. Withayachumnankul, C. Fumeaux, and D. Abbott, “Compact electric-LC resonators for metamaterials,” Opt. Express 18, 25912, (2010)

[25] J. Zhou, L. Zhang, G. Tuttle, T. Koschny, and C. M. Soukoulis, “Negative index materials using simple short wire pairs,” Phys. Rev. B 73, 041101, (2006)

[26] J. Zhou, E. N. Economou, Th. Koschny, and C. M. Soukoulis, “Unifing approach to left-handed material design,” Opt. Lett. 31, 3620, (2006)

[27] J. Zhou, T. Koschny, L. Zhang, G. Tuttle, and C. M. Soukoulis, “Experimental demonstration of negative index of refraction,” Appl. Phys. Lett. 88, 221103, (2006)

[28] K. Aydin, Z. Li, L. Sahin, and E. Ozbay, “Negative phase advance in polarization independent, multi-layer negative-index metamaterials,” Opt. Express 16, 8835, (2008)

[29] N. Liu and H. Giessen, “Coupling effects in optical metamaterials,” Angew. Chem. Int. Ed. Engl.49(51), pp. 9838–9852, (2010)

[30] E. Prodan, C. Radloff, N. J. Halas, and P. Nordlander, “A hybridization model for the plasmon response of complex nanostructures,” Science 302, 419, (2003)

[31] B. Kante, S. N. Burokur, A. Sellier, A. de Lustrac, and J. M. Lourtioz, “Controlling plasmon hybridization for negative refraction metamaterials,” Phys. Rev. B 79, 075121, (2009)

[32] A. Ourir and H. Ouslimani, “Negative refractive index in symmetric cut-wire pair metamaterial,” Appl. Phys.Lett. 98(11), 113505, (2011)

[33] N. Shen, L. Zhang, T. Koschny, B. Dastmalchi, M. Kafesaki, and C. M. Soukoulis, “Discontinuous design of negative index metamaterials based on mode hybridization,” Appl. Phys. Lett. 101, 081913, (2012)

[34] W. Rotman, “Plasma simulation by artificial dielectrics and parallel-plate media,” IRE Trans. Antennas Propag., pp. 82–84, (1962)

[35] J. Brown “Artificial dielectrics having refractive indices less than unity,” Proc. Inst. Elec. Eng., pp. 51–62, (1953)

[36] D. F. Sievenpiper, M. E. Sickmiller, and E. Yablonovitch, “3D wire mesh photonic crystals,” Phys. Rev. Lett., vol. 76, pp. 2480−2483, (1996)

[37] J. B. Pendry, A. J. Holden,W. J. Stewart, and I. Youngs, “Extremely low frequency plasmons in metallic mesostructures,” Phys. Rev. Lett., vol. 76, pp. 4773–4776, (1996)

[38] J. B. Pendry, A. J. Holden, D. J. Robbins, and W. J. Stewart, “Low frequency plasmons in thin-wire structures,” J. Phys. Condens. Matter, vol. 10, pp. 4785–4809, (1998)

[39] S. Enoch, G. Tayeb, P. Sabouroux, N. Guérin, and P. Vincent, “A metamaterial for directive emission,” Phys. Rev. Lett., vol. 89, no. 21, Nov., pp. 213 902-1–213 902-4, (2002)

[40] G. Lovat, P. Burghignoli, F. Capolino,D. R. Jackson, and D. R. Wilton, “Analysis of directive radiation from a line source in a metamaterial slab with low permittivity,” IEEE Trans. Antennas Propag., vol. 54, no. 3, Mar., pp. 1017–1030, (2006)

[41] A. Alù, M. G. Silveirinha, A. Salandrino, and N. Engheta, “Epsilon-near-zero metamaterials and electromagnetic sources: Tailoring the radiation phase pattern,” Phys. Rev. B, vol. 75, no. 15, Apr., p. 155410, (2007)

[42] J. B. Pendry, A. J. Holden, D. J. Robbins, and W. J. Stewart, “Magnetism from conductors and enhanced nonlinear phenomena,” IEEE Trans. Microwave Theory Tech. 47, pp. 2075–2084, (1999)

[43] S. Pillai, K.R. Catchpole, T. Trupke, and M.A. Green, “Surface plasmon enhanced silicon solar cells,” Journal of Applied Physics, 101, p. 093105, (2007)

[44] J. B. Pendry, L. Martin-Moreno, and F. J. Garcia-Vidal, “Mimicking surface plasmons with structured surfaces,” Science, vol. 305, p. 847, (2004)

[45] J. A. Porto, F. J. García-Vidal, and J. B. Pendry, “Transmission resonances on metallic gratings with very narrow slits,” Phys. Rev. Lett., vol.83, Oct., pp. 2845–2848, (1999)

[46] T. W. Ebbesen, H. J. Lezec, H. F. Ghaemi, T. Thio, and P. A. Wolff, “Extraordinary optical transmission through sub-wavelength hole arrays,” Nature, vol. 391, Feb., pp. 667–669, (1998)

[47] L. Martín-Moreno, F. J. García-Vidal, H. J. Lezec, K. M. Pellerin, T.Thio, J. B. Pendry, and T.W. Ebbesen, “Theory of extraordinary optical transmission through subwavelength hole arrays,” Phys. Rev. Lett., vol.86, Feb., pp. 1114–1117, (2001)

[48] C. Cheng, J. Chen, D. J. Shi, Q. Y. Wu, F. F. Ren, J. Xu,Y. X. Fan, J. Ding, and H. T. Wang, “Physical mechanism of extraordinary electromagnetic transmission in dual-metallic grating structures,” Phys. Rev. B 78, 075406, (2008)

[49] M. Beruete, M. Sorolla, I. Campillo, J. S. Dolado, L. Martín-Moreno, J.Bravo-Abad, and F. J. García-Vidal, “Enhanced millimeter wave transmission through quasi-optical subwavelength perforated plates,” IEEETrans. Antennas Propag., vol. 53, no. 6, Jun., pp. 1897–1903, (2005)

[50] F. Medina, F. Mesa, and R. Marqués, “Extraordinary transmission through arrays of electrically small holes from a circuit theory perspective,” IEEE Trans. Microw. Theory Tech.,” vol. 56, no. 12, Dec., pp. 3108–3120, (2008)

[51] M. Beruete, M. Navarro, M.S. Ayza “Understanding anomalous extraordinary transmission from equivalent circuit and grounded slab concepts,” IEEE Trans. Microw. Theory Tech., vol. 59, no. 9, Sep., pp. 2180–2188, (2011)

[52] U. Fano, “Effects of Configuration Interaction on Intensities and Phase Shifts,” Phys. Rev. 124, p. 1866, (1961)

[53] Y. S. Joe, A. M. Satanin, and C. S. Kim, “Classical analogy of Fano resonances,” Phys. Scr. 74, p. 259, (2006)

[54] A. E. Miroshnichenko, S. Flach, and Y. S. Kivshar, “Fano resonances in nanoscale structures,” Rev. Mod. Phys. 82, p. 2257, (2010)

[55] B. Luk'yanchuk, N. I. Zheludev, S. A. Maier, N. J. Halas, P. Nordlander, H. Giessen, and C. T. Chong, “The Fano resonance in plasmonic nanostructures and metamaterials,” Nature Mater. 9, p. 707, (2010)

[56] A. B. Khanikaev, C. Wu, and G. Shvets, “Fano-resonant metamaterials and their applications,” Nanophotonics, vol. 2, pp. 247–264, (2013)

[57] V. A. Fedotov, M. Rose, S. L. Prosvirnin, N. Papasimakis, and N. I. Zheludev, “Sharp trapped-mode resonances in planar metamaterials with a broken structural symmetry,” Phys. Rev. Lett. 99, 147401, (2007)

[58] N. Niakan, M. Askari, and A. Zakery, “High Q-factor and large group delay at microwave wavelengths via electromagnetically induced transparency in metamaterials,” J. Opt. Soc. Am. B 29, 2329, (2012)

[59] K. J. Boller, A. Imamolu, and S. E. Harris, “Observation of electromagnetically induced transparency,” Phys. Rev. Lett. 66, 2593, (1991)

[60] R. Singh, I. A. I. Al-Naib, Y. Yang, D. R. Chowdhury, W. Cao, C. Rockstuhl, T. Ozaki, R. Morandotti, and W. Zhang, “Observing metamaterial induced transparency in individual Fano resonators with broken symmetry,” Appl. Phys. Lett. 99(20), 201107, (2011)

[61] S. Zhang, D. A. Genov, Y. Wang, M. Liu, and X. Zhang, “Plasmon-induced transparency in metamaterials,” Phys. Rev. Lett. 101, 047401, (2008)

[62] N. Papasimakis, Y. H. Fu, V. A. Fedotov, S. L. Prosvirnin, D. P. Tsai, and N. I. Zheludev, “Metamaterial with polarization and direction insensitive resonant transmission response mimicking electromagnetically induced transparency,” Appl. Phys. Lett. 94, 211902, (2009)

[63] N. Papasimakis, V. A. Fedotov, N. I. Zheludev, and S. L. Prosvirnin, “Metamaterial analog of electromagnetically induced transparency,” Phys. Rev. Lett. 101, 253903, (2008)

[64] A. E. Miroshnichenko, S. Flach, and Y. S. Kivshar, “Manipulation of electromagnetically-induced transparency in planar metamaterials based on phase coupling,” Rev. Mod. Phys. 82, 2257, (2010)

[65] R. Singh, C. Rockstuhl, F. Lederer, and W. Zhang, “Coupling between a dark and a bright eigenmode in a terahertz metamaterial,” Phys. Rev. B 79, 085111, (2009)

[66] X. Liu, J. Gu, R. Singh, Y. Ma, J. Zhu, Z. Tian, M. He, J. Han, and W. Zhang, “Electromagnetically induced transparency in terahertz plasmonic metamaterials via dual excitation pathways of the dark mode,” Appl. Phys. Lett. 100, 131101, (2012)

[67] Z. Li, Y. Ma, R. Huang, R. Singh, J. Gu, Z. Tian, J. Han, and W. Zhang, “Manipulating the plasmon-induced transparency in terahertz metamaterials,” Opt. Express 19, 8912, (2011)

[68] J. Zhang, S. Xiao, C. Jeppesen, A. Kristensen, and N. A. Mortensen, “Electromagnetically induced transparency in metamaterials at near-infrared frequency,” Opt. Express 18, 17187, (2010)

[69] W. W. Salisbury, “Absorber body for electromagnetic waves,” U.S. Patent 2 599 944, Jun. 10, (1952)

[70] R. L. Fante and M. T. McCormack, “Reflection properties of the Salisbury screen,” IEEE Trans. Antennas Propag., vol. 36, no. 10, Oct., pp. 1443–1454, (1988)

[71] C. M. Watts, X. Liu, and W. J. Padilla, “Metamaterial electromagnetic wave absorbers,” Adv. Mater. 24, OP98, (2012)

[72] N. I. Landy , S. Sajuyigbe , J. J. Mock , D. R. Smith , W. J. Padilla , “Perfect metamaterial absorber,” Phys. Rev. Lett., 100 , 207402, (2008)

[73] B. Seo, K. Kim, S. G. Kim, A. Kim, H. Cho, and E. Choi, “Observation of trapped-modes excited in double-layered symmetric electric ring resonators,” J. Appl. Phys. 111, 113106, (2012)

[74] F. Che Seman, R. Cahill and V. Fusco, “Low profile Salisbury screen radar absorber with high impedance ground plane,” IET Electronics Letters, vol. 45, pp. 10–12, (2009)

[75] P. V. Tuong, V. D. Lam, J. W. Park, E. H. Choi, S. A. Nikitov, and Y. P. Lee, “Perfect-absorber metamaterial based on flower-shaped structure,” Photonics Nanostruct. 11, 89, (2013)

[76] F. Bilotti, A. Toscano, K. B. Alici, E. Ozbay, and L. Vegni, “Design of miniaturized narrowband absorbers based on resonant magnetic inclusions,” IEEE Trans. Electromagn. Compat., vol. 53, no. 1, Feb., pp. 63–72, (2011)

[77] R. B. Waterhouse, “Design of probe-fed stacked patches,” IEEE Trans. Antennas Propag., vol. 47, Dec., pp. 1780–1784, (1999)

[78] R. Li, G. DeJean, M. Maeng, K. Lim, S. Pinel, M. M. Tentzeris, and J. Laskar, “Design of compact stacked-patch antennas in LTCC multilayer packaging modules for wireless applications,” IEEE Trans. Advanced Packaging, vol. 27, Sep., pp. 581–589, (2004)

[79] T. Huynh and K. F. Lee, “Single-layer single-patch wideband microstrip antenna,” Electronics letters, vol.31, Aug., pp.1310–1312, (1995)

[80] K. L. Wong and W. H. Hsu, “A broad-bBand rectangular patch antenna with a pair of wide slits,” IEEE Trans. Antennas Propag., vol. 49, Sep., pp. 1345–1347, (2001)

[81] R. Chair, M. Chi-Lun, K. F. Lee, and A. A. Kishk, “Miniature wide-band half U-slot and half E-shaped patch antennas,” IEEE Trans. Antennas Propag., vol. 53, Aug. pp. 2645–2652, (2005)

[82] H. Rajagopalan, J. M. Kovitz, and Y. Rahmat-Samii, “MEMS reconfigurable optimized E-shaped patch antenna design for cognitive radio,” IEEE Trans. Antennas Propag., vol. 62, Mar., pp. 1056–1064, (2014)

[83] G. Mayhew-Ridgers, J. W. Odendaal, and J. Joubert, “Single-layer capacitive feed for wideband probe-fed microstrip antenna elements,” IEEE Trans. Antennas Propag., vol. 51, Jun., pp. 1405–1407, (2003)

[84] V. G. Kasabegoudar and K. J. Vinoy, “Coplanar capacitively coupled probe fed microstrip antennas for wideband applications,” IEEE Trans. Antennas Propag., vol. 58, Jun., pp. 3131–3138, (2010)

[85] C. L. Mak, K. M. Luk, K. F. Lee, and Y. L. Chow, “Experimental study of a microstrip patch antenna with an L-shaped probe,” IEEE Trans. Antennas Propag., vol. 48, May pp. 777–783, (2000)

[86] C. L. Mak, K. M. Luk, and K. F. Lee, “Microstrip line-fed L-strip patch antenna,” IEE Proceedings Microwaves, Antennas and Propagation, vol. 146, Aug., pp. 282–284, (1999)

[87] D. M. Pozar “Microstrip antenna aperture-coupled to a microstripline” Electronics Letters, vol. 21, pp. 49–50, (1985)

[88] W. Menzel and W. Grabherr, “A microstrip patch antenna with coplanar feed line,” IEEE Microwave Guided Wave Lett., vol. 1, Nov., pp. 340–342, (1991)

[89] G. P. Gauthier, J. P. Raskin, L. P. B. Katehi, and G. M. Rebeiz, “A 94-GHz aperture-coupled micromachined microstrip antenna,” IEEE Trans. Antennas Propag., vol. 47, no. 12, Dec., pp. 1761–1766, (1999)

[90] S. D. Targonski, R. B. Waterhouse, and D. M. Pozar, “Design of wide-band aperture-stacked patch microstrip antennas,” IEEE Trans. Antennas Propag., vol. 46, no. 9, Sep., pp. 1245–1251, (1998)

[91] S. Mestdagh, R. Walter De, and G. A. E. Vandenbosch, “CPW-fed stacked microstrip antennas,” IEEE Trans. Antennas Propag., vol. 52, no. 1, Jan., pp. 74–83, (2004)

[92] W. S. T. Rowe and R. B. Waterhouse, “Broadband CPW fed stacked patch antenna,” Electron. Lett., vol. 35, no. 9, pp. 681–682, (1999)

[93] G. Rafi and L. Shafai, “Broadband microstrip patch antenna with V-slotted,” IEE Proceedings Microwaves, Antennas and Propagation, vol. 151, Oct., pp. 435–440, (2004)

[94] B. L. Ooi, S. Qin, and M. S. Leong, “Novel design of broad-band stacked patch ntenna,” IEEE Trans. Antennas Propag., vol. 50, Oct., pp. 658–669, (2002)

[95] S. K. Pavuluri, C. Wang, and A. J. Sangster, “High efficiency wideband aperture-coupled stacked patch antennas assembled using millimeter thick micromachined polymer structures,” IEEE Trans. Antennas Propag., vol. 58, no. 11, Nov., pp. 3616–3621, (2010)

[96] K. Kanjanasit, V. Vivek, and N. Homsub, “Novel design of a wideband improved U-slot on rectangular patch using additional loading slots” the 2nd International ECTI conferences, May, (2005)

[97] D. Sievenpiper, Z. Lijun Zhang, R. F. J. Broas, N.G. Alexopolous, E. Yablonovitch, “High-impedance electromagnetic surfaces with a forbidden frequency band,” IEEE Trans. on Antennas and Propagation, vol. 47, Nov., pp. 3140–3145, (1999)

[98] D. Qu, L. Shafai, and A. Foroozesh, “Improving microstrip patch antenna performance using EBG substrates,” Proc. Inst. Elect. Eng. Microw. Antennas Propag., vol. 153, no. 6, Dec., pp. 558–563, (2006)

[99] J. Liang and H. Y. D. Yang, “Radiation characteristics of a microstrip patch over an electromagnetic bandgap surface,” IEEE Trans. Antennas Propag., vol. 55, Jun., pp. 1691–1697, (2007)

[100] F. Yang and Y. Rahmat-Samii, “Reflection phase characterizations of the EBG ground plane for low profile wire antenna applications,” IEEE Trans. Antennas Propag., vol. 51, no. 10, Oct., pp. 2691–2703, (2003)

[101] L. Akhoondzadeh-Asl, D. J. Kern, P. S. Hall, and D. H. Werner, “Wideband dipoles on electromagnetic bandgap ground planes,” IEEE Trans. Antennas Propag., vol. 55, Sep., pp. 2426–2434, (2007)

[102] T. Nakamura and T. Fukusako, “Broadband design of circularly polarized microstrip patch antenna using artificial ground structure with rectangular unit cells,” IEEE Trans. Antennas Propag., vol. 59, no. 6, Jun., pp. 2103–2110, (2011)

[103] H. Boutayeb, T. A. Denidni, “Gain enhancement of a microstrip patch antenna using a cylindrical electromagnetic crystal substrate,” IEEE Trans. Antennas Propag., vol. 55, Nov., pp. 3140–3145, (2007)

[104] R. Coccioli, F. R. Yang, K. P. Ma, and T. Itoh, “Aperture-coupled patch antenna on UC-PBG substrate,” IEEE Trans. Microw. Theory Tech., vol. 47, Nov., pp. 2123–2130, (1999)

[105] Y. Zhang, J. von Hagen, M. Younis, C. Fischer, and W. Wiesbeck, “Planar artificial magnetic conductors and patch antennas,” IEEE Trans. Antennas Propag., vol. 51, no. 10, Oct., pp. 2704–2712, (2003)

[106] G. V. Trentini, “Partially reflecting sheet arrays,” IRE Trans. Antennas Propag., vol. 4, no. 4, Oct., pp. 666-671, (1956)

[107] D. R. Jackson and N. G. Alexopoulos, “Gain enhancement method for printed circuit antennas,” IEEE Trans. Antennas Propag., vol. 33, pp. 976–987, (1985)

[108] D. R. Jackson, A. A. Oliner, and A. Ip, “Leaky-wave propagation and radiation for a narrow-beam multiple-layer dielectric structure,” IEEE Trans. Antennas Propag., vol. 41, no. 3, pp. 344–348, (1993)

[109] M. Thevenot, C. Cheype, A. Reineix, and B. Jecko, “Directive photonic band-gap antennas,” IEEE Trans. Microw. Theory Tech., vol. 47, no. 11, Nov., pp. 2115–2122, (1999)

[110] C. Cheype, C. Serier, M. Thevenot, and T. Monediere, “An electromagnetic bandgap resonator antenna,” IEEE Trans. Antennas Propag., vol. 50, no. 9, pp. 1285–1290, (2002)

[111] A. P. Feresidis and J. C. Vardaxoglou, “High gain planar antenna using optimised partially reflective surfaces”, Proc. Inst. Elect. Eng. Microw. Antennas Propag., vol. 148, no. 6, Dec., pp.345 -350, (2001)

[112] A. R. Weily, L. Horvath, K. P. Esselle, B. C. Sanders and T. S. Bird, “A planar resonator antenna based on a woodpile EBG material,” IEEE Trans. Antennas Propag., vol. 53, no. 1, pp. 216–223, (2005)

[113] Y. J. Lee, J. Yeo, R. Mittra, and W. S. Park, “Application of electromagnetic bandgap (EBG) superstrates with controllable defects for a class of patch antennas as spatial angular filters,” IEEE Trans. on Antennas Propag., vol. 53, no. 1, pp. 224–235, (2005)

[114] A. P. Feresidis , G. Goussetis , S. Wang, and J. C. Vardaxoglou, “Artificial magnetic conductor surfaces and their application to low-profile high- gain planar antennas,” IEEE Trans. Antennas Propag., vol. 53, no. 1, pp.209 -215, (2005)

[115] C. Mateo-Segura, G. Goussetis, and A. P. Feresidis, “Sub-wavelength profile 2-D leaky-wave antennas with two periodic layers,” IEEE Trans. Antennas Propag., vol. 59, no. 2, pp.416 -424, (2011)

[116] J. R. Kelly, T. Kokkinos, and A. P. Feresidis, “Analysis and design of sub-wavelength resonant cavity type 2-D leaky-wave antennas,” IEEE Trans. Antennas Propag., vol. 56, no. 9, pp.2817 -2825, (2008)

[117] A. Ourir, A. de Lustrac, and J.-M. Lourtioz, “All-metamaterial-based subwavelength cavities ($\lambda/60$) for ultrathin directive antennas”, Applied Physics Lett., vol. 88, no. 8, pp.84103-1 -3, (2006)

[118] N. Guerin, S. Enoch, G. Tayeb, P. Sabouroux, P. Vincent, and H. Legay, “A metallic Fabry-Perot directive antenna,” IEEE Trans. Antennas Propag., vol. 54, no. 1, Jan., pp. 220–224, (2006)

[119] A. R. Gardelli, M. Albani, and F. Capolino, “Array thinning by using antennas in a Fabry-Perot cavity for gain enhancement,” IEEE Trans. Antennas Propag., vol. AP-54, no. 7, pp. 1979–1990, (2006)

[120] A. P. Feresidis, G. Goussetis, and J. C. Vardaxoglou, “A broadband high gain resonant cavity antenna with single feed,” in Proc. 1st Eur. Conf. Antennas Propag. (EuCAP), Nice, France, pp. 1–5, (2006)

[121] D. H. Lee, Y. J. Lee, J. Yeo, R. Mittra, and W. S. Park, “Design of novel thin frequency selective surface superstrates for dual-band directivity enhancement,” IET Microw. , Antennas & Propag. , vol. 1, no. 1, pp. 248–254, (2007)

[122] E. Rodes, M. Diblanc, E. Arnaud, T. Monediere, and B. Jecko, “Dual band EBG resonator antenna using a single layer FSS,” IEEE Antennas Wireless Propag. Lett. , vol. 6, pp. 368–371, (2007)

[123] Y. H. Liu, X. P. Zhao, “Investigation of anisotropic negative permeability medium over for patch antenna,” IET Microwave and Antenas Propagation, vol. 2, pp. 737–744, (2008)

[124] H. Attia, L. Yousefi, M. M. Bait-Suwailam, M. S. Boybay, O. M. Ramahi, “Enhanced-gain microtrip antenna using engineered magnetic superstrates,” IEEE Antennas and wireless Progag. Lett., vol. 8, pp. 1198–1201, (2009)

[125] L. Moustafa and B. Jecko, “Design of a wideband highly directive EBG antenna sing double-layer frequency selective surfaces and multifeed technique for application in the ku-band,” IEEE Antennas Wireless Propag. Lett., vol. 9, pp. 342–346, (2010)

[126] Z. H. Wu and W. X. Zhang, “Broadband printed compound air-fed array antennas,” IEEE Antennas Wireless Propag. Lett. , vol. 9 pp. 187-190, (2010)

[127] B. A. Zeb, Y. Ge, K P. Esselle, Z. Sun, and M. E. Tobar, “A simple dual-band electromagnetic band gap resonator antenna based on inverted reflection phase gradient,” IEEE Trans. Antennas Propag., vol. 60, no. 10, pp. 4522–4529, (2012)

[128] M. A. Al-Tarifi, D. E. Anagnostou, A. K. Amert, and K. W. Whites, “Bandwidth enhancement of the resonant cavity antenna by using two dielectric superstrates,” IEEE Trans. Antennas Propag., vol. 61, no. 4, pp. 1898–1908, (2013)

[129] C. Mateo-Segura, A. P. Feresidis,and, and G. Goussetis “Bandwidth enhancement of 2-D leaky-wave antennas with double-layer periodic surfaces,” IEEE Trans. Antennas Propag., vol. 62, no. 7, pp. 586–593, (2014)

[130] U. Fano, ‘‘The theory of anomalous diffraction gratings and of quasi-stationary waves on metallic surfaces (Sommer- field’s waves),’’ J. Opt. Soc. Am. 31,pp. 213–222, (1941)

[131] C. Genet, van M.P. Exter, J.P. Woerdman, “Fano-type interpretation of red shifts and red tails in hole array transmission spectra,” Opt. Commun. 225, 331, (2003)

[132] L. I. Men’shikov, “Superradiance and related phenomena,” Phys. Usp. 42, pp. 107–148, (1999)

[133] F. Marquier, J. Greffet, S. Colin, F. Pardo, and J. Pelouard, “Resonant transmission through a metallic film due to coupled modes,” Opt. Express, vol. 13, no. 1, Jan., pp. 70–76, (2005)

[134] B. Munk and R. J. Lubber, “Reflection properties of two-layer dipole arrays,” IEEE Trans. Antennas Propagat., vol. AP-22, Nov., pp. 766–773, (1974)

[135] A. C. Lima and E. A. Parker, “Fabry–Perot approach to the design of double layer FSS,” Proc. Inst. Elect. Eng. Microw. Antennas Propag.,vol. 143, no. 2, pp. 157–162, (1996)

[136] R. W. Wood, “On a remarkable case of uneven distribution of light in a diffraction grating spectrum,” Philos. Mag. 4, pp. 396–402, (1902)

[137] E. L. Wood, J. R. Sambles, N. P. Cotter, S. C. Kitson, “Diffraction grating characterization using multiple-wavelength excitation of surface-plasmon polaritons,” J. Mod. Opt. 42, 1343–1349, (1995)

[138] V. Giannini, Y. Francescato, H. Amrania, C. C. Phillips, and S. A. Maier, “Fano resonances in nanoscale plasmonic systems: a parameter-free modeling approach,” Nano Lett., 11, pp. 2835−2840, (2011)

[139] Y. Francescato, V. Giannini, and S. A. Maier, “Plasmonic systems unveiled by Fano resonances,” ACS Nano, 6, pp. 1830–1838, (2012)

[140] B. Gallinet and O. J. F. Martin, “Ab initio theory of Fano resonances in plasmonic nanostructures and metamaterials,” Phys. Rev. B83, 235427, (2011)

[141] B. Gallinet and O. J. F. Martin, “Influence of electromagnetic interactions on the line shape of plasmonic Fano resonances,” ACS Nano, 5, pp. 8999−9008, (2011)

[142] C. Girard, C. Joachim, and S. Gauthier, “The physics of the near-field,” Rep. Prog. Phys. 63, pp. 893–938, (2000)

[143] Y. Ding, J. Yoon, M. H. Javed, S. H. Song, and R. Magnusson, “Mapping surface-plasmon polaritons and cavity modes in extraordinary optical transmission,” IEEE Photon. J., vol. 3, no. 3, Jun., pp. 365–374, (2011)

[144] J. D. Jackson, Classical Electrodynamics, 2nd edition, Wiley, New York, 1975.

[145] A. P. Hibbins, J. R. Sambles, and C. R. Lawrence, “The coupling of microwave radiation to surface plasmon polaritons and guided modes via dielectric gratings,” J. Appl.Phys. 87, 2677, (2000)

[146] C. R. Simovski, P. A. Belov, and H. Sailing, “Backward wave region and negative material parameters of a structure formed by lattices of wires and split-ring resonators,” IEEE Trans. Antennas Propagat., vol. 51, Oct., pp. 2582–2591, (2003).

[147] X. Chen, T. M. Grzegorczyk, B. I. Wu, J. Pacheco, and J. A. Kong, “Robust method to retrieve the constitutive effective parameters of metamaterials,” Phys. Rev. E 70, 016608 , (2004)

[148] D. R. Smith D. C. Vier, Th. Koschny, and C. M. Soukoulis, “Electromagnetic parameter retrieval from inhomogeneous metamaterials,” Phys. Rev. E 71, 036617, (2005)

[149] E. L. Holzman, “Wideband measurement of the dielectric constant of an FR4 substrate using a parallel-coupled microstrip resonator,” IEEE Trans. on Microw. Theory Tech., vol. 54, no. 7, pp. 3127−3130, (2006)

[150] D. C. Thompson, O. Tantot, H. Jallageas, G. E. Ponchak, M. M. Tentzeris, and J. Papapolymerou, “Characterization of liquid crystal polymer (LCP) material and transmission lines on LCP substrates from 30 to 110 GHz,” IEEE Trans. Microw. Theory Tech., vol. 52, no. 4, Apr., pp. 1343–1352, (2004)

[151] I. V. Lindell, “Image theory for the soft and hard surface,” IEEE Trans. Antennas Propagat., vol. 43, pp. 117−119, (1995)

[152] H. T. Chen, “Interference theory of metamaterial perfect absorbers,” Opt. Express 20, pp. 7165–7172, (2012)

[153] K. Kanjanasit and C. H. Wang, “Fano resonance in a metamaterial consisting of two identical arrays of square metallic patch elements separated by a dielectric spacer,” Appl. Phys. Lett. vol. 102, p. 251108, (2013)

[154] R. N. Simons, Coplanar Waveguide Circuits, Components and Systems, Wiley-Interscience, New York, USA, (2001)

[155] C. A. Balanis, Antenna Theory: Analysis and Design, 3rd ed. NewYork: John Wiley & Sons, Inc., Hoboken, (2005)

[156] A. R. Lopez, “Double-tuned impedance matching,” IEEE Antennas and Propag. Mag. Vol. 54, no. 2, pp. 109−116, (2012)

[157] G. Zheng , A. Z. Elsherbeni, and C. E. Smith “A coplanar waveguide bow-tie aperture antenna,” Proc. IEEE Int. AP-S Symp., vol. 1, pp. 564−567, (2002)

[158] Y. C. Chen , S. Y. Chen, and P. Hsu, “Modification of radiation patterns of first harmonic mode of slot dipole for dual-frequency operation,” IEEE Trans. Antennas Propag., vol. 59, no. 7, pp. 2707−2710, (2011)

[159] W. H. Tu, “Compact harmonic-suppressedcoplanar waveguide-fed inductively coupled slot antenna,” IEEE Antennas Wirel. Propag. Lett., vol. 7, pp.543−545, (2008)

[160] C. C. Yu and X. C. Lin, “A wideband single chip inductor-loaded CPW-fed inductive slot antenna,” IEEE Trans. Antennas Propag., vol. 56, no. 5, pp. 1498−1501, (2008)

[161] R. Y. Fang, C. T. Wang and C. L. Wang, “Coplanar-to-rectangular waveguide transitions using slot antennas,” IEEE Trans. Compon. Packag., Manuf. Technol., vol. 1, no. 5, pp. 681–688, (2011)

[162] S. M. Deng and M. D. Wu, “Impedance characteristics of microstrip antennas excited by coplanar waveguides with inductive or capacitive coupling slots,” IEEE Microwave and Guide Wave Lett., Vol. 5, No. 11, pp. 391–393, (1995)

[163] J. B. Keller, “Geometrical theory of diffraction,” J. Opt. Soc. Am., vol. 52, no. 2, pp. 116–130, (1962)

[164] B. Zheng and Z. Shen, “Effect of a finite ground plane on microstrip-fed cavity-backed slot antennas,” IEEE Trans. Antennas Propag., vol. 53, no. 2, Feb., pp. 862–865, (2005)

[165] J. S. Colburn and Y. Rahmat-Samii, “Patch antennas on externally perforated high dielectric constant substrates,” IEEE Trans. Antennas Propag., vol. 47, no. 12, Dec., pp. 1785–1794, (1999)

[166] M. Seyyed-Esfahlan, M. Kaynak, B. Gottel, and I. Tekin, “SiGe process integrated on-chip dipole antenna on finite-size ground plane,” IEEE Antennas Wirel. Propag. Lett., vol. 12, pp.1260–1263, (2013)

[167] C. T. Tai and S. A. Long, Dipoles and monopoles, in Antenna Engineering Handbook, J. L. Volakis, Ed., 4th ed. New York: McGraw Hill, (2007)

[168] A. R. Lopez, “Wheeler and Fano impedance matching,” IEEE Ant. and Prop. Mag., 49, 4, Aug., pp. 116–119, (2007)

[169] V. Iyer, S. N. Makarov, D. D. Harty, F. Nekoogar, and R. Ludwig, “A lumped circuit for wideband impedance matching of a non-resonant, short dipole or monopole antenna,” IEEE Trans. Antennas Propag. , vol. 58, no. 1, pp. 18-26, (2010)

[170] M. A. Antoniades and G. V. Eleftheriades, “A multiband monopole antenna with an embedded reactance-cancelling transmission-line matching network,” IEEE Antennas Wirel. Propag. Lett., vol. 9, pp. 1107–1110, (2010)

[171] P. I. Day, “Transmission line transformation between arbitrary impedances using the smith chart,” IEEE Trans. Microwave Theory and Tech., vol. 23, pp. 772–773, (1975)

[172] H. R. Stuart, S. R. Best, and A. D. Yaghjian, “Limitations in relating quality factor to bandwidth in a double resonance small antenna,” IEEE Antennas Wirel. Propag. Lett., vol. 6, pp. 460–463, (2007)

[173] W. Geyi, P. Jarmuszewski, and Y. Qi, “The Foster reactance theorem for antennas and radiation Q,” IEEE Trans. Antennas Propag., vol. 48, pp. 401–408, (2000)

[174] M. Chongcheawchamnan, S. Patisang, S. Srisathit, R. Phromloungsri, and S. Bunnjaweht, “Analysis and design of a three-section transmission-line transformer,” IEEE Trans. Microwave Theory Tech., vol. 53, no.7, Jul., pp. 2458–2462, (2005)

[175] W. S. T. Rowe and R. B. Waterhouse, “Investigation into the performance of proximity coupled stacked patches,” IEEE Trans. Antennas Propag., vol. 54, no. 6, Jun., pp. 1693–1698, (2006)

[176] O. Quevedo-Teruel, Z. Sipus, and E. Rajo-Iglesias, “Characterization and reduction of mutual coupling between stacked patches,” IEEE Trans. Antennas Propag., vol. 59, no. 3, Mar., pp. 1031–1036, (2011)

[177] D. M. Pozar, “Input impedance and mutual coupling of rectangular microstrip antennas,” IEEE Trans. Antennas Propagat., vol. AP-30, pp. 1191−1196, (1982)

[178] R. Maboudian, “Surface processes in MEMS technology,” Surface science report, vol. 30, pp. 207−269, (1998)

[179] J. M. Bustillo, R. T. Howe, R. S. Muller, “Surface micromachining for microelectromachanical systems,” Proceedings of the IEEE, vol. 86, no. 8, pp. 1552−1574, (1998)

[180] A. Hierlemann, O. Brand, C. Hangleitner, and H. Baltes, “Microfabrication techniques for chemical/biosensors,” Proceedings of the IEEE, vol. 91, no. 6, p. 839, (2003)

[181] B. Riddle, J. Baker-Jarvis, and J. Krupka, “Complex permittivity measurements of common plastics over variable temperatures,” IEEE Trans. on Microw. Theory Tech., vol. 54, no. 7, pp. 3127−2130, (2006)

[182] Y. Huang, S. Liu, and W. Yang, and C. Yu “Surface roughness analysis and improvement of PMMA-based microfluidic chip chambers by CO_2 laser cutting,” Applied surface science, pp. 1675−1678, (2010)

[183] T. F. Hong, W. J. Ju, M. C. Wu, C. H. Tai, and C. H. Tsai, “Rapid prototyping of PMMA microfluidic chips utilizing a CO_2 laser,” Microfluid Nanofluid, vol. 9, pp. 1125−1133, (2010)

[184] N. C. Nayak, Y. C. Lam, C. Y. Yue, and A. T. Sinha, “CO_2-laser micromachining of PMMA: the effect of polymer molecular weight,” J. Micromech. Microeng. 18, p. 095020, (2008)

[185] N. B. Dahotre and S. P. Harimkar, Laser Fabrication and Machining of Materials, Springer, US, (2008)

[186] L. Yu, F. E. H. Tay, G. Xu, B. Chen, M. Avram, and C. Iliescu, “Adhesive bonding with SU-8 at wafer level for microfluidic devices,” J. Phys.: Conf. Ser. 34, pp. 776–781, (2006)

[187] G. Mayhew-Ridgers, P. A. Jaarsveld, J. W. Odendaal, and J. Joubert “Accurate gain measurements for large antennas using modified gain-transfer method,” IEEE Antennas Wireless Propag. Lett., vol. 13, pp. 369–371, (2014)

[188] S. K. Pavuluri, C. H. Wang, and A. J. Sangster, “A high-performance aperture-coupled patch antenna supported by a micromachined polymer ring,” IEEE Antennas Wireless Propag. Lett., vol. 7, Sep., pp. 283–286, (2008)

[189] A. A. Oliner and D. R. Jackson, Leaky-wave antennas, in Antenna Engineering Handbook, J. L. Volakis, Ed. New York: McGraw Hill, (2007)

[190] G. Lovat, P. Burghignoli, and D. R. Jackson, “Fundamental properties and optimization of broadside radiation from uniform leaky-wave antennas,” IEEE Trans. Antennas Propag., vol. 54, no. 5, May, pp.1442–1452, (2006)

[191] A. Sutinjo,M. Okoniewski, R. H. Johnston, “Beam-splitting condition in a broadside symmetric leaky-wave antenna of finite length,” IEEE Antennas Wireless Propag. Lett. , vol. 7, pp. 609–612, (2008)

[192] Y. F. Lu and Y. C. Lin, “A hybrid approach for finite-size Fabry-Pérot antenna design with fast and accurate estimation on directivity and aperture efficiency,” IEEE Trans. on Antennas Propag., vol. 61, no. 11, Nov., pp. 5395–5401, (2013)

[193] L. Moustafa and B. Jecko, “EBG Structure with wide defect band for broadband cavity antenna applications,” IEEE Antennas Wireless Propag. Lett. , vol. 7, pp. 693–696, (2008)

[194] J. Coonrod (Rogers Corp.), “Understanding when to use FR-4 or high frequency laminates,” Onboard Technology, Sep., pp. 26-30, (2011)

[195] B. A. Munk, Frequency Selective Surfaces: Theory and Design, 1st ed. New York: John Wiley and Sons, Ltd., (2000)

[196] K. Carver and J. Mink, “Microstrip antenna technology,” IEEE Trans. Antennas Propag., vol. 29, Dec., pp. 2–24, (1981)

[197] G. Kumar and K. P. Ray, Broadband microstrip antennas, Artech house, Inc,. Norwood, MA, (2003)